UNIVERSITÀ DEGLI STUDI DI TRIESTE

XXXVII CICLO DEL DOTTORATO DI RICERCA IN FISICA

Ultrafast dynamics of strongly-coupled charge-density-wave systems

SETTORE SCIENTIFICO-DISCIPLINARE: FIS03/FISICA DELLA MATERIA

Dottorando:
Manuel Tuniz

Coordinatore:
Prof. Francesco Longo

Supervisore di Tesi:
Dott. Federico Cilento

Co-supervisori di Tesi:
Prof. Fulvio Parmigiani
Dott. Wibke Bronsch

ANNO ACCADEMICO 2023-2024

ABSTRACT

This thesis is devoted to the study of the non-equilibrium dynamics of two charge-density-wave (CDW) materials in which the onset of the phase transition is determined by the presence of a peak in the momentum-dependent electron-phonon coupling (EPC). The existence of a strong EPC heavily affects the properties of the resulting CDW phase, determining in particular the nature of the thermal disordering. Given the strong interplay between the structural and the electronic degrees of freedom that characterizes the CDW systems, their out-of-equilibrium response has been investigated by combining time-resolved reflectivity and Time- and Angle-Resolved Photoelectron Spectroscopy (TR-ARPES) experiments. The combination of these techniques allows to access both the electronic band structure and the collective excitation of the CDW ground state.

The first system investigated is the transition-metal dichalcogenide (TMDC) compound VTe_2. Time-resolved reflectivity experiments have allowed to unveil the presence of two amplitude modes (AMs) of the low-temperature CDW phase. By implementing a double-pump excitation scheme, we demonstrated that, despite being linked to the same electronic order parameter, these two collective excitations are independent.

The study of the light-induced quench of the electronic order has revealed that the closure of the CDW gap is not driven by the two AMs of the system, but is instead dominated by an incoherent process. By applying a three-temperature model (3TM), we demonstrated that the quench of the CDW gap arises as a consequence of the excitation of a subset of strongly-coupled phonon modes which determines a loss of the long-range CDW order. These results therefore suggest that the phase transition is driven by non-CDW phonons that interact with the CDW order, thus highlighting the role played by the phonon-phonon interactions.

The second system investigated is the kagome compound ScV_6Sn_6. Systematic time-resolved reflectivity experiments, corroborated by DFT simulations, have allowed to unveil the AM of the system and to highlight the marked resilience of this compound to a near-infrared excitation. Furthermore, by applying a lattice strain to ScV_6Sn_6 crystals, we demonstrated that an elongation of the *c*-axis determines a reduction of the temperature-dependent softening of the CDW amplitude mode. DFT simulations have shown that this reduction of the AM softening arises from an enhancement of the CDW phase, that in the strained compound is characterized by a larger energy gap and larger lattice displacements.

Our findings suggest that the light-induced phase transition in the strongly-coupled CDW materials VTe_2 and ScV_6Sn_6 arises only thanks to increased lattice fluctuations, and thus, its understanding requires the modeling of the electron-phonon and phonon-phonon interactions. Due to the particular nature of the phase transition, the light-induced switching between the CDW and the normal phase turns out to be slower with respect to the one observed in compounds in which the transition is determined by purely electronic phenomena.

CONTENTS

LIST OF ACRONYMS

1D one-dimensional

2D two-dimensional

2TM two-temperature model

3D three-dimensional

3TM three-temperature model

AB antibonding

AM amplitude mode

ARPES angle-resolved photoelectron spectroscopy

B bonding

BBO β-Barium borate

BCS Bardeen-Cooper-Schrieffer

BE Bose-Einstein

BZ Brillouin zone

CDW charge density wave

CEM channeltron electron multiplier

DECP displacive excitation of coherent phonons

DEDC differential energy distribution curve

DFPT density functional perturbation theory

DFT density functional theory

DOS density of states

EDC energy distribution curve

EL-PH electron-phonon

EPC electron-phonon coupling

FD Fermi-Dirac

FS Fermi surface

FT Fourier transform

FWHM full width at half maximum

HFHM half width at half maximum

GR grooves

HHG high-harmonic generation

HT high-temperature

IXS inelastic X-Ray scattering

LAPE laser-assisted photoemission

LEED low-energy electron diffraction

LT low-temperature

MDC momentum distribution curve

MF mean-field

NB non-bonding

OPA optical parametric amplifier

OPM off-plane mount

PDOS projected density of states

PH–PH phonon-phonon

PLD periodic lattice distortion

PM phase mode

QE Quantum Espresso

SOC spin-orbit coupling

TMDC transition-metal dichalcogenides

TR–ARPES time- and angle- resolved photoelectron spectroscopy

TR–OS time-resolved optical spectroscopy

VHS van Hove singularity

WAM wide-angle mode

XRD X-Ray diffraction

1 INTRODUCTION

The critical need for faster, smaller and more energy-efficient nanotechnologies requires the development of a new generation of functional materials. This quest could be accomplished thanks to the use of the so-called quantum materials, whose discovery has revolutionized the fields of both condensed matter and material engineering [1, 2]. The growing interest in this class of materials resides on the fact that the quantum nature of these compounds manifests at a macroscopic level [1]. Indeed, quantum materials exhibit rich phase diagrams due to the coupling of charge, lattice, spin and orbital degrees of freedom, making these compounds highly attractive also for fundamental studies, besides their technological applications. These intertwined interactions can give rise to fascinating phenomena like high-temperature superconductivity [3], spin- and charge-density waves [4] and magnetism [5]. The emergence of such states is controlled by a competition of correlation and fluctuation effects, that results in a phase transition at a specific critical temperature. Thus, the understanding of this delicate balance between correlation and fluctuation effects constitutes a first crucial step for the realization of a new generation of electronic devices [2].

Among the plethora of interactions relevant in quantum materials, electron-phonon coupling (EPC) has been a persistent subject of study since it stands at the origin of a broad variety of phenomena. While a strong EPC is desirable in many quantum systems like conventional superconductors [6], it is deleterious for conductivity in normal metals, hindering the application of many compounds as electronic devices [7]. One of the manifestations of strong EPC which is lately attracting a large interest is the appearance of a charge-density wave (CDW) phase in many materials [8–10]. In CDW systems, electrons and phonons cooperatively interact to form a new symmetry broken state below a critical transition temperature [11]. The resulting low-temperature phase is characterized by the coexistence of a spatial modulation of the electron density and a periodic distortion of the crystalline structure. The phase transition towards the CDW phase therefore takes place only thanks to a complex balance between the energy cost required to distort the crystal lattice and the energy gain deriving from the modifications of the electronic band structure. Furthermore, the CDW ground state exhibits new low-energy collective excitations, named amplitude (AM) and phase (PM) modes, corresponding to distortions and translations of the modulated charge density [11].

The complex interplay between electronic and structural degrees of freedom that characterizes the CDW systems naturally reveals the fundamental role played by the electron-phonon coupling in the stabilization of the charge-ordered phase [4, 8]. Despite the fact that conventionally the charge-density wave transition is treated in the weak EPC limit [4], the discovery of compounds characterized by the presence of a strong momentum-dependent EPC has motivated both theoretical [12–15] and experimental studies [16–18]. Due to the complexity of these systems, however, a universal microscopic picture is far from being achieved [8].

Giving the fundamental role played by the EPC in determining the CDW phase transition, an increase of its strength can lead to a dramatic change in the properties of the low-temperature charge-ordered phase. One of the main differences with respect to the weakly-coupled CDW compounds resides in the presence of much larger energy gaps with respect to their critical temperatures. Indeed, while in the weakly-coupled systems the ratio between gap size and critical temperature agrees with the one predicted by the BCS theory of superconductivity ($2\Delta_{CDW}/k_B T_{CDW} \approx 3.52$ [6]), in the strongly-coupled systems this ratio turns out to be more than two times larger [12]. This crucial difference dramatically affects the origin of the thermal disordering which determines the transition towards the normal phase. Indeed, while in the

weak-coupling limit the phase transition is driven by the electronic entropy, in the strong-coupling limit the transition is driven by the lattice entropy, resulting in an order-disorder transition [12, 19]. These systems therefore constitute an ideal platform to study the interplay between lattice fluctuations and the formation of a coherent macroscopically ordered CDW phase. The understanding of the mechanisms resulting in the melting of a macroscopically ordered CDW phase and the control of the CDW phase itself, constitute the first building bricks to develop a new generation of electronic devices based on these materials. More generally, the importance of lattice fluctuations goes beyond the study of charge-density wave systems considered in this thesis, since they are thought to play a crucial role in the phase transitions observed in many quantum materials [20, 21].

Due to the strong interplay between the electronic and the structural degrees of freedom that characterize the CDW compounds, a profound investigation of these systems requires the use of complementary techniques, able to access the different properties of the compounds under investigation. The most direct experimental access to the electronic properties of a material is provided by the Angle-Resolved Photoelectron Spectroscopy (ARPES). This technique is based on the photoelectric effect, for which an electron can be emitted from a material as a consequence of the absorption of a photon of sufficient energy. The energy and the momentum conservation laws allow to retrieve, from the measurement of the energy and the emission angle of the electron, the energy and the crystal momentum of the electron inside the material. Moreover, since it encodes information on the band structure of the system, an ARPES measurement can unveil the interactions felt by the electron before the photoemission [22]. Under equilibrium conditions, however, the different interactions governing the microscopic behavior of a system occur simultaneously on similar energy scales, hence making it challenging to tell them apart by inspection of the equilibrium band structure alone. An approach to disentangle different coexisting interaction is to extend the ARPES technique to the time domain, exploiting the different timescales over which these interactions evolve. The extension of ARPES to the time domain, with the realization of the Time- and Angle-Resolved Photoelectron Spectroscopy (TR-ARPES), is done by exploiting the so-called *pump-probe* scheme. This approach is based on the use of two kinds of ultrashort light pulses, aimed respectively to impulsively excite and to measure the relaxation dynamics of the system towards the equilibrium conditions. By accessing the non-equilibrium dynamics of the electronic band structure, important insights on the processes determining the equilibrium properties of the compound under investigation can be gained [23, 24].

The strength of the pump-probe approach resides in the fact that it can be extended to different techniques, generalizing them to the time domain [25–27]. Among these techniques, time-resolved optical spectroscopy (TR-OS) stands as one of the most diffuse realizations of this experimental scheme. In particular, TR-OS and especially time-resolved reflectivity, have proven to be a valuable tool for the study of lattice vibrations, thanks to their high sensitivity and high signal-to-noise ratio. For this reason this technique has been widely adopted to study the low-energy excitations of many CDW compounds [28–31]. Therefore the combination of TR-ARPES and time-resolved reflectivity experiments allows to give access to both electronic band structure and low-energy excitations of the CDW phase, providing a more complete picture of the system under investigation.

THESIS OVERVIEW

This thesis is devoted to the study of the out-of-equilibrium dynamics of two charge-density wave systems: the transition metal dichalcogenide compound VTe_2 and the kagome compound ScV_6Sn_6. The strong momentum depended EPC that stands at the origin of these CDW phases affects both the equilibrium and the non-equilibrium properties of these compounds, making them ideal candidates to investigate the mechanism governing the melting of macroscopically

ordered CDW phases and to study the possibility of controlling their properties by means of external stimuli.

The non-equilibrium dynamics of these CDW systems are investigated by combining TR-ARPES and time-resolved reflectivity experiments. Hence, particular attention is drawn to the characterization of the CDW amplitude modes and to the study of the light-induced quench of their electronic order. Moreover, the possibility of manipulating the CDW phase of these compounds by means of lattice strain is also investigated. All the experimental results presented have been obtained by exploiting the high-harmonic generation (HHG) source and the TR-OS setups developed in the T-ReX laboratory at Elettra Sincrotrone Trieste.

The thesis is structured as follows:

- Chapter 2 presents a brief theoretical introduction of the charge-density-wave transition in one-dimensional systems. Specifically, after having presented the Peierls theory for the CDW transition in the weak-coupling limit, particular attention is drawn to the discussion of the CDW transition in systems characterized by the presence of a strong EPC. The chapter ends with the Ginzburg-Landau theory for the fundamental low-energy excitations of the CDW ground state.

- Chapter 3 introduces the basic concepts of the ARPES, TR-ARPES and TR-OS techniques. In particular, the physical quantities that can be extracted from an ARPES experiment are discussed together with those aspects that turn out to be critical in the extension of this technique to the time domain. This introduction is then followed by a brief comparison between TR-ARPES and TR-OS, aimed to highlight the complementary aspects of the two techniques. The chapter ends with a description of the experimental setups employed to perform the measurements reported in this thesis.

- Chapter 4 presents the time-resolved reflectivity experiments performed on the TMDC compound VTe_2. Specifically, after having discussed the lattice reconstruction that occurs in the low-temperature phase, we present a systematic temperature-dependent study of the phonon modes that characterize the low-temperature charge-ordered state. From this study, with the aid of density functional perturbation theory (DFPT) simulations, we unveil the presence of two amplitude modes of the CDW phase. Finally, by applying a double-pulse excitation scheme, we demonstrate that, even if coupled to the same electronic order parameter, the two amplitude modes are independent.

- Chapter 5 presents the time-resolved ARPES experiments performed on VTe_2. Given the presence of multiple domains in the CDW state, these experiments have required the realization of a strain device aimed to promote the formation of larger domains. The chapter therefore starts with the discussion of the domain structure of VTe_2 and the presentation of the strain device developed for TR-ARPES experiments. This introductory part is followed by the presentation of the time-resolved photoemission experiments performed. These measurements show that the quench of the electronic order, with the consequent closure of the CDW gap, is not dominated by the excitation of the CDW amplitude modes, but is instead driven by an incoherent process that evolves on longer timescales. In the last part of the chapter, by applying a so-called three-temperature model, we show that the CDW gap dynamics observed can be explained by considering the incoherent excitation of a subset of strongly-coupled optical phonon modes triggered by the hot carrier relaxation.

- Chapter 6 discusses the time-resolved reflectivity experiments performed on the kagome compound ScV_6Sn_6. After having presented the general properties of the kagome compounds and having discussed the emergence of the CDW phase in ScV_6Sn_6, we present a temperature-dependent study of the non-equilibrium reflectivity across the CDW transition. This investigation, that has allowed to identify the CDW amplitude

mode, is then followed by the presentation of a fluence-dependent study which highlights the resilience of this compound to near-infrared photoexcitation. Finally, we demonstrate that the application of a modest uniaxial strain on a ScV_6Sn_6 crystal, results in a reduction of the temperature-dependent softening of the CDW amplitude mode. This result, corroborated by extensive DFT simulations, suggests a possible path to enhance the CDW order in ScV_6Sn_6.

2 CHARGE-DENSITY-WAVE SYSTEMS

This chapter is devoted to a brief theoretical introduction to the charge-density-wave (CDW) transition in simple one-dimensional systems. Specifically, after having introduced the Peierls theory for the CDW transition in the weak electron-phonon coupling limit and having considered the role played by the lattice fluctuations, particular attention will be drawn to the discussion of the CDW transition in the strong electron-phonon coupling limit. Finally, in the last section of this chapter, the excitations of the CDW ground state will be presented in the framework of the Ginzburg-Landau theory.

2.1 THE PEIERLS TRANSITION

As firstly pointed out by Peierls in 1955, a one dimensional metal in which the interaction between electrons and lattice is taken into account, is not stable at low temperatures [32]. As the name suggests, the resulting charge-density-wave ground state consists of a periodically modulated electronic charge density and a periodic lattice distortion (PLD) with the same wave vector (shown in Fig. 2.1(a)). As a consequence of the interaction between the two subsystems, both the electronic and phononic spectra are strongly affected by the CDW formation [11]. Said δE_{ele} the change in the energy of the electronic subsystem, and δE_{lat} the change in the total lattice energy due to the atomic rearrangement, the transition towards the CDW phase is possible only if the gain in the electronic part overcomes the cost required to distort the lattice, namely:

$$\delta E_{ele} + \delta E_{lat} < 0. \tag{2.1}$$

The simplest treatment to study the charge-density-wave transition is based on the description of a coupled one-dimensional system in which the ions form a linear chain and the electrons a one dimensional electron gas [8, 11]. The phase transition of such a system is presented in the following section.

2.2 CDW TRANSITION IN THE WEAK-COUPLING LIMIT

2.2.1 A mean-field theory approach

In the weak electron-phonon coupling (EPC) limit, the Peierls transition of a one-dimensional electron-lattice system can be described quantitatively by a mean-field (MF) theory. The simplest approach, here presented, takes advantage of the independent electron, harmonic and adiabatic approximations. In this framework, the coupled electron-lattice system is described by the Fröhlich Hamiltonian [33]:

$$H_{PI} = \sum_{\mathbf{k}} \epsilon_{\mathbf{k}} a^{\dagger}_{\mathbf{k}} a_{\mathbf{k}} + \sum_{\mathbf{q}} \hbar\omega_{\mathbf{q}} b^{\dagger}_{\mathbf{q}} b_{\mathbf{q}} + \frac{1}{N} \sum_{\mathbf{k},\mathbf{q}} g_{\mathbf{q}} a^{\dagger}_{\mathbf{k}+\mathbf{q}} a_{\mathbf{k}} (b^{\dagger}_{-\mathbf{q}} + b_{\mathbf{q}}), \tag{2.2}$$

where $\epsilon_{\mathbf{k}}$ is the energy of the electron in the state $\mathbf{k}$, $a^{\dagger}_{\mathbf{k}}$ and $a_{\mathbf{k}}$ are the creation and annihilation operators for state $\mathbf{k}$, $\omega_{\mathbf{q}}$ is the frequency of the phonon mode at the wave vector $\mathbf{q}$, $b^{\dagger}_{\mathbf{q}}$ and $b_{\mathbf{q}}$ are the creation and annihilation operators for a phonon at $\mathbf{q}$. Finally, $g_{\mathbf{q}}$ is the

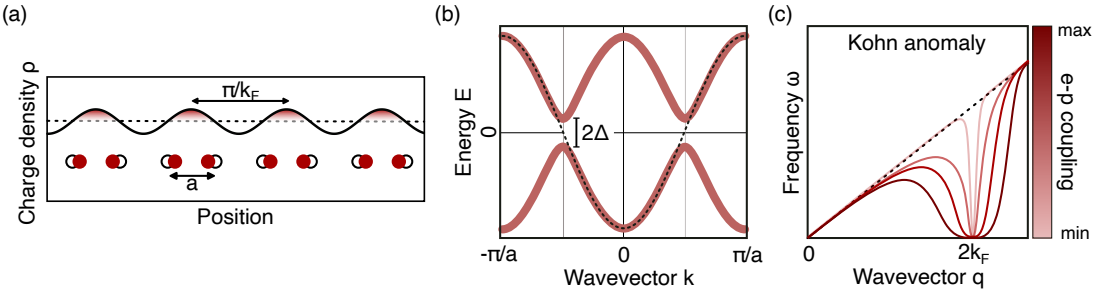

Figure 2.1: (a) Schematic representation of the CDW/PLD showing the modulations of the conduction electron density and of the ionic position. The normal state is characterized by a lattice parameter a and a constant electron density (dashed line). (b) Schematic representation of the electronic band dispersion in the normal state (dashed line) and in the CDW state (red line). The opening of the CDW gap at $\pi/2a$ is also shown. (c) Acoustic phonon anomaly for $T \ll T_{\mathrm{CDW}}^{\mathrm{MF}}$ and for different EPC values. For a weak EPC the phonon anomaly is localized in reciprocal space around $\mathbf{q}$=2$\mathbf{k}_{\mathrm{F}}$, while for the case of strong EPC the renormalization of the phonon mode frequency takes place on a much larger region of reciprocal space. Adapted from [34].

electron-phonon coupling constant (assumed to be independent of $\mathbf{k}$) and N is the number of lattice sites per unit length [8, 11].

As anticipated above, the coupled electron-phonon (e-p) system described by Eq. (2.2) is unstable at low temperatures and this instability has fundamental consequences for both lattice and electronic subsystems. In the following we consider a 1D chain with lattice parameter a (shown in Fig. 2.1(a)), and a single half-filled band with tight-binding band dispersion:

$$\epsilon_{\mathbf{k}} = -E_{\mathrm{F}} \cos(ka), \tag{2.3}$$

where E_{F} is the Fermi energy and $|\mathbf{k}_{\mathrm{F}}|$=2$\pi$/a is the Fermi wave vector. This system is characterized by a diverging electronic susceptibility at $\mathbf{q}$=2$\mathbf{k}_{\mathrm{F}}$ for $T \to 0$:

$$\chi_0(2\mathbf{k}_F, T) = \frac{1}{2} N(0) \ln\left(\frac{2.28 E_{\mathrm{F}}}{\mathrm{k_B} T}\right), \tag{2.4}$$

where $N(0)$ is the density of states at the Fermi level at high temperature. Due to the presence of a finite electron-phonon coupling in the system, this sharp temperature-dependent peaking of the electronic susceptibility causes a strong renormalization of the frequency of an acoustic phonon mode, in a narrow range around the wave vector $\mathbf{q}$=2$\mathbf{k}_{\mathrm{F}}$ (shown in Fig. 2.1(c)) [8, 12]. This phenomenon is generally referred as Kohn anomaly, and the frequency of this peculiar phonon mode (often named "soft phonon mode") is described by the expression:

$$\tilde{\omega}_{\mathbf{q}}^2 = \omega_{\mathbf{q}}^2 \left(1 - \frac{4 g_{\mathbf{q}}^2}{\hbar \omega_{\mathbf{q}}} \chi_0(\mathbf{q})\right), \tag{2.5}$$

where $\tilde{\omega}_{\mathbf{q}}$ and $\omega_{\mathbf{q}}$ denote the renormalized and the normal-state phonon frequency respectively [8]. Hence, for a non-zero electron-phonon coupling constant $g_{\mathbf{q}}$ we have:

$$\tilde{\omega}_{\mathbf{q}}^2 \to 0 \tag{2.6}$$

for a finite temperature $T = T_{\mathrm{CDW}}^{\mathrm{MF}}$. This complete softening of an acoustic phonon mode at the wave vector $\mathbf{q}_0$ signals the phase transition towards a state with a froze-in periodic lattice distortion (PLD) characterized by a wavelength $\lambda_0 = 2\pi/|\mathbf{q}_0| = \pi/|\mathbf{k}_{\mathrm{F}}|$ (shown in Fig. 2.1(a)) [8, 11, 35]. Close to the transition temperature, the frequency of the mode is described by the equation:

$$\tilde{\omega}_{\mathbf{q}}^2 = \omega_{\mathbf{q}}^2 \left(\frac{T - T_{\mathrm{CDW}}^{\mathrm{MF}}}{T_{\mathrm{CDW}}^{\mathrm{MF}}}\right). \tag{2.7}$$

It is worth noting that since $\mathbf{k}_F$ is determined by the filling of the band structure, in general the periodicity of the lattice reconstruction will be incommensurate with the underlying crystal structure.

From equations (2.4)-(2.6) it is possible to obtain the mean-field transition temperature:

$$k_B T_{CDW}^{MF} = 2.28 E_F e^{-1/\lambda}, \tag{2.8}$$

where λ is the dimensionless electron-phonon coupling constant defined as:

$$\lambda = \frac{2 g_{\mathbf{q}0}^2 N(0)}{\hbar \omega_{\mathbf{q}0}}. \tag{2.9}$$

The renormalized phonon frequency which signals the transition to a state characterized by a frozen-in lattice distortion finds its formalization on a macroscopically occupied phonon mode with non-vanishing expectation values $\langle b_{2k_F} \rangle = \langle b_{-2k_F}^\dagger \rangle$ [11]. Therefore, the order parameter of the CDW phase can be defined as:

$$\mathbf{\Delta} = |\mathbf{\Delta}| e^{i\phi} = g \left(\langle b_{2k_F} \rangle + \langle b_{-2k_F}^\dagger \rangle \right), \tag{2.10}$$

where g is the e-p coupling constant, here assumed to be independent of $\mathbf{q}$ [11]. By rewriting the lattice displacement using the expression for the order parameter, and by reconsidering Eq. (2.2), it is possible to show that, instead of the dispersion typical of a metallic system, in the CDW state the spectrum of excitations develops a gap (shown in Fig. 2.1(b)). In the special case considered here, with half-filled tight binding bands, the normal-state band $\epsilon_{\mathbf{k}}$ splits in two branches:

$$E_{1,2}(\mathbf{k}) = \frac{\epsilon_{\mathbf{k}} + \epsilon_{\mathbf{k}+\mathbf{q}0}}{2} \pm \sqrt{\left(\frac{\epsilon_{\mathbf{k}} - \epsilon_{\mathbf{k}+\mathbf{q}0}}{2} \right)^2 + \Delta^2}, \tag{2.11}$$

separated by an energy gap of size 2Δ at $\mathbf{q}_0/2 = \mathbf{k}_F$. The opening of a uniform and complete gap at the Fermi level deeply affects the electronic density of states N(E), which now shows a divergence at $E = \pm\Delta$ and is zero in between [8]. The size of the energy gap that opens in the low temperature phase is related to the displacement of the atoms $u_{\mathbf{q}0}$, the electron-phonon coupling parameter $g_{\mathbf{q}0}$ and the unrenormalized phonon frequency $\omega_{\mathbf{q}0}$ by the expression:

$$\Delta = u_{\mathbf{q}0} g_{\mathbf{q}0} \sqrt{\frac{2M\omega_{\mathbf{q}0}}{\hbar}}, \tag{2.12}$$

where M is the ionic mass. In the weak-coupling limit and for $T = 0$, it can be shown that the change in the sum of the occupied one-electron energies satisfies the expression:

$$\delta E_{ele} \propto \frac{\Delta^2}{E_F} ln \left(\frac{\Delta}{E_F} \right), \tag{2.13}$$

and from the minimization of the total energy change, $\delta E_{ele} + \delta E_{lat}$, it is possible to extract the zero temperature energy gap:

$$\Delta(0) = 4 E_F e^{-1/\lambda}. \tag{2.14}$$

Finally, by using Eq. (2.8) it is possible to obtain the well known BCS relation between the zero-temperature gap and the mean field transition temperature:

$$2\Delta(0) = 3.52 k_B T_{CDW}. \tag{2.15}$$

At this point it is useful to reconsider the stability condition introduced with Eq. (2.1). In the model considered, the static displacement $u_{\mathbf{q}}$, that arises from the softening of the phonon mode at $\mathbf{q}$, sets up the potential:

$$v_{\mathbf{q}} = g_{\mathbf{q}} u_{\mathbf{q}} \sqrt{\frac{2M\omega_{\mathbf{q}}}{\hbar}}, \tag{2.16}$$

and the associated lattice strain energy is given by:

$$\delta E_{lat} = \frac{1}{2} M \omega_{\mathbf{q}}^2 u_{\mathbf{q}}^2. \tag{2.17}$$

The change in the total energy of the electronic system due to the potential $v_{\mathbf{q}}$ can be calculated using the second order perturbation theory:

$$\delta E_{ele} = -\left|v_{\mathbf{q}}\right|^2 \chi_0(\mathbf{q}). \tag{2.18}$$

Therefore imposing $\delta E_{ele} + \delta E_{lat} < 0$ we obtain the expression:

$$\frac{4g_{\mathbf{q}}^2}{\hbar\omega_{\mathbf{q}}} > \frac{1}{\chi_0(\mathbf{q})}, \tag{2.19}$$

which shows that the charge-density-wave transition is favored by the presence of a large electron-phonon coupling constant $g_{\mathbf{q}}$ and by a large electronic susceptibility $\chi_0(\mathbf{q})$ [8]. It is worth noting that the divergence of the susceptibility discussed so far arises from the particular topology of the Fermi surface in the one-dimensional case [11]. Indeed, the non-interacting susceptibility for a one-dimensional system can be written as:

$$\chi_0(\mathbf{q}) = \frac{1}{L} \sum_{\mathbf{k}} \frac{f_{\mathbf{k}+\mathbf{q}} - f_{\mathbf{k}}}{\epsilon_{\mathbf{k}} - \epsilon_{\mathbf{k}+\mathbf{q}}}, \tag{2.20}$$

where $f_{\mathbf{k}}$ represents the Fermi function $f(\epsilon_{\mathbf{k}})$ and L is the length of the atomic chain. Hence, a large χ_0 requires a large numerator $f_{\mathbf{k}+\mathbf{q}} - f_{\mathbf{k}}$, a small denominator $\epsilon_{\mathbf{k}} - \epsilon_{\mathbf{k}+\mathbf{q}}$ and many of such a $\mathbf{q}$-coupled states. The largest contribution is expected to arise from couples of states close to the Fermi level, where the two electrons have similar energies, thus giving a divergent contribution. This leads to the concept of Fermi surface nesting, i.e. the possibility to displace one section of the Fermi surface by a wave vector $\mathbf{q}$ and to superimpose it exactly onto another section. However, the perfect nesting condition is fulfilled only in the one-dimensional case where large flat parallel sections are present. In higher dimensions the topology of the $\mathbf{k}$-space is generally not favorable, therefore the contribution coming from the electron-phonon coupling in Eq. (2.19) becomes fundamental to stabilize the low-temperature CDW phase [8, 11].

2.2.2 Role of lattice fluctuations

Even though the model presented in the previous section is able to highlight the fundamental ingredients that determine the phase transition, it has many weaknesses which arise from the different approximations made. One among all, the mean-field solution presented, neglects the role of lattice fluctuations and predicts the development of a long range order at a finite temperature. However, in many of the quasi-one-dimensional compounds, the zero point lattice motion is of the same order of magnitude of the Peierls distortion, therefore one can expect a dramatic effect on the electronic and structural properties when the lattice fluctuations are taken into account [36, 37].

For a one-dimensional chain described by the Fröhlich Hamiltonian, the order parameter is complex (see Eq. (2.10)) hence both amplitude and phase fluctuations can occur. In general, at temperatures $T > T^{\text{MF}}$ the amplitude of the order parameter fluctuates near $|\Delta| = 0$. By decreasing the temperature, the fluctuations are progressively reduced, and well below T^{MF} the amplitude of the order parameter approaches its $T = 0$ value, while the phase of the order

parameter rotates in the bottom of the double-well potential. It can be shown that, due to these fluctuations in the order parameter, a strictly one dimensional system cannot develop a long range order at finite temperatures [11, 38]. The transition to a long range order is recovered only for a quasi-one-dimensional system with weakly coupled one-dimensional chains (like for example the case of $K_{0.3}MoO_3$ and $(TaSe_4)_2I$), in which the coupling between neighboring chains is fundamental for the stabilization of the low temperature phase [11]. Both the zero-point and thermal lattice motions are a source of disorder, and they have an effect on the electronic properties similar to that of a random potential with Gaussian correlations. These fluctuations can cause a significant modification of the electronic density of states with respect to the behavior predicted from a rigid lattice distortion [38]. In particular, the lattice fluctuations remove the inverse-square-root singularity found in the density of states of many one-dimensional systems and produce a large tail of localized states inside the energy gap [38]. Furthermore, by increasing the temperature towards the CDW critical temperature, the correlation length decreases and the density of states at the Fermi level increases, i.e. the gap fills in [38, 39]. Specifically, theoretical and experimental studies have linked the temperature-dependence of the lattice fluctuations to the energy scale of the CDW excitations, showing that when the temperature of the system becomes of the same order of the amplitude mode frequency (low-energy excitation of the CDW ground state responsible for the change in its amplitude), the disorder increases [36, 38]. Therefore the lattice fluctuations lead to a smearing of the electronic gap, that accompanies its simple closure discussed in the mean-field theory of the CDW transition [38]. As shown in the following section, the role of the lattice fluctuations becomes increasingly important when the strength of the EPC is increased.

2.3 CDW TRANSITION IN MATERIALS WITH STRONG EPC

The increase of the electron-phonon coupling strength entails a different driving mechanism for the charge-density wave transition, therefore even if the properties of the low temperature phase do not change fundamentally, the expressions developed in the previous section cannot be applied anymore [8]. Indeed, while in the weak EPC limit the phase transition is triggered by the divergence of the electronic susceptibility, in the strong EPC limit the CDW phase results from a peak in the wave vector dependent EPC and manifests through a phonon softening over an extended region in $\mathbf{q}$-space (as schematically shown in Fig. 2.1(c)) [12, 18, 40]. In both cases the origin of the energy gain is electronic, but compared to a weak-coupling CDW, a strong-coupling CDW is characterized by a larger lattice distortion, a larger energy gap and a smaller coherence length [8].

As shown in Fig. 2.2, the thermodynamic behavior near the transition temperature is markedly different in the two limits. In the weak-coupling scenario, the thermal disordering is dominated by the electronic entropy, meaning that close to the transition temperature the thermally excited electrons have enough energy to be promoted above the energy gap ($k_B T \sim \Delta$) and as a consequence of that, they trigger the phase transition towards the normal phase. At the mean field critical temperature T_{MF}, the CDW phase completely vanishes, as signaled by the evolution of the order parameter and the lattice distortion in the left side of Fig. 2.2. In the strong EPC scenario, a small coherence length picture has to be applied [12], and as a consequence of that, the phonon entropy rather than the electronic entropy turns out to be the key quantity that drives the phase transition towards the normal state [12, 19, 41]. Indeed, electrons near the gap edge cannot respond to lattice vibrations with wave vectors farther than $1/\xi$ from $\mathbf{q_{CDW}}$, with ξ being the coherence length. The number of phonon modes which participate to the CDW transition is limited by this physical cutoff [12]. Therefore, as mentioned above, in the strong coupling limit, the phonon spectrum is modified over a large region of the reciprocal space (Fig. 2.1(c)) and consequently the role played by the lattice entropy becomes increasingly important [12, 19]. Indeed, if the phonon entropy is large enough, it reduces the transition temperature sufficiently that the electronic entropy becomes

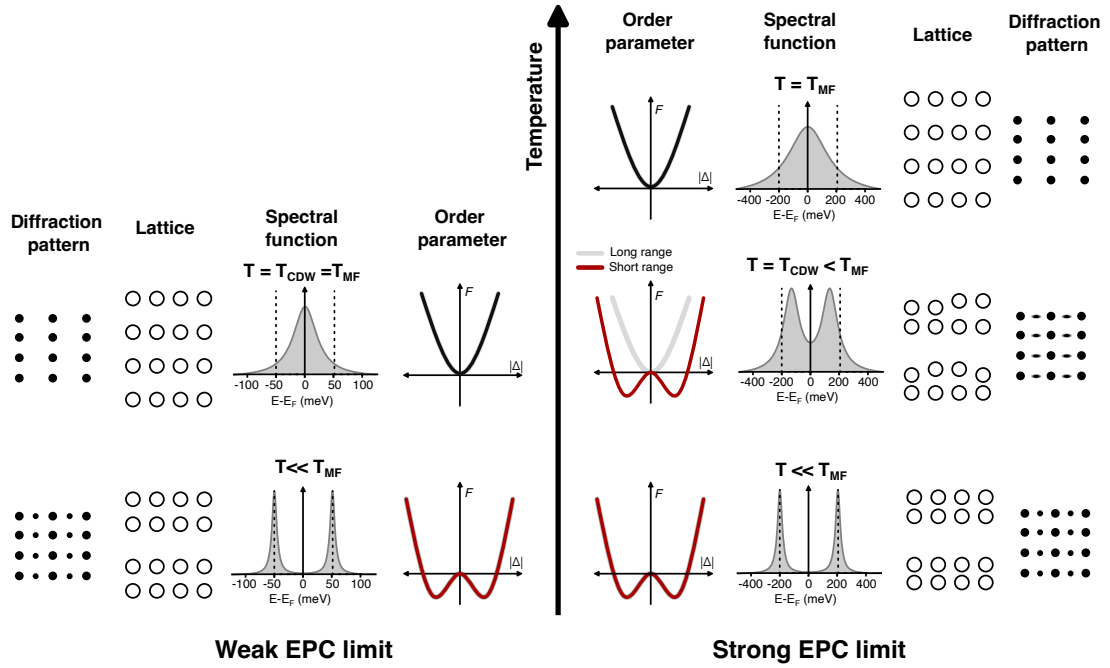

Figure 2.2: Temperature-driven phase transition in the weak and strong EPC limits. In the weak-coupling limit the phase transition is driven by the electronic entropy and at $T_{CDW} = T_{MF}$ the CDW order completely vanishes. In the strong-coupling limit the phase transition is driven by the lattice entropy and at T_{CDW} only the long-range oder is lost, while a non-zero short-range order persist up to T_{MF}. Adapted from [43].

unimportant since in this limit $k_B T_{CDW} \ll \Delta$ (with $T_{CDW} < T_{MF}$), and the thermally excited electrons cannot be promoted above the energy gap. At the transition temperature, only the long-range coherence is lost, while fluctuating short-range distortions remain, causing a smearing and not the complete vanishing of the energy gap, with the formation of a so-called pseudogap [40, 42]. Consequently, in this temperature region, the system is characterized by a non vanishing short-range order parameter, proportional to the mean-square local lattice displacement and to the mean-square local energy gap (shown in the right side of Fig. 2.2) [12, 43]. The undistorted state is recovered only at a temperature well above T_{CDW} [8, 12].

At this point it is useful to consider the short coherence length picture originally proposed by McMillan [12], to explain the CDW transition in the strongly-coupled system 2H-$TaSe_2$. In this picture, the CDW modes in different superlattice unit cells can be treated as independent local modes, with intercell interactions. Each superlattice unit cell is thus characterized by a localized longitudinal phonon and by a local energy gap. Only below the critical temperature a long-range phase coherence develops, resulting in a uniform lattice distortion and in a constant energy gap. At the phase transition instead, the long-range phase coherence brakes up and the long-range order parameter goes to zero. However, above the critical temperature the system is still characterized by the presence of a large but fluctuating local energy gap, *i.e.* a non-zero local order parameter.

For what said above, the transition towards the normal phase is obtained as a consequence of an order-disorder transformation, in contrast to the displacive transition of the conventional Peierls picture [40, 44–46]. In a displacive transition the atoms move under the effect of one or a few well-defined, spatially coherent vibrational modes, that link the low- and high-temperature phases. In an order-disorder transition instead, the atoms move in a spatially incoherent manner, with no characteristic correlation length [21]. It is worth noting that, in both cases of order-disorder and displacive transitions, the average atomic position may follow the same trajectories. As a consequence of that, a conventional diffraction measurement cannot distinguish between these two different scenarios (as visible in the diffraction patterns

	Weak-coupling	**Strong-coupling**
PLD/CDW amplitude	Small	Large
Energy gap	Small ($\Delta/E_F \ll 1$)	Large ($\Delta/E_F \lesssim 1$)
Coherence length	Large ($\xi/a \gg 1$)	Small ($\xi/a \ll 1$)
CDW periodicity	Incommensurate	Tends to be commensurate
Thermal disordering	Due to electron entropy	Due to lattice entropy
Qualitative picture	*Fermi surface instability*	*Local chemical bonding*

Table 2.1: Comparison between charge-density-wave phases in the weak and strong EPC limits [8].

shown in Fig. 2.2). However, since in a order-disorder transition the atoms move in a spatially incoherent manner, the study of the diffuse intensity in reciprocal space has proven to be a valuable tool to unveil the origin of the phase transition [21, 47].

As discussed above, a large phonon entropy leads to a strong reduction of the mean field CDW transition temperature. Therefore, in the strong EPC scenario, a significant deviation from the BCS relation between zero-temperature energy gap and transition temperature is expected. As a guiding principle, the short coherence-length picture has to be applied when $2\Delta(0) \gtrsim 7\ k_B T_{CDW}$ [12].

As a final remark, to further define these two different scenarios it is useful to consider the extreme limits of weak and strong EPC, where two qualitatively different pictures emerge. As already discussed, in the long coherence-length picture, the CDW phase transition is understood in terms of a Peierls instability. This instability is strongly linked to the concept of Fermi surface nesting, and therefore deeply rooted in $\mathbf{k}$ space. Consequently the PLD is in general incommensurate with respect to the underlying lattice. In the short coherence-length picture, due to the much larger atomic displacements, a local chemical bonding picture is often more appropriate. Atoms tend to form pairs with shortened bonds and due to their large displacements the non-linear terms in the electron-phonon coupling become important. Hence the PLD locks on the underlying crystal structure and tends to give rise to a commensurate CDW phase [8, 12]. These differences are summarized in Tab. 2.1.

2.4 COLLECTIVE EXCITATIONS OF THE CDW GROUND STATE

Ginzburg-Landau theory

The excitations of the CDW ground state are described by the spatially- and time-dependent complex order parameter $\boldsymbol{\Delta}$ introduced in Sec. 2.2.1. Given the complexity of a full microscopic theory, this problem is usually treated by using the time-dependent Ginzburg-Landau theory in the long wavelength limit [11]. In this framework, the free energy of a one-dimensional chain can be written as:

$$F = F(0) + n(\epsilon_F) \int dx \left[a|\boldsymbol{\Delta}|^2 + b|\boldsymbol{\Delta}|^4 + c\left|\frac{d\boldsymbol{\Delta}}{dx}\right|^2 + d\left|\frac{d\boldsymbol{\Delta}}{dt}\right|^2 \right], \tag{2.21}$$

where a, c and d are temperature dependent coefficients, while b is constant. The third term describes the energy associated with the spatial variation of the order parameter while the last term represents the kinetic energy due to the temporal fluctuations of the order parameter [11].

For a complex order parameter both phase and amplitude excitation can occur and at the first order the two can be thought as independent. In this limit, the time- and spatially-dependent order parameter can be written as:

$$\boldsymbol{\Delta}(\mathbf{x}, \mathbf{t}) = [|\boldsymbol{\Delta}| + \delta(x,t).]\, e^{i\phi(x,t)}. \tag{2.22}$$

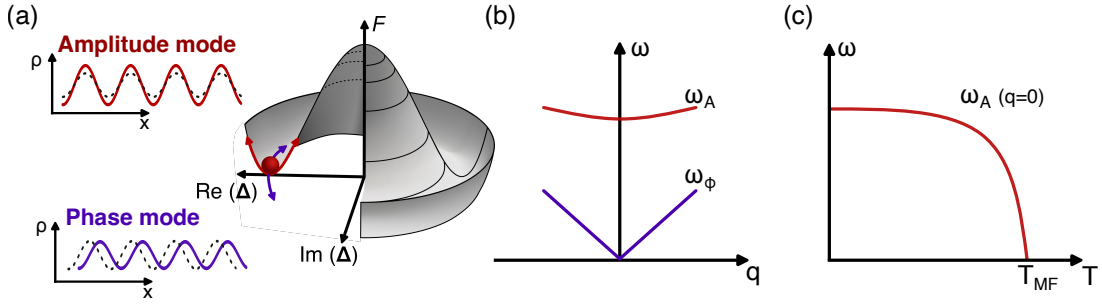

Figure 2.3: (a) Ginzburg-Landau free energy (F) and real-space representation of the amplitude and phase modes for an incommensurate CDW system. (b) Amplitude and phase modes dispersion near q= 0 for an incommensurate CDW at $T = 0$ K. (c) Temperature dependence of the frequency of the amplitude mode at q= 0. Adapted from [11].

Here $|\mathbf{\Delta}|$ is the magnitude of the spatially and temporally averaged electronic gap, $\delta(x,t)$ describes the amplitude fluctuations of the order parameter and $\phi(x,t)$ describes the phase fluctuations. Within this framework, two modes, an amplitude mode (AM) and a phase mode (PM) (schematized in Fig. 2.3(a)), represent the excitations of the ground state of the CDW condensate [11]. For an incommensurate CDW phase, in the limit of long wavelength excitations and for $T = 0$, it is possible to obtain the following dispersion relations (shown in Fig. 2.3(b)) for the phase and amplitude excitations:

$$\omega_\phi = \left(\frac{m}{m^*}\right) v_F q = c_\phi q, \qquad \omega_A = \left(\lambda\omega_{2k_F}^2 + \frac{m}{3m^*}v_F^2 q^2\right)^{1/2}, \tag{2.23}$$

where m^* is the effective mass, v_F is the Fermi velocity, ω_{2k_F} is the unrenormalized soft phonon mode frequency and c_ϕ is called phason velocity. As shown by these relations, for an incommensurate CDW in absence of pinning effects (that can arise from defects and impurities) the phase mode is massless. Since in the $q = 0$ limit the phase excitation corresponds to the translational motion of the undistorted condensate with respect to the atomic position, the presence of a zero gap dispersion implies that the condensate can freely slide for an excitation at $q = 0$. In any real material, however, random impurities and disorder restrict the sliding motion, leading to a small gap in the phase mode dispersion (pinning frequency) [11, 48]. On the contrary, the amplitude mode, being directly linked to the change of the gap size, is characterized by the presence of a gap in its spectrum.

It is also worth noting that, since the phase mode involves the displacement of the electronic charge distribution with respect to the ionic position, this mode is expected to be infrared active. Such displacements do not occur for the amplitude fluctuations and therefore the AM is expected to be Raman active [4]. In the last two decades, a large number of articles discussing the observation of amplitude and phase modes has been published [48–53]. In particular, the study of the CDW amplitude mode has attracted a large interest, being this excitation directly linked to the modulation of the CDW gap and the PLD, and hence being accessible by different time-resolved techniques sensitive to the electronic or structural degrees of freedom. These experiments have revealed marked deviations from the simple theory presented in the previous sections, highlighting the fact that the properties of the CDW ground state and its low-energy excitations are strongly material dependent, and making therefore difficult the development of a comprehensive microscopic theory.

At finite temperatures both ω_A and c_ϕ are determined by the temperature dependence of the electronic gap $\Delta(T)$ and of the condensate density $f(T)$. Close to the transition temperature, the evolution of the amplitude mode frequency is describe by the expression:

$$\omega_A \propto \lambda^{1/2}\omega_{2k_F}\left(1 - \frac{T}{T_{CDW}^{MF}}\right)^{1/4}. \tag{2.24}$$

Hence the frequency of the amplitude mode approaches zero for $T \to T_{\mathrm{CDW}}^{\mathrm{MF}}$ while it can be shown that the velocity of the phase fluctuations remains finite for $T \to T_{\mathrm{CDW}}^{\mathrm{MF}}$ [11]. This renormalization of the AM frequency, has been observed in many CDW materials, and has been used to identify the AM among the many phonon modes observed in the low-temperature CDW phase [28, 49–52].

As a final remark, it is worth noting that the amplitude and phase modes discussed in this section are formally different from the Higgs and Goldstone modes defined in the case of superconductivity [54]. As discussed here, a spontaneous symmetry-breaking phase transition leads to the appearance of a massless phase mode representing the low-energy excitation of the Mexican-hat potential. However, in the case of superconductivity, due to the presence of a charged condensate, the phase mode is lifted towards higher energies. This results in a low-energy excitation spectrum governed by the amplitude mode, i.e. the Higgs mode [55]. Therefore only the superconducting phase represents a one-to-one analogy to the Anderson-Higgs model used in high-energy physics [56].

3 METHODS AND EXPERIMENTAL SETUPS

In this chapter the basic concepts of ARPES, TR-ARPES and TR-OS are introduced. In particular, the physical quantities that can be extracted from an angle-resolved photoemission experiment are discussed together with the aspects that turn out to be critical in the extension of the technique to the time domain. This introduction is then followed by a brief comparison between TR-ARPES and TR-OS. Finally, a detailed description of the experimental setups employed to perform the experiments discussed in this thesis is reported.

3.1 BASIC PRINCIPLES OF ARPES

ARPES is a photon-in electron-out technique that relies on the photoelectric effect, *i.e.* the capability of a photon of suitable energy to emit an electron from the bound state of a material to the vacuum [57]. The importance of ARPES as a spectroscopic tool derives from the fact that, by exploiting the kinematics of the photoemission process, it is possible to obtain the binding energy E_B and the component of the crystal momentum parallel to the surface $\hbar k_{||}$ of the electron inside the material:

$$E_{kin} = h\nu - E_B - \phi, \qquad \hbar k_{||} = \sqrt{2m\,E_{kin}}\,sin(\theta)\,. \tag{3.1}$$

Here E_{kin} is the kinetic energy of the photoemitted electron, $h\nu$ is the energy of the incident photon, ϕ is the work function of the material, *i.e.* the difference between the Fermi level of the system and the vacuum level, and θ is the polar angle with respect to the surface normal (the geometry of an ARPES experiment is shown in Fig. 3.1(a)) [22, 58]. Due to the presence of the material's surface that breaks the translation symmetry, only the component of the crystal momentum parallel to the surface is conserved throughout the photoemission process, while the component orthogonal to the surface is not (Fig. 3.1(b)). To recover the orthogonal component it has to be assumed that the final-state dispersion of the electron within the crystal, can be parametrized by a free electron dispersion offset by a potential V_0, named inner potential [58]. Therefore, under this assumption, the inner potential accounts for the discontinuity at the crystal surface and the orthogonal component of the crystal momentum can be obtained from the expression:

$$\hbar k_{\perp} = \sqrt{2m\,[E_{kin}cos^2(\theta) + V_0]}\,. \tag{3.2}$$

V_0 is *a priori* unknown, but it can be determined experimentally, exploiting the periodicity of the dispersion along the k_z direction with E_{kin} [58]. It is worth noting that since E_{kin} has to be a positive quantity, equations (3.1) and (3.2) set a limit for the momentum reachable at a given photon energy $h\nu$.

At this point it is useful to remind that Eq. (3.1) and (3.2) have been obtained under certain assumptions. First of all, the momentum of the incoming photon has been neglected. This approximation is routinely used in ARPES experiments when photon energies below $\sim 100\,eV$ are used, and therefore can be applied to all the photoemission experiments shown in this thesis [22]. Furthermore, the expressions reported above are valid only if the electron does not undergo any scattering event while traversing the sample thickness during the photoemission process. These electrons are called *primary* electrons, in contrast to the *secondary* electrons that

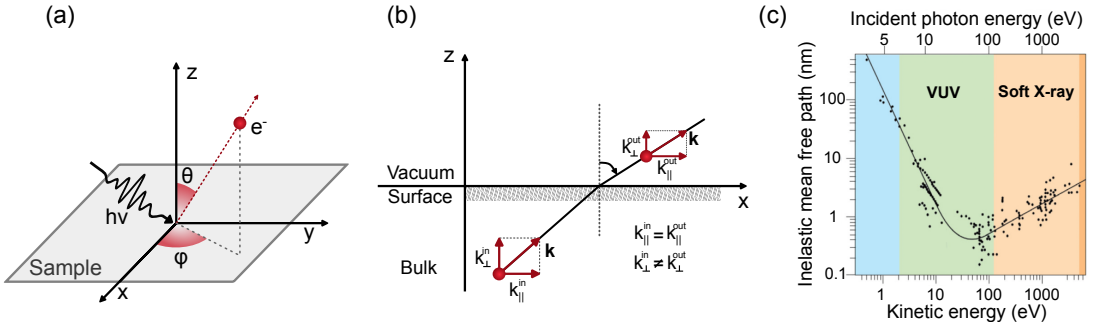

Figure 3.1: (a) Geometry of an ARPES experiment, in which the emission direction of the photoemitted electron is determined by the polar (θ) and the azimuthal (φ) angles. Adapted from [22]. (b) Vectorial representation of the momentum conservation relations. Adapted from [61]. (c) Universal curve of the inelastic mean free path as a function of the photoelectron kinetic energy (bottom axis) and the incident photon energy (top axis). Adapted from [59].

undergo scattering events [22, 58]. The average distance that an electron can traverse without undergoing a scattering process is named *mean free path* and its dependence on the photon energy typically follows the so called universal curve show in Fig. 3.1(c) [59, 60]. As shown by this curve, the minimum free path is reached for photon energies of a few tens of eV and corresponds to less than 10 Å. Since the lattice parameter can vary from few to several tens of Angstroms, the universal curve shown in Fig. 3.1(c) implies that the largest contribution to the photoemission intensity comes from the first few layers close to the surface. This makes photoemission a surface-sensitive technique. However the sensitivity to the bulk is recovered at the extremes of the curve, *i.e.* for photon energies smaller than 10 eV or in the soft X-Ray region [59].

After having discussed the kinematics of the photoemission process, we now move to the modeling of the photoemission intensity. Formally, the photoemission process can be described by the transition probability w_{fi}, from an N-electron initial state $|\Psi_i^N\rangle$ to an excited final state $|\Psi_f^N\rangle$. Therefore, by using the Fermi golden rule we obtain:

$$w_{fi} = \frac{2\pi}{\hbar} \left| \langle \Psi_f^N | \, H_{int} \, | \Psi_i^N \rangle \right|^2 \delta(E_f^N - E_i^N - h\nu), \tag{3.3}$$

where E_i^N and E_f^N are the initial- and final-state energies of the N-electron system while H_{int}, is a perturbative Hamiltonian describing the electron-photon interaction [58]. The total photoemission intensity is then given by $I(\mathbf{k}, \omega) = \sum_{f,i} w_{f,i}$.

The most rigorous approach to deal with Eq. 3.3 is to use the so-called *one-step model*, in which photon absorption, electron excitation and electron detection are treated as a single coherent process [62]. However, given the complexity of such a treatment, it is often more convenient to use a phenomenological *three-step model*, which divides the photoemission process into three subsequent and independent steps [63]. In the first step, the incoming photon drives a direct transition of the electron inside the bulk of the material. In the second step, the excited electron traverses the sample till the surface, eventually forming secondary electrons in the case of scattering events. In the third step, the electron is transmitted through the surface barrier and emitted to the vacuum, with the electron ultimately occupying a free-electron plane wave state that extends to the detector. The three-step model has the advantage of being of easier implementation since the three steps in which the photoemission process is decomposed are decoupled. However, in many cases a one step formalism may be required to fully explain the spectral intensities observed in the experiments [22, 58].

In the discussion of the photoemission from solids, and in particular for the case of correlated electron systems, the most powerful and commonly used approach to treat Eq. 3.3

is based on the Green's function formalism [22]. Within this formalism the photoemission intensity measured in an ARPES experiment can be factorized into three contributions:

$$I(\mathbf{k},\omega) = I_0(\mathbf{k},h\nu,\mathbf{A})A(\mathbf{k},\omega)f(\omega,T). \tag{3.4}$$

The relevance of the three terms in Eq. 3.4 in the interpretation of the ARPES spectra is discussed in the following paragraphs.

Matrix elements effects: $I_0(\mathbf{k},h\nu,\mathbf{A})$

This term accounts for the probability of the transition of one electron from the initial Bloch state $|\varphi_i^{\mathbf{k}}\rangle$ to the final free-electron state $|\varphi_f^{\mathbf{k}}\rangle$ as a consequence of the interaction with a photon [64]. The one-electron dipole matrix element connecting these two states can be written as:

$$M_{f,i}^{\mathbf{k}} = \langle\varphi_f^{\mathbf{k}}|\, H_{int}\,|\varphi_i^{\mathbf{k}}\rangle\,. \tag{3.5}$$

Within the semiclassical picture, the interaction between the electric field of the incident radiation, described by the vector potential $\mathbf{A}$, and an electron with momentum $\mathbf{p}$, is described by the Hamiltonian $H_{int} \propto \mathbf{p}\cdot\mathbf{A}$. Within this approximation, Eq. 3.5 becomes:

$$M_{f,i}^{\mathbf{k}} \propto \langle\varphi_f^{\mathbf{k}}|\,\mathbf{p}\cdot\mathbf{A}\,|\varphi_i^{\mathbf{k}}\rangle\,. \tag{3.6}$$

The matrix element thus modulates the photoemission intensity depending on the relative orientation between the polarization of the incident light and the momentum of the electron, which is linked to the orbital symmetry of the electronic initial state. Therefore, suitable configurations of photon energy and polarization can be used to enhance or suppress the contribution coming from particular states, and to reconstruct the orbital character of specific bands [22, 65].

One-particle removal spectral function: $A(\mathbf{k},\omega)$

This term encodes both the single-particle band structure of the system $E_B(\mathbf{k})$ and the many-body correlation effects. As anticipated above, this term finds its origin from a description of the photoemission process in terms of the Green functions formalism, which is the most used to account for the effect of the electronic correlations [66, 67].

For a non-interacting system, upon the removal of an electron with energy $E_B(\mathbf{k})$, the system left behind would not undergo any relaxation process. In such a system, the spectral function A_0 takes the form of a Dirac-delta function centered at the energy and momentum position given by the band structure dispersion:

$$A_0(\mathbf{k},\omega) \propto \delta(E - E_B(\mathbf{k})). \tag{3.7}$$

Hence in this scenario, the particle at $E_B(\mathbf{k})$ would have an infinite lifetime [68]. For an interacting system instead, the interaction among the electrons, or with collective excitations of the system, modifies the dispersion relation in a way described by the Green function formalism by means of the complex *self energy* Σ [69, 70]. A detailed discussion on the formalism of the self energy is beyond the scope of this thesis, here we only report the form of the spectral function A for an interacting system once the self energy has been taken into account:

$$A(\mathbf{k},\omega) \propto \frac{\Sigma''(\mathbf{k},\omega)}{[E - E_B(\mathbf{k}) - \Sigma'(\mathbf{k},\omega)]^2 + [\Sigma''(\mathbf{k},\omega)]^2}, \tag{3.8}$$

where Σ' and Σ'' indicate the real and imaginary parts of the self energy. These two terms encompass all the energy renormalization and lifetime changes with respect to the

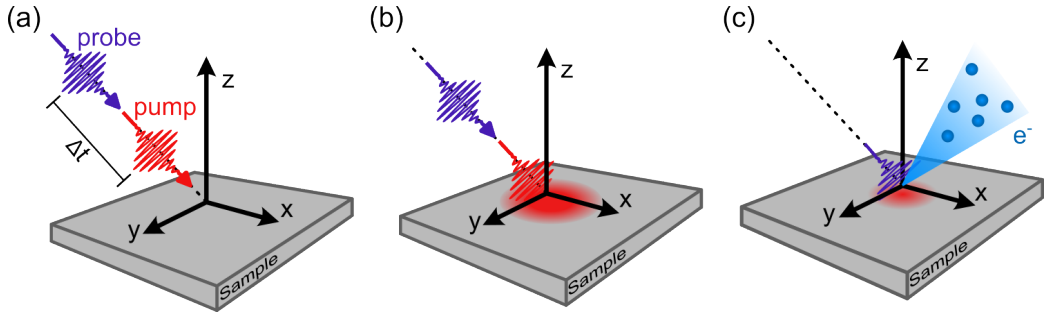

Figure 3.2: Illustration of the pump-probe approach used in TR-ARPES. (a) The pump and the probe pulses are directed onto the sample, separated by a time interval $\Delta t > 0$. (b) The pump pulse impinges on the sample and drives the system out of equilibrium. (c) The probe pulse triggers the photoemission process from the out-of-equilibrium state. Adapted from [58].

non-interacting case [22, 68]. Intuitively, Σ' leads to a shift of the bare band dispersion $E_B(\mathbf{k})$, while Σ'' is responsible for the broadening of the delta function that we find in the non-interacting case, and it accounts for the finite lifetime of the state [68].

Band structure population: $f(\omega, T)$

The Fermi-Dirac distribution accounts for the fact that direct photoemission probes only the occupied electronic states. Moreover, it is worth noting that a finite temperature acts as a physical source of Fermi edge broadening, that adds up to the experimental sources of broadening.

3.2 BASIC PRINCIPLES OF TR-ARPES

Time-resolved ARPES (TR-ARPES) originates from the extension of ARPES to the time domain. Like other time-resolved techniques, TR-ARPES takes advantage of the so called pump-probe approach [27, 68]. As it is shown in Fig. 3.2, this technique requires the use of two kinds of ultrashort laser pulses separated by a tunable time delay Δt. A first intense pulse, named *pump*, excites the system into an out-of-equilibrium condition, whereas a second ultraviolet pulse, named *probe*, triggers the photoemission process from the excited state of the material. By changing the time delay between the pump and the probe pulses it is then possible to study the relaxation dynamics towards the equilibrium conditions.

An introduction to the principles of the TR-ARPES technique is given in Fig. 3.3, where the surface state of the topological insulator Bi_2Se_3 is studied. The top panels display the TR-ARPES energy-momentum maps for three different pump-probe delays. The time at which the two pulses overlap on the sample ($\Delta t = 0$) is known as temporal overlap. Therefore, negative delays (Fig. 3.3(a)) correspond to the scenario in which the pump pulse impinges on the sample after the arrival of the probe pulse, hence the system is measured under quasi-equilibrium conditions. Indeed this condition might differ from the true equilibrium condition in the case in which effects lasting longer than the separation between two pump pulses, like local heating effects, are present. Panel (b) shows a photoemission spectrum acquired at a pump-probe delay of $\Delta t = 900$ fs, in which the electrons have thermalized into a quasi-equilibrium Fermi-Dirac distribution, characterized by an increased electronic temperature. Finally, panel (c) shows a spectrum acquired at larger pump-probe delays, in which the system has almost completely relaxed back to the equilibrium condition. The bottom row in Fig. 3.3 presents differential TR-ARPES maps, computed by calculating the difference between the spectra shown in the top row with one acquired at a large negative time

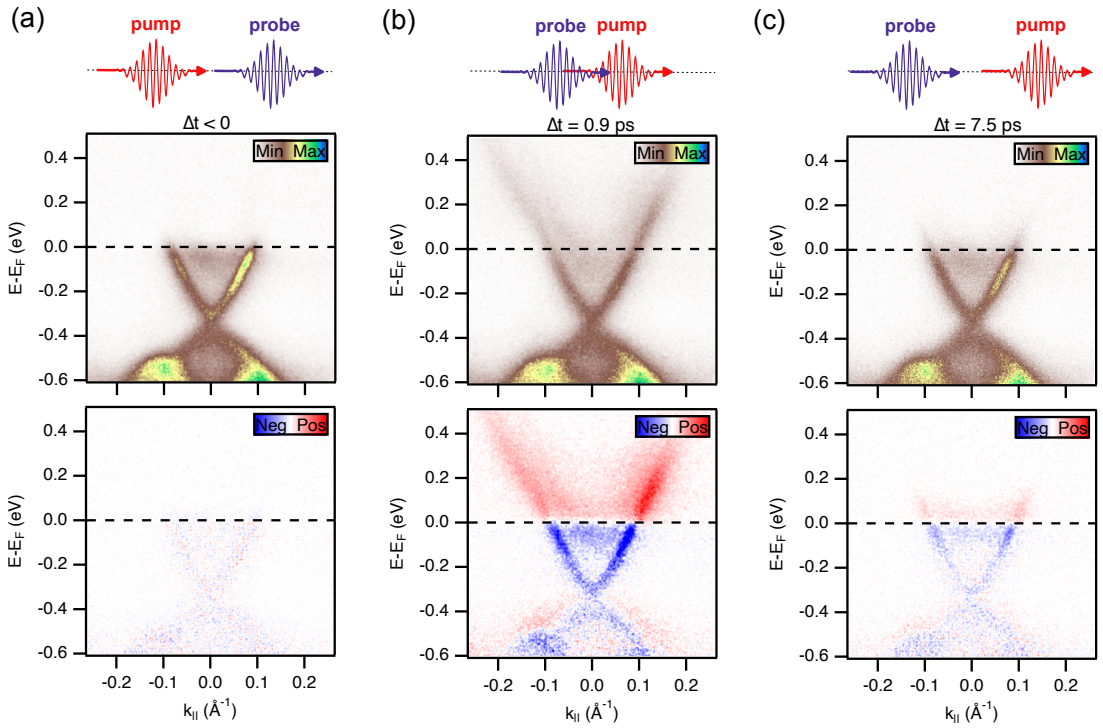

Figure 3.3: TR-ARPES signal on the surface state of the topological insulator Bi_2Se_3. The top panels show three TR-ARPES spectra acquired at different pump-probe delays Δt, while the bottom row shows the differential maps, highlighting the pump-induced redistribution of spectral weight. These measurements were performed with a probe photon energy of 10.8 eV and a pump photon energy of 1.2 eV. The time resolution of the experiment was $\sim$ 800 fs.

delay. In these maps, red (blue) regions denote an increase (decrease) of the photoemission intensity with respect to the equilibrium conditions. It is worth noting that a change in the photoemission intensity is not solely linked to a change in the population of specific bands, but, as discussed in the following, can arise from a complex interplay of different effects [68].

In the scenario in which, after the initial light-induced excitation of the electronic bath, the electrons can be assumed to be thermalized into a quasi-equilibrium states, the TR-ARPES signal can be approximated by extending the equilibrium formalism of Eq (3.4) into the time domain:

$$I(\mathbf{k}, \omega, \Delta t) = I_0(\mathbf{k}, h\nu, \Delta t) A(\mathbf{k}, \omega, \Delta t) f(\mathbf{k}, \omega, \Delta t). \tag{3.9}$$

The relevance of the three terms in Eq. (3.9) is discussed in the following paragraphs.

Band structure population dynamics: $f(\mathbf{k}, \omega, \Delta t)$

A large number of TR-ARPES experiments were performed to study the population dynamics induced by the pump pulse [71–75]. In addition to the sudden temperature increase of the electronic system, the pump redistributes the electrons in a nonthermal manner by triggering direct optical transitions from the occupied to the unoccupied electronic states above E_F, in specific regions of the 3D Brillouin Zone. As a consequence of that, the Fermi-Dirac distribution that in the conventional ARPES scenario doesn't have any momentum dependence, is modified to take into account the highly anisotropic electronic distribution in momentum space (at least for short time delays $\Delta t \sim 0$) [68].

The light-induced nonthermal electronic distribution at short pump-probe delays, provides a valuable approach to map the band dispersion of the unoccupied electronic states [73] and a method to extract the size of the electronic band gaps in different systems [24, 76].

Moreover, by tracking the hot carrier relaxation dynamics towards the equilibrium conditions, it is possible to extract information on the multiple scattering processes [71] and on the fundamental electron-boson coupling constants [7, 74].

Spectral function modifications: $A(\mathbf{k}, \omega, \Delta t)$

This term accounts for all the transient modifications of the band structure, density of states (DOS) and many-body interactions. Indeed, an optical pump pulse can modify the bare electronic band structure by driving coherent and incoherent phonons [77, 78] or transiently changing the many-body interactions, *i.e* $\Sigma(\Delta t)$. The transient change of the self energy can arise from a large variety of effects, like for example a modification of the screening and the scattering phase space or a light-induced phase transition [23]. It worth noting that, all the different contributions to $A(\mathbf{k}, \omega, \Delta t)$ are often deeply intertwined and therefore difficult to disentangle [68]. In the quasi-equilibrium approximation, however, the spectral function can still be explored via equilibrium analysis methods, and therefore Σ can be extracted by analyzing the ARPES line shape as a function of the pump-probe delay [23].

Matrix elements effects: $I_0(\mathbf{k}, h\nu, \Delta t)$

The transient modification of the matrix elements have been recently demonstrated to be an alternative possibility to account for the changes in the photoemission intensity observed in a TR-ARPES experiment [79]. Its validation, however, requires a detailed study of the photoemission intensity as a function of the probe polarization, and a system where this effect can be disentangled from the possible momentum-dependent redistribution of charges that could overshadow the change in the matrix elements [79].

3.3 TECHNICAL ASPECTS OF TR-ARPES

No single set of source parameters can provide the optimal conditions for all the TR-ARPES experiments, and therefore the choice of the source parameters is of paramount importance. Indeed, a state of the art TR-ARPES setup derives from a complex tradeoff between technical and physical limitations. In this section we present some of the physical and technical aspects relevant in the realization of this kind of setups.

Time and energy resolutions

The light sources generally used in equilibrium ARPES experiments are characterized by very narrow spectral bandwidths ($\sim$ meV), hence the energy resolution of the experiments is mostly determined by the electron spectrometer [80, 81]. However, the pump-probe approach used in TR-ARPES requires the use of ultrashort light pulses, whose duration is directly linked to their bandwidth by the energy and time uncertainty principle (a pulse of 100 fs requires a bandwidth of 20 meV). Therefore, the pulse bandwidth, which sets the energy resolution, and its duration, which determines the time resolution of the experiment, are fundamentally connected (even if some theoretical works have suggested a way to circumvent this limit [82]). Specifically, while the energy resolution is determined only by the probe bandwidth, the time resolution depends on the duration of both pump and probe pulses. For

the case of Gaussian pulses (in the time domain), the cross-correlation is also Gaussian and the total FWHM is given by the expression:

$$\mathrm{FWHM}_{\mathrm{XC}} = \sqrt{\mathrm{FWHM}^2_{\mathrm{probe}} + \mathrm{FWHM}^2_{\mathrm{pump}}}. \tag{3.10}$$

At this point, it is worth noting that, in the case in which the pump and the probe pulses are not collinear, the time smearing that arises from the presence of a finite angle between the two has to be taken into account while calculating the time resolution of the apparatus [83].

A simple method to retrieve the experimental time resolution is to look for relaxation dynamics shorter than the time resolution itself. In this case, if the dynamics is not exceedingly short, the trace extracted from the measurement follows the pump-probe cross correlation and therefore can be used to estimate the time resolution of the setup.

From a scientific prospective, the balance between bandwidth and pulse duration is driven by the physics being studied [80]. Depending on the harmonics generation process, the probe bandwidth can easily vary from $10 - 500$ meV [23, 84].

Space-charge effects

Space-charge is a drawback in photoemission spectroscopy arising from the Coulomb interaction among the photoemitted electrons. This interaction leads to a distortion of the energy-momentum distribution of the photoelectrons [85]. At a first approximation, the effect of the Coulomb interaction is to shift and broaden the energy distribution (due to both acceleration and retardation of the electrons) leading to a loss of the experimental resolution [80, 85]. Pulsed sources and small spot sizes are thus the conditions where the space-charge effects are more severe, since the density of photoelectrons in real space is higher, and thus, the Coulomb interactions are stronger. Moreover, in a time-resolved experiment both pump and probe pulses can be source of space-charge effects. Since light pulses in the visible or near-infrared range are usually used in time-resolved experiments to excite the materials under examination, photoemission from the pump can arise only as a consequence of a multi-photon process and hence usually occurs only for large excitation densities [80, 86].

Thermal effects

Thermal dissipation in time-resolved experiments depends both on the material under investigation (in particular on its thermal conductivity and shape) and on the characteristics of the laser source. In particular, most of the thermal effects can be ascribed to the pump pulse, which brings the majority of the average power. At low repetition rates, the pump energy is typically dissipated before the arrival of the next pulse. Conversely, at higher repetition rates, the thermal dissipation may not be sufficient to bring the system to equilibrium before the arrival of the next pulse. In this case, the upper limit on the average power (and hence on the excitation fluence) has to be set accordingly to the sample damage threshold and to the maximum sample temperature [7, 80]. It is worth noting that the steady state temperature depends on the sample thickness, which can be reduced to increase the thermal dissipation [80]. Since the repetition rate simultaneously determines the pump average power and the probe flux, a tradeoff between maximum excitation fluence and photoemission count rates has to be found.

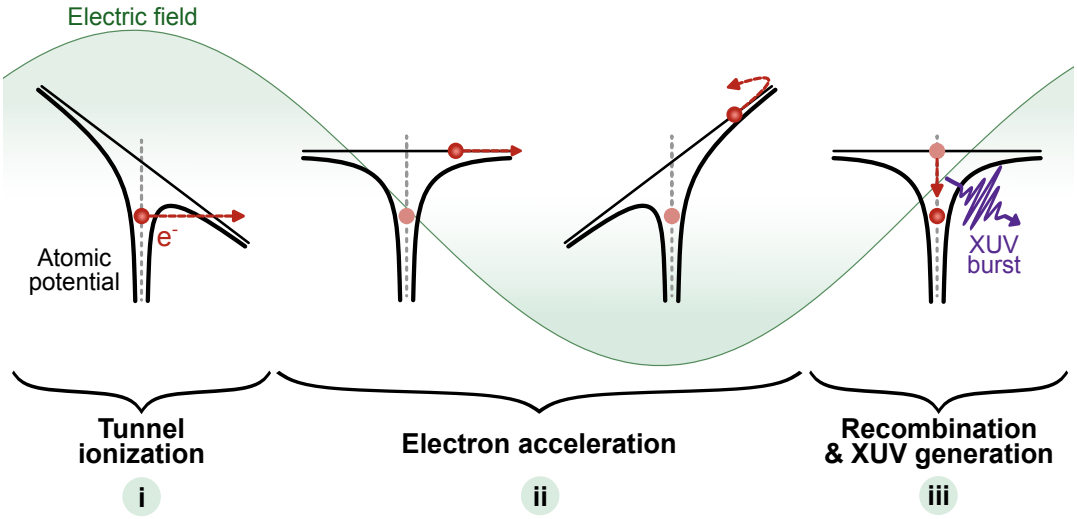

Figure 3.4: Semiclassical three step model description of high-harmonic generation in gases. (i) The electric field of an intense laser pulse distorts the atomic potential and induces the tunnel ionization of an electron. (ii) The electron is accelerated from the electric field of the laser pulse. (iii) The recollision of the electron with the ion generates a burst of high energy radiation.

3.4 HIGH-ORDER HARMONIC GENERATION

General aspects

The easiest way to generate a probe beam with sufficient photon energy for a photoemission experiment is via nonlinear frequency conversion, hence exploiting the second order optical susceptibility χ^2 [87]. The ultimate limit for the crystal-based sources is set around $6-7\,\mathrm{eV}$ by the transparency of the nonlinear media [80]. To push the generation beyond the transparency limits of solids, one can employ nonlinear frequency conversion via the third-order optical susceptibility χ^3 in gases [88]. However, to reach photon energies higher than $\sim 11\,\mathrm{eV}$, one must drive materials beyond the perturbative limit and exploit the so-called high-order harmonic generation (HHG) process. When an intense short pulse interacts with an atomic gas, the atoms respond in a nonlinear way and emit coherent radiation at frequencies that are odd multiples of the laser fundamental frequency. When the frequency of the laser is much smaller than the ionization potential, the harmonic's spectra is characterized by a universal shape: it falls off for the first harmonics, then it exhibits a plateau where all the harmonics have very similar intensity, and then it ends up with a sharp cut-off [89].

The HHG process is here presented following the semiclassical model developed in Ref. [90], being able to capture the essential information of a full microscopic treatment [89]. As shown in Fig. 3.4, a strong driving field induces a distortion in the atomic potential and enables the tunneling ionization of an electron that reaches the continuum with zero velocity (i). The subsequent motion of the electron is treated classically: the emitted electron is accelerated by the electric field of the driving pulse, which reverses sign after half optical cycle, hence driving the electron back towards the parent ion (ii). Only those electrons that return to the nucleus can emit harmonics by recombining to the ground state (iii). Classical simulations show that, the maximum kinetic energy acquired by a free electron from the electric field when it recombines to the nucleus is $3.2\,U_p$, where $U_p \propto E^2/4\omega^2$ is the ponderomotive energy acquired in a laser field of strength E and frequency ω [89, 90]. Therefore the maximum energy of the emitted photons is give by the expression:

$$\hbar\omega_{\mathrm{cutoff}} = I_P + 3.2\,U_p, \tag{3.11}$$

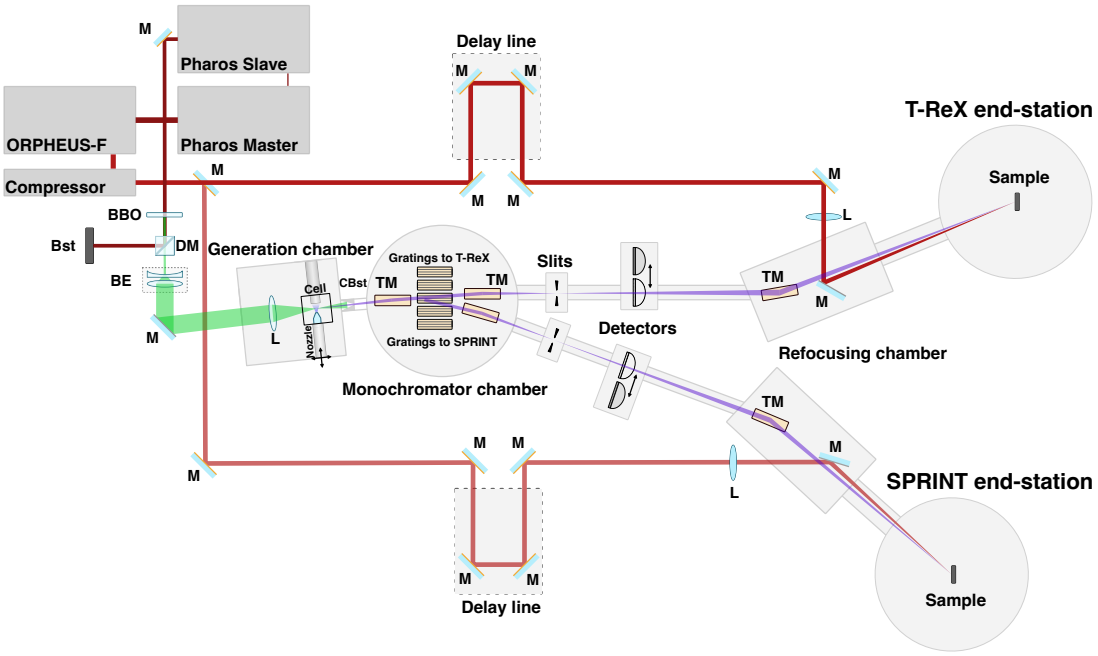

Figure 3.5: Scheme of the TR-ARPES experimental setup with an HHG probe ($17-31$ eV) and a tunable pump ($640-900$ nm and $1200-2400$ nm) developed at the T-ReX laboratory. M, mirror; BE, Beam expander; Bst, beam stopper; CBst, conical beam stopper; DM, dichroic mirror; L, lens; TM, toroidal mirror.

where I_P is the atomic ionization potential. Hence, by increasing the wavelength of the driving field and by using light noble gases (increase of I_P), it is possible to move the cutoff towards higher energies.

The temporal structure of the harmonics, consisting of bursts of radiation emitted at every half-cycle of the driving field, has opened the door to the world of attosecond spectroscopies based on table top sources [89, 91]. Indeed, in recent years, the use of mid-infrared few-optical-cycle light pulses to drive the HHG process has proved to be a valuable technique to generate isolated attosecond pulses [92–94]. The generation of such pulses, however, requires the use of high-energy and low-repetition rate laser sources, and results in a low photon flux, that, as discussed in the previous sections, is not suitable to perform TR-APRES experiments.

The use of high repetition rate laser sources (with a reduced energy per pulse), requires to reduce the beam size on the gas target (to keep constant the energy density) and therefore to work in the so-called *tight-focusing regime* [95]. The high photon flux required in a TR-ARPES experiment can only be achieved if the harmonic radiation produced across the volume of the gas target adds coherently. This phase-matching condition is more difficult to achieve in a tight-focusing regime, due to the increasingly importance of the Guy phase of the laser beam when the focal spot gets smaller [95]. A detailed analysis shows that the conversion efficiency can be made invariant of the pulse energy, provided that the spot size, the gas target length and the gas pressure are suitably rescaled. Specifically, a tight-focusing regime requires the use of higher gas pressures and a smaller interaction volumes [95, 96].

Moreover, it has been shown that even if the cutoff energy (Eq. (3.11)) is pushed to higher energies by increasing the wavelength of the driving field, the generation efficiency follows the opposite behavior. In particular, for a driving field in the visible/near-infrared region the generation efficiency is proportional to $\approx \lambda^{-5}$ [97]. Hence, in TR-ARPES experiments, the use of the second harmonic of the laser's fundamental is generally used to drive the HHG process [96, 98, 99]. This scheme has also the advantage to increase the energy spacing between the harmonics, making them easier to separate.

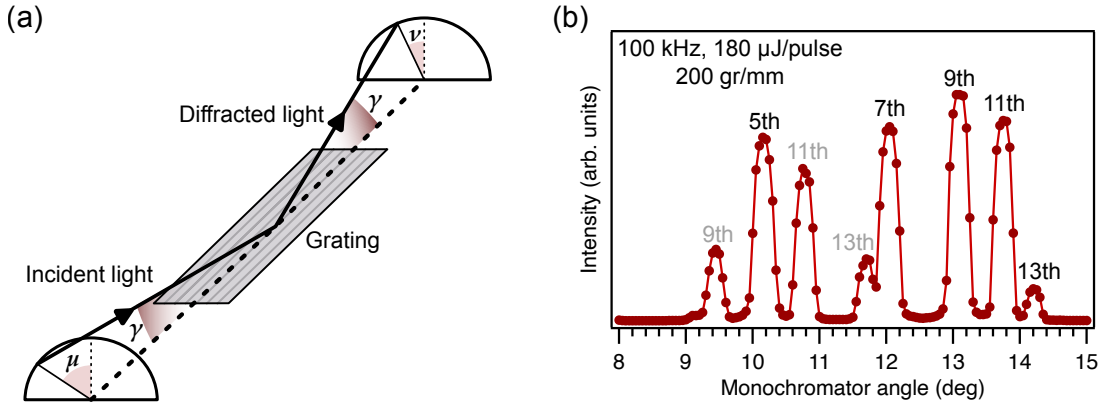

Figure 3.6: (a) Geometry of the OPM scheme. The grating equation for the OPM scheme turns to be: $\sin\gamma(\sin\mu + \sin\nu) = m\lambda\sigma_{op}$; where σ_{op} is the groove density, λ is the wavelength of the diffracted light and all the other angles are indicated in figure. Adapted from [100]. (b) HHG spectra as resolved by a grating with 200 gr/mm and measured by using a channeltron electron multiplier. The identification of the harmonics is also reported, the ones in grey refer to the second diffraction order. A second grating with 400 gr/mm can be used to fully separate the first from the second diffraction order. The repetition rate of the laser was set to be 100 kHz.

3.5 HHG SOURCE AT T-REX

This section is devoted to the presentation of the TR-ARPES setup used in this thesis and developed at the T-ReX laboratory. As shown in Fig. 3.5, the HHG system is powered by two Yb:KGW-based integrated femtosecond laser system (PHAROS, Light Conversion) seeded by the same oscillator. Each amplifier produces ~ 300 fs light pulses at a central wavelength of 1030 nm, with a tunable repetition rate and a maximum power of 20 W above 50 kHz. The maximal energy per pulse, equal to 400 μJ, is available in the $0 - 50$ kHz interval. At higher repetition rates, the energy per pulse is set by the maximum power and the actual repetition rate (e.g. at 100 kHz, which is the repetition rate used for the experiments presented in this thesis, the energy per pulse is 200 μJ) [99]. One of the two amplifiers is used to drive the HHG process, while the other is used to seed an optical parametric amplifier (OPA) (Orpheus F, Light Conversion) whose output constitutes the pump beam in the time-resolved experiments. With this scheme it is therefore possible to tune the pump wavelength in the ranges $640 - 900$ nm and $1200 - 2400$ nm, which correspond respectively to the signal and the idler of the OPA.

As discussed in the previous section, to increase the generation efficiency, the HHG process is seeded by the second harmonic of the laser, at 515 nm. This beam is then focused into the generation chamber which has been designed to work in the tight-focusing regime (Fig. 3.5). Indeed, this regime allows to drive the HHG process starting with a pulse duration (at the output of the laser) of ~ 300 fs, without the use of any compressor (the only time reduction takes place with the generation of the second harmonic [101]). In order to maintain a good vacuum level in the generation chamber, a second cell is installed around the gas nozzle and directly connected via an in-vacuum feedthrough to a 620 m^3/h primary pump (Edwards GX600). In the present configuration the aperture of the nozzle is of 50 μm and the spot-size of the beam in the focus (i.e. in front of the nozzle) is of the order of ~ 8 μm. The maximum efficiency for the HHG generation is achieved by applying an Argon pressure at the input of the gas nozzle of 5.5 bars.

The spectral selection of single harmonics is performed by an off-plane-mount (OPM) grating monochromator [100, 102]. Differently from the classical diffraction gratings, where the grating grooves (gr) are perpendicular to the incident plane, in the off-plane geometry the incident plane is almost parallel to the grooves (shown in Fig. 3.6(a)). The main advantage

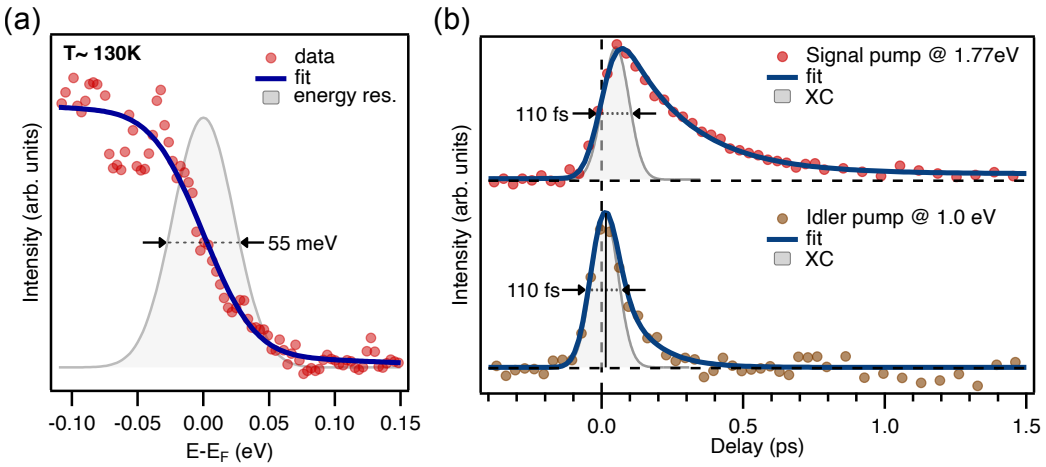

Figure 3.7: (a) Fermi level measured on a polycrystalline gold foil. To take into account the finite energy resolution, the Fermi-Dirac distribution has been convoluted with a Gaussian function (grey curve). To work with higher count rates, which allow to obtain a better signal to noise ratio, a small amount of space charge ($\sim$ 15 meV) has been tolerated. (b) Photoemission intensity extracted from short lived states of VTe_2 in a TR-ARPES experiment. The upper trace has been obtained by using the signal of the OPA as a pump, while the lower trace has been obtained by using the idler. In both configurations the cross correlation of the pump and probe pulses turns to out be $\sim$ 110 fs.

of this scheme is that the groove density needed to have the same spectral resolution and temporal response is higher in the OPM than in the conventional scheme. This results in a reduced pulse-front tilt, which corresponds to a lower temporal broadening. Moreover, the OPM scheme allows to achieve a higher efficiency with respect to the classical configurations [100, 102]. As shown in Fig. 3.5, the monochromator consist of two toroidal mirrors and five OPM plane gratings. The beam is collimated by the first toroidal mirror into a specific grating and subsequently refocused onto the exit slit by the second toroidal mirror, characterized by the same focal length to reduce the aberrations [100]. By selecting the proper grating it is possible to route the beam towards the SPRINT or the T-ReX end-stations [99]. It is worth noting that, given the small bandwidth of the harmonics ($\sim$ 20 meV), the monochromator here presented is generally used only to select the different harmonics generated. In particular, the harmonics from the seventh to the thirteenth can be used in a TR-ARPES experiment, allowing therefore to use 16.8, 21.6, 26.4 or 31.2 eV as a probe photon energy [99]. The tunability of the probe photon energy, even if limited, is exploited to find favorable matrix element conditions and to select the proper k_z value inside the Brillouin zone. Figure 3.7(a) shows the typical energy resolution achieved in a time-resolved experiment. In order to work with higher count rates a small amount of space charge ($\sim$ 15 meV) is usually tolerated.

After the exit slit of the monochromator the intensity of the different harmonics can be measured by using a channeltron electron multiplier (CEM) from Dr. Sjuts (model KBL 10RS/90). Fig. 3.6(b) shows the intensity of the different harmonics recorded as a function the angle of the monochromator. This procedure allows to reconstruct the full spectrum of the harmonics generated and is used to check the alignment of the beamline. It is worth noting that, when gratings with a low density of grooves are used (to minimize the pulse-front tilt), due to the smaller angular dispersion, the second diffraction order of the most intense harmonics is visible and overlaps with the first diffraction order (Fig. 3.6(b)).

The refocusing chamber is equipped with a toroidal mirror, which images the beam spot at the slit position onto the sample position, with a 1 : 1 ratio. The dimension of the HHG beam onto the sample is of the order of $\sim$ 100 µm [99]. Moreover, as shown in Fig. 3.5, an aluminum mirror is placed in the refocusing chamber to direct the pump beam on the sample. The mount of the mirror is placed in such a way that the pump beam forms an angle of less

than two degrees with respect to the HHG beam, keeping therefore as low as possible the temporal smearing. With this configuration, the cross correlation between the pump and the probe pulses turns out to be ~ 110 fs (Fig. 3.7(b)).

Finally, the measurement chamber is equipped with a six-axes cryo-manipulator over which the samples are mounted. The electrons photoemitted from the sample are analyzed and detected by a SPECS Phoibos 225 hemispherical spectrometer, equipped with a delay-line detector. All the experiments reported in this thesis have been performed using the wide-angle mode (WAM) of the spectrometer, which results in an angular acceptance of 30°. The base pressure in the chamber is 2×10^{-10} mbar.

3.6 NON-EQUILIBRIUM OPTICAL SPECTROSCOPY

This section is devoted to a general introduction to the time-resolved optical spectroscopy (TR-OS) techniques, with particular emphasis to the reflectivity experiments. Since however the general framework of the pump-probe experiments has already been introduced in Sec. 3.2, in the following we report an experimental comparison between TR-OS and TR-ARPES with the purpose of showing the complementarity of these two techniques.

3.6.1 A comparison between TR-OS and TR-ARPES

In the last 20 years, the possibility of studying ultrafast dynamics with relatively cheap table-top laser sources has stimulated a dramatic development of the time-resolved version of the conventional optical spectroscopies, with a prominent role played by reflectivity and transmissivity experiments [27]. Being these techniques based on the detection of photons (instead of electrons) the experimental setups turn out to be less complex than the ones used in TR-ARPES. In particular, the most common acquisition scheme for these experiments requires the presence of a mechanical modulator (chopper) to modulate the pump beam at a known frequency. With the pump beam modulated by the chopper, the pump-induced variation of the sample reflectivity (transmissivity) is measured acquiring the ac-component, at the chopper frequency, of the photo-current produced by a photodiode measuring the reflected (transmitted) probe beam. This acquisition scheme allows to achieve a very high signal to noise ratio, of the order of $\sim 10^{-5}$, that can be pushed to $\sim 10^{-8}$ in experimental setups specifically designed for low noise measurements [27, 103, 104]. Thanks to its high signal-to-noise ratio, TR-OS has proven to be one of the most suitable techniques to study the phonon modes triggered by the pump excitation even at very low excitation fluences [28, 105]. This aspect constitutes one of the main advantages of the time-resolved optical spectroscopies with respect to TR-ARPES, where much lower signal-to-noise ratios can be achieved.

Moreover, as discussed in Sec. 3.3, the energy-time uncertainty principle imposes a tradeoff between the energy and time resolutions in a TR-ARPES experiment. Given the different observable used in the time-resolved reflectivity and transmissivity experiments, the energy-time uncertainty principle doesn't affect these experiments. Therefore in these techniques, the time resolution can be pushed to much higher values without the drawbacks observed in photoemission [106–108]. Furthermore, in the case in which broadband time-resolved reflectivity measurements are performed, an increased bandwidth of the probe pulse allows to extend the range of accessible energies on which the out-of-equilibrium response is studied [109, 110].

As a final remark, it is worth emphasizing that the information extracted from a TR-OS experiment generally arises from an average over the pump-induced dynamics in large sections of the Bz, being this technique not able to resolve the response of the system at specific momenta (even if thanks to polarization dependent measurements a momentum sensitivity can be achieved [111]). Therefore, TR-ARPES and TR-OS can be thought as two

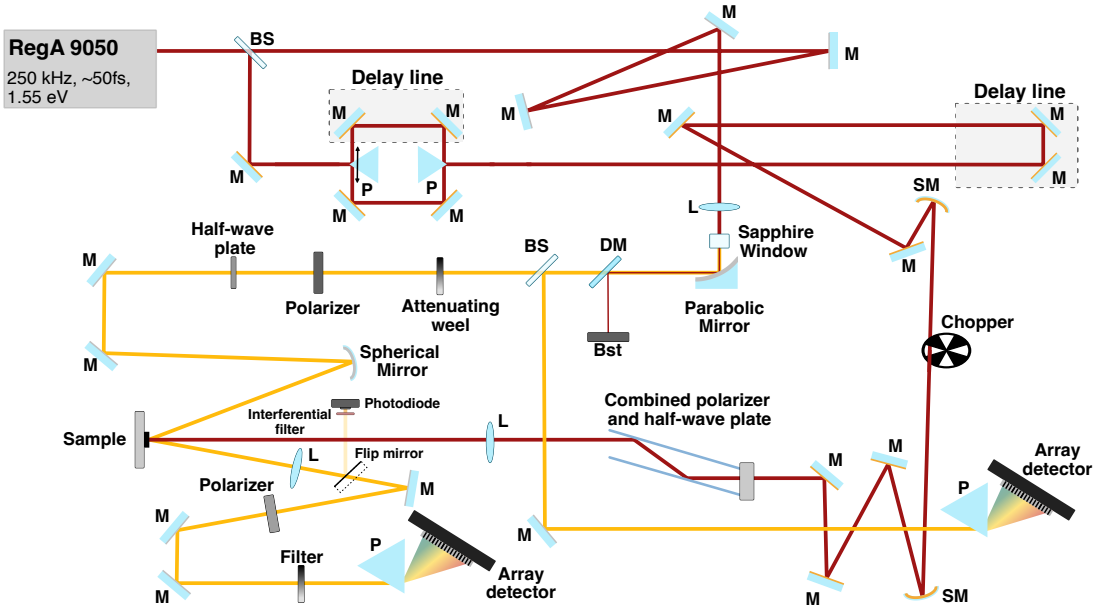

Figure 3.8: Scheme of the near-infrared broadband time-resolved reflectivity setup available at the T-ReX laboratory. M, mirror; DM, dichroic mirror; SM, spherical mirror; BS, beam splitter; L, lens; P, prism; Bst, beam stopper.

complementary techniques, whose combination can be used to tackle the same physical problem from different perspectives.

3.7 NEAR-INFRARED BROADBAND TR-OS SETUP AT T-REX

This section is devoted to the presentation of the near-infrared broadband TR-OS setup used in this thesis. This setup allows to perform reflectivity measurements over a broadband spectral range ($515 - 1650\,\text{nm}$, which correspond to $0.75 - 2.4\,\text{eV}$) [109, 110]. This unique feature is obtained thanks to a careful optimization of the supercontinuum generation in a sapphire window and to two linear InGaAs (Hamamatsu G11608-256) array detector, which allow to simultaneously acquire the data in the full spectral range.

The setup is seeded by a Ti:Sapphire laser system made by two laser cavities that work in conjunction: an ultrafast oscillator (Mira 900F, working at 80 MHz) and a regenerative amplifier (RegA 9050), based on a chirped pulse amplification scheme. The resulting beam has a central wavelength of $\sim 800\,\text{nm}$ and a full width at half maximum bandwidth of $\sim 35\,\text{nm}$ which allows to support $\sim 50\,\text{fs}$ light pulses. The system operates at a repetition rate of 250 kHz, delivering an average output power of 1.5 W, which corresponds to an energy per pulse of $6\,\mu\text{J}$ [112].

Figure 3.8 shows the optical scheme of the TR-OS setup. The beam that arrives on the optical table is splitted in two arms (pump and probe) by a beam splitter. The probe beam is then tightly focused on a 3-mm-thick sapphire window, to generate the supercontinuum beam (about $1\mu\text{J}$/pulse is needed to generate a stable single-filament supercontinuum beam). The broadening of the frequency spectrum of the probe pulse is obtained thanks to different nonlinear optical processes, among which a prominent role is played by the self-phase modulation [113, 114]. The supercontinuum beam is then collimated by a parabolic mirror and after having removed the laser's fundamental it is focused onto the sample. Finally, the reflection of the sample is directed towards one of the two InGaAs detectors. Before impinging on the detector, the supercontinuum beam is dispersed by using a prism, in this way different wavelengths impinge on different pixels and the full spectrum can be acquired

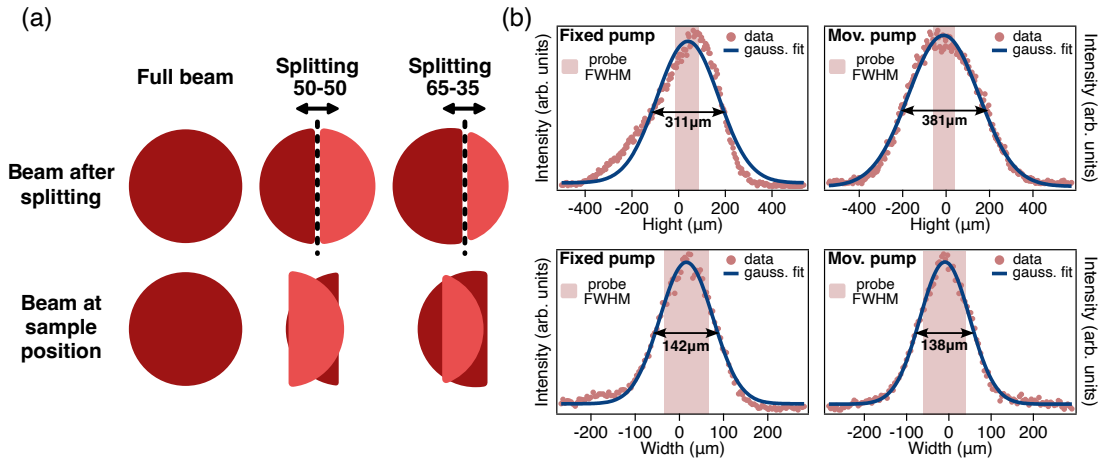

Figure 3.9: (a) The scheme shows the splitting of the pump pulse in two halves. By using the sharp edge of a movable prism (shown in Fig. 3.8) it is possible to cut the pulse in different positions, therefore changing the energy per pulse of the two halves. In the second row the drawings do not show the real dimensions of the beams at the sample position, but only schematize how the overlap is made. The splittings reported refer to the ratio between the power of each pump and the total power impinging on the sample. (b) Measured dimensions of the two pump beams at the sample position. The arrows in figure indicate the FWHM of the Gaussian curve used to fit the intensity profiles measured by using a beam profiler. The measurement has been performed using a splitting for the two pump pulses of $65-35$, *i.e.* the one used for the measurements reported in Ch. 4. The shaded areas show the FWHM of the probe beam.

simultaneously. After the generation of the supercontinuum, a small portion of the beam is directed to the other InGaAs detector and used as a reference.

The experiments presented in Ch. 4 have required the implementation of a double-pump excitation scheme that has been designed on purpose for this investigation. After the beam splitter, the pump pulse is cut in two by using the sharp edge of a movable prism [115]. As shown in Fig. 3.9(a), by moving the prism it is possible to cut the beam in a different position, allowing therefore to switch from conventional single pump experiment (prism not inserted) to a double pump experiment. After the splitting, one of the two halves (named as "mov. pump" in Fig. 3.9(b)) goes through a delay stage which allows to change the relative delay between two. The two halves are then recombined by using a second prism, and the two go together through a second delay stage (which allows to tune their delay with respect to the probe beam). After that, the pump beam is modulated by a chopper with a 50 % duty cycle to impose the pumped/unpumped conditions. Finally, the fluence of the pump beam can be modified by using a device consisting of a double Brewster-window polarizer preceded by a rotatable half-wave plate. The s-polarized component is chosen and focused onto the sample. It is worth noting that, if the pump is cut in two (prism inserted), this stage controls the power of both pumps simultaneously. Hence the only way of controlling the relative fluence of the two pump pulses is to change their splitting by moving the prism.

Given the fact that after the splitting the beam does not retain its Gaussian spatial profile, the estimation of the excitation fluence has required to measure the dimensions and shape of the two pump beams at the sample position. Figure 3.9(b) shows the measured beam profiles (hight and width for every pump pulse) obtained for a splitting between the two halves of $65-35$, *i.e.* the one used for the measurements presented in Ch. 4. This comparison shows that, although after the splitting the two pump pulses have rather different dimensions, at the sample position the two turn out to be very similar, thus suggesting that their final dimensions are mainly limited by aberration effects. Furthermore, Fig. 3.9(b) demonstrates that both axes of the two pump beams can be described by Gaussian profiles having different

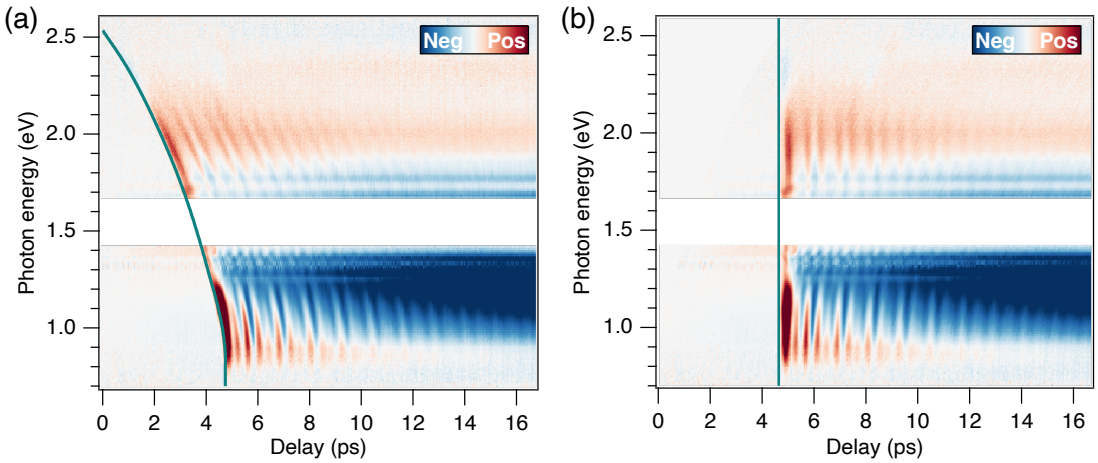

Figure 3.10: Two-dimensional maps showing the evolution of the $\Delta R/R$ signal of VTe_2 as a function of the pump-probe delay and of the probe photon energy. The spectral region around 1.55 eV was disturbed by the pump photons scattered from the sample, so it is not considered. (a) Map as acquired from the photodiode array detector. A pronounced chirp is visible. The green curve shows the profile used to correct the chirp. (b) Map after the chirp correction. After the correction the green curve shown in (a) has become a straight line.

FWHM, therefore, despite the splitting of the pump pulse, we assumed both beams to be Gaussian with an elliptical shape at the sample position.

The experimental data acquired with this setup are plotted as:

$$\frac{\Delta R(\omega,t)}{R} = \frac{R_{\text{pumped}}(\omega,t) - R_{\text{unpumped}}(\omega)}{R_{\text{unpumped}}(\omega)}, \tag{3.12}$$

where $R(\omega) = S_1(\omega)/S_2(\omega)$, with:

- $S_1(\omega)$ being a vector of signals collected by the individual pixels of the InGaAs detector placed after the sample;
- $S_2(\omega)$ being a vector of signals collected by the individual pixels of the InGaAs detector placed after the supercontinuum generation.

This definition of $R(\omega)$ is therefore used to reduce the noise arising from the fluctuations in the supercontinuum generation.

3.7.1 Supercontinuum chirp correction

Due to the large spectral content of our supercontinuum beam, a progressive elongation of the probe pulses takes place during their propagation to the sample position [116]. Indeed, thanks to the wavelength dependence of the refractive index, different colors propagate at different velocities and this results in a non-negligible *temporal chirp* of the probe pulses: the low frequencies travel in the leading edge of the pulse, while the high frequencies travel in the tail. The temporal structure of the supercontinuum beam clearly emerges in our broadband pump-probe experiments where, as shown by Fig. 3.10(a), the near-infrared part arrives ~ 3 ps earlier than the visible part, resulting in a frequency-dependent temporal overlap between the pump and the probe pulses. Since the chirp of the supercontinuum pulses is not compensated in the setup, each map has to be post-processed to compensate for the dispersion of the probe pulses. In particular, the correction is performed by shifting each row of the two-dimensional map shown in Fig. 3.10(a) along the delay axis by an amount determined by a correction curve, which depends only on the specific configuration of the

setup (and not on the sample measured). The correction curve used for the experiments presented in this thesis (green trace in Fig. 3.10(a)) has been built starting from the map displayed in panel (a), which shows the non-equilibrium reflectivity measured on VTe_2. In particular, we extracted the delay at which the $\Delta R/R$ signal reaches 1/4 of its maximum amplitude and we fitted this profile with a polynomial fit function. The resulting fit has been used as a correction curve. The measurement performed on this compound turned out to be well suited for building the correction curve. Indeed, being in this case the raise time of the non-equilibrium reflectivity limited only by our time resolution, the study of the $\Delta R/R$ signal provides a precise information on the arrival of the probe pulse. The result of the chirp correction is shown in Fig. 3.10(b). All the measurements reported in this thesis have been corrected using this approach.

3.7.2 Single-color probe experiments

The experimental setup presented in the previous section can also be used to perform single-color probe experiments without changing the probe beam or the sample position. As shown in Fig. 3.8, a foldable mirror can be used to pick the reflection of the sample. This mirror is then used to send the beam towards a single photodiode preceded by an interferential filter. Therefore by changing the filter it is possible to select the wavelength to be measured. The advantage of this experimental scheme is that, by using a single photodiode, it is possible to switch to a lock-in detection. This detection allows to obtain much higher signal-to-noise ratios and to reduce the acquisition time of the experiment. Thus this configuration can be useful in the case in which temperature or fluence scans need to be performed.

4 CDW COLLECTIVE MODES IN VTe_2

This chapter is devoted to the presentation of the time-resolved reflectivity experiments performed on the charge-density-wave compound VTe_2. These results are corroborated by the DFT simulations performed by Prof. Maria Peressi and Dr. Davide Bidoggia, which are discussed alongside to the experimental results. In particular, after having discussed the lattice reconstruction that occurs in the low temperature phase, we present a systematic temperature-dependent study of the coherent phonon modes observed in the CDW phase. From this study, with the aid of density functional perturbation theory simulations, we unveil the presence of two collective amplitude modes of the CDW phase. Furthermore, by applying a double-pulse excitation scheme, we show the possibility to manipulate these modes, gaining insights into the mutual coupling between these two collective excitations.

4.1 THE TRANSITION-METAL DICHALCOGENIDE COMPOUND VTe_2

Transition-metal dichalcogenides (TMDCs) are a class of materials with properties that make them highly attractive for both fundamental studies and for industrial applications, ranging from nano-electronics to chemical sensing [117]. Despite their rich history [118], in the last years, there has been a renewed interest in this class of materials, pushed by the possibility to reduce their thickness down to the monolayer limit and to manipulate their properties by means of external stimuli, like strain, electric fields and light pulses [119–121]. Furthermore, TMDCs usually display rich phase diagrams characterized by an interplay between different phases [122–124]. Among these phases, the presence of low-temperature CDW orders has been extensively investigated in many materials [124–126].

In this landscape, VTe_2 is currently attracting wide interest since recent angle-resolved photoemission experiments have demonstrated the presence of a CDW phase strongly coupled to the band inversion involving the vanadium 3d and tellurium 5p orbitals. As a consequence of that, the emerge of the CDW phase leads to the selective disappearance of the Dirac-like states that characterize its normal phase [124]. Furthermore, as discussed in the following, the CDW phase transition in VTe_2 cannot be explained solely in terms of Fermi surface nesting, as it would be expected from the conventional Peierls picture; conversely its origin must be sought in a peak of the wavevector dependent EPC. The presence of a strong electron-phonon coupling (EPC) dramatically affects both the low-temperature properties and the thermodynamic behavior across the CDW phase transition, making VTe_2 a promising candidate to study this unconventional CDW phase.

4.1.1 High-temperature crystal structure and CDW reconstruction

By studying the high-temperature lattice symmetry and the changes that occur due to the emergence of the CDW phase, valuable insights on the low-temperature phase can be gained.

In its normal phase, VTe_2 has a CdI_2 structure, consisting of trigonal layers formed by edge-sharing VTe_6 octahedra (shown in Fig. 4.1(a)) [127]. Upon cooling, at around 480 K, VTe_2 undergoes a first order phase transition towards a commensurate CDW phase, whose appearance is signaled by a jump in the temperature dependent resistivity and by the appearance of new diffraction peaks [46, 127, 128]. The resulting CDW phase exhibits a

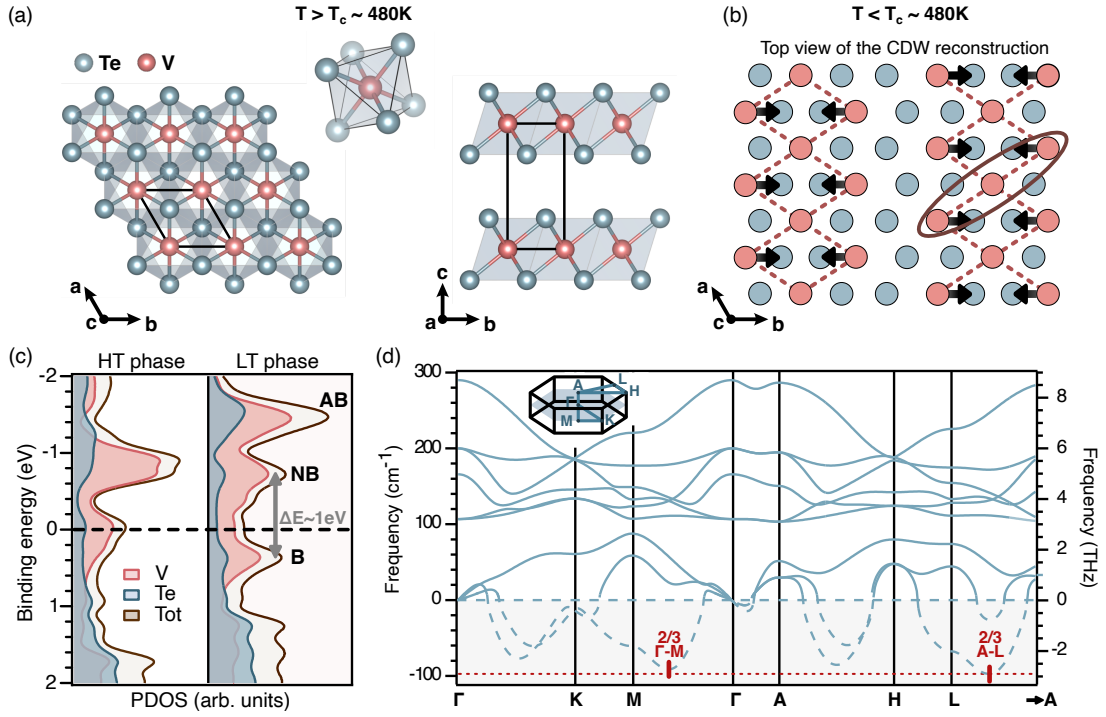

Figure 4.1: (a) Top and side views of the high-temperature crystal structure of VTe_2. In the upper part of the panel, the VTe_6 octahedron forming the trigonal layers is shown. (b) Projection of a low-temperature single VTe_2 layer on the pseudo-hexagonal plane, showing the lattice reconstruction that occurs in the CDW phase. The black arrows show the displacement direction of the vanadium atoms, while the dashed lines highlight the contraction of the V-V bonds resulting in a double zigzag structure. The brown ellipse highlights the trimerization-like bonding between three adjacent vanadium atoms, in which the position of the central atom remains almost completely unaltered. (c) Calculated total density of states (DOS) and projected density of states (PDOS) for the high-temperature (HT) and low-temperature (LT) phases. The bonding (B), non-bonding (NB) and antibonding (AB) states, arising from the trimerization-like bonding highlighted in (b), are labelled. (d) Calculated phonon dispersion along selected high-symmetry directions for the first Brillouin zone of the high-temperature phase of VTe_2. The vertical red lines denote the position of the most negative frequencies. The calculations have been performed in the zero-temperature limit using norm-conserving pseudopotentials. Modified figure based on the published version in Tuniz *et al.* [110].

3 x 1 x 3 superstructure, characterized by double zigzag chains of vanadium atoms, as depicted in Fig. 4.1(b). This pattern, commonly observed in group-V transition metal ditellurides [129], arrises due to the trimerization-like bonding of three adjacent vanadium atoms (highlighted by the brown ellipse in Fig. 4.1(b)), which results in a large contraction of the V-V bond length, with a relative change in metal-metal bond legth ($\Delta a_{max}/a$) of the order of 9 % [127, 128]. Moreover, in response to the displacements of the vanadium atoms, the tellurium octahedra are distorted, resulting in a corrugation of the VTe_2 layers and in a monoclinic lattice symmetry [127]. To quantify the extent of the lattice distortion, it is useful to compare the CDW reconstruction that occurs in VTe_2 with the one observed in 2H-$TaSe_2$, which constitutes the prototypical CDW system driven by strong EPC [12]. In $TaSe_2$, where the critical temperature is $T_{ICDW} \sim 120$ K, the relative change in the length of the unit cell triggered by lattice reconstruction is of the order of 1.5 % [130]. As discussed in section 2.3, one of the experimental evidences of a EPC-driven CDW is the presence of a large lattice distortion with respect to the transition temperature. Given the values reported above, this ratio turns out to be larger in VTe_2 than in $TaSe_2$, thus suggesting the presence of a strong EPC in VTe_2.

As a final remark about the lattice reconstruction, it is worth noting that the formation of a 3 x 1 x 3 superstructure leads to the appearance of equivalent domains, rotated by 120 degrees. As further discussed in the following chapter, the existence of these domains has to be taken into account carefully when momentum resolved techniques are employed.

The trimerization-like bonding between different vanadium atoms, not only affects the lattice symmetry, but it also deeply modifies the electronic properties of VTe_2. Figure 4.1(c) shows the calculated density of states (DOS) for the normal and the CDW phases of VTe_2. Three peaks at a binding energy of $+0.35$, -0.7 and -1.4 eV are clearly visible in the DOS calculated in the CDW phase. These peaks correspond respectively to the bonding (B), non-bonding (NB) and antibonding (AB) states that arise from the trimerization-like displacements of the vanadium atoms. Orbital-resolved calculations have shown that the vanadium d_{xy} orbitals remain almost completely unaltered during the phase transition and constitute the non-bonding (NB) peak, while the d_{yz} and the d_{zx} orbitals give rise to the bonding and antibonding states [124]. Moreover, as further elaborated in the following chapter, the localized nature of the d_{yz} and the d_{zx} orbitals has a profound effect on the electronic band structure that characterizes the CDW phase of VTe_2 [124].

4.1.2 High-temperature phonon dispersion and lattice instabilities

Important insights on the low-temperature CDW phase can be gained also from the study of the high-temperature phonon dispersion [131]. Figure 4.1(d) shows the calculated phonon spectrum along selected high-symmetry directions of the first BZ. These calculations, performed in the zero-temperature limit, show the presence of different phonon modes characterized by a negative frequency. In the framework of the density functional perturbation theory (DFPT) calculations, an imaginary phonon mode denotes an atomic displacement that lowers the free energy of the system, and thus drives a second order displacive phase transition [131, 132]. The most negative frequencies, found at about 2/3 of the ΓM and AL directions, suggest therefore a lattice instability towards an in-plane reconstruction with triple periodicity along one crystallographic direction. Moreover, the fact that the most negative value of the imaginary mode is observed along the AL direction suggests the concomitant presence of an out-of-plane reconstruction, in full agreement with the one experimentally observed in the CDW transition. Therefore, phonon calculations can give important clues about the stability of a particular crystal structure and can allow to study the relevance of the anharmonic effects and of the lattice fluctuations in the stabilization of a particular phase [131]. However, it is worth pointing out that, although the phonon calculations performed in the zero-temperature limit can be used as a starting point, in general, the lattice reconstruction occurring in the CDW phase can be inferred theoretically only by calculating the full phonon spectra as a function of the temperature, and studying at which wavevector $\mathbf{q}$ a phonon becomes unstable upon cooling [131].

Although the possibility to photoinduce the phase transition towards the normal state in VTe_2 has been investigated by means of different structural probes [133–135], to the best of our knowledge, a systematic study on the properties of the low-temperature CDW is still missing. Therefore, in the following sections we study the effect of a non-resonant excitation ($h\nu_{\mathrm{pump}} = 1.55\,\mathrm{eV}$) on the electronic and structural properties of VTe_2, analyzing in particular the behavior of the collective modes that characterize the low temperature CDW phase. If not otherwise specified, all the experiments presented in this chapter have been performed using the broadband time-resolved reflectivity setup presented in Sec. 3.7.

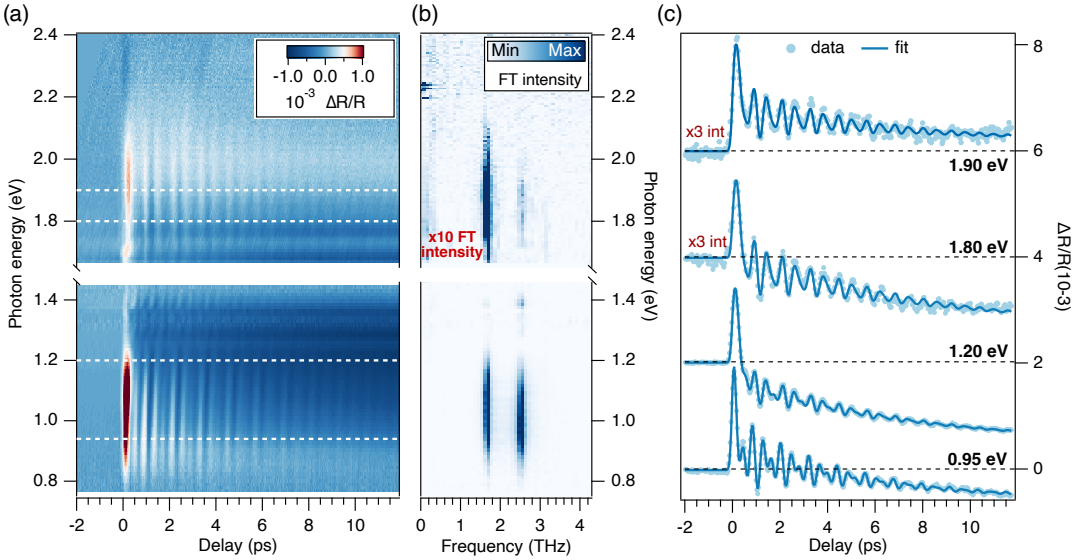

Figure 4.2: (a) Two-dimensional map showing the evolution of the $\Delta R/R$ signal of VTe_2 as a function of the pump-probe delay and of the probe photon energy. The spectral region around 1.5 eV was disturbed by the pump photons scattered from the sample, so it was not considered. (b) Two-dimensional map showing the magnitude of the Fourier Transform (FT) of the coherent part of the $\Delta R/R$ extracted from (a) as a function of the frequency and of the probe photon energy. For better visibility, in the range between 1.6 and 2.4 eV the intensity of the FT has been multiplied by a factor 10. (c) Traces extracted from (a) showing the evolution of the $\Delta R/R$ signal as a function of the pump-probe delay at four selected probe energies. Modified figure based on the published version in Tuniz *et al.* [110].

4.2 LOW-TEMPERATURE PHONON MODES

In the last two decades, all-optical pump-probe techniques have demonstrated their effectiveness in studying Raman-active collective excitations with unprecedented dynamic range and frequency resolution [28, 29, 136, 137]. In particular, by studying the reflectivity dynamics on quasi-one-dimensional CDW systems, it was shown that numerous Raman-active modes appear upon lowering the temperature through the CDW transition, thus demonstrating the capabilities of this technique [29–31]. Following this established path, we investigate the low-temperature response of VTe_2.

The two-dimensional map reported in Fig. 4.2(a) shows the evolution of the $\Delta R/R$ signal as a function of the pump-probe delay, in the spectral range accessible through our supercontinuum probe. The measurement was performed at a base temperature of 80 K and with an absorbed fluence of $\sim 250\,\mu J/cm^2$. At this fluence we estimate a single-pulse-induced lattice heating of the order of ~ 30 K (the details of this estimation will be given in the following chapter). Therefore, given the high critical temperature of this material, we reside in the low perturbation regime of the CDW ground state.

As shown by Fig. 4.2(a), for a wide range of probe photon energies the nonequilibrium reflectivity is dominated by the presence of strong coherent oscillations that add up to the incoherent exponentially decaying signal. As for other CDW systems, in the low temperature phase, the response of the incoherent part of the $\Delta R/R$ signal is characterized by a first decay that ends within 1 ps, and a by slow recovery which evolves on a timescale of ~ 10 ps [28, 29, 31]. The former, which usually slows down critically upon approaching the critical temperature, is attributed to the recombination time of hot carriers across the temperature-dependent CDW gap [28], while the latter has been suggested to be linked to the recovery of the coupled electron-lattice order parameter [138]. Although useful informations on the closure of the CDW gap could be extracted from the analysis of the incoherent part of the

non-equilibrium reflectivity [28], being interested in studying the collective excitations of the CDW phase, in the following we will mainly focus on the study of the coherent part of the nonequilibrium reflectivity.

Figure 4.2(b) shows the square magnitude of the Fourier transform (FT) of the coherent part of the signal, isolated by subtracting a double exponentially decaying fit function to the data shown in Fig. 4.2(a). Two sharp peaks at a frequency of ~ 1.65 and ~ 2.50 THz appear over a wide range of photon energies, in agreement with what has been observed in a previous work [139]. As confirmed by our DFPT calculations, these frequencies are linked to A_1 zone-center optical phonon modes peculiar of the CDW phase, being the two not present in the high-temperature phonon dispersions reported in Fig. 4.1(d). For notation purposes, since the frequency of these phonon modes varies with the temperature, as we will see in the following, we refer to these modes by labelling "A" the one with a low-temperature frequency of ~ 1.65 THz and "B" the one with a frequency of ~ 2.50 THz.

With the aim of tracking the dependence of both coherent and incoherent parts of the out-of-equilibrium reflectivity on the probe photon energy, we model the full temporal evolution of the $\Delta R/R$ signal after the perturbation as:

$$\frac{\Delta R}{R}(t, h\nu) = G(t) \otimes \Bigg[\sum_{i=1}^{2} A_i(h\nu) e^{-t/\tau_i^e(h\nu)} + B(h\nu) + \sum_{j=1}^{2} C_j(h\nu) e^{-t/\tau_j^{ph}} \cos[\omega_j t + \phi_j(h\nu)] \Bigg], \tag{4.1}$$

where G(t) represents the cross correlation between the pump and the probe pulses. The term $A_i(h\nu)$ denotes the amplitude of the electronic relaxation phenomena with time constant $\tau_i^e(h\nu)$. $B(h\nu)$ represents the amplitude of a much slower process (likely related to a thermal heating effect) that in our time window can be approximated by a constant term. Finally, the term $C_j(h\nu)$ denotes the amplitude of the oscillating component used to describe the modulation induced by a phonon mode with angular frequency ω_j, decay time τ_j^{ph} and phase $\phi_j(h\nu)$. Only the phase is assumed to be dependent on the probe photon energy. Conventionally, the excitation of coherent phonons in opaque materials is described by the DECP theory [140]. Within this theory, the phase of the resulting oscillation is directly related to the lifetime of the driving force on the vibrational coordinate. In the displacive limit, realized when the lifetime of the force is long compared to the period of the mode, a cosine oscillation with phase $\phi \approx 0$ or π is predicted, while for the impulsive limit a cosine oscillation with phase $\phi \approx \pi/2$ is expected [141, 142]. Here, however, we observe an energy dependent change in the phase of the two modes in the infrared part of the spectrum ($h\nu_{\text{probe}} < 1.55$ eV). This behavior can be explained by considering that in this spectral range the penetration depth of the probe is larger than the one of the pump, therefore a change in the probe wavelength entails a different effective fluence in the probed region. Since the phase of the two modes has proven to depend on the excitation fluence, the change of the effective fluence in the probed region could explain the continuous phase variation observed here.

Figure 4.2(c) shows four traces extracted at selected photon energies from the map shown in Fig. 4.2(a), together with the best fits obtained by using Eq. (4.1). For energies lower than 1.3 eV, a beat between the two modes is clearly visible, while for higher energies there is a predominant contribution of phonon A, which is well visible in all the investigated spectral range. The density of states calculations reported in Fig. 4.1(c) show that for energies around ~ 1 eV, the probe beam is resonant to the transition between the hybridized bonding and non-bonding vanadium states, which are strongly affected by the emergence of the CDW phase. As shown by the traces reported in panel (c), at this energy we observe an increase of the amplitude of the out-of-equilibrium reflectivity and a strong beat between the two phonon modes, thus confirming that this spectral region is maximally sensitive to a perturbation of the CDW order.

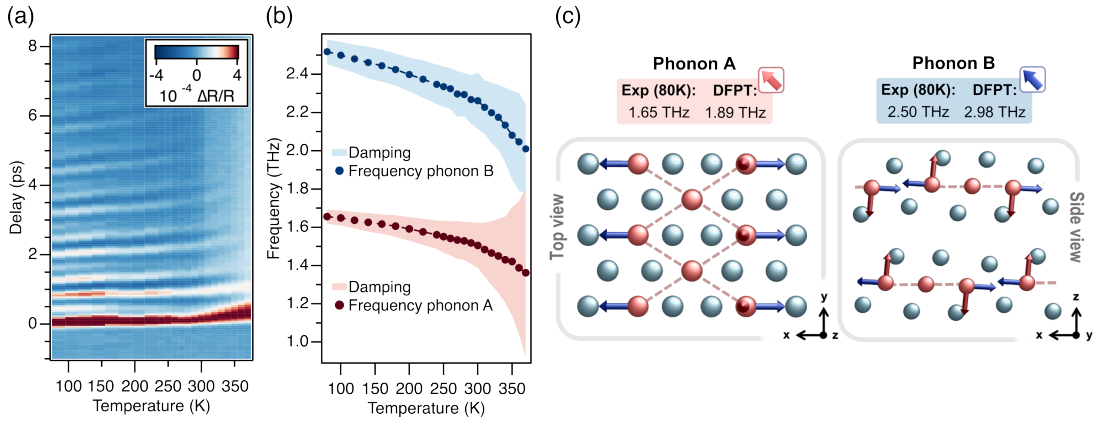

Figure 4.3: (a) Two-dimensional map showing the evolution of the ΔR/R signal as a function of the sample temperature and of the pump-probe delay. The measurements have been performed using a probe photon energy of $\sim 0.95\,\text{eV}$ (1300 nm). (b) Evolution of the frequency and damping (shaded area whose width correspond to the damping) of the two phonon modes as a function of temperature. (c) Schematic representation of the displacements associated with phonon A (red arrows) and phonon B (blue arrows). Vanadium atoms are in red, while tellurium atoms are in teal. The colored boxes show a comparison between the experimental results and the calculated frequency of the two modes. The calculations have been carried out using the QUANTUM ESPRESSO (QE) suite [143–145]. In particular, to obtain the zone-center phonon eigenvalues and eigenvectors, the dynamical matrix was calculated and diagonalized in a density functional perturbation theory (DFPT) approach [146] under the scalar relativistic approximation [147] as implemented in QE [110]. Modified figure based on the published version in Tuniz *et al.* [110].

4.3 TEMPERATURE-DEPENDENT STUDY OF THE CDW AMPLITUDE MODES

To investigate the origin of the two coherent phonon modes detected, and in particular their interplay with the CDW phase, we performed a systematic study of the evolution of the non-equilibrium reflectivity as a function of the temperature. To do so, we employed a probe photon energy resonant with the transition between the bonding and the non-bonding CDW states. Specifically, as discussed in section 3.7.2, in order to improve the signal to noise ratio we performed single-color probe measurements by filtering the supercontinuum probe with a bandpass filter at $\sim 0.95\,\text{eV}$ (1300 nm), and allowing therefore to adopt a lock-in detection of a single InGaAs photodiode. For these experiments we set the same excitation fluence used in the supercontinuum-probe measurements.

The two dimensional map reported in Fig. 4.3(a) shows the evolution of the non-equilibrium reflectivity as a function of the temperature of the system, in the range $80 - 370\,\text{K}$ (the upper boundary of this range has been set due to the experimental difficulties encountered at higher temperatures). To extract the temperature (T) evolution of the coherent part of the ΔR/R signal, we model the full temporal evolution of the non-equilibrium reflectivity after the arrival of the pump pulse as:

$$\frac{\Delta R}{R}(t,T) = G(t) \otimes \left[\sum_{i=1}^{2} A_i(T) e^{-t/\tau_i^e(T)} + B(T) + \sum_{j=1}^{2} C_j(T) e^{-t/\tau_j^{ph}(T)} \cos[\omega_j(T)t + \phi_j(T)] \right], \tag{4.2}$$

in which all the fit parameters have the same meaning of the ones already introduced in Eq. (4.1), with the difference that the photon energy dependence has been substituted by the

temperature dependence, that extends also to the frequency and the damping of the phonon modes [110].

Figure 4.3(b) shows the evolution of the frequency and of the damping constant (defined as $\Gamma = 1/(\pi\tau^{ph})$ [28]) of the two phonon modes, extracted by using Eq. (4.2), as a function of the temperature. A strong renormalization of the frequency of the two phonon modes occurs upon increasing the temperature towards the CDW critical temperature. This effect goes along with a marked increase of their damping at high temperatures. The peculiar behavior described here has been observed in many other CDW system and has been used to identify the AM mode of the system [28–31, 136, 148]. This identification is also supported by our DFT simulations [110]. Indeed, Fig. 4.3(c) shows the calculated eigendisplacements of the two phonon modes, for the vanadium atoms involved in the CDW reconstruction. For both phonon modes, there is a component of the atomic motion along the main direction of the CDW reconstruction (x axis in the figure), meaning that both phonon modes can modulate the amplitude of the PLD, and hence of the CDW, as expected for the amplitude mode of the system [11, 110, 149]. However, although both modes are intertwined with the CDW reconstruction, as shown by Fig. 4.3(c), for phonon B the movement of the vanadium atoms is more localized along the in-plane direction, where the lattice distortion is larger. Therefore phonon B is expected to modulate the CDW reconstruction more effectively. This observation is in agreement with the fact that phonon B shows a more pronounced softening when the temperature is increased, suggesting a stronger link to the charge-ordered phase. Conversely, phonon A involves smaller displacements along the in-plane direction but more pronounced movements along the out-of-plane direction [110].

We emphasize that there is a reasonable agreement between the calculated and the experimental values of the frequencies (Fig. 4.3(c)). Indeed, it has to be taken into account that the lowest temperature reached in the experiments was 80 K, while the calculations were performed in the zero temperature limit. We expect that experiments performed at lower temperatures would show a further increase of the phonon mode frequency, thus reaching values closer to the ones obtained from the calculations [11].

4.4 FLUENCE-DEPENDENT STUDY OF THE CDW AMPLITUDE MODES

4.4.1 Comparison with the temperature-dependent study

By varying the excitation fluence, additional information about the nature of the CDW phase transition can be obtained. In particular, it has been shown that the absorbed energy density required to drive the phase transition from the CDW phase to the normal state can provide additional information about the energetics of the phase transition [29]. Indeed, time-resolved reflectivity studies performed on the prototypical quasi one-dimensional CDW systems, like $K_{0.3}MoO_3$ and $(TaSe_4)_2I$, have demonstrated that the absorbed energy density required to optically melt the electronic modulation (non-thermally) is comparable to the energy gain of the electronic system upon entering the CDW phase [29, 50]. Moreover, it has been shown in different CDW systems that the energy density required to completely suppress the CDW order is substantially higher than the electronic part of the condensation energy, and comparable to the energy required to transiently heat up the sample across the phase transition [29, 50, 138, 150].

The two-dimensional map reported in Fig. 4.4(a) shows the evolution of the non-equilibrium reflectivity as a function of the absorbed fluence. The traces that compose this map have been normalized to the absorbed fluence to facilitate the comparison between curves whose intensity would otherwise differ by more than one order of magnitude. To better visualize the effect of a change in the excitation fluence in the response of the system, in the left panel of Fig. 4.4(b) we report four traces extracted at selected fluences (denoted by the dashed lines)

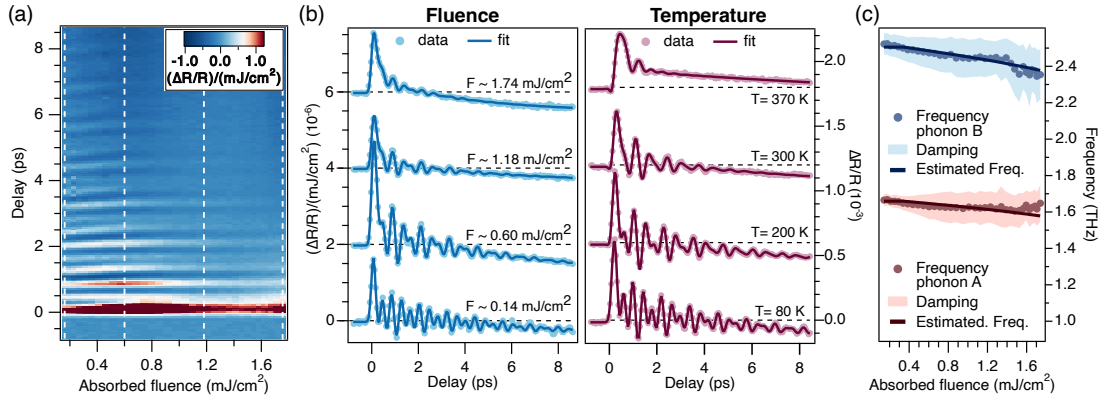

Figure 4.4: (a) Two-dimensional map showing the evolution of the normalized $\Delta R/R$ signal as a function of the absorbed fluence and of the pump-probe delay. The measurements have been performed at a probe photon energy of $\sim 0.95\,\text{eV}$ (1300 nm) and at a base temperature of 80 K. (b) Comparison between traces extracted from (a) at selected fluences (denoted by the dashed lines in (a)) and traces extracted from Fig 4.3(a) at selected temperatures. (c) Evolution of the frequency and damping (shaded area whose widths correspond to the damping) of the two phonon modes as a function of the absorbed fluence. The solid lines show the estimated evolution of the frequency of the two AMs based on the transient increase of the lattice temperature obtained by using the 3TM presented in Sec. 5.5.1.

from the map shown in Fig. 4.4(a), together with their best fits. The first important aspect to note is that, as shown by these traces, even at the highest excitation fluence reachable by our experimental setup, the absorbed energy density is not large enough to completely drive the phase transition. Indeed, even at an absorbed fluence of $\sim 1.7\,\text{mJ/cm}^2$, clear oscillations, linked to the excitation of the CDW amplitude modes, are well visible, demonstrating that the system is still in the CDW phase. Even if this fluence scan cannot be used to study the possibility to non-thermally melt the CDW phase, it is anyhow useful to compare these traces with the ones acquired at different temperatures and reported in the right side of Fig. 4.4(b). Indeed, although the two sides of this figure can look quite similar at a first glance, some differences appear in the behavior of the CDW amplitude modes.

As discussed in the previous section, when the temperature of the system is increased, we observe a pronounced softening of the AM frequencies that comes together with a large increase of their damping. Conversely, when the excitation fluence is increased by more than one order of magnitude, the frequency of the modes is only weakly perturbed (Fig. 4.4(c)). Also the damping evolution is different from the one extracted from the temperature-dependent measurements. Indeed, after a first increase, the damping of the two modes remains almost constant up to the highest fluence.

It is worth noting that the changes in the frequency of the two modes are compatible with the ones expected from the transient increase of the lattice temperature induced by the pump pulse. By using the three-temperature model presented in Sec. 5.5.1 we estimated the maximum temperature reached by the lattice after the arrival of the pump pulse and, by using the temperature scan presented in the previous section, we calculated the expected frequencies of the two modes based only on the increased lattice temperature. This procedure is based on the assumption that, since in the temperature scan a low excitation fluence has been used, these measurements can be used to extract the frequency of the modes as determined solely by the temperature of the system (and in particular of the lattice). The estimated evolution of the frequency of the two modes is shown by the two solid lines reported in Fig. 4.4(c). The excellent agreement with the values of frequency extracted from the fluence scan confirms that the changes in the AMs frequency arise mainly from the transient increase of the lattice temperature. The increased damping, instead, might originate from the anharmonic coupling of the two AMs to the non-thermal bosonic population generated by the relaxation of the

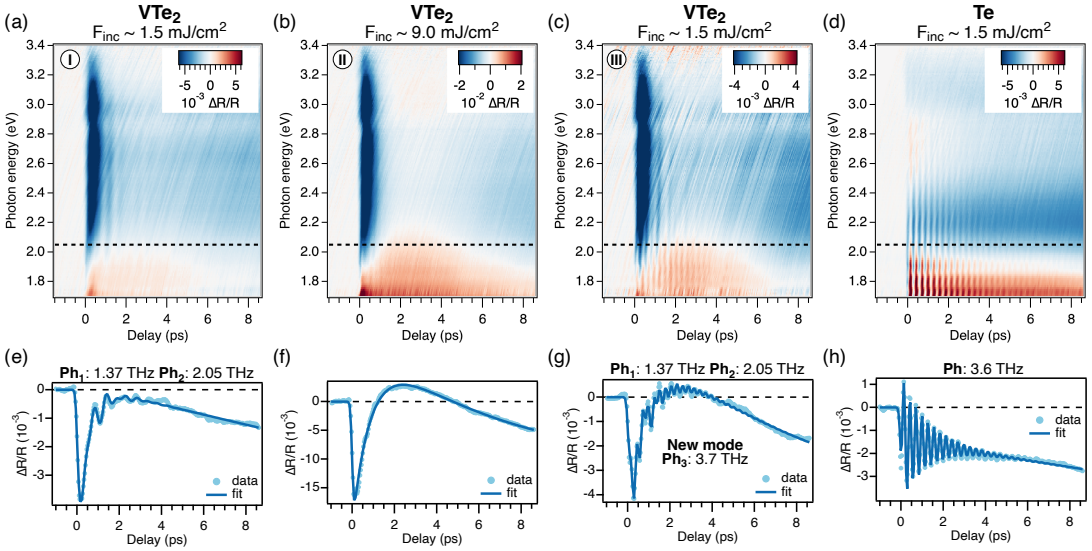

Figure 4.5: (a)-(c) Two dimensional maps showing the evolution of the $\Delta R/R$ signal of VTe_2 as a function of the pump-probe delay and of the probe photon energy. As denoted by the roman numbers, these three measurements have been performed consecutively. (d) Two dimensional map showing the evolution of the $\Delta R/R$ signal of a single crystal of tellurium as a function of the pump-probe delay and the of probe photon energy. The measurements shown in (a)-(d) were performed at a base temperature of 300 K and using a pump photon energy of $\sim$ 0.95 eV (1300 nm). (e)-(h) Traces extracted from (a)-(d) at a probe photon energy of 2.05 eV together with their best fits.

hot carriers [24, 74]. Therefore, the results reported in this paragraph show that the behavior observed in the fluence scan can be explained by considering the energy deposited in the lattice by the pump pulse, and are compatible to the ones reported in literature for other CDW systems [29, 50, 138, 150]. When a non resonant pump is used, the complete phase transition towards the normal phase is observed only at a fluence for which the deposited energy allows to transiently increase the lattice temperature above the transition temperature. Hence, using again the results of the 3TM model, it is possible to estimate the fluence required to drive the phase transition towards the normal state. Starting from a base temperature of 80 K, we obtain that to transiently increase the lattice temperature up to $\sim$ 500 K, an absorbed fluence higher than 4 mJ/cm^2 is required. This high value of fluence has proven to be unreachable with the setup presented in Sec. 3.7, and therefore, the study of the light-induced phase transition required the use of a different laser system.

4.4.2 Damage threshold in VTe_2

As shown in the previous paragraph, very high excitation fluences are required to drive the complete phase transition in VTe_2. Therefore, to reach the fluences needed while also simultaneously keeping the average heating (induced by the pump beam) as low as possible, a different broadband time-resolved reflectivity setup was used. In particular, to meet the experimental conditions required, a setup seeded by a Ti:Sapphire ultrafast amplifier (Coherent Legend Elite DUO He + USP) delivering an energy per pulse of $\sim$ 7 mJ at a repetition rate of 1 kHz was used. Being the conceptual scheme of this setup very similar to the one presented in section 3.7, here we shortly highlight only the main differences between the two. At the output of the amplifier the beam is splitted in two parts: $\sim$ 5 mJ are send to a Twin-OPA system (Light Conversion) and are used to generate the pump pulse employed in the time-resolved experiments; the remaining $\sim$ 2 mJ are send to the optical table and are used to generate the supercontinuum probe ($\sim$ 100 µJ) and to seed other setups (the remaining part). One of the

main differences with respect to the setup introduced in section 3.7, is that a continuously rotating CaF_2 crystal is used to generate the supercontinuum light instead of a sapphire window (the rotation of the crystal is needed to avoid the damaging of the crystal itself). The use of this different generation scheme is motivated by the fact that it allows to obtain a broadening of the spectral content of the pulses towards higher energies ($h\nu > 3\,eV$) [151]. Hence, given the different energy range in which the setup operates, the InGaAs array detector is replaced in favor of a NMOS photodiode array detector (S3901-256Q from Hamamatsu).

The two-dimensional map reported in Fig. 4.5(a) shows the evolution of the non-equilibrium reflectivity in the spectral range accessible by the described setup. In particular, by using the generation and detection schemes introduced above, it has been possible to investigate the response of the system up to 3.4 eV, at the expense of the near-infrared part of the spectra, that is lost. Thanks to that, the fast negative component that characterizes the $\Delta R/R$ signal of VTe_2 for probe energies higher than 2 eV, barely visible in the upper part of the map shown in Fig. 4.2(a), can be easily investigated. As demonstrated by the profile extracted at 2.05 eV and reported in Fig. 4.5(e), also in this part of the spectrum the two amplitude modes that characterized the CDW phase of VTe_2 are well visible, demonstrating the good crystalline quality of the sample under investigation. The fact that frequency, amplitude and lifetime of the two are strongly reduced (with respect to the ones shown in Fig. 4.2(a)) originates from the fact that this measurement has been performed at 300 K and using an incident fluence of $1.5\,mJ/cm^2$.

The two-dimensional map reported in Fig. 4.5(c) shows the result of a measurement performed in the same experimental conditions, after having exposed the sample to an incident fluence of $\sim 9\,mJ/cm^2$ (Fig. 4.5(b)). As demonstrated by these maps, the exposure to very high excitation fluences leads to a permanent modification of the response of the system. In particular, this permanent change is signaled by the appearance of a new phonon mode at a frequency of ~ 3.7 THz. Interestingly, the trace reported in Fig. 4.5(g) shows that although the response of the system is now dominated by the appearance of the new phonon mode, for probe photon energies higher than 2 eV, the two amplitude modes are still visible, demonstrating that at least part of the probed volume has maintained the pristine properties.

The origin of this permanent change in the response of VTe_2 has not to be sought in a photoinduced transition to an hidden state, like in the case of 1T-TaS_2 [152], but rather to a laser-induced tellurium segregation [153]. Indeed, new marked coherent oscillations at a frequency of 3.6 THz, after having exposed the samples to high laser fluences, have been observed also on other telluride compounds [153–155] and have been considered to arise from the Raman-active totally symmetric A_1 mode of tellurium [156]. Therefore, the appearance of this mode reflects the gradual formation of an at least partially crystalline Te phase induced by the incident pump pulse [154]. Moreover, the observable change in the color of the sample's surface exposed to the laser spot, together with the fact that two AMs are still visible after the exposure of the VTe_2 to high excitation fluences, suggest that the tellurium segregation takes place only at the uppermost layers (where the excitation fluence is higher) while deeper in the material the pristine properties are preserved.

To further corroborate the assignment of the new mode observed in VTe_2 to the A_1 mode of Te, in Fig. 4.5(d) we report the non-equilibrium reflectivity measured on a tellurium single crystal in the same experimental conditions. As can be seen from this figure, the $\Delta R/R$ signal is dominated by the presence of a strong coherent oscillation at a frequency of 3.6 THz (Fig. 4.5(h)) that is compatible with new frequency observed in VTe_2, hence confirming the scenario explained above. It is worth noting that neither in our measurements nor in the previous other works on Te segregation, the concomitant segregation of other species was detected [153–155]. As a final remark, we emphasize that, given the low repetition rate of the laser system employed for these measurements, the damaging of the VTe_2 crystals cannot be simply linked to the pump-induced continuous heating of the samples. Additional experiments are therefore required to investigate the origin of this permanent damage.

In conclusion, the segregation of tellurium to the surface limits the maximum fluence that can be used in the time-resolved experiments. This limitation, together with the high critical

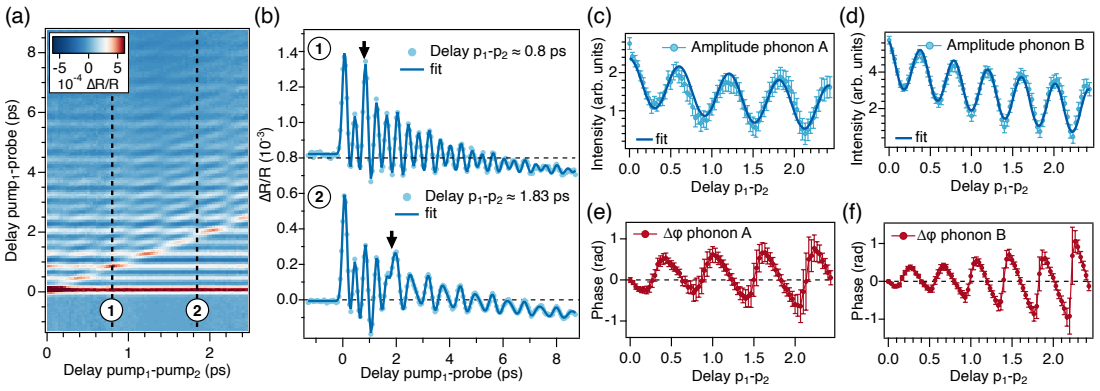

Figure 4.6: (a) Two-dimensional map showing the evolution of the $\Delta R/R$ signal as a function of the delay between the two pump pulses (x axis) and the delay between the first pump and the probe pulses (y axis). The measurements have been performed at a probe photon energy of $\sim 0.95\,\text{eV}$ (1300 nm) and at a base temperature of 80 K. (b) Traces extracted from (a) together with their best fits, showing the evolution of the $\Delta R/R$ signal as a function of the delay between the first pump and the probe pulses, for two selected delays between the pump pulses. The black arrows denote the arrival of the second pump pulse. (c)-(e) Evolution of the amplitude and of the phase shift of the two phonon modes, after the arrival of the second pump pulse, as a function of the delay between the two pulses. Modified figure based on the published version in Tuniz *et al.* [110].

temperature of VTe_2 (which instead would require high excitation fluences), has hindered the study of the photoinduced phase transition. The attempts made have proven to be not fully reproducible and therefore are not reported in this thesis.

4.5 COHERENT CONTROL OF THE CDW AMPLITUDE MODES

As discussed in section 2.4, the amplitude mode represents the fundamental excitation of the real part of the complex order parameter that describes the CDW phase. Hence, the observation of two amplitude modes in VTe_2 leads one to wonder whether these two are independent or whether they are mutually coupled because of the simultaneous link to the same order parameter. Indeed, in CDW systems the phonon-mode potentials are inherently anharmonic due to their coupling to the electron density modulation. The anharmonicity is strongest for the Khon anomaly modes, which become the amplitude and the phase modes in the CDW state. This results in a possible coupling between the different collective excitations of the low-temperature phase [157].

Additional insights into a possible coupling between the two amplitude modes of the system can be gained by performing double-pump experiments. In particular, coherent control of phonon modes have been demonstrated in a wide variety of crystalline material, including quasi-one-dimensional CDW systems [158–163], and can be used to study the coupling between different modes [164]. Here we apply this approach to the case of VTe_2.

4.5.1 Single color probe measurements

In general, after the photoexcitation, the motion of the vanadium atoms in real space, is defined by the combination of the eigendisplacements of phonon A and B, as shown in Fig. 4.4(c). Using a double-pump excitation scheme, and tuning the delay between the two pump pulses, it is possible to selectively enhance or reduce the amplitude of one of the two phonon modes, while studying the effect on the other mode. We show the result of this approach in the two-dimensional map reported in Fig. 4.6(a), where the evolution of the

non-equilibrium reflectivity is studied as a function of the delay between the two pump pulses. Here, the first pump pulse, named "$pump_1$" (p_1), excites the two amplitude modes, while the second pump pulse, named "$pump_2$" (p_2), is used to control them. For this experiment, we set the absorbed fluence to be F_{p1} =2F_{p2} $\sim$ 230 $\mu J/cm^2$.

In order to better visualize the effect of the second pump pulse on the two AMs, in Fig. 4.6(b) we show two traces extracted from Fig. 4.6(a) at selected delays between the two pump pulses. Trace 1 shows the effect of a second excitation that is in phase with phonon B but almost completely out of phase with phonon A. The result is an enhancement of the amplitude of the former and a suppression of the latter. Considering again the movement of the atoms in real space, this implies that the large out-of-plane component in the movement of the vanadium atoms, given by the excitation of phonon A, is deeply reduced while the movement along the in-plane coordinate of the PLD is amplified. Conversely, trace 2 shows the opposite case. Specifically, the excitation of the second pump pulse here is in phase with phonon A but out of phase with phonon B. This leads to an enhancement of phonon A and a suppression of phonon B.

Up to now we just considered the effect of the second pump pulse at two selected delays, however from the two-dimensional map reported in Fig. 4.6(b) it is possible to extract the complete evolution of the amplitude of the two AMs, after the arrival of the second pump pulse, as a function of the delay between the two pump pulses (Fig. 4.6(c) and (d)). This choice is motivated by the fact that, from the evolution of their amplitude, it is possible to gain information on the coupling between the two. Indeed, in the case of independent oscillators, the temporal evolution after the perturbation induced by the second pump pulse can be modeled as [164, 165]:

$$I(t_{PP}) = I_i^0 e^{-(t-t_{PP})/\tau_i^{ph}} + \Delta I_i^0 \cos(\omega_i(t - t_{PP}) + \phi_i), \quad i = A,B. \tag{4.3}$$

Where I_i^0 is the amplitude of the phonon at the arrival of the second pump pulse and τ_i^{ph} is the decay time of the mode. ΔI_i^0 denotes the magnitude of the change in the intensity of the AM mode induced by the arrival of the second pump pulse; ω_i and ϕ_i denote respectively the frequency and the phase of the mode.

As shown in Fig. 4.6(c) and (d) the fits obtained by using Eq. 4.3 allow to describe with a very good agreement the evolution of the intensity of the amplitude modes. This implies that the intensity of one of the two modes can be enhanced or suppressed without affecting the other. Therefore, even if the two amplitude modes are coupled to the same electronic order, the two are completely independent.

Furthermore, as shown by Fig. 4.6(e) and (f), the double-pump excitation scheme allows also to control the phase of the two modes [166, 167]. Indeed, the second pump pulse induces a phase shift in the motion of the ions, whose extent depends on the delay between the two pump pulses (Fig. 4.6(e) and (f)). This effect can be explained considering the fact that two AMs are described by damped cosine oscillations and, as time passes, their intensity decreases while the intensity of the second pump pulse remains fixed. Hence, the effect of the second pump pulse grows with the delay between the two pump pulses.

4.5.2 Spectrally resolved double-pump excitation

Up to now, the double-pump excitation scheme has been considered only in conjunction to a single-color probe acquisition. However, this excitation scheme can be also applied to the case in which a supercontinuum probe is used, allowing therefore to simultaneously study the effect of the second pump pulse at different probing energies.

The two-dimensional map reported in Fig. 4.7(a) shows the evolution of the non-equilibrium reflectivity as a function of the probe photon energy and of the pump-probe delay for an excitation scheme in which the second pump pulse is completely out of phase with phonon A and thus almost completely in phase with phonon B. As shown by the FT reported in

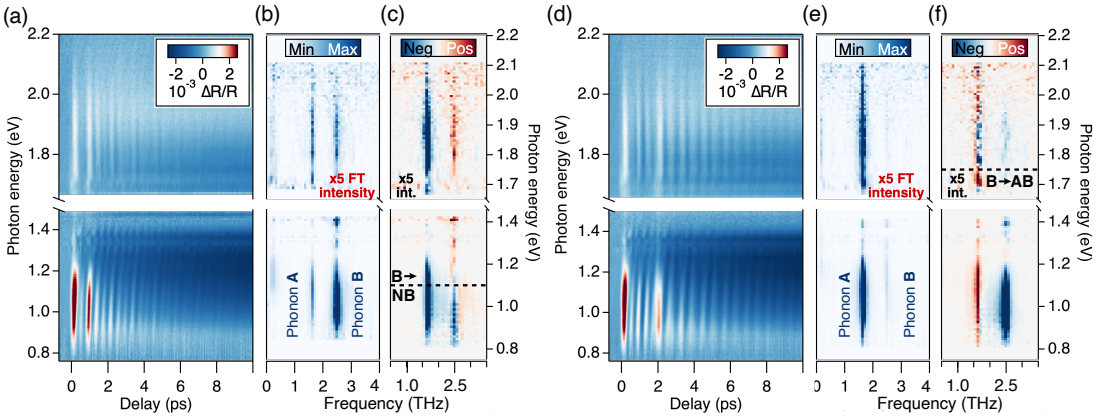

Figure 4.7: (a) Two-dimensional map showing the evolution of the ΔR/R signal as a function of the probe photon energy and the pump-probe delay for an excitation scheme in which the second pump pulse is completely out of phase with phonon A. The measurement has been performed at 80 K and the absorbed fluence was set to be $F_{p1} = 2F_{p2} \sim 250\,\mu J/cm^2$. (b) Two-dimensional map showing the magnitude squared of the Fourier Transform of the coherent part of the ΔR/R signal extracted from (a), as a function of the probe photon energy. (c) Difference between the map reported in (b) and the one reported in Fig. 4.2(b), showing the change in the magnitude squared of the FT induced by the arrival of the second pump pulse. (d)-(f) are analogue to (a)-(c) with the only difference that the second pump pulse is completely out of phase with phonon B. Modified figure based on the published version in Tuniz *et al.* [110].

Fig. 4.7(b), a clear reduction in the intensity of the peak at 1.6 THz is observed in the full spectral range. The changes induced by the second pump pulse on the coherent part of the ΔR/R signal can be better visualized by considering Fig. 4.7(c), which shows the difference between the map shown in panel (b) and the one shown in Fig. 4.2(b), acquired by using a conventional single-pump excitation scheme. It is worth noting that, these measurements have been performed consecutively, and that the difference between the two has been calculated after having carefully normalized the intensity of the ΔR/R signal, to account for possible variations in the generation of the supercontinuum beam. Unexpectedly, while the intensity of phonon A is reduced in all the spectral range, the effect on phonon B depends on the range considered. Indeed, the intensity of phonon B is enhanced in the visible part of the spectrum while it is reduced in the infrared part. A similar behavior is observed also in the case in which the second pump pulse arrives in antiphase with phonon B (Fig. 4.7(d)-(f)). In particular, Fig. 4.7(f) shows that, while phonon B is suppressed in all the spectral range accessible by our probe pulse, the intensity of phonon A is reduced only in a narrow range around 1.85 eV, while it is enhanced in the remaining parts.

Since the phase that characterizes the motion of the atoms is uniquely defined for each phonon modes, the fact that the second pump pulse seems to have an energy dependent effect on the phonon modes must be a consequence of the probing mechanism [103]. Indeed, the changes of sign observed in panels (c) and (f) are located at energies close to the ones required to trigger an optical transition between the bonding-nonbonding and the bonding-antibonding states, suggesting therefore that this peculiar behavior might originate from the fact that different optical transition are involved (we remind that phonon B is mostly localized in the infrared part of the spectrum, i.e. for phonon energies resonant to the bonding-nonbonding transition, while phonon A is well visible in the full energy range accessible by our probe beam). The complete understanding of the effect here described requires the detailed modeling on how the energy-dependent dielectric function of the material is modified by the excitation of the two phonon modes [109]. These calculations however go beyond the scope of this thesis.

Despite the lack of a microscopic explanation, the results reported in this section show that the use of a supercontinuum probe gives access to an information inaccessible by means of a single-probe acquisition, highlighting the importance of broadband probes in time-resolved reflectivity experiments.

4.6 CONCLUSIONS

In this chapter we reported a detailed study of the low-energy collective excitations of the CDW compound VTe_2. In particular, the broadband time-resolved reflectivity experiments performed in the CDW phase have shown that the low-temperature response of the material is dominated by the presence of two phonons modes. By performing a systematic temperature-dependent study, we unveiled the presence of a mean-field like softening of their frequency when the temperature of the system is raised towards the CDW critical temperature, as expected from the amplitude mode of the system. The identification of the phonon modes as the amplitude modes of the system has then been corroborated by DFPT calculations, which have shown that both phonon modes modulate the amplitude of the lattice reconstruction.

The observation of two AMs simultaneously linked to the same order parameter has motivated the study of their possible mutual coupling. This study has required the implementation of a new double-pulse excitation scheme, which has been specifically designed for these experiments. Indeed, the use of a double-pump excitation allows to study the indirect effect of the enhancement or suppression of one AM to the other one, thus gaining insights on their possible coupling. Interestingly, these experiments have shown that the two modes can be independently modulated, and therefore, even if coupled to the same order parameter, the two are independent.

Furthermore, the possibility to photoinduce the phase transition has been investigated. This study, however, has been hindered by the fact that the excitation fluence limited to photoinduce the transition towards the normal phase is higher than the damage threshold of the material. Indeed, we demonstrated that high excitation fluences cause the segregation of Te atoms to the surface, with the gradual formation of an at least partially crystalline tellurium phase. The presence of this segregated phase has therefore overshadowed the response of pristine VTe_2.

Finally, we emphasize that, despite the presence of a large lattice reconstruction and a marked resilience upon excitation with near infrared light pulses, which point towards the presence of a CDW phase originating from a strong momentum dependent electron-phonon coupling, our findings show that the AMs of the charge-ordered phase are characterized by a behavior similar to the one observed in the prototypical quasi-one-dimensional systems [28–30].

5 QUENCH OF THE ELECTRONIC ORDER IN VTe_2 BY ENHANCED LATTICE FLUCTUATIONS

This chapter is devoted to the presentation of the time-resolved ARPES experiments performed on VTe_2. In particular, after having discussed the domain structure that characterizes the low-temperature phase of VTe_2 and having presented a procedure to increase the size of the domains, we report a systematic temperature-dependent study of the CDW gap. These results are then used as a starting point to analyze and interpret the TR-ARPES experiments performed on VTe_2. Specifically, the time-resolved experiments have unveiled that the light-induced quench of the electronic order, with the consequent (partial) collapse of the CDW gap, is not dominated by the excitation of the CDW amplitude modes, but it is instead driven by an incoherent process. In the last part of the chapter, by applying a so-called three-temperature model, we demonstrate that the measured dynamics can be modeled by considering the incoherent excitation of a subset of strongly-coupled optical phonon modes arising from the hot carrier relaxation.

5.1 DOMAIN STRUCTURE OF VTe_2

As anticipated in Sec. 4.1.1, the lattice reconstruction that occurs in the low-temperature CDW phase leads to the formation of different domains. In particular, during the transition from the high-temperature CdI_2 structure to the monoclinic form, a particular vanadium atom can be displaced in six possible directions. Indeed, as shown in Fig. 5.1(a), these directions correspond to the three possible orientations of the *a*-axis defined by the in-plane 3×1 superstructure (one every 120°, denoted by the roman numbers in figure), and by the two possible directions available for each orientation (denoted by the two arrows for every orientation). Since the direction of displacement of the vanadium atom in the octahedral surrounding determines the orientation of the *c*-axis (the possible orientations are named c and c' in Fig. 5.1), this degeneracy leads to the formation of six domains [127]. Fig. 5.1(b) and (c) show the two orientations of the *c*-axis available for a given in-plane direction. Following the original work from Bronsema *et al.*, the resulting structures are named "normal variant" and "anti-variant" [127].

Although, as explained above, an exhaustive analysis of the domain structure of VTe_2 requires to distinguish the presence of three normal variant and three anti-variant domains, from here on, we will consider only the presence of the three in-plane domains, neglecting the relative orientation of the *c*-axis. This choice originates from the fact that the presence of different in-plane domains directly affects the ARPES data, since a change of domain implies a rotation of the unit cell, and thus of the Brillouin zone, of 120°. Moreover, the size of the in-plane domains is of the same order of magnitude of the spot size of the HHG probe (FWHM $\sim 100\,\mu m$ [99]) that we use in the ARPES experiments. Thus, an ARPES experiment performed using our HHG source on a pristine sample, gives access only to a superposition of rotated Brillouin zones which arises from a mixture of different in-plane domains. This effect is exemplified in panels (b) and (c) of Fig. 5.2.

Figure 5.2(a) shows the first Brillouin zone of VTe_2 in the normal phase (left) and in the CDW phase (right). The disappearance of two of the three mirror planes that characterize the normal phase of VTe_2 triggers a profound modification of the electronic band structure at the M points. Given the importance of these high symmetry points, in the following we refer to the M points of the low-temperature phase by naming M_1 the ones that reside on a mirror

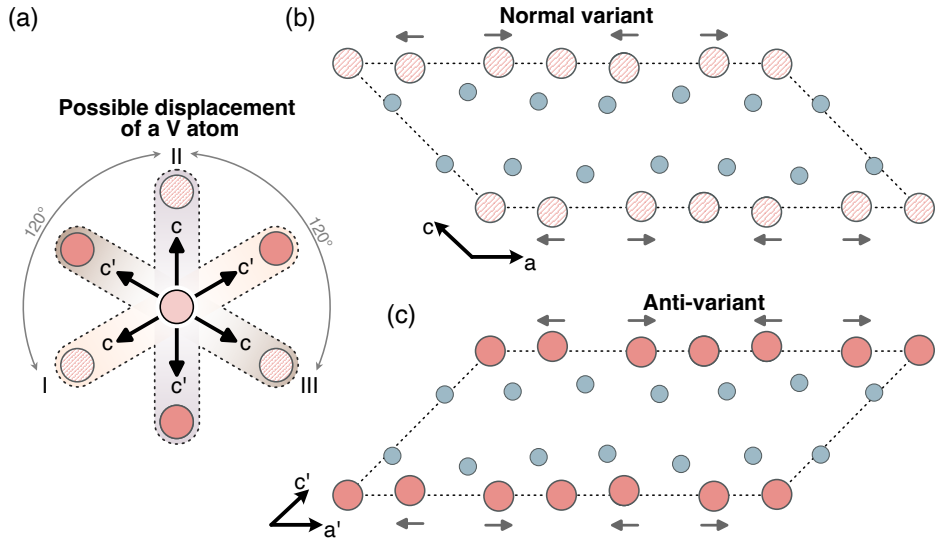

Figure 5.1: (a) Possible displacement directions of a vanadium atom in the octahedral surrounding. The orientations of the three in-plane domains (I-III) and the two possible directions of displacement, which determine the direction of the c-axis, are indicated. The normal variant is indicated with the letter "c" while the anti-variant with the letter "c'". Adapted from [127]. (b) and (c) Projection of the CDW structure on the (010) plane of the normal variant (a) and the anti-variant (b) for a given in-plane domain. The grey arrows denote the direction of movement of the vanadium atoms. The corrugation of the VTe_2 layers is also illustrated. As for the other figures, vanadium atoms are in red and tellurium atoms are in teal. Adapted from [127].

plane and M_2 the ones that, due to the lattice reconstruction, do not reside anymore on a mirror plane. As further discussed in the following, this peculiar reconstruction is promoted by the energy gain that arises from the opening of the CDW gap. As a consequence of that, the study of the electronic band structure at the M points turns out to be of paramount importance for the understanding of the physics of the CDW transition in VTe_2. This study is however hindered by the presence of the different domains. Indeed, as shown in Fig. 5.2(b) and (c), when a probe beam larger than the domain size is used, the resulting superposition of BZs makes the M_1 and M_2 points to overlap, hence complicating the study of the CDW gap that opens at the M_2 point. A possible solution to overcome the problem of the different domains that characterize the CDW phase of VTe_2 is presented in the next section.

5.2 STRAIN-INDUCED DOMAIN STABILIZATION

The use of external stimuli to manipulate the diverse phenomena observed in quantum materials is attracting a large interest since it may allow to achieve a tunable control over technologically relevant materials properties. Within this contest, uniaxial strain has recently emerged as a powerful approach to control the properties of solids [168–172]. While a lot of efforts have been made to control, by means of an applied strain, the phase transition in different materials [173–175], only in the last few years it has been shown that uniaxial strain can be used also to control the domain structure of a material. For instance, it has been recently demonstrated that in 1T-$IrTe_2$ a modest uniaxial strain can promote the formation of domains that are four orders of magnitude larger than in the unstrained samples [176]. Here we apply the same approach on VTe_2.

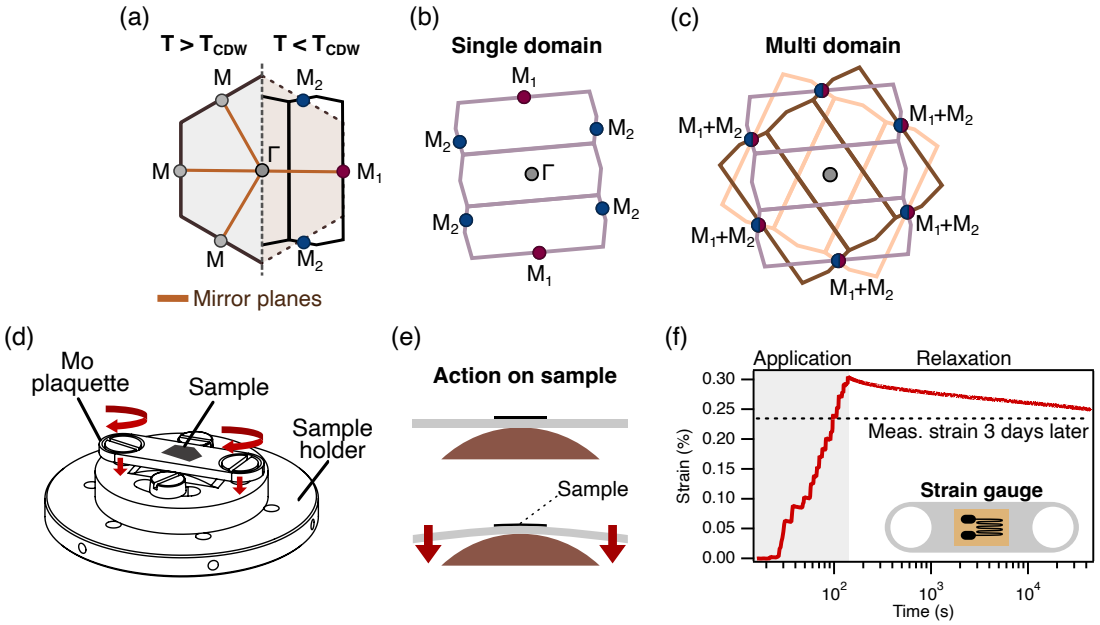

Figure 5.2: (a) High-temperature (left) and low-temperature (right) first Brillouin zones of VTe_2. The mirror planes that characterize the two BZs are also shown. (b) View of the reciprocal space as seen by a probe beam smaller than the size of the domains. (c) View of the reciprocal space as seen by a probe beam larger than the domain size. Due to the averaging over different domains, the M_1 and M_2 points are perfectly overlapped. (d) Three-dimensional view of the strain device used. The sample is glued on top of a molybdenum bridge that can be bent by screwing the two screws located at the edges of the plaquette. (e) Schematic side-view of the bending process. Thanks to the bicomponent epoxy glue, the strain is transferred from the plaquette to the sample. (f) Measurement of the applied strain obtained by using the SGT-3N/350-TY43 OMEGA strain gauge depicted as inset. The first part of the graph (denoted by the gray area) has been recorded while screwing the two screws in an alternating and symmetrical manner. After having reached the desired deformation of the bridge, a mechanical relaxation of the strain device is observed, with the concomitant reduction of the applied strain. The strain was constantly monitored for 11.4 hours. The value of strain measured 3 days after the application is shown by the dashed line.

5.2.1 Characterization of the strain device

The strain device developed for the experiments presented in this chapter is shown in Fig. 5.2(d). This apparatus is based on a home-built design consisting of two parts: a molybdenum (Mo) plaquette over which the samples are mounted, and a GLIDCOP block (copper alloy system obtained by adding a small amount of aluminum oxide particles) characterized by the presence of a rounded protrusion placed below the molybdenum plaquette. When the pieces are screwed together, the molybdenum plaquette is forced to bend by the GLIDCOP block, thus delivering the strain to the sample (as depicted in Fig. 5.2(e)). The choice of this alloy for the lower block arises from the fact that it ensures higher strength values with respect to the pristine copper, therefore limiting its deformation and maximizing the amount of strain transferable to the sample. Finally, by means of other two screws, the strain device is mounted on the sample holder usually used in the ARPES experiments. These screws also allow to set the relative orientation of the sample with respect to the slit of the analyzer.

The samples were mounted on top of the molybdenum bridge using a two-component epoxy glue (EPO-TEK H20E-PFC), which was cured and allowed to cool before the strain was applied. The strain was applied by manually tightening the two screws at the sides of the molybdenum plaquette in an alternating fashion. To maximize the amount of strain transferred to the samples, their thickness has been reduced by cleaving them in air using a Kapton tape.

Moreover, to have a more precise control over the application of the strain, this procedure has always been performed outside from the photoemission chamber, before inserting the samples.

The strain magnitude transferred to the sample was measured by using a commercial strain gauge from Omega Engineering (a sketch of the strain gauge is reported in Fig. 5.2(f)), that was attached to the unstrained molybdenum bridge using the same epoxy glue used for the samples. These gauges are characterized by a nominal resistance of 350 Ω, that varies when a small amount of strain is applied. Hence, by measuring the change in their resistance, it is possible to quantify the strain transferred to the sample. Specifically, the value of the applied strain can be obtained by using the equation [177]:

$$\epsilon = \frac{1}{\kappa}\frac{R - R_0}{R_0}, \tag{5.1}$$

where κ is the gauge factor, that for the specific gauge used was $\kappa = 2.13$, and ϵ is the total strain. In general, the measured value results from the sum of the bending (tensile) strain and the perpendicular compressive strain. In the geometry defined by our strain device, however, the perpendicular strain is considerably smaller than the bending strain [174], hence from here on with "strain" we will refer only to the tensile strain [176]. Indeed, the independent measure of the compressive and the tensile strains would require the use of an additional strain gauge, that is impractical given the reduced size of the sample plaquette [177].

The value of the applied strain obtained by measuring the variation of resistance of the strain gauge, and by using Eq. (5.1), is reported in Fig. 5.2(f). The gray region in this graph denotes the time interval in which the strain was applied (the small jumps visible in the value of strain arise due to the alternate tightening of the two screws). At the end of the application, a maximum strain of the order of 0.3% was initially reached thanks to the plastic deformation of the molybdenum bridge. Immediately after, however, we observe a slow relaxation of the applied strain, that continues for the full time interval in which the strain was constantly monitored ($\sim$ 11.4 hours). The origin of this relaxation has to be sought in a mechanical relaxation of the strain device used. The value of the measured strain after three days from the application is also reported. From this measurement, we can estimate the value of the applied strain on the VTe_2 samples to be of the order of $\sim$ 0.2 % during the ARPES experiments.

As a final remark, it is worth nothing that, to reach these values of strain, the molybdenum plaquette has to be bent beyond the threshold of the elastic deformation, therefore the application of the strain to the samples is not reversible.

5.2.2 Effect of strain on the structural and electronic properties of VTe_2

To study the possibility of increasing the domain size by applying a tensile strain, we performed low energy electron diffraction (LEED) and ARPES experiments. Figure 5.3(a) shows a comparison between two LEED images acquired on the same sample (and at the same temperature): the left one has been acquired before the application of strain, while the right one has been acquired after the application of strain. The effect of the applied strain is clearly visible from these images. Indeed, while the complex pattern that appears in the unstrained sample arises from the superposition of the three different domains, the one observed on the strained sample clearly denote the presence of a single domain in the probed region (the diameter of the LEED beam stays within the range: 1 mm > d > 250 μm). This comparison demonstrates therefore the possibility to increase the size of the domains in a VTe_2 by applying a tensile strain of the order of 0.2 %. Specifically, the original domain whose direction is closer to the direction of the applied strain appears to be the one which shows a more pronounced increase in its size (the domain enlarged by strain application was already visible in the unstrained image, thus the applied strain does not induce a rotation of the domains). Hence, the relative orientation of the sample with respect to the direction of the applied strain doesn't play a crucial role on the possibility to promote the formation of larger domains. This degree of freedom can be used to select a particular domain whose size will be increased.

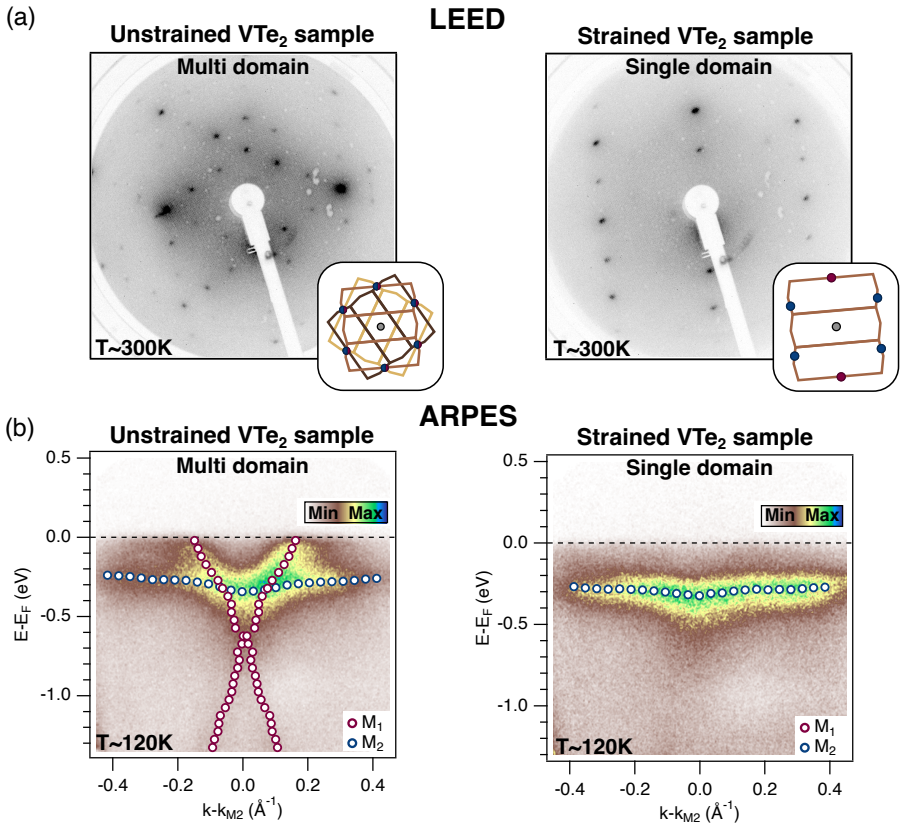

Figure 5.3: (a) LEED images taken before (left panel) and after (right panel) the application of strain on the same VTe_2 sample. A single domain with 3×1 superstructure is observed in the strained case. The images have been taken at a temperature of ~ 300 K and with a kinetic energy of 75 eV. (b) ARPES spectra acquired along the K-M_2-K direction on an unstrained (left panel) and on a strained (right panel) samples. The superposition of the bands coming from the M_1 and M_2 points is clearly visible on the unstrained sample, while on the strained sample only the nearly-flat band coming from the M_2 point is visible. The measurements have been performed at a temperature of 120 K and with a probe photon energy of $h\nu = 21.6$ eV. The colored circles denote the central position of the bands extracted from the fits of the EDCs.

We emphasize that the reproducibility of this approach has been tested by performing experiments on different VTe_2 samples. These measurements have always given results very similar to the ones reported here, thus demonstrating the reliability of this approach.

As a second step, we investigated the effect of the applied strain on the electronic band structure. Figure 5.3(b) shows a comparison between two ARPES spectra acquired on a unstrained (left) and on a strained (right) samples. To obtain a clean surface suitable for the ARPES experiments, the samples were cleaved in situ by means of a Kapton tape. The same procedure has been used for all the photoemission experiments reported in this thesis.

As for the LEED image, the ARPES map acquired on the unstrained sample shows a superposition of bands coming from different Brillouin zones. Indeed, as discussed above and as expected from the symmetry of the Brillouin zone, this image clearly shows the superposition of the bands coming from the M_1 and the M_2 points [124]. On the strained sample instead, only the nearly-flat band coming from the M_2 point is visible. These spectra therefore demonstrate the possibility of performing photoemission experiments on a single domain. Moreover, they also show that the amount of strain used to promote the formation of larger domains doesn't entail sizable modifications of the electronic band structure. Hence, no changes in the physics of the CDW transition are expected to occur due to the application of the tensile strain (a detailed discussion is reported in appendix A).

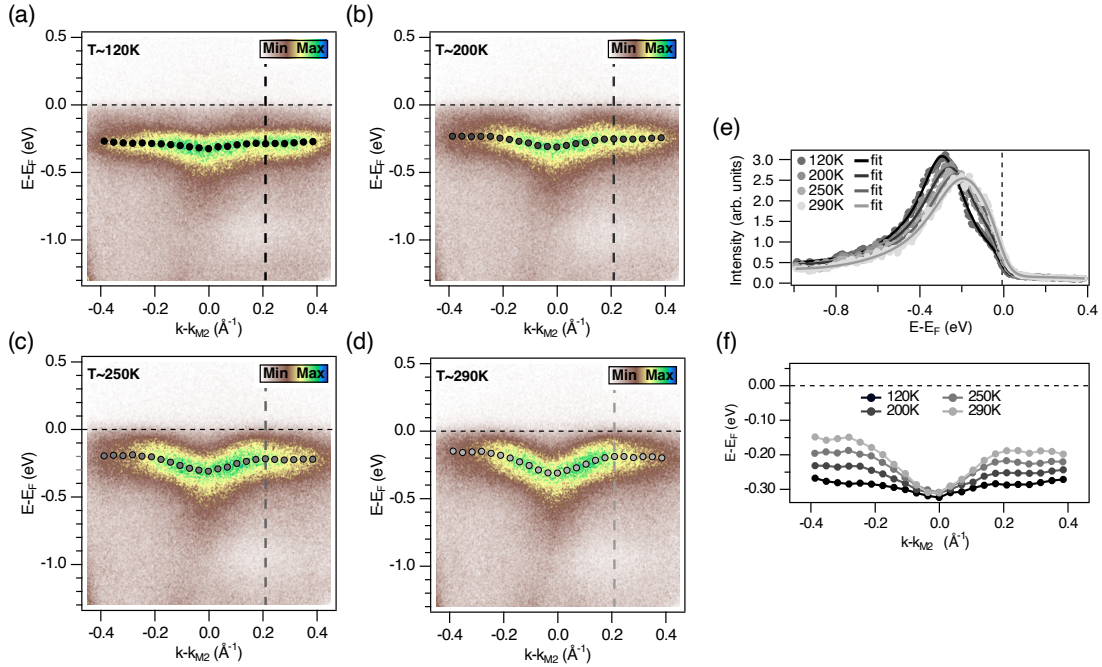

Figure 5.4: (a)-(d) Photoemission spectra acquired along the K-M_2-K direction at different temperatures, using photon energy of 21.6 eV. The grey circles denote the central position of the Lorentzian peaks used to fit the EDCs, and thus show the dispersion of the vanadium 3d band. (e) EDCs extracted from (a)-(d) at the momentum position denoted by the dashed lines. The fits obtained by using the global fitting procedure described in the text are superimposed to the original data. (f) Evolution of the dispersion of the hybridized vanadium 3d band as a function of the temperature. The traces reported in this graph correspond to the ones shown in panel (a)-(d).

Being the increase of the domain size the only detectable effect of the tensile strain, to facilitate the analysis and the interpretation of the ARPES spectra, in the following sections we will present only photoemission experiments performed on strained samples.

5.3 EQUILIBRIUM ARPES: TEMPERATURE EFFECT AT M_2

As mentioned in the previous sections, the interest in studying the band structure at the M_2 point originates from the fact that this is the region of reciprocal space where the CDW gap opens. Before studying the effect of a temperature change, however, it is useful to reconsider the modifications of the electronic band structure in view of the change in the lattice symmetry triggered by the CDW reconstruction, keeping in mind that anyhow the reconstruction is possible only thanks to the gain in energy of the electronic system, thus the two are strongly intertwined. As shown by Fig. 5.2(a), in the normal phase, the M points reside on a mirror plane which prohibits the hybridization between the Te 5p orbitals (odd with respect to the mirror plane) and the V 3d orbitals (even with respect to the mirror plane). On the other hand, in the low-temperature phase, while the M_1 point keeps a similar situation with respect to the high-temperature phase, the M_2 point does not reside anymore on a mirror plane. Hence the V 3d and the Te 5p orbitals can now mix, thus leading to a significant change in the band structure [124]. Indeed, the V-shaped band that characterizes the M points in the normal phase of VTe_2 disappear, and a peculiar nearly-flat band appears at $E_B \sim 0.25$ eV. Therefore, by changing the temperature of the system in a range far from the transition temperature, a continuous

transition from a V-shaped to a nearly-flat band is expected to take place. Conversely, being the CDW phase transition of the first order, an abrupt change is expected to take place at T_{CDW}.

With these considerations in mind, it is useful to reconsider the analysis of the DOS presented in Sec. 4.1.1. Indeed, the nearly-flat band that appears in the low temperature phase is responsible for the peak that appears in the DOS at $E_B \sim 0.25$ eV. This peak has been discussed to originate from the bonding states that arise due to the trimerization-like process between three adjacent vanadium atoms, and thus constitutes the lower branch of the CDW gap. The flatness of this band reflects the localized nature of the d_{yz} and d_{zx} orbitals in real space [124].

All the photoemission experiments reported in this chapter have been performed using the HHG source described in Sec. 3.5. In particular, the ninth harmonic of the fundamental, characterized by a photon energy $h\nu = 21.6$ eV, has been used to perform both ARPES and TR-ARPES experiments. Starting from this photon energy and using the estimate of ~ 8.8 eV for the inner potential of VTe_2 [124], we obtain $k_z \sim 2.6$ Å^{-1}, that places us on the A-L plane of the undistorted hexagonal Brillouin zone [110]. Since, however, it has been proven that the nearly-flat vanadium band has a negligible k_z-dependence [124], for clarity in the following sections we will keep the in-plane ($\Gamma-M$) nomenclature for the high symmetry points of the BZ.

Figure 5.4(a) shows the band structure measured along the K-M_2-K direction, at a temperature of ~ 120 K. Being this temperature much lower than the transition temperature ($T_{CDW} \sim 480$ K, $T/T_{CDW} \sim 0.25$), the nearly-flat band that characterizes the CDW of VTe_2 is clearly resolved. As expected from the change in the lattice symmetry, by increasing the temperature towards the critical temperature, we observe a folding towards the Fermi level of the hybridized vanadium 3d band, in such a way that the V-shaped band is partially restored (Fig. 5.4(b)-(d)).

To quantitatively analyze the folding of the vanadium 3d band and thus the temperature-driven closure of the CDW gap, we developed an *ad-hoc* line shape fitting procedure. Every ARPES spectrum is sliced into 30 Energy Distribution Curves (EDCs), obtained by dividing the range of the accessible momentum into 30 identical intervals. All the EDCs are then fitted simultaneously using a global fitting procedure that allows to link together some of the fitting parameters used to describe the single traces. In particular, the single EDCs are fitted using a Lorentzian-shaped density of states (DOS) multiplied by the Fermi-Dirac distribution at which is then added a third order polynomial function, used to describe the background. The resulting expression is convoluted with a Gaussian function (G, with a FWHM of 55 meV) to account for the finite energy resolution of our experimental setup. The resulting fit function is therefore:

$$I(E) = G(E) \otimes \left[\left(\sum_{i=1}^{2} L_i(E) \right) \times \frac{1}{e^{(E-E_F)/k_B T} + 1} + bkg \right], \tag{5.2}$$

with:

$$L_i(E) = \left(\frac{I_i(\Gamma_i/2)}{(E - E_{Bi})^2 + (\Gamma_i/2)^2} \right) \quad \text{and} \quad bkg = A + B \cdot E + C \cdot E^2 + D \cdot E^3.$$

All the EDCs have been fitted by using a single Lorentzian peak with the exception of the ones extracted around $k\text{-}k_{M2} \sim 0$, for which a second peak has been added to describe the tail that develops towards higher binding energies (visible in Fig. 5.4(a)-(c)).

For the photoemission experiments reported in this section, the fits have been obtained by linking together the chemical potential and the electronic temperature of all the energy distributions curves, and leaving instead free the parameters of the Lorentzian peaks. Figure 5.4(e) shows the EDCs extracted from the ARPES spectra at the position denoted by the dashed lines, together with the fits obtained by using the global fitting procedure described here. This comparison shows that the simple model used to approximate the spectral function is able to well describe the ARPES spectra at all the temperatures considered. The reason why this global fitting procedure has been developed is that it allows to stabilize the fits. For this reason, the procedure described in this section has been used as a starting point to analyze the time-resolved experiments.

Figure 5.4(f) shows the evolution of the central position of the vanadium band (*i.e.* the central position of the Lorentzian peak) extracted from Fig. 5.4(a)-(d) as a function of temperature. By looking at this comparison, it becomes evident that the closure of the of CDW gap arises only thanks to the folding of the vanadium band, while no shift of the band towards the Fermi level is observed (the position of the band at k-$k_{M2} \sim 0$ stays almost unaltered during the phase transition). Moreover, despite the large folding of the band observed, at the highest temperature reached (T$\sim$ 290 K) the minimum distance between the Fermi level and the vanadium band is of the order of $\sim$ 150 meV, confirming that the CDW gap is only partially closed.

5.4 TR-ARPES: LOW-TEMPERATURE ELECTRON DYNAMICS AT M_2

Having characterized the temperature-driven phase transition, we now investigate the possibility to perturb the electronic order using an ultrashort visible pump pulse. To do so, we used a pump photon energy of $h\nu_{pump} = 1.77$ eV, resonant with the transition between the bonding and the ani-bonding states that arise as a consequence of the trimerization-like process described in the previous sections. Moreover, being the aim of these experiments to perturb as much as possible the ground state of the CDW phase, we set the absorbed fluence to $\sim 1.2\,mJ/cm^2$. Because of this value, to reduce the average heating of the sample induced by the pump pulse, we exploited the possibility of our HHG setup to change its repetition rate, and we set it to 50 kHz. Indeed, this choice allows to limit the average heating from the pump pulse while also maintaining a reasonably high count rate, essential to achieve a good signal-to-noise ratio.

To better visualize the light induced quench of the CDW gap, we start by analyzing the low-temperature measurements ($T \sim 120$ K) where the gap is fully open and well formed. Figure 5.5(a) shows an ARPES map acquired before the arrival of the pump, hence only the photoinduced effects lasting more than 20 µs and the contribution of the average heating play a role. However, by comparing this spectrum to the one reported in Fig 5.4(a), we can see that there are no appreciable changes in the dispersion of the vanadium band, which is very sensitive to a change of temperature. Therefore, we can assume that the amount of average heating induced by the pump is negligible even at this fluence, and we can proceed with the analysis of the photoinduced changes in the electronic band structure.

Figure 5.5 shows three ARPES spectra acquired at different delays between the pump and the probe pulses, along with the differential images that highlight the changes induced by the pump pulse. Panels (a)-(c) show that the dispersion of the vanadium band after the arrival of the pump pulse is modified in a way that is very similar to the one observed for the temperature-driven phase transition. In particular, we observe a partial reappearance of the V-shaped band that characterizes the normal phase of VTe_2. Interestingly, from the comparison of these three spectra it appears that the changes in the dispersion of the vanadium 3d band are more pronounced in the spectrum acquired at a pump-probe delay of 500 fs rather than in the one acquired at a delay of 100 fs. These differences are well resolved in the differential images shown in Fig. 5.5(e) and (f), where two qualitatively different scenarios appear. Indeed, while panel (e) shows only the fingerprint of a small shift of the whole vanadium band towards the Fermi level, the alternated red-blue pattern clearly visible in (f) is likely to arise from the folding of the vanadium band. These differences are better quantified in Fig. 5.5(g), where the dispersion of the vanadium band extracted at the three different delays is reported. This plot also shows that, despite the high fluence used in this experiment, the maximum folding achieved for the vanadium band is smaller than the one obtained at equilibrium by raising the temperature to 290 K.

Comparing the photoinduced changes at three selected delays allows to capture the modifications of the band structure, however, the detailed study of light-induced quench of the electronic gap requires the complete analysis of the time-resolved experiments. This analysis is addressed in the following sections.

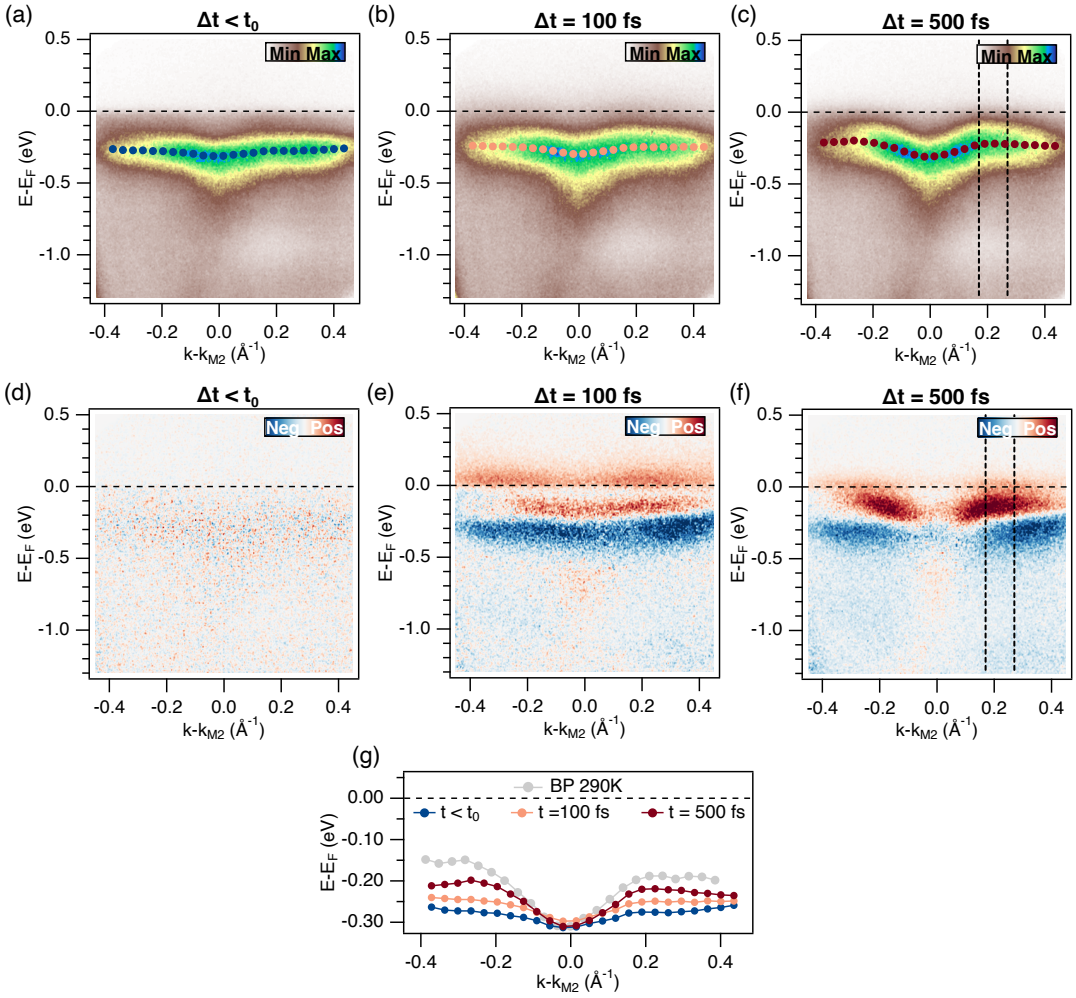

Figure 5.5: (a)-(c) Selected ARPES spectra acquired along the K-M_2-K direction at different pump-probe delays: (a) before the arrival of the pump, (b) and (c) respectively 100 and 500 fs after the arrival of the pump pulse. The colored circles denote the central position of the vanadium band extracted from the fits of the EDCs. (d)-(f) Differential ARPES maps showing the changes in the photoemission intensity induced by the pump pulse. The measurements were performed at a base temperature of ~ 120 K, using a pump photon energy of $h\nu_{\text{pump}} = 1.77$ eV (700 nm) and an absorbed fluence of ~ 1.2 mJ/cm^2. (g) Dispersion of the vanadium band extracted from (a)-(c). The dispersion of the vanadium band extracted from the equilibrium measurement performed at 290 K is also reported in gray for comparison.

5.4.1 Analysis of the photoemission intensity

We start by analyzing the time evolution of the changes in the photoemission intensity triggered by the pump pulse. Indeed, even if a change in the photoemission intensity might have different origins (*e.g.* a change in the band population or a change in the spectral function, as discussed in Sec. 3.2), this analysis, being based on the study of the raw photoemission data, allows to directly access the pump-induced changes in the electronic band structure. Figures 5.6(a) and (b) show respectively the evolution of the EDCs and the differential EDCs (dEDCs), integrated in the momentum region delimited by the dashed lines shown in Fig. 5.5(c) and (f), as a function of the pump-probe delay. Having verified that the dynamics extracted from the two sides (left and right with respect to k-$k_{M2} = 0$) of the vanadium band are equivalent, here only the ones extracted from the right side of the V-shaped band are analyzed.

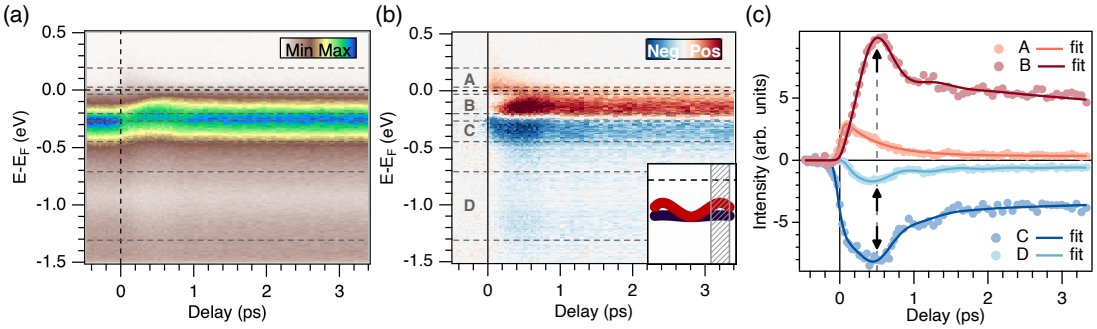

Figure 5.6: (a) and (b) EDCs and dEDCSs extracted by integrating the photoemission intensity from the momentum region delimited by the dashed lines in Fig. 5.5(c) and (f), plotted as a function of the pump-probe delay. The inset in (b) shows the region of reciprocal space from which the EDCs have been extracted. (c) Evolution of the photoemission intensity extracted from the boxes reported in (b). The same boxes are drawn also in (a) to allow for the comparison between the two maps. The gray dashed line shows the pump-probe delay at which traces B and C reach their maximum change. The measurement has been performed at a base temperature of $\sim 120\,\mathrm{K}$ and with an absorbed fluence of $\sim 1.2\,\mathrm{mJ/cm^2}$.

Figure 5.6(c) shows the traces obtained by integrating the photoemission intensity inside the boxes drawn in panel (b). These traces reveal how the spectral weight dynamics proceed in four different energy regions. As observed in many other systems [24, 178, 179], after having reached the maximum change, the four traces can be described by a two step relaxation process: the first one ends within $\sim 1\,\mathrm{ps}$ after the arrival of the pump pulse, while the second one evolves on longer timescales. Interestingly, however, while trace A (obtained by integrating the photoemission intensity above the Fermi level) has a rise time limited only by the time resolution of the setup, and reaches its maximum about $\sim 100\,\mathrm{fs}$ after the arrival of the pump pulse, the other traces show larger rise times. In particular, the maximum change for traces B and C is recorded at a pump-probe delay of $\sim 500\,\mathrm{fs}$, indicating that the folding of the vanadium band, and the consequent closure of the CDW gap, evolves on a much slower timescale with respect to the one of the hot carriers, described by trace A. Also trace D, extracted from a box located at higher binding energies, has a rise time similar to the one of traces B and C, thus suggesting that the structural changes triggered by the pump pulse also affect states located far from the Fermi level.

The absence of clear oscillations of the gap size (the presence of small bumps in the data, here ignored, will be discussed in the following sections), together with the fact that the maximum closure of the CDW gap is achieved only at a pump-probe delay of $\Delta t \sim 500\,\mathrm{fs}$, signal that the photoinduced phase transition in VTe_2 is not governed by the excitation of the CDW amplitude modes, as it has been observed in many other CDW systems [53, 76, 84, 180, 181]. Indeed, in these systems, it has been shown that the maximum closure of the CDW gap, after the initial quench, is achieved on a time scale that corresponds to one half-cycle of the CDW amplitude-mode oscillation [84, 178]. As shown in chapter 4, VTe_2 has two amplitude modes with a low-temperature frequency of 1.6 THz and 2.5 THz, for which a characteristic timescale of 300 and 200 fs would be expected, respectively. The fact that the timescales observed here are almost two times slower, suggests the presence of a bottleneck in the melting of the charge-ordered phase in VTe_2.

To further investigate this hypothesis, however, a more detailed analysis is required. Indeed, the analysis of the photoemission intensity as a function of the pump-probe delay presented in this section does not allow to effectively disentangle the different contribution coming for example from a broadening, shift or depletion of the vanadium band, and can only provide a quick overview of the most relevant changes in the electronic band structure. This aspect becomes evident when considering the dynamics extracted from box C of panel (b): while the initial fast drop of the photoemission intensity could be ascribed to the depletion of the vanadium

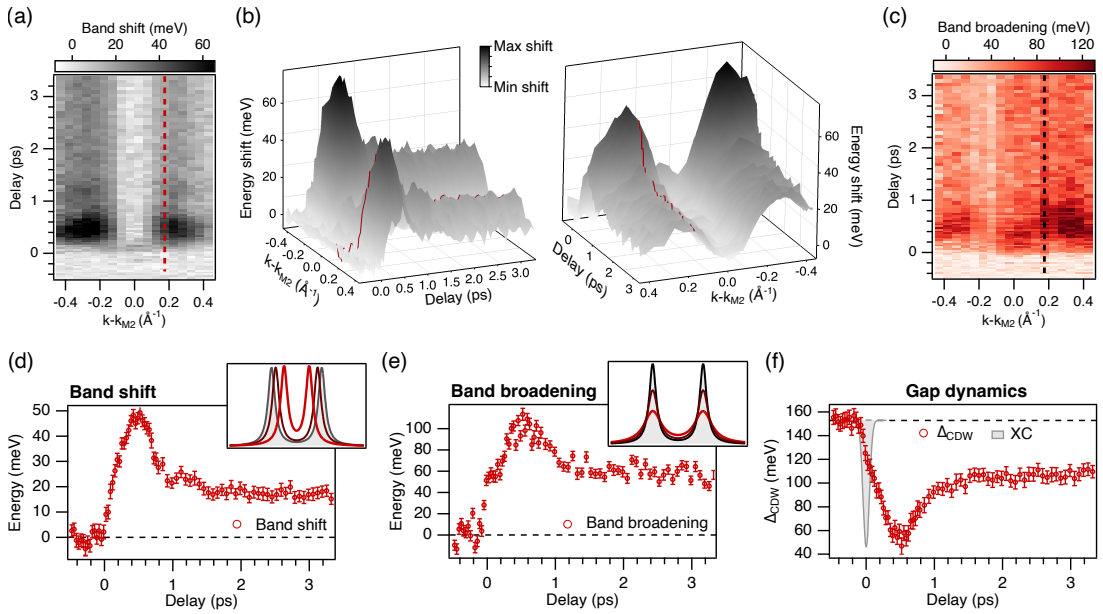

Figure 5.7: (a) Two-dimensional map showing the shift of the vanadium band with respect to the equilibrium position, as a function of pump-probe delay and momentum. (b) Three-dimensional representations of the band shift reported in (a). (c) Two-dimensional map showing the change in the FWHM of the vanadium band, as a function of pump-probe delay and momentum. (d) Evolution of the band position extracted from (a) at the momentum position denoted by the dashed line. The inset depicts the effect of the band shift on the CDW gap. (e) Evolution of the band broadening extracted from (c) at the momentum position denoted by the dashed line. The inset depicts the effect of the band broadening on the CDW gap. (f) Edge midpoint estimation of the CDW gap, obtained from the gap broadening and the gap closure reported respectively in (d) and (e). The grey trace shows the cross correlation between the pump and the probe pulses. The position of time zero in these graphs has been obtained by fitting the evolution of the photoemission intensity from states located far above the Fermi level.

band, the second slower component probably arises from the shift of the band. Therefore, to further quantify and elucidate the gap dynamics, we performed a detailed line shape analysis.

5.4.2 Line shape analysis

To quantitatively analyze the closure of the CDW gap, the global fitting procedure introduced in Sec. 5.4 has been extended to the time-resolved measurements. The ARPES spectra acquired at every pump-probe delay have been sliced in 20 EDCs (the number of the EDCs is lower than the one used in the equilibrium measurements due to the fact that these images have a lower statistics). As for the temperature dependent measurements, Eq. (5.2) has been used to fit the data. Therefore, the vanadium band has been approximated by using a Lorentzian-shaped density of states (DOS) multiplied by the Fermi-Dirac distribution, irrespective of the fact that immediately after the arrival of the pump pulse the electronic distribution might be non-thermal and the spectral function non-Lorentzian [39, 178, 182].

Thanks to the global fitting procedure, all the EDCs share the same chemical potential and electronic temperature, while the parameters of the Lorentzian peaks can vary independently. Hence, at the available energy resolution ($\sim$ 55 meV), the model can capture the dynamics of three characteristic parameters: change of the electronic temperature ($k_B T_e$), shift and broadening of the vanadium band. This procedure therefore allows to reconstruct the full temporal evolution of the vanadium band as a function of the pump-probe delay. As a remark, it is worth noting that, since no band crosses the Fermi level, the value of the electronic

temperature extracted from this region of the reciprocal space has to be considered only as a measure of the broadening of the Fermi edge.

We start by considering separately the evolution of the band position and broadening. The two-dimensional map reported in Fig. 5.7(a) shows the momentum-resolved changes in the position of the vanadium band as a function of the pump-probe delay. To better visualize the evolution of the band shift, a three-dimensional plot of this figure is shown in panel (b). Immediately after the arrival of the pump pulse, a small shift of the whole vanadium band towards the Fermi level is observed. After that, while the central part of the band relaxes back, the shift of the band at large momenta ($|k - k_{M2}| > 0.15\,\text{Å}^{-1}$) keeps increasing, reaching its maximum around a pump-probe delay of 500 fs. The relaxation dynamics is then characterized by a fast component that ends within 1 ps from the arrival of the pump pulse and by a second slower dynamics that lasts for several picoseconds. The momentum-dependent shift here described is therefore compatible with the folding of the vanadium band observed in the temperature-driven phase transition, in which the partial reappearance of the V-shaped band is observed.

The time evolution of the photoinduced changes in the FWHM of the Lorentzian peaks used to describe the vanadium band is shown in Fig. 5.7(b). As a consequence of the arrival of the pump pulse, a large change in the width of the band is observed. Indeed, by comparing the maps reported in (a) and (c), one can recognize that the change in the FWHM of the band is almost two times larger than the one of the band position. It is also worth noting that, the band width evolves on a timescale similar to the one of the band shift, suggesting the presence of a possible common origin for the two.

A close inspection of panels (a) and (b) reveal a slight asymmetry between that magnitude of the changes extracted at positive and negative momenta for both band shift and band broadening (while the timescales are the same). This difference is likely to originate from an intrinsic asymmetry of the vanadium band that is probably due to a not perfect orientation of the sample (we estimate the misalignment from the K-M_2-K direction to be of $\sim 5°$).

Figures 5.7(d) and (e) show the evolution of the band shift and of the band broadening extracted from Fig. 5.7(a) and (c) around the momentum region denoted by the dashed lines. These lines are located at the position at which the vanadium band crosses the Fermi level at the M_1 point, and thus at the position that should be reached by the band also at M_2 in the case in which the complete phase transition is obtained. Therefore, these traces can be used to quantify the closure and the broadening of the lower gap edge. To better visualize the changes in the CDW gap, in Fig. 5.7(f) we report its dynamics obtained by using the so-called edge midpoint estimation of the gap size. In general, the midpoint energies of the gap edges can be expressed as a shift by the half width at half maximum (HFHM) from the central position of the Lorentzian peak used to model the gap edges [183]. Following this definition, the expression of the CDW gap results:

$$\Delta_{CDW}(t) = \left(E_2(t) - \frac{\Gamma_2(t)}{2}\right) - \left(E_1(t) - \frac{\Gamma_1(t)}{2}\right), \tag{5.3}$$

where E_1 and Γ_1 are the position and the FWHM of the Lorentzian peak describing the gap edge located below the Fermi level, while E_2 and Γ_2 are the parameters describing the gap edge located above the Fermi level. We emphasize that this edge midpoint approach is a common and reliable method in ARPES to estimate the size of the energy gaps, and it has been applied to various CDW and superconducting systems [183–186]. Since, however, from our measurements it is not possible to resolve the gap edge located above the Fermi level, in Fig. 5.7(f) we report only the evolution of the lower part of the gap. This quantity therefore corresponds to the distance between the leading edge of the vanadium band and the Fermi level. Although, as suggested by the DFT calculations presented in the previous chapter, the CDW gap is not symmetric around the Fermi level (the upper part is expected to be located ~ 0.7 eV above the Fermi level, at the position of the non bonding peak), the temporal evolution of the two edges is expected to be similar, as observed also on other

CDW systems with asymmetric band gaps [76]. Hence, the dynamics shown in Fig. 5.7(f) is expected to be a good approximation of the temporal evolution of the full CDW gap.

Being the gap evolution obtained from the ones of the shift and the broadening of the vanadium band, it shows similar features. In particular, the maximum closure of the gap is achieved at a pump-probe delay of 500 fs. After that, the relaxation to the equilibrium conditions shows a two step dynamics: the first component ends within ~ 1.5 ps after the arrival of the pump pulse, while a second one lasts for several picoseconds. At this point it is worth noting that although after the arrival of the pump pulse the size of the CDW gap, defined using Eq. (5.3), reduces almost by 65 %, the complete phase transition is reached only when the vanadium band has reached its high-temperature dispersion (and thus the lattice reconstruction has vanished). Hence, much higher fluences are required to drive the full phase transition, in agreement with the results of our time-resolved reflectivity measurements.

Although small bumps related to the excitation of the CDW amplitude mode can be resolved in the evolution of the band position (Fig. 5.7(d)), the timescale on which the gap size evolves demonstrates that the melting of the electronic order is not driven by the excitation of the CDW amplitude modes. The line shape analysis reported here, indeed shows the presence of an incoherent process that controls the light-induced phase transition, likely related to the energy flow from the excited electrons to the lattice [150]. Therefore, in order to model the energy transfer from the electronic to the phononic system, we implemented a so called three-temperature model.

5.5 MODELING OF THE CDW GAP DYNAMICS

5.5.1 Electron-phonon coupling and energy flow in metals

Modeling the interaction between electrons and lattice vibrations is of paramount importance for the understanding of both ground state and out-of-equilibrium properties of solids. The most used approaches to describe the energy transfer from the excited electrons to the lattice are the so-called two-temperature model, developed by Anisimov [187] and Allen [188], and its generalization, the so-called three-temperature model [74]. This section is devoted to the presentation of the theoretical framework on which these models are based.

Two-temperature model

The physical picture on which the model is based is the following. The energy injected by the laser pulse in the system is absorbed by the electrons which are excited above the Fermi level. In general, immediately after the photoexcitation, the electronic system is far from an equilibrium condition and its description requires the use of a non-thermal distribution. However, after a few tens of femtoseconds, the electron-electron scattering processes drive the thermalization of the electronic population. After this thermalization time, the electrons can be described by a thermal-like distribution having an elevated temperature $T_e > T_0$, with T_0 being the temperature of the system before the arrival of the laser pulse [189]. On this first and short timescale, the electrons can be thought as completely decoupled from the lattice, hence their temperature is determined mainly by their specific heat. On longer timescales instead, the electrons start to loose their energy through electron-phonon scattering processes, and reach a common temperature with phonons. It is worth noting that the heat capacity of the phonons is much larger than the one of the electrons, hence they act as an heat sink, gradually absorbing the energy of the hot electrons. Finally, on a much slower timescale, heat diffusion makes the system return to the initial temperature T_0. Given the much larger timescale on which this process evolves, the heat diffusions is typically neglected in the model [188].

As said above, one of the basic assumptions of this model is that electron-electron and phonon-phonon (anharmonic) processes are active in keeping the electronic and phononic

distributions equal to their local equilibrium distributions (given respectively by the Fermi-Dirac, FD, and by Bose-Einstein, BE, distributions) characterized by separate electron (T_e) and lattice (T_l) temperatures [188, 189].

The system of coupled differential equations describing the energy flow between the two subsystems after the excitation is:

$$\frac{\partial T_e}{\partial t} = -\gamma_{e-ph}(T_e - T_l) + \frac{p}{C_e} \tag{5.4a}$$

$$\frac{\partial T_l}{\partial t} = \gamma_{e-ph}\frac{C_e}{C_l}(T_e - T_l), \tag{5.4b}$$

where γ_{e-ph} is the coupling constant between the electron and the phonon subsystems. $C_e = \gamma_e T_e$ is the electronic specific heat, being γ_e the coefficient of the linear electronic specific heat. C_l is the lattice specific heat. p is the absorbed power, with the same profile of the laser pulse. Both the specific heat and the laser power are expressed per unit of volume [190].

The solution of this system of equations indicates that the evolution of the electronic temperature follows an exponential decay with a time constant given by $\tau = (\gamma_{e-ph})^{-1}$. This measurable quantity can be expressed in terms of the electron-phonon coupling constant λ. Indeed, the electron-phonon coupling constant can be directly inferred from τ once the electronic temperature and the mean phonon energy $\langle\hbar^2\omega^2\rangle$ are known. The relation that combines these quantities together is [188]:

$$\gamma_{e-ph} = \frac{3\lambda\langle\hbar^2\omega^2\rangle}{\hbar\pi k_B^2 T_e}. \tag{5.5}$$

$T_e(t_{PP} = 0)$ can be evaluated starting from the laser energy delivered to the electrons and the electronic specific heat. This value, together with $T_e(\infty) = T_l(\infty)$ (which can be estimated from the lattice specific heat and the pump laser energy), constitute the initial condition to solve the system of coupled differential equations. The mean phonon energy $\langle\hbar^2\omega^2\rangle$ turns out to be more difficult to evaluate, and can be calculated from the measured phonon spectra or approximated with $\hbar^2\omega_D^2/2$ [191]. As a final remark, it is worth emphasizing that Eq. 5.5 has been obtained in the high temperature limit [188] and therefore it is valid only when the system is considerably heated by the laser pulse.

The 2TM is based on the assumption that the electrons and phonons can be described by thermal distributions at all times [192]. Although widely adopted, this approximation can be inadequate in the case of marked nonequilibrium situations also in simple systems. Indeed, as shown by Waldecker *et al.* for the case of aluminum [192], in a thermal state, phonons follow the Bose-Einstein statistics and their occupation is given by the product between the phonon density of states and the BE statistics. However, the coupling between electrons and phonons, given by the Eliashberg function, is strongest for the high-energy phonon whose occupation is lower in a thermal state [192]. Hence, the energy transfer between electrons and phonons that follows a strong optical excitation leads to the formation of a transient non-thermal phonon distribution in the system which originates from the preferential population of the high-energy phonons [192]. The limits of the 2TM have therefore required the development of a generalized model.

Three-temperature model

To describe the relaxation dynamics observed in systems with a strong anisotropy in the electron-phonon interaction (that might arise from phonon branches with different coupling strength), Perfetti *et al.* proposed a generalization of the 2TM, the so called three-temperature model (3TM) [74]. The physical picture on which the model is based is the following: after the first fast thermalization, the electronic population with temperature T_e starts to transfer its energy to a subset of strongly coupled optical phonon modes (also named hot phonons),

whose temperature is T_p. Here the idea is that only a small subset ($0 \lesssim f < 1$) of the total phonon modes is involved in this first relaxation process. Because of their small specific heat, this small subset of phonon modes can acquire a large effective temperature $T_p > T_l$. After a first thermalization, electrons and hot phonons reach a common temperature and their dynamics become similar. Then the relaxation of both populations proceeds on a picosecond time scale, governed by the phonon-phonon anharmonic scattering which takes place between the two independent subsets of phonon modes: the more strongly coupled ones (f modes) and the nearly non-interacting phonon modes ($1-f$) [74].

The rate of energy transfer from electrons to phonons is related to the Eliashberg coupling function $\alpha^2F(\Omega)$ through the integral $\int \Omega^2\alpha^2F(n_e - n_p)\,d\Omega$, with the distributions n_j given by $(e^{\Omega/k_BT_e}-1)^{-1}$, and being F($\omega$) and $\alpha^2(\omega)$ respectively the phonon density of states and the phonon-frequency-dependent electron-phonon coupling [74, 188]. By using the Einstein model to approximate the phonon spectrum $F(\Omega) = \delta(\Omega - \Omega_0)$ and by introducing the dimensionless electron-phonon coupling parameter $\lambda = 2\int \Omega^{-1}\alpha^2F\,d\Omega$, the system of rate equations that describes the evolution of the temperatures $T_j(t)$ can be written as:

$$\frac{\partial T_e}{\partial t} = -\frac{3\lambda\Omega_0^3}{\hbar\pi k_B^2}\frac{n_e - n_p}{T_e} + \frac{p}{C_e} \tag{5.6a}$$

$$\frac{\partial T_p}{\partial t} = \frac{C_e}{C_p}\frac{3\lambda\Omega_0^3}{\hbar\pi k_B^2}\frac{n_e - n_p}{T_e} - \frac{T_p - T_l}{\tau_\beta} \tag{5.6b}$$

$$\frac{\partial T_l}{\partial t} = \frac{C_p}{C_l}\frac{T_p - T_l}{\tau_\beta}. \tag{5.6c}$$

Where n_j are the Bose-Einstein distributions at the temperature T_j. $C_j(T)$ are the specific heats for electrons (j=e), strongly coupled phonons (j=p) and nearly non-interacting phonons (j=l), with $C_e(T) = \gamma_e T_e$. The fraction f of strongly coupled modes enters in the model through the two phononic specific heats. Finally, τ_β is the phenomenological time decay constant for the anharmonic phonon-phonon interaction, while p is the absorbed power. On the contrary to the 2TM, a particular form for the electron-phonon coupling, *i.e.* $\alpha^2F(\Omega) \propto \delta(\Omega - \Omega_0)$, has been assumed (electrons are coupled just with one phonon branch at frequency $\Omega = \Omega_0$), but no approximations are applied to the BE statistics [190]. It is worth noting that this version of the 3TM neglects the electron-phonon coupling with the $(1-f)$ weakly coupled phonon modes, which thus would only barely contribute to the evolution of the electronic temperature [74].

A task of fundamental importance in the implementation of the 3TM is the modeling of the phonon specific heats. Since the phonon spectrum has been approximated by the Einstein model, $F(\Omega) = \delta(\Omega - \Omega_0)$, all the phonon modes have the same frequency Ω_0. Therefore the specific heat within this model follows directly from the definition:

$$C = 3N_A k_B \int_0^\infty d\Omega F(\Omega)\left(\frac{\Omega}{k_BT}\right)\frac{e^{\Omega/k_BT}}{(e^{(\Omega/k_BT)}-1)^2}, \tag{5.7}$$

from which we obtain:

$$C_p(T) = 3N_A f\frac{\Omega_0^2}{k_BT^2}\frac{e^{\Omega_0/k_BT}}{(e^{(\Omega_0/k_BT)}-1)^2} = 3N_A f\Omega_0\frac{\partial n_p}{\partial T_p}, \tag{5.8}$$

$$C_l(T) = 3N_A(1-f)\frac{\Omega_0^2}{k_BT^2}\frac{e^{\Omega_0/k_BT}}{(e^{(\Omega_0/k_BT)}-1)^2} = 3N_A(1-f)\Omega_0\frac{\partial n_p}{\partial T_p}, \tag{5.9}$$

with $C_{tot}(T) = C_p(T) + C_l(T)$. In this expression N_A is intended to give the correct normalization for C_{tot} and has to be intended as the number of molecules per cm^3. An improvement to this approach is to use the functional form of C_{tot} obtained from the experiments. In this case, the specific heat of the strongly coupled phonon, $C_p(T)$, is calculated as before but with

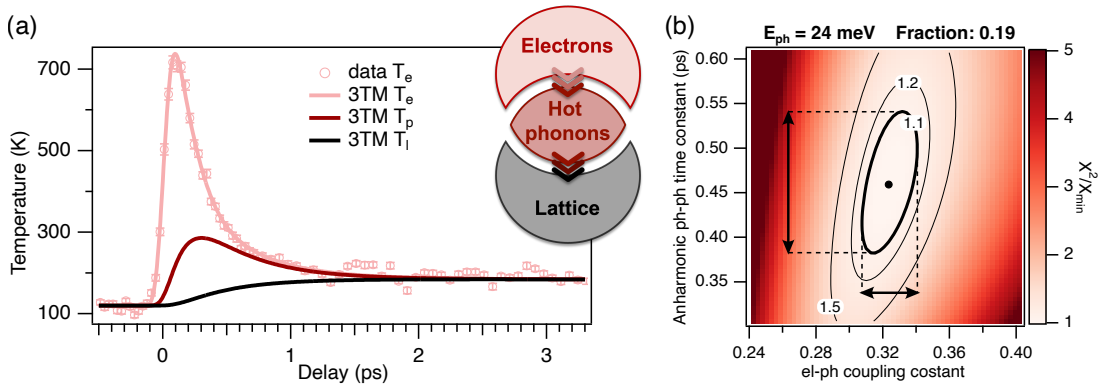

Figure 5.8: (a) Fit of the electronic temperature extracted from the data taken at the M_1 point, as performed by using the three-temperature model. The measurement was performed at a base temperature of 120 K and at an absorbed fluence of $\sim 600\,\mu J/cm^2$. The evolution of the temperatures of the strongly-coupled optical phonon modes and the temperature of the lattice are shown respectively by the red and black traces. (b) Two dimensional map showing the evolution of χ^2/χ^2_{min}, obtained from the fit of the electronic temperature, as a function of the time decay constant for the anharmonic phonon-phonon interaction (τ_B) and of the electron-phonon coupling constant (λ). The fits have been performed assuming an energy of the strongly-coupled modes of 24 meV and a fraction of such coupled modes of 0.19. The fit shown in (a) has been obtained using the parameters that minimize χ^2/χ^2_{min}. To calculate the errors on the estimation of λ and τ_B, we considered the region in which χ^2 lays within 10% of its minimum value ($\chi^2/\chi^2_{min} < 1.1$) and we considered the projection of the ellipse the encloses this region to the x and y-axes.

the constraint that for high temperatures and for $f \to 1$ it must be $C_p(T) \to C_{tot}(T)$. Finally, the lattice specific heat, $C_l(T)$, is obtained as $C_l(T) = C_{tot}(T) - C_p(T)$ [104, 190].

As a final remark, it is worth noting that the NTM models presented in these sections can be applied only when the excited electrons can be described by a thermal distribution characterized by a well defined temperature T_e. Therefore, these models cannot be directly applied if a gap in the density of states is present.

5.5.2 Application of the three-temperature model

Given the timescale of the processes involved and the absence of clear oscillations, we propose that the dynamics of the CDW gap can be explained by considering the energy flow from the excited electrons to the lattice [193–195]. In general, a solid-solid phase transition, where the symmetry of the crystal is raised, can be dominated by either a displacive process or an order-disorder process [21, 52, 196]. While in a displacive transition the atoms collaboratively reshuffle their positions under the effect of a few well-defined spatially coherent vibrational modes, in an oder-disorder transition the atoms move from the low to the high-symmetry structure in such a way that the motion remains correlated only along one dimension, while along the others it proceeds in a spatially incoherent manner, with no characteristic correlation length [21, 197–201]. Here we suggest that the dynamics observed are consistent with a loss of the long-range order of the CDW phase, triggered by an increase of disorder in the system. In the present case, the role played by the increased lattice fluctuations could be resolved as a consequence of the large energy gaps that characterize the strongly-coupled CDW systems like VTe_2, which make the electronic entropy (that otherwise would have overshadowed these effects) unimportant in determining the phase transition [12]. Therefore, to model the energy flow from the excited electrons to the lattice, we implement the three-temperature model presented in the previous section.

3TM parameters	fit results
Frequency of the strongly-coupled phonons (ω_0)	24 meV
el-ph coupling constant (λ)	0.32 ± 0.02
Fraction of strongly coupled phonons (f)	0.19
Anharmonic decay time constant (τ_β)	0.46 ± 0.08 ps
Linear term electronic specific heat (γ_e)	5.3×10^{-4} J/(cm^{3}K^2)

Table 5.1: Summary of the parameters used in the three-temperature model. The errors estimated by our fitting procedure for the el-ph constant (λ) and the anharmonic decay time constant (τ_β) are reported. The remaining parameters have been kept fixed.

The implementation of the 3TM requires the knowledge of the transient electronic temperature, that in the present case can be directly extracted from the TR-ARPES spectra measured on the ungapped regions of the Fermi surface. In particular, we obtained the evolution of the electronic temperature by fitting the EDCs extracted from the M_1 point, where the V-shaped vanadium band crosses the Fermi level (the detailed procedure is described in the Sec. 5.7). The transient electronic temperature extracted from the M_1 point is reported in Fig. 5.8(a), together with the result of the fit obtained by solving the system of coupled equations described by Eq. (5.6). To numerically solve these equations, the knowledge of the specific heats of the three subsystem is required. To this aim, the specific heat of the strongly-coupled optical phonons and the one of the remaining weakly-coupled phonos have been obtained from the measured values of the total specific heat [46], by following the procedure presented in the previous section. Moreover we assumed the electronic specific heat to be linear in the electronic temperature (with the linear term being 5.3×10^{-4} J/(cm^{3}K^2)). It is worth noting that, since the Fermi surface of VTe_2 consists of metallic and CDW-gapped regions, in general the electronic heat capacity is expected to follow a linear metallic-like temperature dependence with an additional nonlinear increase, resulting from the redistribution of spectral weight due to the closure of the CDW gap [24, 189]. However, since the opening of CDW gap affects only a limited region of the reciprocal space, and even at the highest fluence the gap is only partially perturbed (the modifications induced by the pump pulse are limited in reciprocal space and relatively small), we expect the non-linear correction to be small compared to the linear term. Therefore, we neglected the non-linear contribution and we used only the linear term.

As discussed in the previous section, the implementation of the 3TM requires the identification of a subset of strongly-coupled modes. The fit shown in Fig. 5.8(a) has been obtained by assuming an energy for the subset of strongly-coupled optical phonon modes of 24 meV, and by considering a fraction of such coupled modes (f) of 19 %. A detailed discussion on the motivation of this choice is presented in Sec. 5.5.3; here we only proceed by studying the dynamics obtained from this assumption. Starting from these values, the fit of the electronic temperature gives an electron-phonon coupling constant (for subset of strongly coupled optical phonon modes) $\lambda = 0.32$, and a time constant for the anharmonic phonon-phonon interaction $\tau_\beta = 0.46$ ps. In order to reliably extract these values and the associated uncertainties, we evaluated the trend of the χ^2 of the fits while simultaneously changing λ and τ_β. To do so we created a 60×60 grid, corresponding to different pairs of values of λ and τ_β and we calculated the χ^2 resulting from the fit of the electronic temperature for every point of the grid. Therefore, the pair of values that minimize the χ^2 is the one that better describes the evolution of the electronic temperature. This approach directly allows to estimate the errors that affect the fitting parameters. Indeed, by considering the elliptical region where χ^2 stays within 10% of its minimum value ($\chi^2/\chi^2_{\text{min}} < 1.10$) and by projecting the resulting ellipse on the x and y-axes, it is possible to obtain the range of variation of the fitting parameters [202, 203]. This procedure is schematically shown in Fig. 5.8(b), while the results obtained are summarized in Tab. 5.1.

By using the values reported in Tab. 5.1 and by solving the set of coupled differential equations reported in Eq. (5.6), it is possible to obtain both the evolution of the temperature of

the strongly-coupled phonon modes and the one of all the remaining phonons. These traces are shown together with the evolution of the electronic temperature in Fig. 5.8(a). Starting from the evolution of the temperature of the strongly-coupled modes, and assuming that the population of this subset of modes can be described by the Bose-Einstein distribution (assumption being already embedded in the 3TM):

$$n_p(t) \propto \left[\exp\left(\frac{\hbar\omega_p}{k_B T_p(t)}\right) - 1\right]^{-1}, \tag{5.10}$$

it is possible to calculate the change in the population of the strongly-coupled modes due to the increase of their temperature, triggered by the hot carrier relaxation [194].

We emphasize that these modes are excited without the presence of a macroscopic coherent phase, and therefore their excitation leads to an increase of the lattice fluctuations in the system. As discussed in Sec. 2.2.2, increased lattice fluctuations give rise to a smearing of the gap edges, establishing therefore a link between the transient disorder in the system and the broadening of the CDW gap [41]. Therefore, we tentatively compare the timescales on which these processes evolve.

Figure 5.9(a) shows a comparison between the transient broadening of the CDW gap and the change in the population of the strongly coupled modes. Interestingly, these two traces evolve on similar timescales. The excitation of the strongly coupled optical phonon modes is governed by the hot carrier relaxation through the electron-phonon coupling constant, therefore the maximum change in the population of the modes is achieved only $400 - 500$ fs after the arrival of the pump pulse. This timescale matches well the one observed for the smearing of the CDW gap. Moreover, also the second relaxation process of both traces is similar, with the two showing a plateau for pump-probe delays larger than 2 ps. Indeed, as shown in the following, this plateau persists for several tens of picoseconds (see also appendix B).

The results obtained by applying the 3TM can be used to model also the dynamics of the gap closure. Indeed, the broadening of the gap discussed above entails a reduction of the gap size itself, and therefore a reduction of the energy gain of the electronic subsystem with the consequent reduction of the amplitude of the PLD. With this in mind we can tentatively compare the incoherent dynamics of the closure of the CDW gap with the one describing the change in the population of the strongly coupled optical phonon modes (rescaled by a constant factor). Moreover, given the presence of small bumps in the trace showing the evolution of the band shift, on top of this incoherent dynamics we summed a damped cosine oscillation with the frequency of one of the two CDW amplitude modes observed in the TR-OS experiments. Therefore, the evolution of the band shift (BS) has been modeled using the equation:

$$BS(t) = A \cdot n_p(t) + I\, e^{-t/\tau} \cos(\omega_{AM} t + \phi), \tag{5.11}$$

where A is the constant used to rescale the change in the population of the strongly-coupled modes. I is the intensity of the oscillating component with angular frequency ω_{AM}, decay time τ and phase ϕ. Only the amplitude mode with a low temperature frequency of 1.6 THz has been considered in this fitting function. The choice of including only one of the two amplitude modes originates from the need of keeping as low as possible the number of additional free parameters. Moreover, the fact that this mode is more clearly visible is in agreement with the results shown in Sec. 4.4.1, where indeed this AM (named phonon A) has proven to be more resilient to high excitation fluences.

The result of the fit obtained by using Eq. 5.11 is shown in Fig. 5.9(b), together with the coherent part of the fit, reported separately. As for the case of the gap broadening, the timescales extracted from the 3TM match well with the ones extracted from the experiments, supporting therefore the thermal origin of the dynamics observed.

At this point, being able to describe both the dynamics of the gap closure and the one of the broadening in terms of the change in the population of the strongly-coupled modes, it is possible to merge the two models together to describe the dynamics of the CDW gap. The result is shown in Fig. 5.9(c). It is worth emphasizing that no other free parameters were added

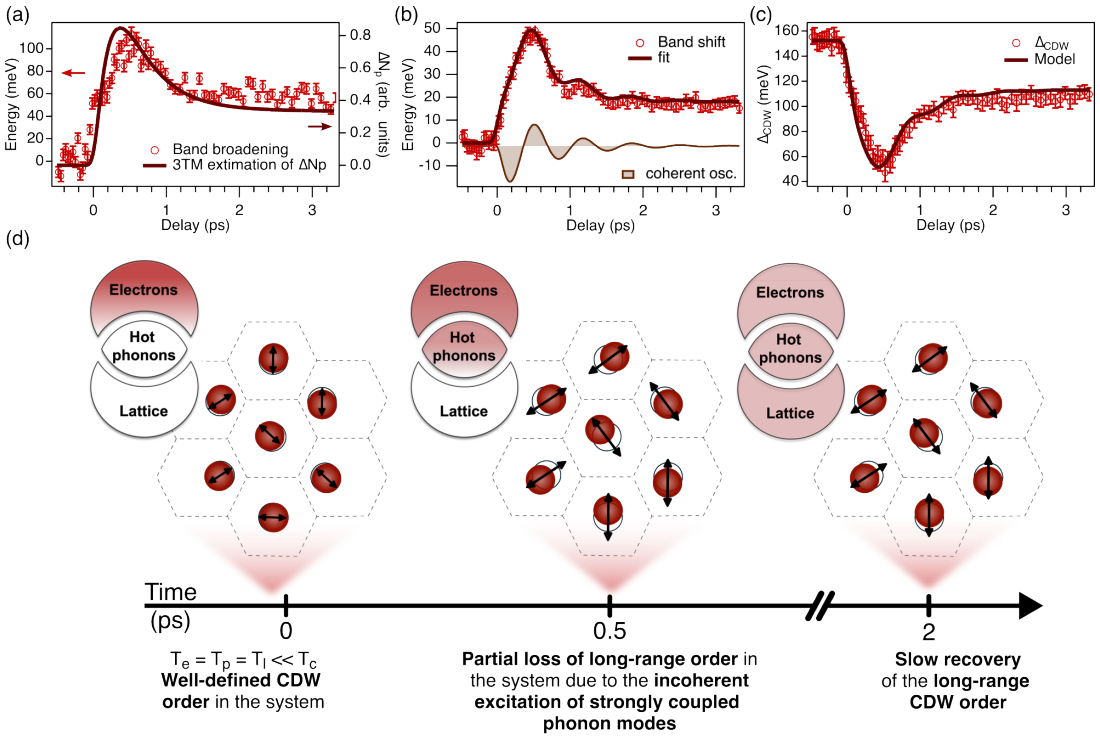

Figure 5.9: (a) Comparison between the transient broadening of the CDW gap and the change in the population of the strongly coupled optical phonon modes. (b) Fit of the gap closure obtained by summing to the trace describing the transient change in the population of the strongly-coupled modes (rescaled by a constant) an oscillating term with the frequency of one of the two CDW amplitude modes, as determined from the TR-OS experiments. (c) Comparison between the dynamics of the CDW gap (distance between the leading edge of the lower branch and the Fermi level) and the model obtained by summing the curves shown in (a) and (b). (d) Sketch showing the partial loss of the long-range CDW order, occurring as a consequence of the incoherent excitation of the strongly-coupled optical phonon modes. The red spheres represent the vanadium atoms while the black arrows depict the amplitude of their displacements. Before the arrival of the pump pulse the three subsystems are in equilibrium ($T_e = T_p = T_l \ll T_{CDW}$) and the system is characterized by a well-defined CDW order. The energy injected by the pump in the system is initially absorbed by the electrons and then transferred to a subset of strongly coupled optical phonon modes. The excitation of these phonon modes, without a macroscopic phase coherence, leads to a partial loss of the long range order of the system. After ≈ 2 ps from the arrival of the pump pulse, the three subsystems are again in equilibrium and from there on the relaxation dynamics is governed solely by heat diffusion.

at this point, the model shown in figure has been obtained only summing the traces shown in panels (a) (divided by a factor 2) and (b), as we did for the edge midpoint estimation of the gap.

We can now summarize the microscopical qualitative physical picture that stands at the base of the comparison between the dynamics obtained from the 3TM and the ones obtained from the fits of the EDCs (Fig. 5.9(d)). Before the arrival of the pump pulse, the three subsystems given by electrons, hot phonons and lattice are in equilibrium, and their temperature is much lower than the CDW critical temperature: $T_e = T_p = T_l << T_{CDW}$. Hence, the system is characterized by a well-defined long-range CDW order. After the arrival of the near infrared pump pulse, the energy injected in the system is absorbed by the electrons and then transferred to the subset of strongly-coupled optical phonon modes. The crucial point is that the excitation of these modes occurs without the presence of a macroscopic phase coherence,

thus leading to a partial loss of the long-range order of the system [21]. This partial loss of the long-range order, that therefore evolves on the same timescale of the population of the strongly-coupled phonon modes, entails a smearing and a partial closure of the CDW gap. This sets a link between the population of the strongly-coupled phonon modes and the dynamics of the CDW gap. In other words, the pump pulse triggers an increase of the lattice fluctuations that profoundly affect the CDW gap. This result could suggest that the photoinduced phase transition in VTe_2 is dominated by the disordering of the vanadium trimers, similarly to what has been observed in VO_2 [21, 196, 204–206].

After a first thermalization, electrons and hot phonons reach a common temperature and their dynamics become similar. Subsequently, the relaxation proceeds thanks to the anharmonic phonon-phonon interaction, which continues until a thermal equilibrium with all the other modes is reached. From here on, the relaxation is governed only by the thermal diffusion, and hence it evolves on a much slower timescale that is not captured by the 3TM. Therefore, this cascade process also explains the dynamics observed at large pump probe delays, i.e. the presence of a plateau in both the gap closured and the gap broadening (see also appendix B). At these delays the strongly coupled phonon modes have reached a common temperature with all the other modes, hence the relaxation is brought forward only by the heat diffusion on a much slower time scale [207].

In summary, this model shows that the dynamics of the CDW gap in VTe_2, triggered by a strong optical excitation, can be fully described by considering the incoherent excitation of a subset of strongly-coupled optical phonon modes and the excitation of the CDW amplitude modes, with the second playing only a marginal role in determining the dynamics of the CDW gap when a large excitation fluence is used. These results therefore point towards a phase transition dominated by an order-disorder process rather than a displacive process [21, 208]. We emphasize that VTe_2 constitutes a promising candidate to study the interplay between lattice fluctuations and CDW order. Indeed, the presence of a large energy gap allows to use high excitation fluences without completely melting the charge order, thus allowing to study the effect of transiently increased lattice fluctuations on the CDW order [12].

5.5.3 Dependence on the initial choice of parameters

The results presented in the previous section are based on the assumption that the subset of the strongly-coupled phonon modes has an energy of 24 meV and the fraction of such coupled modes is 0.19. These values have been chosen after having performed extensive simulations, investigating the range of possible energies and fractions. As a first step, following a procedure similar to the one presented in the previous section, we evaluated the evolution of the χ^2 of the fit of the electronic temperature while simultaneously changing energy and fraction of the strongly-coupled modes. To do so, we built a 45×45 points grid, corresponding to different pairs of energies and fractions, and we calculated the resulting χ^2 for every point of the grid. These fits have been performed leaving λ and τ_β as free fitting parameters while keeping fixed all the remaining parameters. It is worth noting that the change of the energy of the subset of strongly coupled modes requires the calculation of their specific heat at every step. The two-dimensional map showing the evolution of $\chi^2/\chi^2_{\text{min}}$ for the fit of the electronic temperature is reported in Fig. 5.10(a). This map shows that in order to obtain appreciable changes in the χ^2, large changes of the fraction and the energy of the modes are required, thus making difficult to obtain a reliable estimation of these parameters from this fit only. Hence, in order to refine the procedure, starting from the values of λ and τ_β obtained from the fit of the electronic temperature, for every combination of phonon energy and fraction we performed a fit of the evolution of the band broadening and of the band shift. As explained in the previous section, this procedure has required the calculation of $n_p(t)$ for every combination of parameters. In particular, the evolution of the band broadening has been fitted using the dynamics of n_p, rescaled by a constant factor, while the evolution of the band shift has been fitted using Eq. (5.11). Figures 5.10(b) and (c) show the evolution of

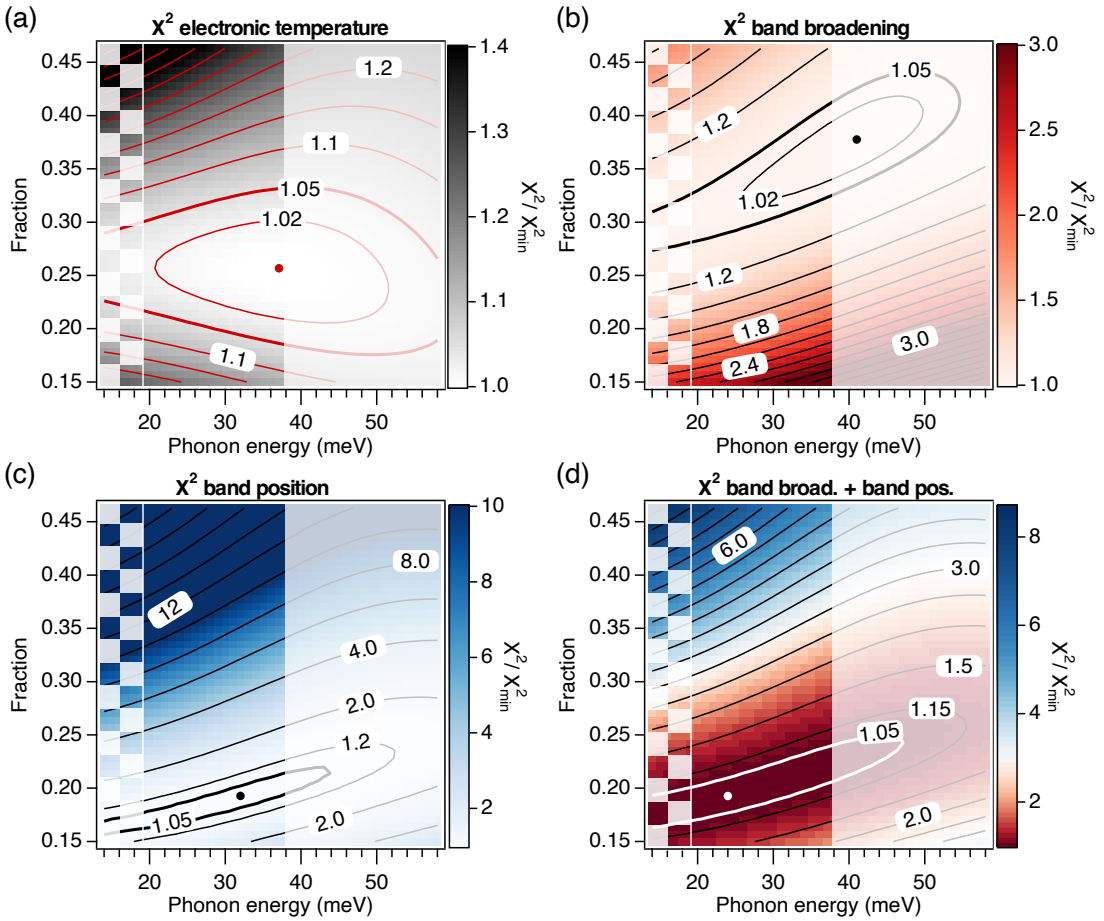

Figure 5.10: (a) Two dimensional map showing the evolution of $\chi^2/\chi^2_{\text{min}}$ obtained from the fit of the electronic temperature, as a function of the energy and of the fraction of the strongly-coupled optical phonons. (b) Two dimensional map showing the evolution of $\chi^2/\chi^2_{\text{min}}$ obtained from the fit of the band broadening, as a function of the energy and of the fraction of the strongly-coupled optical phonons. The fit has been obtained calculating the evolution of $n_{\text{p}}(t)$ for every couple of parameters. (c) Two dimensional map showing the evolution of $\chi^2/\chi^2_{\text{min}}$ obtained from the fit of the band shift, as a function of the energy and of the fraction of the strongly-coupled optical phonons. The fit has been obtained using Eq. (5.11). (d) Two dimensional map showing the evolution of $\chi^2/\chi^2_{\text{min}}$ obtained by summing the maps reported in (b) and (c). The semi-transparent white box covers the pairs of parameters for which the phonon energy is higher than ~ 38 meV, which, according to our DFT simulations, corresponds to the highest phonon energy existing in VTe_2. The region of parameters for which the resulting EPC constant is higher than 0.4 is highlighted by a checkered white pattern.

$\chi^2/\chi^2_{\text{min}}$ respectively for the fit of the band broadening and of the band position. Finally, in order to obtain the pairs of parameters that better describe both evolutions simultaneously, the maps reported in panel (b) and (c) have been summed (and normalized again to their minimum value); the result is shown in panel (d). The values of energy and fraction that minimize the χ^2 reported in this map are respectively: 24 meV and 0.19, *i.e.* the ones used in the previous section. Interestingly, this simulation shows that it exists a relatively large region of parameters for which the resulting χ^2 stays with 5% of its minimum value. This result therefore demonstrates the robustness of the model presented here, and suggests a scenario in which a continuum of modes, enclosed in a specific energy region, is involved in the energy transfer from the electrons to the lattice, similarly to what has been observed in VO_2 [21, 196]. Moreover, it is worth emphasizing that this range of energies encloses different

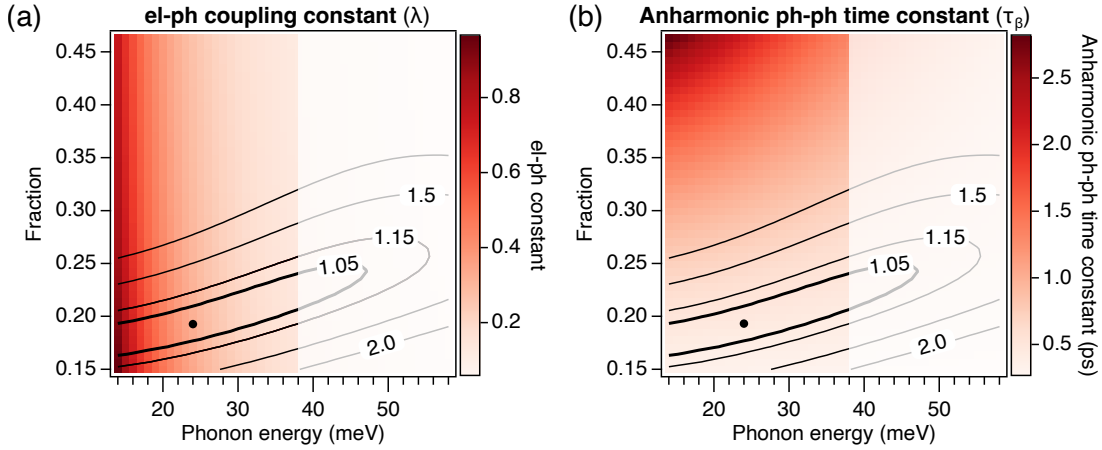

Figure 5.11: (a) Two dimensional map showing the evolution of the el-ph constant (λ) as a function of energy and fraction of the subset of strongly-coupled optical phonon modes. (b) Two dimensional map showing the evolution of the anharmonic phonon-phonon time constant (τ_B) as a function of energy and fraction of the subset of strongly-coupled optical phonon modes. The contour lines superimposed to the two panels show the evolution of the χ^2/χ^2_{min} reported in Fig. 5.10(d), thus allowing to evaluate the intervals of variation of λ and τ_B for the couple of parameters that minimize the χ^2 of both band broadening and band shift. The semi-transparent white box covers the pairs of parameters for which the phonon energy is higher than $\sim$ 38 meV, which, according to our DFT simulations, corresponds to the highest phonon energy existing in VTe_2.

phonon branches truly existing in VTe_2, as confirmed by Raman experiments and theoretical simulations [209], with one of these branches located at $\sim$ 25 meV, the value for which our model gives the best results. For completeness in appendix C we report the fits of band broadening and position obtained by starting from the pairs of parameters that minimize separately the four maps shown in Fig. 5.10.

The checkered white pattern reported in all the panels of Fig. 5.10 highlights the region of parameters for which the resulting electron-phonon coupling constant is larger than 0.4. This value corresponds to the coupling constant of the strongly-coupled optical phonons estimated in the high-temperature superconductor $Bi_2Sr_2Ca_{0.92}Y_{0.08}Cu_2O_{8+\delta}$ [104]. Although the two systems are unrelated, being the modes considered not directly linked to the CDW transition, values of EPC much higher than 0.4 are considered unlikely [210]. The region covered by the checkered white pattern corresponds to pairs of parameters for which the energy of the strongly-coupled modes is lower than $\sim$ 19 meV. Indeed, we remind that $\tau_e \propto 1/(\lambda\langle\hbar^2\omega^2\rangle)$, therefore a reduction of the energy entails an increase of λ to unphysical values. The two-dimensional map reported in Fig. 5.11(a) shows the evolution of the electron-phonon coupling obtained by fitting the dynamics of the electronic temperature. As expected, a progressive reduction of the EPC constant is observed for an increase of the energy of the strongly coupled modes, while only a weak dependence on the fraction of such modes is observed. For completeness, in Fig. 5.11(b) it is reported also the evolution of the anharmonic phonon-phonon time constant, which shows a more pronounced dependence on the fraction of the strongly-coupled modes.

5.6 INDEPENDENCE OF THE GAP DYNAMICS ON THE PUMP PHOTON ENERGY

All the time-resolved photoemission experiments discussed up to now have been performed using a pump photon energy of 1.77 eV. This choice was made in order to be resonant with

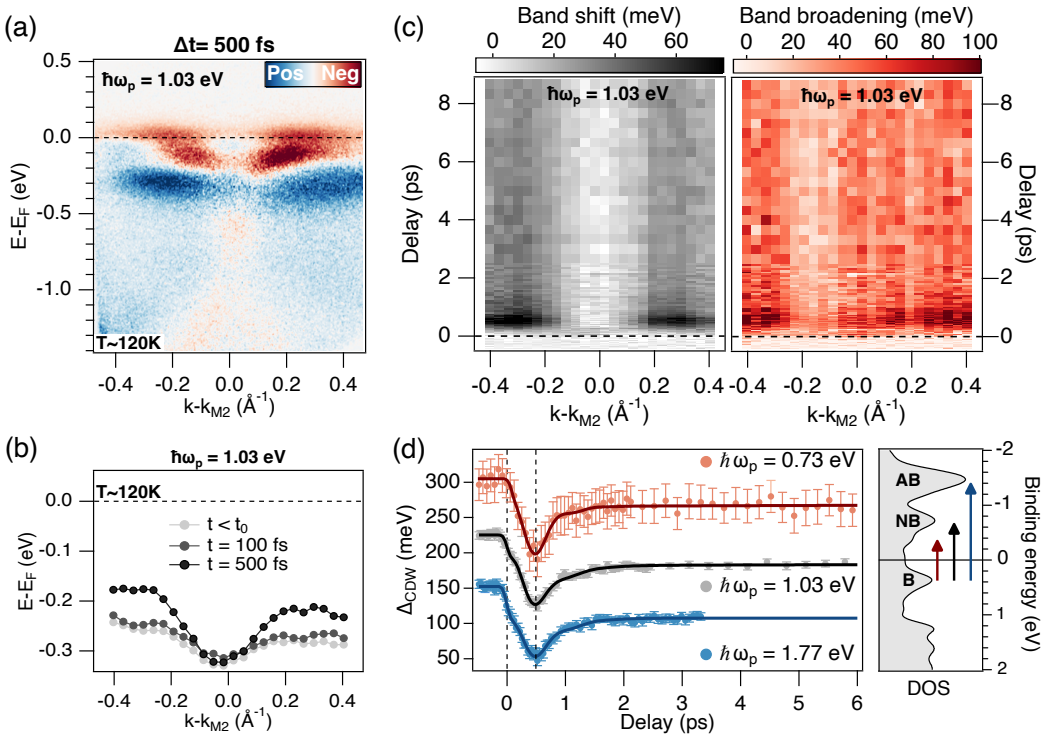

Figure 5.12: (a) Differential ARPES map showing the changes in the photoemission intensity induced by the pump pulse. The measurement was performed at a base temperature of $\sim 120\,\mathrm{K}$, using a pump photon energy of $h\nu_{\mathrm{pump}} = 1.03\,\mathrm{eV}$ (1200 nm), and an incident fluence of $\sim 700\,\mu\mathrm{J/cm^2}$. (b) Dispersion of the vanadium band for three selected pump-probe delays. (c) Two-dimensional maps showing the shift and the change in the FWHM of the vanadium band with respect to the equilibrium position, as a function of the momentum and the pump-probe delay. (d) Gap dynamics extracted from measurements performed with different pump photon energies: 1.77, 1.03 and 0.73 eV (corresponding respectively to 700, 1200 and 1700 nm). The intensity of the traces has been normalized to a common value to facilitate the comparison of the dynamics. Superimposed to the traces are shown the fits obtained by using a double exponential decay with the addition of a damped oscillation. A graph showing the total density of states and the optical transition triggered by the three different photon energies is also reported.

the optical transition between the bonding and antibonding states that arise due to the trimerization process that takes place during the CDW phase transition. One could now wonder whether the dynamics observed are a result of the peculiar pump photon energy used, or, as the implementation of the 3TM would instead suggest, they are independent on the pump photon energy. To answer this question, we took full advantage of the OPA system coupled to the HHG source, and we performed additional TR-ARPES experiments using different pump photon energies. In particular, photon energies of 1.03 and 0.73 eV were used. This choice originates from the fact that the former allows to trigger a resonant transition between the bonding and the non-bonding states, while the latter doesn't allow to excite a direct transition between states directly affected by the CDW transition. Hence, the use of these three excitation energies should allow to unveil the role played by the pump photon energy in the determination of the CDW dynamics [211–213]. All the other parameters of the experiment have remained unchanged, namely the measurements have been performed on strained samples kept at a base temperature of $\sim 120\,\mathrm{K}$.

We start by considering the results obtained using a pump photon energy of 1.03 eV. Figure 5.12(a) shows a differential ARPES map highlighting the changes in the photoemission intensity induced by the pump pulse. A comparison with Fig. 5.5(f) shows no significative changes

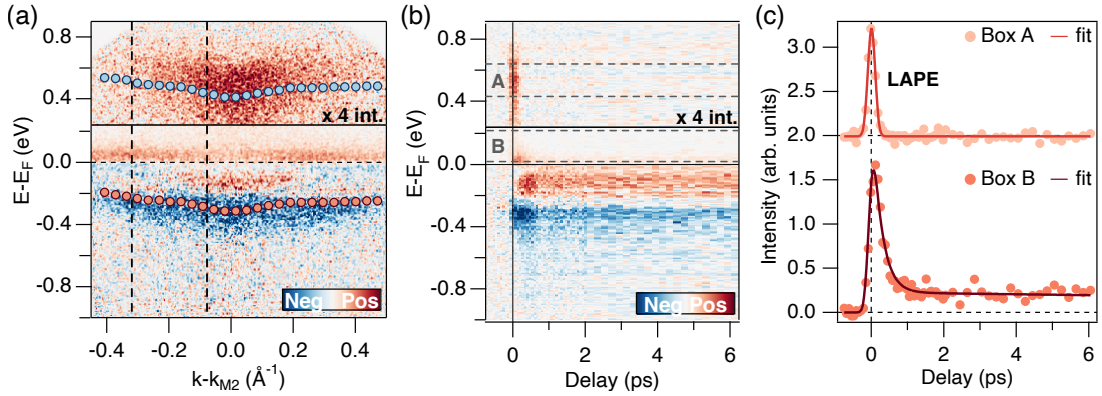

Figure 5.13: (a) Differential ARPES map acquired at $\Delta t_{pp} \approx 0$, showing the replica of the vanadium band above the Fermi level. The red circles show the dispersion of the vanadium band extracted from the fits of the EDCs, while the blue circles show the same dispersion displaced by the pump photon energy of 0.73 eV. (b) Evolution of the dEDCs obtained by integrating the photoemission intensity from the momentum region delimited by the dashed lines in (a). (c) Evolution of the photoemission intensity extracted from the boxes depicted in (b). The replica of the vanadium band (box A) persist only for a time equal to the cross-correlation between the pump and the probe pulses. For this measurement the idler of the OPA has not been compressed, thus the cross-correlation between the pump and the probe pulses turns out to be $\sim$ 230 fs.

in the electronic band structure of the photoinduced VTe_2 sample. This observation is also confirmed by the dispersion of the vanadium band extracted at three selected pump-probe delays and shown in Fig. 5.12(b). The effect of the pump pulse is to trigger the folding of the vanadium band in a way similar to the one observed in the temperature-driven phase transition.

At this point, it is worth noting that panel (a) shows a pronounced differential signal also for binding energies larger than 1 eV, corresponding to the energy of our pump pulse. This observation confirms that the changes in the photoemission intensity observed far from the Fermi level (also in Fig. 5.5(f)) arise from a change in the lattice symmetry triggered by the pump pulse, and are not simply due to a change in the bands occupation triggered by the absorption of pump photons.

We now move to the study of the photoinduced dynamics. The two-dimensional maps reported in Fig. 5.12(c) show the changes in the position and in the FWHM of the vanadium band as a function of the pump-probe delay. Once again, the dynamics extracted are very similar to the ones reported in Fig. 5.7. Both quantities show a larger rise time with respect to the one of the hot carriers, with their the maximum change occurring only at a pump-probe delay of 500 fs. Interestingly, also the experiments performed using a pump photon energy of 0.73 eV, i.e. non-resonant with an optical transition that directly involves CDW states, have shown equivalent outcomes. The results of the experiments performed by using different pump photon energies are summarized in Fig. 5.12(d). In particular, this graph shows a comparison between the dynamics of the lower edge of the CDW gap (also here the edge midpoint estimation of the gap is used) extracted from the three experiments performed. Given the fact that the reflectivity of the sample is different at different photon energies, and that the reflectivity in the near infrared has not been reported in the literature to the best of our knowledge, it was not possible to calculate the absorbed fluence for these experiments. Therefore, given the different excitation regimes used, the three traces reported in this graph have been multiplied by a different constant factor in order to normalize their intensity to a common value, thus facilitating their comparison.

The fact that the dynamics of the CDW gap turns out to be independent on the pump photon energy is in agreement with the interpretation brought by the three-temperature model. Indeed, the model presented in the previous section is independent on the particular

optical transition triggered, since it relies only on the generation and relaxation of the hot carriers with the subsequent incoherent emission of phonons. Furthermore, the dynamics obtained by using pump photon energies of 1.03 and 0.73 eV, being acquired on a longer time window, highlight the presence of a plateau at large pump-probe delays, thus confirming the scenario presented in the previous section.

As a final remark, it is worth noting that despite the use of a resonant pumping with the bonding-nonbonding and the bonding-antibonding transitions, the population of the upper part of the CDW gap has not been observed. As shown by Fig. 5.13(a), the only additional effect observed is the appearance of a replica of the lower gap edge above the FERMI level, for $\Delta t_{pp} \approx 0$. This process, known as LAPE (laser assisted photoemission), originates from the interaction of the photoemitted electrons with the electric field of the pump pulse, and leads to the formation of replicas of the occupied bands spaced by a pump photon energy. The LAPE process is therefore linked to a dressing of the free electron final states by means of the pump photons, and not to a change in the electronic band structure [214–216]. Indeed, as demonstrated by Fig. 5.13(b) and (c), the replica of the vanadium band persist only for a time equal to the cross-correlation between the pump and the probe pulses, *i.e.* for the time of interaction between the photoemitted electrons and the electric field of the pump pulse. Furthermore, the intensity of the replica has proven to be sensitive to the polarization of the pump beam with respect to the slit of the hemispherical analyzer, as expected from the LAPE process [216].

5.7 EXTRACTION OF THE ELECTRONIC TEMPERATURE FROM M_1

The implementation of the three-temperature model presented in Sec. 5.5.2 requires the knowledge of the electronic temperature. Its evolution can be extracted directly from TR-ARPES spectra measured on the ungapped regions of the Fermi surface. Figure 5.14(a) shows an ARPES spectrum acquired along the K-M_1-K direction, at a base temperature of ~ 120 K. As expected from the change in the lattice symmetry, in contrast to what happens at the M_2 point, no modifications in the electronic band structure take place during the CDW phase transition at M_1, thus here the V-shaped vanadium band crosses the Fermi level without the presence of the CDW gap. Thanks to that, the value of the electronic temperature can be extracted directly from the fits of the EDCs [24, 74, 212]. The differential image reported in Fig. 5.14(a) shows that the only effect of the pump pulse is to trigger a redistribution of the spectral weight, without affecting the dispersion of the band. This observation is confirmed by the fits of the MDCs reported in Fig. 5.14(c). The three traces depicted in this graph, show the dispersion of the V-shaped band for different pump probe delays. The fact that the three curves are perfectly overlapped, demonstrates that the dispersion of the vanadium band is not affected by the arrival of the pump pulse.

Figure 5.14(d) shows the evolution of the EDCs extracted from the momentum region delimited by the dashed lines reported in (a). As for the fits performed at the M_2 point, the vanadium band has been modeled by using a Lorentzian-shaped density of states multiplied by the Fermi-Dirac distribution. The full fit function has then been obtained by adding a third order polynomial to describe the background and by convolving the resulting expression with a Gaussian function (G), to take in to account the finite energy resolution of our apparatus. The resulting fit function is therefore:

$$I(E) = \mathrm{G}(E) \otimes \left[\left(\frac{I \cdot (\Gamma/2)}{(E - E_\mathrm{B})^2 + (\Gamma/2)^2} \right) \times \frac{1}{e^{(E-E_\mathrm{F})/k_\mathrm{B}T_\mathrm{e}} + 1} + \mathrm{bkg} \right] \tag{5.12}$$

with:

$$\mathrm{bkg} = A + B \cdot E + C \cdot E^2 + D \cdot E^3.$$

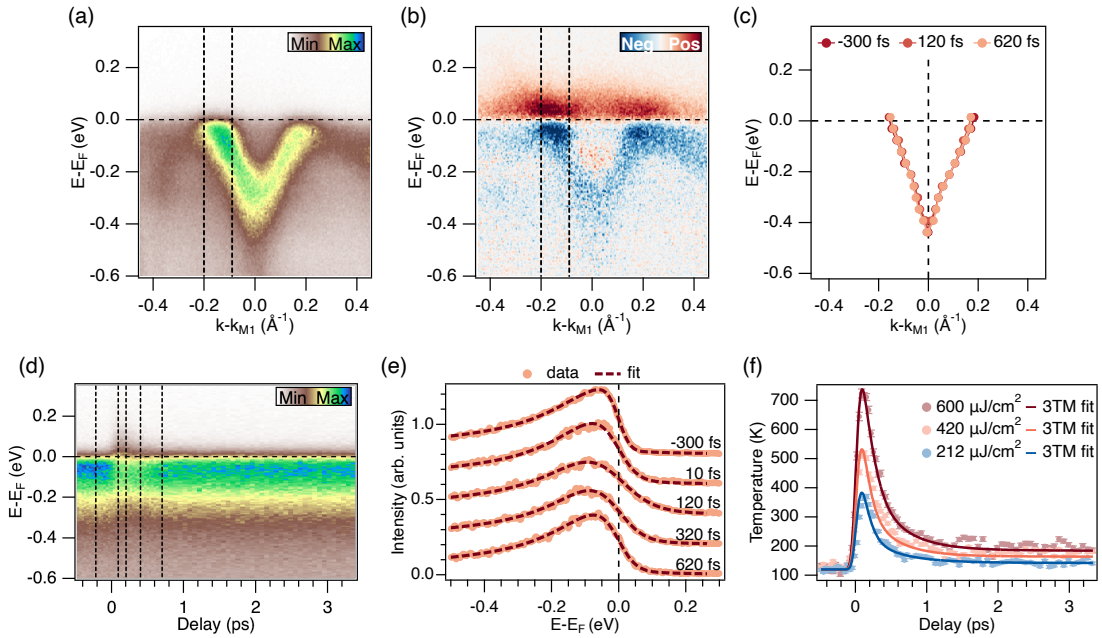

Figure 5.14: (a) ARPES spectrum acquired along the K-M_1-K direction at $T \sim 120$ K. (b) Differential ARPES spectrum highlighting the changes in the photoemission intensity induced by the pump pulse. The image has been acquired 100 fs after the arrival of the pump pulse. The absorbed fluence was set to 420 μJ/cm^2. (c) Dispersion of the V-shaped vanadium band extracted from the fits of the MDCs, for three different pump-probe delays. The fact that three traces are overlapped demonstrates that the dispersion of the band is not affected by the arrival of the pump pulse. (d) Temporal evolution of the EDCs extracted from the momentum region delimited by the dashed lines in (a). (e) EDCs extracted from (c) at selected pump-probe delays together with their fits. (f) Evolution of the electronic temperature obtained from the fits of the EDCs extracted from experiments performed with different absorbed fluences. The fits obtained using the 3TM are also reported. All the experiments have been performed at a base temperature of ~ 120 K and by using a pump photon energy of 1.77 eV.

Figure 5.14(e) shows the EDCs extracted at selected pump-probe delays, together with the fits obtained. Despite for the temporal region located immediately after the arrival of the pump pulse ($\Delta t < 100$ fs), where the hot carrier population is characterized by a non-thermal distribution, the simple model used is able to describe well the experimental data and thus it can be used to extract the electronic temperature of the system [178]. The evolution of the electronic temperature extracted from this fitting procedure is shown in Fig. 5.14(f). In particular, this graph shows the comparison between the dynamics obtained by using three different absorbed fluences (well below the critical fluence required to drive the phase transition), demonstrating that no saturation effects are observed, since the maximum change in the electronic temperature scales linearly with the pump fluence.

5.8 ROOM-TEMPERATURE LIGHT-INDUCED CHANGES IN THE BAND DISPERSION AT M_2

Having characterized the low-temperature electron dynamics triggered by the pump pulse, we now investigate the room-temperature electron dynamics, where the size of the CDW gap is already strongly reduced due to the increased temperature. Given the difficulty in obtaining good cleaves, to allow for a direct comparison between the low- and high-temperature band

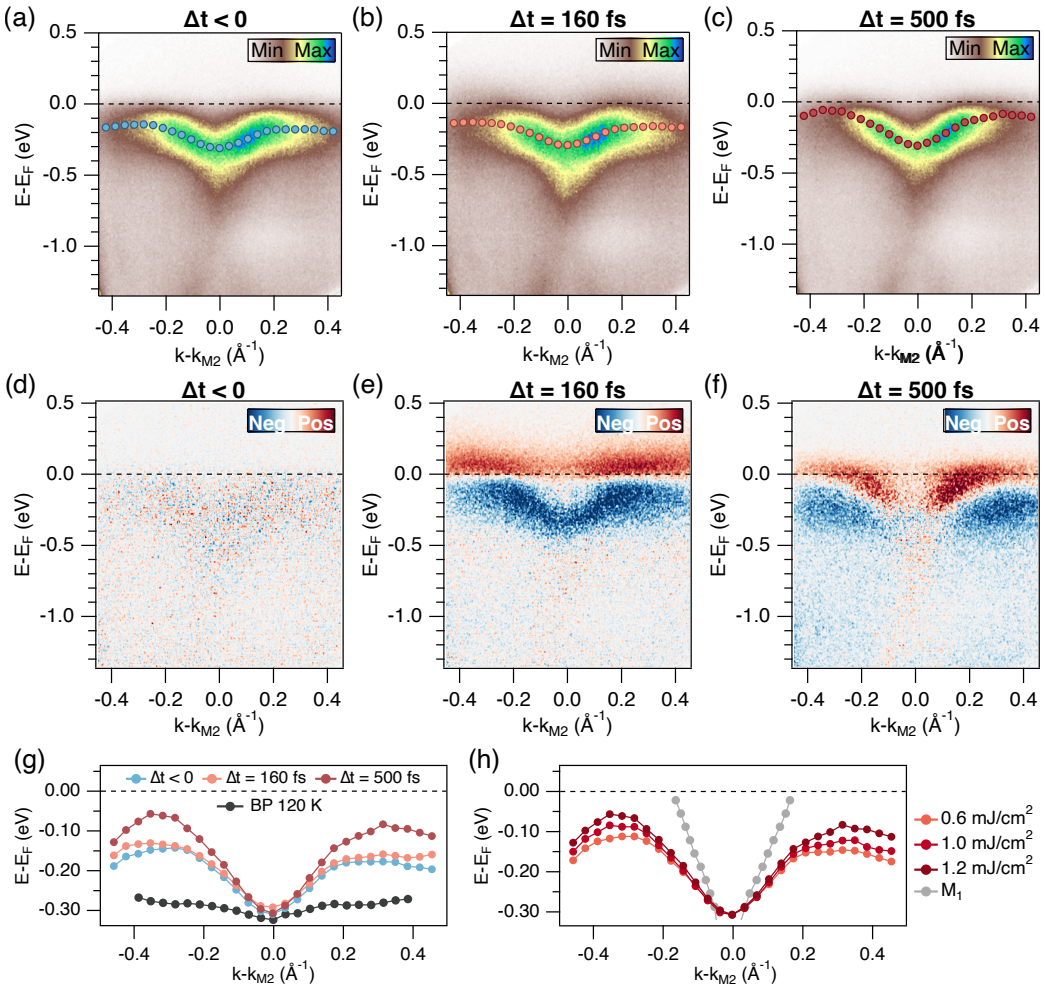

Figure 5.15: (a)-(c) Selected ARPES spectra acquired along the K-M_2-K direction at different pump-probe delays: (a) before the arrival of the pump, (b) and (c) respectively 160 and 500 fs after the arrival of the pump pulse. The colored circles denote the central position on the vanadium band extracted from the fits. (d)-(f) Differential ARPES maps highlighting the changes in the photoemission intensity induced by the pump pulse. The measurement was performed at a base temperature of $\sim$ 290 K, using a pump photon energy of $h\nu_{\text{pump}} = 1.77$ eV (700 nm) and an absorbed fluence of $\sim 1.2\,\text{mJ/cm}^2$. (g) Dispersion of the vanadium band extracted from (a)-(c). The dispersion of the vanadium band extracted from the equilibrium measurement performed at 120 K is also reported in gray for comparison. (h) Maximum folding of the vanadium band extracted at different absorbed fluences. The grey circles in (c) denote the dispersion of the vanadium band extracted from the M_1 point (shown in Fig. 5.14.(a)).

dispersion, the measurements here presented have been performed consecutively to the low-temperature ones presented in Sec. 5.4. The drawback of this approach however, resides in the fact that the outgassing of the manipulator, that takes place when it is warmed up from the liquid nitrogen temperature, has resulted in a pronounced broadening of the band structure [217]. This large broadening has therefore overshadowed the one resulting from the thermal population of the strongly-coupled-modes (we remind that $k_B T \approx \hbar\omega_0 = 24$ meV), and has hindered the study of the photoinduced changes in the width of the vanadium band. However, due to beamtime limitations it was not possible to repeat the measurement on a fresh cleave. Therefore in this section only the changes induced by the pump pulse in the dispersion of the vanadium band will be investigated.

As for the experiments performed at a base temperature of $\sim 120\,K$, the pump photon energy has been set to 1.77 eV. Unlike those experiments however, even if the energy of the pump pulse has been kept fixed, the pump pulse is not anymore resonant to the transition between the bonding and the antibonding vanadium states. Indeed, due to the increased temperature, the distance between these pair of states is expected to be strongly reduced [11]. Although this different excitation path has to be taken in mind, from the results shown in Sec. 5.6, it is not expected that the use of a non-resonant pump affects the melting of the CDW phase.

Figure 5.15 shows three ARPES spectra acquired at different pump-probe delays, together with the corresponding differential ARPES maps. These images give a qualitative picture similar to the one obtained from the low temperature experiments (Fig. 5.5). Immediately after the arrival of the pump pulse the main change in the occupied band structure arises from the depletion of the vanadium band. Subsequently a pronounced change in the dispersion of the vanadium band is observed, as confirmed also by the appearance of a V-shaped red region in panel (f). Moreover, this panel also shows that the folding of the band is accompanied by an increase of the photoemission intensity that takes place around $k\text{-}k_{M_2} \sim 0$ for high binding energies. As discussed in Sec. 5.6, these changes are likely to be related to the changes in the lattice symmetry triggered by the pump pulse.

The changes in the dispersion of the vanadium band are quantified in panel (g), where the central position of the band extracted from the fits of the EDCs is reported. Once again this comparison shows that the change in the dispersion observed at a pump-probe delay of 500 fs is more pronounced than the one extracted at the delay in which the maximum value of the electronic temperature is reached. The dispersion of the vanadium band extracted at 120 K is also reported here for comparison, showing that the changes induced by increasing the temperature are larger than the ones obtained by exciting the sample with a light pulse, despite the moderate excitation fluence used. This observation suggests again that the light-induced melting of the electronic order in VTe_2 is governed by a relatively slow and inefficient process, like the one proposed in the previous sections.

It is now useful to quantify the maximum closure of the CDW gap obtainable in our experiments. Indeed, even if, as a consequence of the arrival of the pump pulse, the dispersion of the vanadium band becomes more similar to the one found at the M_1 point, it never reaches the Dirac-like dispersion expected in the normal phase of VTe_2. A comparison between the dispersion of the V-shaped band extracted from the M_1 point, and the one extracted at the maximum folding (obtained for different excitation fluences) from the M_2 point is shown in Fig. 5.15(h). These measurements clearly show that even starting from an already partially closed gap, the excitation fluence required to drive the complete phase transition towards the normal phase of VTe_2 is higher that the one reachable by our experimental setup ($F_{abs} \sim 1.2\,mJ/cm^2$). These results are therefore in full agreement with the time-resolved reflectivity measurements presented in the previous chapter.

5.9 CONCLUSIONS

Strongly-coupled charge-density-wave materials, being characterized by the presence of large energy gaps, constitute an ideal systems to study the interplay between lattice fluctuations and the properties of the charge-ordered phase. Due to the large ratio between the gap size and the critical temperature ($2\Delta/k_B T_{CDW} \gtrsim 7$), the electronic entropy becomes negligible during the temperature-driven phase transition [12, 19]. This unique characteristic, dramatically affects also the out-of-equilibrium properties of this class of material. Indeed, as a consequence of that, high excitation fluences are required to photoinduce the transition from the low-temperature phase to the high-temperature normal phase.

The TR-ARPES measurements performed on VTe_2 and reported in this chapter, have shown that the dynamics of the CDW gap, triggered by a strong optical excitation, is not dominated by the excitation of the two amplitude modes of the system, but it is instead governed by an

incoherent process that evolves on slower timescales. By using a three-temperature model to describe the energy flow from the excited electrons to the lattice, we were able to show that the dynamics of the CDW gap can be completely described considering the population of a subset of strongly-coupled optical phonon modes, with only a marginal role played by the excitation of the CDW amplitude modes. In particular, the excitation of the strongly-coupled phonons, that takes place without a macroscopic phase coherence, has the effect of increasing the lattice fluctuations and thus the so-called transient disorder of the system [178, 194]. These increased lattice fluctuations are responsible for the loss of the long-range CDW order, which results in a quench of the electronic order parameter. Therefore, our findings suggest the presence of a light induced order-disorder transition in VTe_2, similarly to what has been observed in VO_2 [21, 196, 199]. This scenario has been corroborated by studying the dynamics of the gap size as a function of the pump photon energy. Indeed, these measurements have revealed that the timescale on which the (partial) closure of the CDW gap takes place, is independent on the particular optical transition triggered. This finding is in agreement with our microscopic picture, which is based on the relaxation of the hot carriers with the consequent excitation of strongly-coupled optical phonon modes.

To further confirm the scenario here proposed, additional calculations will be performed in the following months. Specifically, particular attention will be devoted to study the effect of the incoherent excitation of strongly-coupled non-CDW modes on the low temperature charge-ordered phase. Indeed, the scenario presented in this chapter is founded on the assumption that the excitation of non-CDW modes entails a reduction of the order parameter of the system, suggesting therefore the presence of a coupling between these modes and the charge-ordered phase. Hence, a simplified microscopic model will be developed to test this hypothesis. Moreover, the possibility to perform femtosecond X-Ray total scatting measurements will be investigated. These experiments, allowing to directly study the diffuse intensity across the momentum space, are perfectly suited to study order-disorder transitions in which the movement of the atoms proceed in a spatially incoherent manner [21, 199].

More generally, this investigation calls for a deeper understanding of the interplay between lattice fluctuations and the CDW phase, and paves the way for further exploration of the nonequilibrium properties of the strongly-coupled CDW systems by means of TR-ARPES experiments.

6 CONTROL OF THE CDW PHASE IN THE KAGOME COMPOUND ScV_6Sn_6

Strongly correlated systems and topological materials are two rich research fields in condensed matter physics. Kagome lattice materials, due to their crystal structure made by corner-sharing triangles, lie at the intersection of these two fields, being able to combine Dirac Fermions [218], van Hove singularities (vHS) [9] and flat bands across the Brillouin zone [219]. Furthermore, these compounds have shown to host a variety of exotic phases, like high-temperature superconductivity [9, 220, 221], charge-density waves [9, 222], Bose-Einstein condensation [223] and anomalous Hall effect [224]. However, the link between the distinctive electronic structure of the kagome compounds and the observed many-body phenomena remains to be understood [9].

This chapter is devoted to the presentation of the time-resolved reflectivity experiments performed on the kagome compound ScV_6Sn_6, which hosts a low-temperature CDW phase. These results are corroborated by extensive DFT simulations performed by Prof. Domenico Di Sante and by Dr. Armando Consiglio which are discussed alongside to the experimental results. In particular, after having presented the general properties of the kagome compounds and having discussed the emergence of the CDW in ScV_6Sn_6, we present a systematic temperature-dependent study of the non-equilibrium reflectivity across the CDW phase transition. This study has allowed to reveal the presence of a new phonon mode below T_{CDW} that, with the aid of DFT calculations, has been identified as the amplitude mode of the system. Furthermore, by performing a fluence-dependent study, we demonstrate the marked resilience of this compound upon a near-infrared photoexcitation. Finally, we show that the application of a modest uniaxial strain on a ScV_6Sn_6 crystal results in a reduction of the temperature-dependent softening of the CDW amplitude mode. This result, corroborated by DFT simulations, suggests a possible path to enhance the CDW order in ScV_6Sn_6.

6.1 BASIC PROPERTIES OF KAGOME COMPOUNDS

The arrangement of atoms in a kagome lattice is shown in Fig. 6.1(a). As depicted by the simplest nearest-neighbor electronic hopping model of the s-orbital kagome lattice, an exact solution of the electronic problem on such lattice is one where the wavefunctions at the neighboring corners of the hexagons have opposite signs (plus and minus signs in Fig. 6.1(a)) [219, 225]. This causes the hopping pathways to the nearest-neighbors to vanish [226]. As a consequence of this destructive quantum interference, electrons turn out to be localized inside the blue hexagonal region depicted in Fig. 6.1(a). Hence, this localization in real space translates in momentum space with the appearance of dispersionless bands (namely flat bands) [227]. In addition to the flat bands, the tight-binding model of the kagome lattice predicts the presence of a pair of Dirac bands (located at the K points) that are protected by the lattice symmetry, similarly to the case of the honeycomb lattice (blue band structure shown in panel (b)) [219]. Both the linear band crossing at K and the quadratic band touching point at Γ become gapped once the spin-orbit coupling (SOC) is included (black band structure in panel (b)), and the Dirac and flat bands become topologically nontrivial [219, 228, 229]. Furthermore, the diverging density of states at the vHS (located at the M points) and the flat bands can support the emergence of correlated many-body ground states [225].

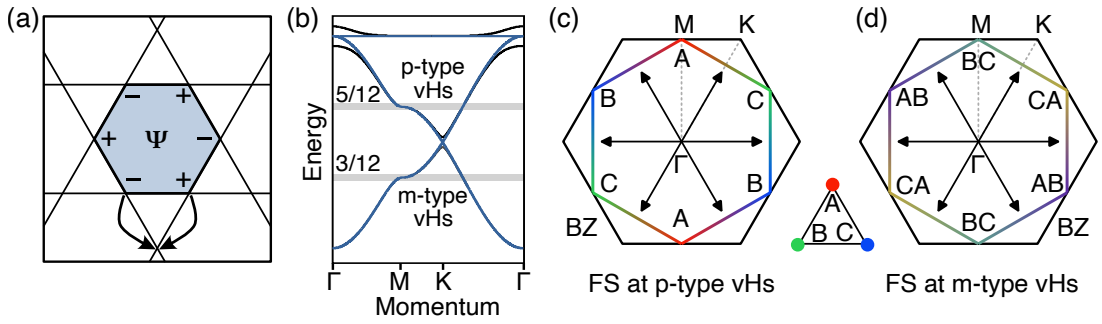

Figure 6.1: (a) Confinement of electrons in a kagome lattice with nearest-neighbor hopping. The atoms lay at the intersection of the lines. Plus and minus indicate the phase of the wavefunction at neighboring sublattices. Any hopping outside the hexagon is canceled due to destructive interference, hence resulting in the localization of the electrons inside the blue hexagon. Adapted from [219]. (b) Prototypical tight-binding band structure (blue) of the kagome lattice. The black bands show the case in which the spin-orbit coupling is included. The two vHS are marked by the grey shades. (c) and (d) Fermi surface of a kagome lattice at $n = 5/12$ filling with p-type vHS and at $n = 3/12$ filling with m-type vHS. The red, green and blue colors used on the Fermi surface represent the weights of the three sublattices. The nesting vector $\mathbf{Q} = (\pi, 0)$ and its equivalents are shown by the black arrows. Adapted from [9].

Despite all the fascinating properties of the kagome compounds, in the following we will only consider and discuss the role played by the vHS. Indeed, the characteristics of the vHS are crucial in determining the Fermi surface instabilities that reside at the origin of many exotic phases observed in kagome materials [230]. It has been predicted that both chiral density wave and unconventional superconductivity may naturally arise from the kagome-derived vHS at the filling fractions $n = 5/12$ and $n = 3/12$ (the two filling levels are highlighted by the grey shades in panel (b)) [231]. At these filling fractions, the Fermi surface and the vHS at the M points are perfectly nested by a reciprocal vector $\mathbf{Q} = (\pi, 0)$, consistent with a 2×2 charge-ordered phase. In support of this prediction, recent ARPES studies have shown that the vHS located near the Fermi level set the stage for the transition towards a 2×2 inverse star-of-David CDW phase in the kagome compounds belonging to the family of AV_3Sb_5 (A= K, Rb, Cs) [9, 232–234]. Moreover, due to the intrinsic asymmetry of the kagome band structure across the Dirac point, the two vHS found at filling fractions $n = 5/12$ and $n = 3/12$ are fundamentally distinct and this aspect affects the properties of the new emerging phases. Indeed, due to the presence of three inequivalent sites per unit cell, the Fermi surfaces at the two fillings are characterized by two different flavors, corresponding to the pure (p-type) and mixed (m-type) sublattice characters of the vHS (the two possible FS are depicted in Fig. 6.1(c) and (d)). Such sublattice character is critical to understand the unconventional many-body phases emerging from the kagome lattice, since it determines the momentum dependence of the electronic susceptibility and the pairing symmetry of the low-temperature phases (electron-electron for the superconducting phase or electron-hole for the charge-density wave phase) [9, 235, 236].

As a final remark, it is worth noting that the properties discussed in this paragraph are strictly true for a purely two-dimensional system. When, instead of a single layer, a layered 3D system is considered, the finite interlayer coupling must be taken into account. As a result, the system can lack the quasi-2D behavior [237], or display bands which remain flat only for subregions of the Brillouin zone [238].

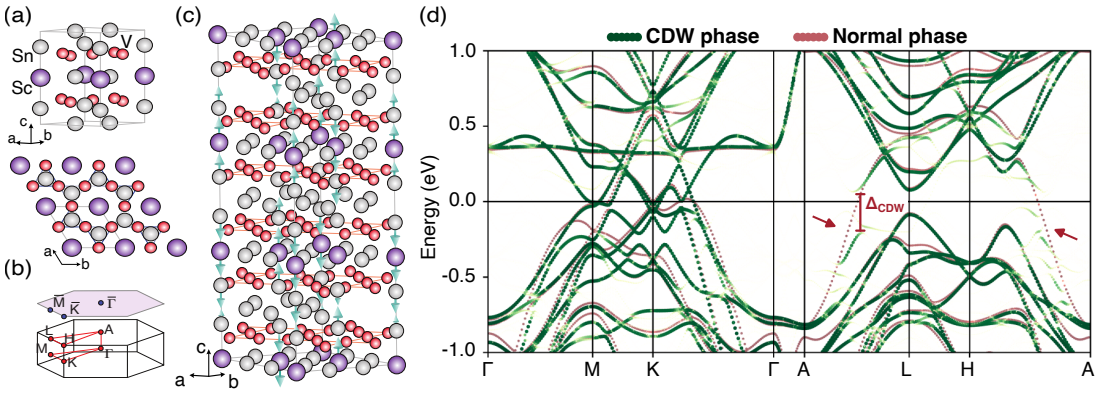

Figure 6.2: (a) High-temperature crystal structure of ScV_6Sn_6. The top-view corresponds to a 2×2 unit cell. (b) Brillouin Zone of the high-temperature phase of ScV_6Sn_6. (c) Low-temperature crystal structure of ScV_6Sn_6. The teal arrows indicate the out-of-plane distortion of the lattice due to the CDW reconstruction. The length of the arrows is proportional to the displacement. (d) Calculated electron band structure of ScV_6Sn_6 in the normal (red dots) and the CDW (green dots) phases. For visual clarity, the pristine band structure has been translated by $+0.029$ eV. In this way the van Hove singularities and the d_{z^2} flat band of the CDW and pristine systems are aligned. The red arrows indicate the regions in which the largest changes in the band structure are observed. Modified figure based on the published version in Tuniz *et al.* [239].

6.2 THE KAGOME COMPOUND ScV_6Sn_6

Bilayer kagome metals are an emerging class of correlated topological compounds with chemical formula RV_6Sn_6 (R: rare earth), featuring unconventional topological phases and collective magnetic excitations at low temperature [239–241]. Among these compounds, ScV_6Sn_6 is the only one that exhibits a low-temperature CDW phase, thus raising the question about the microscopic origin of this new ordered phase. Despite the joint efforts and the large number of experimental and theoretical works, the origin and the nature of the CDW phase remain to be understood [18, 222, 239, 242]. This section is devoted to the characterization of the structural and electronic properties of ScV_6Sn_6. Particular attention will be drawn to those properties linked to the emergent charge-ordered phase.

6.2.1 High-temperature crystal structure and CDW reconstruction

ScV_6Sn_6 has a hexagonal $HfFe_6Ge_6$-type crystal structure [240, 243, 244]. As anticipated above, unlike the one of the binary (T_mX_n, with T: 3d transition metals and X= Sn, Ge) and ternary (AV_3Sb_5, with A= K, Rb, Cs) kagome metals, this crystal structure is characterized by the presence of two kagome sheets per unit cell, separated by alternating $ScSn_2$ and Sn_2 layers, as shown in Fig. 6.2(a) [243]. Despite this structural difference however, it is worth emphasizing that ScV_6Sn_6 shares a partially filled vanadium kagome lattice with the ternary compounds AV_3Sb_5, with V-V distances that in both cases are between 2.73 and 2.75 Å [243, 245]. The presence of a common vanadium kagome lattice results in a similar electronic band structure around the Fermi level, thus establishing a possible link between these compounds [9, 222].

As signaled by diffraction and transport experiments [222, 243], at around 92 K ScV_6Sn_6 undergoes a first order phase transition towards a novel $\sqrt{3} \times \sqrt{3} \times 3$ charge-density-wave phase. The resulting charge-ordered phase is characterized by the presence of large out-of-plane displacements involving the scandium and the tin atoms (highlighted in Fig. 6.2(c)), whereas the position of the vanadium atoms is only weakly perturbed [239, 243]. Specifically, diffraction measurements have shown that while the CDW-induced movement of the Sc and Sn atoms along the c-axis is of 0.16 Å, the displacement of the vanadium atoms in the kagome mesh is only of the order of $0.004 - 0.006$ Å [243]. At this point, it is worth noting that despite

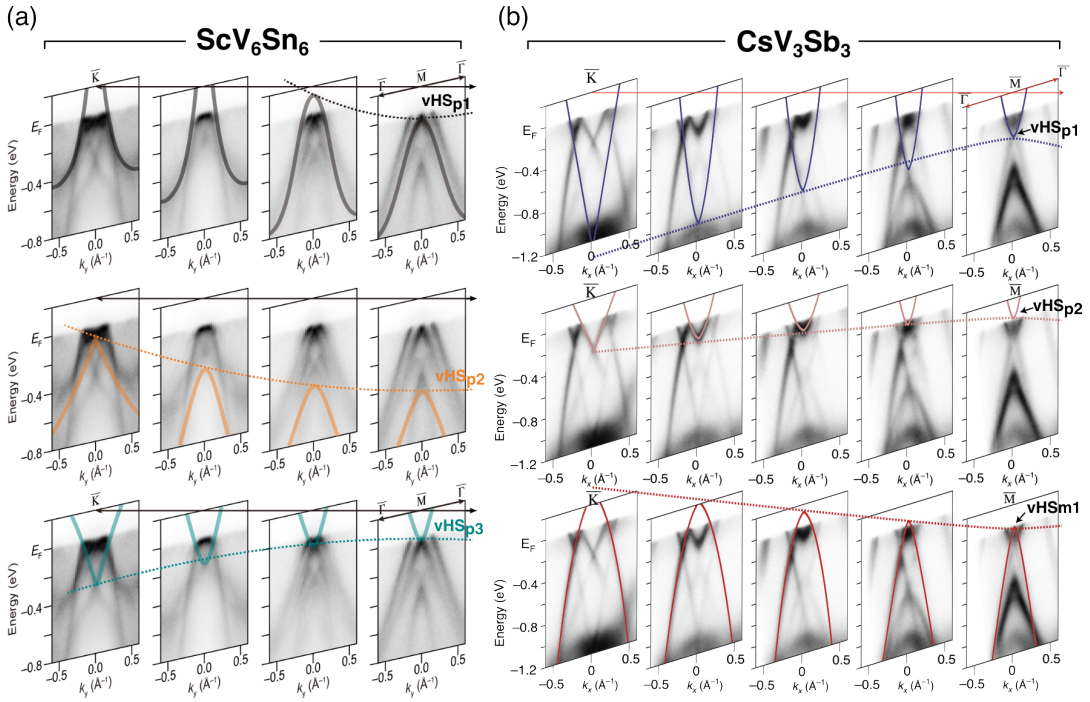

Figure 6.3: (a) ARPES spectra measured perpendicularly to the $\overline{K}-\overline{M}-\overline{K}$ direction, showing the dispersion of the three vHS in ScV_6Sn_6. vHS_{p1} and vHS_{p2} have an electron-like dispersion along the $\overline{K}-\overline{M}-\overline{K}$ direction (dashed line) and an hole-like dispersion along the $\overline{\Gamma}-\overline{M}-\overline{\Gamma}$ direction, while the concavity is opposite for vHS_{p3}. The data were collected using a photon energy of 129 eV, which translates to $k_z \approx 0$. Adapted from [222]. (b) ARPES spectra measured perpendicularly to the $\overline{K}-\overline{M}-\overline{K}$ direction showing the dispersion of the three vHS in CsV_3Sb_5. vHS_{p1} and vHS_{p2} have a hole like dispersion along the $\overline{K}-\overline{M}-\overline{K}$ direction (dashed line) and an electron-like dispersion along the $\overline{\Gamma}-\overline{M}-\overline{\Gamma}$ direction, while the concavity is opposite for vHS_{m1}. The data were collected using a photon energy of 88 eV, which translates to $k_z \approx 0.4\pi/c$. Within the color scale used, darker colors indicate higher electron counts. Adapted from [9].

the similar kagome mesh, the lattice reconstruction of ScV_6Sn_6 is remarkably different from the one observed in the sister compound CsV_3Sb_5. Indeed, in CsV_3Sb_5 the vanadium atoms have an in-plane displacement of the order of $0.0085-0.009$ Å, forming either a Star of David or a trigonal arrangement, while no out-of-plane distortions are observed [243].

As discussed in the introductory chapter on the CDW systems, a large lattice reconstruction is possible only thanks to the energy gain arising from the opening of an electronic gap. Therefore we now consider the modifications induced in the electronic structure by the onset of the CDW phase. Figure 6.2(d) shows a comparison between the calculated electronic band structure in the normal and in the CDW phases of ScV_6Sn_6 [239]. This comparison shows that the largest changes in the band structure are expected in the A-L-H plane, where also the opening of a large energy gap is observed. In agreement with the diffraction measurements, the kagome-derived structures appear to be weakly perturbed by the onset of the charge-ordered phase. However, since these DFT calculations highlight the presence of multiple vHS in proximity of the Fermi level, in analogy to the AV_3Sb_5 family [9], it is necessary to carefully analyze the possible role played by the vHS in the stabilization of the charge-ordered phase in ScV_6Sn_6.

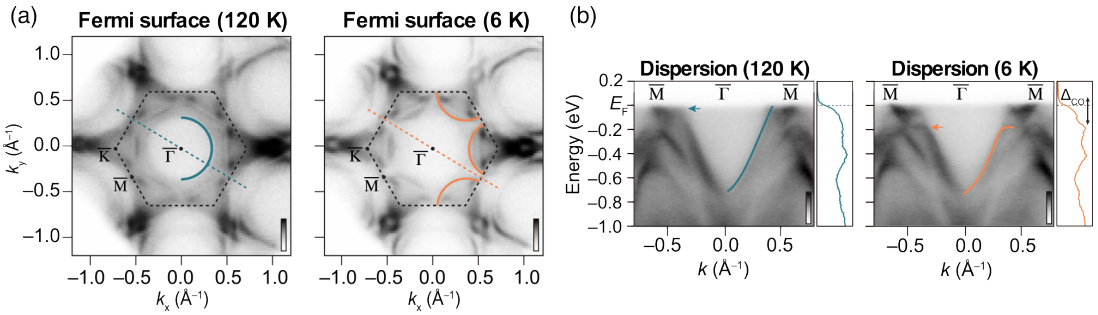

Figure 6.4: (a) Fermi surface of ScV_6Sn_6 measured in the normal (left) and in the CDW (right) states. (b) Band dispersion measured along the $\overline{\Gamma} - \overline{M}$ direction in the normal (left) and CDW (right) phases. The solid lines are guides to the eye highlighting the band dispersion around the $\overline{\Gamma}$ point. The data were obtained using a photon energy of 115 eV, corresponding to the $k_z \approx \pi$ high-symmetry plane. Within the color scale used, darker colors indicate higher electron counts. Adapted from [222].

6.2.2 van Hove singularities and CDW gap

As anticipated in Sec. 6.1, in AV_3Sb_5 compounds it has been shown that the vHS derived from the vanadium kagome lattice set the stage for the CDW phase [9, 232]. Since ScV_6Sn_6 shares the same kagome network, it is tempting to consider a similar scenario also in this compound. Figure 6.3(a) shows the dispersion of the three p-type vHS found at the M point in ScV_6Sn_6. While vHS_{p2} is located at high binding energies, the other two are located very close to the Fermi level, and can in principle promote various electronic instabilities. For comparison, the dispersion of the three vHS (two of them are p-type while the other is m-type) found in CsV_3Sb_5 is reported in Fig. 6.3(b), showing the presence of two vHS located very close to the Fermi level, similarly to what is observed for ScV_6Sn_6 [9]. Despite these similarities, and the fact that the vHS lie at the folded Brillouin zone boundary of the $\sqrt{3} \times \sqrt{3} \times 3$ of charge-ordered phase, temperature dependent measurements performed on ScV_6Sn_6 have shown that the vHS stay unaltered across T_{CDW} [222]. This observation therefore confirms the hypothesis according to which the vanadium kagome lattice plays a marginal role in driving the $\sqrt{3} \times \sqrt{3} \times 3$ CDW phase in ScV_6Sn_6 [222, 232, 239].

After having discussed the role played by the vHS, we analyze the opening of the charge order gap. The Fermi surfaces reported in Fig. 6.4(a) show that upon entering in the CDW phase, the circular intensity pattern well visible in the normal phase (left) is modified in a star-shaped pattern (right) [222]. The changes induced in the band structure can be better understood by considering the ARPES spectra measured along the $\overline{\Gamma} - \overline{M}$ direction and reported in panel (b). The normal phase band structure is characterized by the presence of a large electron pocket centered at $\overline{\Gamma}$, which constitutes the circular intensity pattern observed in the normal-phase Fermi surface. Below T_{CDW} this electron band is folded towards higher binding energies, developing a large CDW gap [222]. The reduction of intensity at the Fermi level, that arises as a consequence of the opening of the charge order gap, results in the star-shaped pattern observed in the low-temperature Fermi surface. We note that the opening of the gap is observed at about 2/3 of the $\overline{\Gamma} - \overline{M}$ direction, which perfectly matches the boundaries of the folded $\sqrt{3} \times \sqrt{3}$ Brillouin zone [222].

It is now also useful to compare the gap size extracted in ScV_6Sn_6 with the one observed in the AV_3Sb_5 compounds. Indeed, despite the similar critical temperatures ($T_{CDW} \approx 80 - 100$ K), the gap size of the two compounds is rather different. While in ScV_6Sn_6 the gap is of ≈ 260 meV [222, 239], in the sister compounds AV_3Sb_5 is of the order of $\approx 50 - 80$ meV [222, 246, 247]. It is worth emphasizing that the gap size of ScV_6Sn_6 is remarkably large, given the critical temperature of the compound. Indeed, the ratio between the CDW transition temperature and the gap size is $2\Delta/k_B T_{CDW} \approx 30$, highlighting the unconventional nature

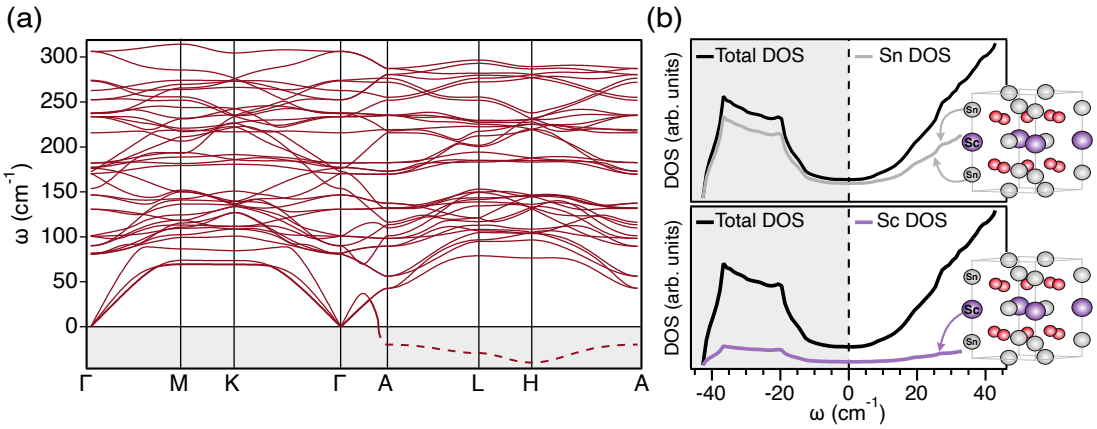

Figure 6.5: (a) Calculated phonon dispersion for the high-temperature phase of ScV_6Sn_6. The dashed line is used to highlight the phonon branch with negative frequencies. (b) Calculated phonon total and projected density of states of ScV_6Sn_6. The imaginary modes, indicating a lattice instability, arise only from the Sc and from the Sn atoms with the same (x, y) coordinates of the Sc atoms (two of them are indicated by the grey arrows). Modified figure based on the published version in Tuniz *et al.* [239].

of this phase and placing ScV_6Sn_6 among the compounds in which the CDW transition is driven by a strong electron-phonon coupling [12].

6.2.3 Competing lattice instabilities and high-temperature calculated phonon dispersion

Conventionally, as discussed in Sec. 2.1, the phase transition towards the CDW state is signaled by the complete softening of an acoustic phonon mode at $\mathbf{q_{CDW}}$, when the temperature approaches T_{CDW} from above. However, Inelastic X-Ray Scattering (IXS) measurements performed on ScV_6Sn_6 have revealed that the CDW phase arises from a competition between different lattice instabilities. Indeed, whereas the long-range CDW order occurs at $\mathbf{q_s} = (\frac{1}{3}, \frac{1}{3}, \frac{1}{3})$, corresponding to a $\sqrt{3} \times \sqrt{3} \times 3$ CDW phase, above the critical temperature the phonon softening is more prominent at $\mathbf{q}^* = (\frac{1}{3}, \frac{1}{3}, \frac{1}{2})$, which would lead to a $\sqrt{3} \times \sqrt{3} \times 2$ CDW order [18, 40]. These experiments therefore suggest that the wavevector of the CDW phase is different from the one of the leading lattice instability above T_{CDW}. This scenario has been confirmed by first principle calculations which have shown that, although a $\mathbf{q}^*$-CDW is energetically more favorable at the density functional theory level, a peak in the $\mathbf{q}$-dependent EPC promotes the $\mathbf{q_s}$-CDW as a ground state [18, 40]. This strong EPC also leads to a strong electron scattering above T_{CDW} and accounts for the large resistivity drop observed upon cooling below T_{CDW} [18].

As shown for the case of VTe_2, important insights on the low-temperature lattice instabilities can be gained by studying the high-temperature phonon dispersion. Figure 6.5(a) shows the calculated phonon dispersion in the zero temperature limit for the normal phase of ScV_6Sn_6. These calculations show the presence of a weakly dispersive phonon branch in the A-L-H plane, characterized by large negative frequency values. We remind that, in the DFPT framework, imaginary phonon modes denote an atomic displacement that lowers the total free energy of the system, therefore signaling the presence of a lattice instability. Interestingly, the lattice instability is not peaked around a single wavevector, like it has been shown for CsV_3Sb_5 [222], but instead it spans a large portion of the BZ.

By projecting the total density of states on the different atoms that constitute the unit cell, it is possible to understand which atoms are responsible of the large instabilities observed. Figure 6.5(b) shows the contributions of the Sc and Sn atoms to the imaginary branch. This comparison demonstrates that the lattice instability arises only from the Sc atoms and the two Sn atoms having the same scandium's (x, y) coordinates, *i.e* the ones involved in the lattice

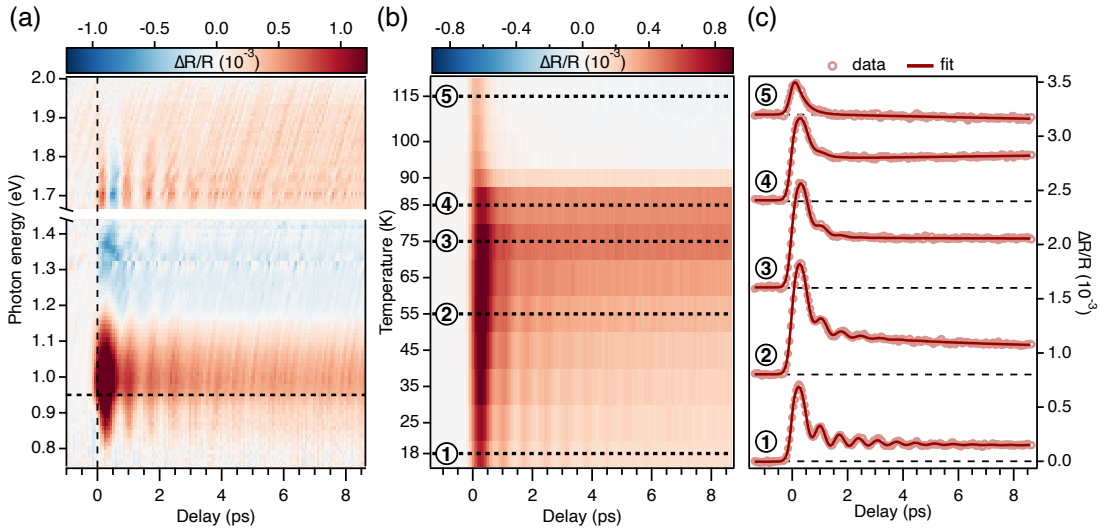

Figure 6.6: (a) Two-dimensional map showing the evolution of the $\Delta R/R$ signal of ScV_6Sn_6 as a function of the pump-probe delay and of the probe photon energy. The spectral range around 1.5 eV was disturbed by the pump photons scattered from the sample, so it was not considered. The measurement was performed at a base temperature of 30 K (well below T_{CDW}) and with an incident fluence of $\sim 200\,\mu J/cm^2$. (b) Two-dimensional map showing the evolution of the $\Delta R/R$ signal of ScV_6Sn_6 as a function of temperature and of the pump-probe delay. The measurements have been performed at a probe photon energy of ~ 0.95 eV (1300 nm) and with the same excitation fluence used in the supercontinuum experiment. This photon energy is marked in (a) by the horizontal dashed line. (c) Traces extracted from (b), showing the evolution of the $\Delta R/R$ signal across the phase transition, together with the best fits obtained using Eq. (6.1). Modified figure based on the published version in Tuniz *et al.* [239].

reconstruction. Hence these calculations, in agreement with the results of the diffraction experiments [243], further confirm that the kagome lattice composed by the vanadium atoms does not contribute to the the onset of the CDW order. It is worth noting that, similar calculations performed for CsV_3Sb_5 have instead revealed the presence of lattice instabilities localized in specific regions of the BZ and dominated by the vanadium atoms [222].

Finally, the fact that, consistently with other phonon calculations [18, 222], the imaginary phonon branch in Fig. 6.5(a) spans a large portion of the BZ, and that, the most negative frequency is not located at $\mathbf{q}_{CDW}$, is in agreement with the scenario described above. The $\sqrt{3} \times \sqrt{3} \times 3$ CDW phase emerges only thanks to a peak in the $\mathbf{q}$-dependent EPC [18]. However, as discussed in Sec. 4.1.2, the study of the phonon calculations performed in the zero-temperature limit alone might lead to wrong interpretations [131]. Therefore the calculations reported in this thesis cannot be used to confirm the presence of competing lattice instabilities.

To further investigate the interplay between the electronic and structural degrees of freedom in the stabilization of the charge-ordered phase of ScV_6Sn_6, we performed time-resolved reflectivity experiments in both normal and CDW phases of this compound. As for the case of VTe_2, particular attention has been put in the study of the collective excitations of the CDW phase.

6.3 TEMPERATURE-DEPENDENT STUDY OF THE CDW PHASE IN ScV_6Sn_6

This section is devoted to the presentation of the temperature-dependent non-equilibrium reflectivity measurements performed on ScV_6Sn_6. Here we will follow the same path already

established for VTe_2, with the key difference that the measurements will be extended also above the critical temperature, giving therefore access to the normal-phase dynamics.

The two-dimensional map reported in Fig. 6.6(a) shows the evolution of the non-equilibrium reflectivity measured at 30 K in the spectral range accessible through our supercontinuum probe. This map shows that the low-temperature response of the system is characterized by the presence of a coherent oscillation, with a low-temperature frequency of 1.45 THz, which adds up to the incoherent exponentially decaying background. As for VTe_2 and many other CDW compounds, the incoherent part of the $\Delta R/R$ signal is characterized by a first fast decay that ends within 1 ps from the arrival of the pump pulse and by a second slow recovery that evolves on a timescale of $10 - 15$ ps [28]. We recall here that the former, which usually slows down critically upon approaching the transition temperature, is attributed to the recombination time of the hot carriers through the temperature-dependent CDW gap [28], while the latter has been suggested to originate from the recovery of the coupled electron-lattice order parameter [138].

The supercontinuum measurement reported in Fig. 6.6(a) highlights that even if the phonon mode that characterizes the low-temperature response of the system can be resolved in all the spectral range accessible through our probe beam, the intensity of the $\Delta R/R$ signal, and thus of the phonon mode oscillations, is strongly enhanced in the near infrared region around 1 eV. Therefore, being interested in studying the interplay between this phonon mode and the CDW phase in ScV_6Sn_6, we performed a systematic study of the non-equilibrium reflectivity as a function of the temperature, focusing our attention in the energy range around 1 eV. Specifically, as discussed in Sec. 4.3, we performed single-color probe measurements by filtering the supercontinuum beam with a bandpass filter at ~ 0.95 eV, allowing therefore to adopt a lock-in detection of a single InGaAs photodiode.

The reflectivity measurements performed in the temperature range $18 - 115$ K are stacked on top of each other in Fig. 6.6(b) (no appreciable changes in the response of the system have been observed between 115 K and room temperature). This map highlights the presence of an abrupt change in the response of the system in proximity to T_{CDW}. Therefore, to extract the temperature evolution (T) of both coherent and incoherent parts of the $\Delta R/R$ signal across the phase transition, we modeled the full temporal evolution of the non-equilibrium reflectivity after the arrival of the pump pulse as:

$$\frac{\Delta R}{R}(t,T) = G(t) \otimes \left[\sum_{i=1}^{2} A_i(T) e^{-t/\tau_i^e(T)} + B(T) e^{-t/\tau^{ph}(T)} \cos[\omega(T)t + \phi(T)] + C(T) \right], \quad (6.1)$$

where $G(t)$ represents the cross correlation between the pump and the probe pulses. $A_i(T)$ denotes the amplitude of the electronic relaxation phenomena with time constant $\tau_i^e(T)$. $B(T)$ denotes the amplitude of the oscillating component used to describe the modulation induced by a phonon mode with angular frequency $\omega(T)$, decay time $\tau^{ph}(T)$ and phase $\phi(T)$. Finally, $C(T)$ represents the amplitude of a much slower process that in our time window can be approximated by a constant term.

Figure 6.6(c) shows five traces extracted from panel (b) at selected temperatures, together with the fits obtained using Eq. (6.1). These traces allow to better visualize the abrupt change in the out-of-equilibrium response of the system that takes place around 90 K, in correspondence to the CDW phase transition. Indeed, above the critical temperature (trace 5) no oscillations in the $\Delta R/R$ signal are detected and the response of the system can be described by a fast exponential decay that ends within 1 ps from the arrival of the pump pulse and by a slowly growing negative component barely visible at large pump-probe delays. When the temperature of the system is reduced below the critical temperature, a new phonon mode appears, whose frequency, lifetime and amplitude grow when the temperature of the system is further reduced. Moreover, also the incoherent part of the $\Delta R/R$ signal shows a marked temperature dependence in both relaxation channels. Indeed, while the slow relaxation dynamics is characterized by a pronounced change in its amplitude, the first fast component shows a change in its lifetime (τ_1). The evolution of τ_1 as a function of the

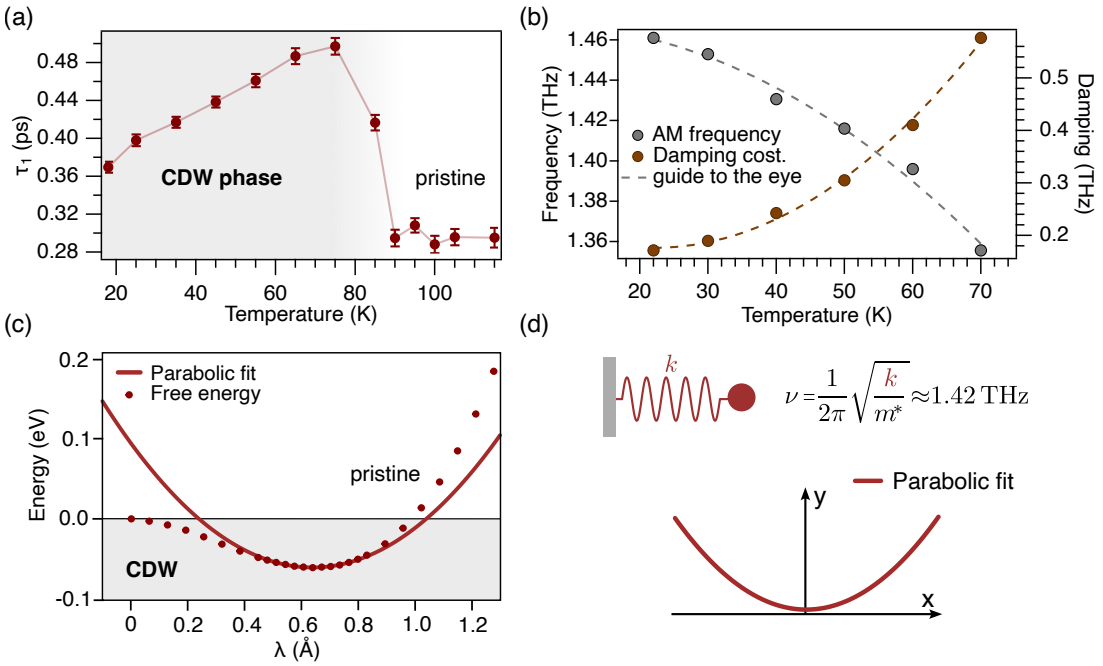

Figure 6.7: (a) Evolution of the lifetime of the first fast decay (τ_1) as a function of the temperature. (b) Evolution of the frequency and of the damping constant of the amplitude mode as a function of the temperature. The error bars estimated through our fitting procedure are comparable with the size of the dots and thus are not reported. (c) Total energy of ScV_6Sn_6 constant-volume superlattice while interpolating between the pristine ($\lambda = 0$ Å) and an exaggerated ($\lambda > 0.64$ Å) CDW phase. The parabola represented by a continuous line is the quadratic fit of the energy profile around the minimum. (d) Schematic sketch of the procedure followed to compute the frequency of the phonon mode. The effective mass (m^*) has been obtained from the mass tensor and the normalized displacement vector, while the spring constant has been obtained from the quadratic fit of the energy profile. Modified figure based on the published version in Tuniz *et al.* [239].

temperature of the system is reported in Fig. 6.7(a). A linear increase of the relaxation time is observed when the temperature is risen towards the CDW critical temperature, with a sudden drop at the transition temperature. For higher temperatures, the relaxation time remains constant. In contrast to other CDW [28, 248] and superconducting [10] systems for which it has been shown that $\tau \propto 1/\Delta$ [249], no divergence in the lifetime is observed when the temperature approaches the critical temperature. This behavior could be explained by considering that ScV_6Sn_6 unlike other conventional CDW compounds, displays a first order phase transition. Indeed our results are in agreement with the ones obtained on the CDW system 1T-TaS_2, which similarly to ScV_6Sn_6, displays a first order phase transition [250]. The evolution of the lifetime reflects the one of the CDW gap, and thus of the order parameter of the system. In systems in which the phase transition is of the second order, the CDW order parameter reduces continuously thus resulting in a divergence of the lifetime. At the contrary, in systems characterized by a first order phase transition, the CDW order parameter has an abrupt change at T_{CDW}, thus a different evolution of the lifetime is expected [250].

From the fits obtained using Eq. (6.1) it is possible to extract the temperature evolution of the frequency and of the damping of the phonon mode, as shown in Fig. 6.7(b). By increasing the temperature towards the CDW critical temperature we observe a mean-field like softening of the phonon frequency, together with a marked increase of its damping (the damping constant has been calculated using the expression $\Gamma = 1/(\pi\tau^{ph})$ [28]). As discussed for VTe_2, this peculiar renormalization of the phonon frequency has been used in many other CDW materials to identify the amplitude mode of the system [28–31, 136, 148]. Before proceeding,

we emphasize that even if $T_{CDW} \approx 92\,\mathrm{K}$, the frequency of the phonon mode can be reliably extracted only up to $\approx 70\,\mathrm{K}$, due to the reduction of its amplitude and lifetime observed close to the transition temperature.

To corroborate the identification of the CDW amplitude mode, we performed *ab-initio* DFT calculations to extract the low-temperature frequency of the AM of the system. However, the calculation of the full phonon dispersion in the low-temperature phase has been hindered from the very large number of atoms that constitute the CDW unit cell (due to the lattice reconstruction the unit cell contains 117 atoms). Therefore, a different procedure has been used to calculate the AM frequency [239]. The total energy of the system has been calculated while interpolating between the pristine and an exaggerated CDW structure. To obtain the structural interpolation between these two structures, the 351-dimensional (117 atoms $\times$ 3 directions) displacement vector $\mathbf{e} = \mathbf{r}_{\text{non-pristine}} - \mathbf{r}_{\text{pristine}}$ has been calculated. Figure 6.7(c) shows the total energy of the system as a function of the norm of the displacement vector $\lambda = \|\mathbf{e}\| = \|\mathbf{r}_{\text{non-pristine}} - \mathbf{r}_{\text{pristine}}\|$ (in the following also called polarization length), therefore $\lambda = 0$ corresponds to the pristine sample. As expected from a system described by a complex order parameter, the total energy profile reported in Fig. 6.7(c) follows the shape of a double-well potential, with a clear minimum centered at $\lambda \sim 0.64\,\text{Å}$, indicating the presence of a stable CDW reconstruction. The frequency of the amplitude mode has then been obtained by considering an harmonic approximation of the system around its equilibrium position. The process is schematized in Fig. 6.7(d). Specifically, we fitted the shape of the potential around the minimum using a quadratic expression. The fit gives the equation $y = 0.379202 \cdot x^2$. From this harmonic approximation it is then possible to calculate the equivalent "spring" constant of the system, obtaining $k = 2 \times 0.379202\,\mathrm{eV/Å^2}$. The effective mass m^* is computed using the normalized displacement vector $\mathbf{n} = \mathbf{e}/\|\mathbf{e}\|$ and the mass tensor $\mathbf{M} = \mathrm{diag}(m_1, m_1, m_1, \ldots, m_{117}, m_{117}, m_{117})$ via the expression $m^* = \mathbf{n} \cdot (\mathbf{M} \cdot \mathbf{n})$, obtaining the value $m^* = 91.02\,\mathrm{u}$. It is worth noting that the mass obtained is intermediate among the one of Sn and Sc atoms, *i.e.* the ones that mostly participate to the CDW transition. Finally, the frequency ν can be calculated using the expression: $\nu = 1/(2\pi)\sqrt{k/m^*}$, from which we obtain $\nu = 1.42\,\mathrm{THz}$. Further details on the calculations can be found in [239].

The value of the phonon frequency estimated from our calculations is in excellent agreement with the one extracted from the time-resolved reflectivity experiments, confirming that the coherent phonon mode observed in the low temperature phase of ScV_6Sn_6 is the CDW amplitude mode. As expected, this mode involves the out-of-plane movements of the scandium and tin atoms, and thus results in a modulation of the lattice reconstruction.

6.4 FLUENCE-DEPENDENT STUDY OF THE CDW PHASE IN ScV_6Sn_6

As discussed for the case of VTe_2, additional insights about the nature of the CDW phase can be gained by varying the excitation fluence. In particular, the absorbed energy required to non-thermally drive the phase transition from the CDW phase to the normal state, provides information about the energetics of the phase transition [29]. Here we apply this approach to ScV_6Sn_6.

The two-dimensional map reported in Fig. 6.8(a) shows the evolution of the non-equilibrium reflectivity as a function of the incident fluence. The traces that compose this map have been normalized to the incident fluence to facilitate the comparison between traces whose intensity would otherwise differ by more than one order of magnitude. In particular, every trace is multiplied by the ratio F_{max}/F, where F_{max} is the maximum fluence used and F is the fluence used in the specific measurement considered. To better visualize the effect of a change in the excitation fluence, in panel (b) we report five traces extracted at selected fluences, together with the fits obtained using Eq. (6.1), in which the temperature dependence

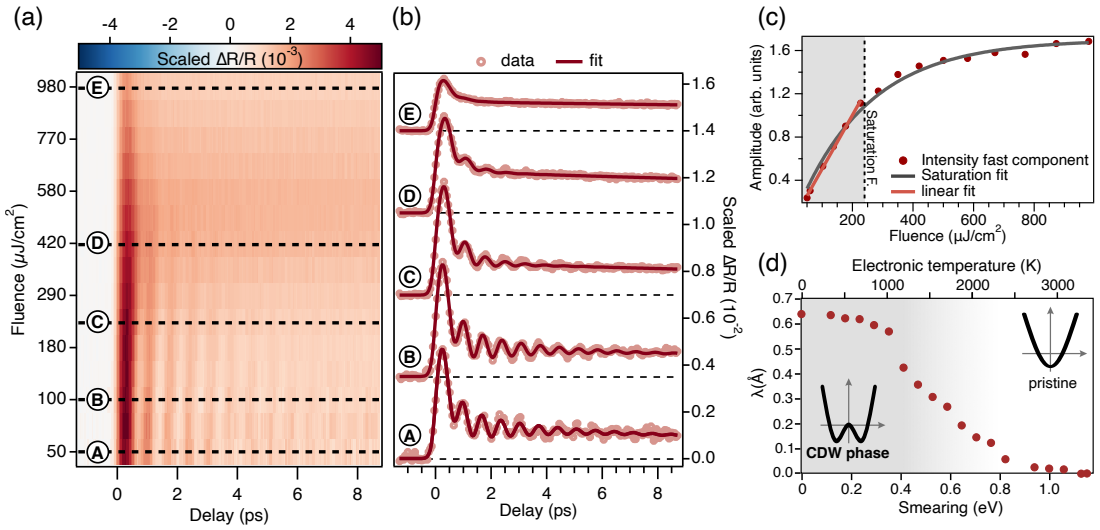

Figure 6.8: (a) Two-dimensional map showing the evolution of the $\Delta R/R$ signal of ScV_6Sn_6 as a function of the incident fluence and of the pump-probe delay. The different profiles have been rescaled to facilitate the comparison between traces whose intensity would otherwise differ by more than one order of magnitude. The measurements have been performed at a base temperature of 30 K and using a probe photon energy of ~ 0.95 eV. (b) Traces extracted from (a) at selected excitation fluences. (c) Evolution of the amplitude (A_1) of the first exponential decay as a function of the absorbed fluence. (d) Norm of the 351-dimensional displacement vector $\mathbf{e} = \mathbf{r}_{\text{non-pristine}} - \mathbf{r}_{\text{pristine}}$, as a function of the gaussian smearing (the values reported on the x-axis represent the FWHM of the Gaussian) applied to the electronic density of states during the constant-volume ionic relaxation. The top axis shows the electronic temperature of the Fermi-Dirac distribution that best approximates the effect of the application of the gaussian smearing. Modified figure based on the published version in Tuniz *et al.* [239].

has been substituted by the fluence dependence. This comparison shows that, while in the low-fluence regime the oscillations of the $\Delta R/R$ signal that arise from the excitation of the AM are well visible, by increasing the fluence they get progressively suppressed, similarly to what happens in the temperature-driven phase transition. Moreover, by increasing the fluence, clear changes are observed also in the incoherent part of the non-equilibrium reflectivity.

As mentioned in the previous section, the first fast component that ends within 1 ps from the arrival of the pump pulse is generally linked to the recombination of the hot carriers through the temperature-dependent CDW gap. Therefore, by studying the fluence dependence of this first fast component, information on the response of the electronic order of the CDW phase can be gained. In particular, in the prototypical quasi-1D systems $K_{0.3}MoO_3$ and $(TaSe_4)_2I$, it has been shown that the absorbed energy density required to optically melt the electronic order is comparable to the energy gain of the system upon entering the CDW state [29, 50]. Specifically, it has been demonstrated that, while in the low perturbation regime the amplitude of the fast component linearly scales with the excitation density, upon approaching the phase transition the signal related to the CDW order shows a saturation, since the maximum induced change is expected to occur at a fluence for which the electronic order is transiently melted. Hence, by studying at which fluence the evolution of the intensity of the fast component deviates from the linear behavior, it is possible to extract the energy density required to melt the electronic order [29, 50]. It is worth noting that if the penetration depth of the probe is larger than the one of the pump, the deviation from the linear trend is expected to occur for the fluence at which the electronic order is melted only in the top layers.

We apply here a similar analysis, comparing the maximum change of the electronic temperature achieved at the saturation fluence with the size of the CDW gap, thus providing additional insights on the role played by the electronic subsystem in the stabilization of the CDW phase.

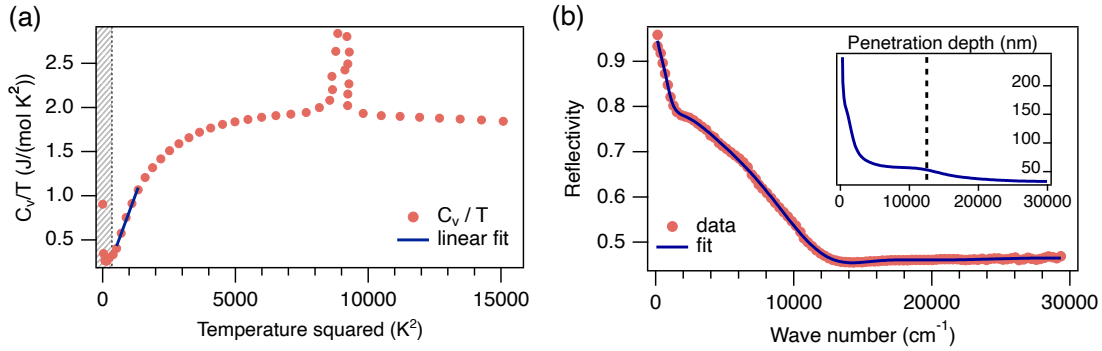

Figure 6.9: (a) Plot of C_v/T against T^2, being C_v the specific heat of ScV_6Sn_6. The linear fit performed in the temperature range $20-35\,\mathrm{K}$ has been used to estimate γ_e. The points at lower temperature were ignored since no clear trend has been detected. Data digitized from [243]. (b) Reflectivity of ScV_6Sn_6 measured at 300 K. The fit superimposed to the data has been obtained using the Drude-Lorentz model. In particular, 1 Drude component and 4 Lorentz oscillators have been used to model the dielectric function of the system. The inset shows the penetration depth of ScV_6Sn_6 obtained starting from the fit of the reflectivity. The vertical dashed line highlights the pump photon energy. Data digitized from [251].

Figure 6.8(c) shows the evolution of the amplitude (A_1) of the first exponential decay, as a function of the incident fluence. This evolution can be qualitatively described by the phenomenological model [29]:

$$A(F) = A_{sat}\left[1-\exp\left(-\frac{F}{F_{sat}}\right)\right], \tag{6.2}$$

where F is the incident fluence, F_{sat} is the saturation fluence and A_{sat} is the maximum amplitude at the saturation [29]. By fitting the evolution of the amplitude of the first exponential decay with this simple model we obtain a saturation fluence of the order of $240\,\mu\mathrm{J/cm^2}$ (highlighted by the dashed line in Fig. 6.8(c)). The linear fit to the data shown in Fig. 6.8(c) highlights that for fluences higher than the saturation fluence the behavior of the system becomes sub-linear. Starting from this value of fluence it is possible provide a rough estimation of the change in the electronic temperature triggered by the absorption of the pump pulse. This estimation requires the knowledge of the optical properties (reflectivity and penetration depth) and of the electronic specific heat of ScV_6Sn_6. Furthermore also the geometrical properties of the beams, like their different dimension at the sample position, and their different penetration depth has to be taken carefully into account. We proceed by analyzing all these contributions separately.

As for VTe_2, the electronic contribution to the specific heat has been assumed to be linear with the temperature, being the system metallic in both CDW and normal phases. To estimate the electronic contribution to the total specific heat we started from the measured specific heat reported in Ref. [243]. Using the Sommerfeld model for the specific heat: $C_v = \gamma_e T + AT^3$ [252], plotting C_v/T against T^2 and extrapolating C_v/T linearly down to $T^2 = 0$, it is possible to estimate the linear coefficient of the electronic specific heat (γ_e). Hence, as shown in Fig. 6.9(a), following this procedure we plotted C_v/T against T^2 and by performing a linear fit in the temperature range $20-35\,\mathrm{K}$ (the points at lower temperature have been ignored since no clear trend has been detected), we obtained $\gamma_e = 7.3\,\mathrm{mJ/(mol\cdot K^2)}$.

The calculation of the electronic temperature requires the knowledge of both reflectivity and penetration depth at the pump photon energy. Being the latter not reported in the literature to the best of our knowledge, we estimate the penetration depth starting from the published

reflectivity data measured at 300 K [251]. Specifically, by considering the relation that links the reflectivity of a material to its dielectric function $\epsilon(\omega)$:

$$R(\omega) = \left| \frac{1 - \sqrt{\epsilon(\omega)}}{1 + \sqrt{\epsilon(\omega)}} \right|^2, \tag{6.3}$$

we fitted the reflectivity of ScV_6Sn_6 using the classical Drude-Lorentz model (Fig. 6.9(b)) [116, 253, 254]. We recall that this model allows to reproduce the dielectric function of a material. In particular, the Drude term is used to describe the low-energy region of the dielectric function, associated to the metallic behavior, while the Lorentz terms are used to reproduce the high-energy part of the dielectric function, associated to interband optical transitions [116]. The fit shown in Fig. 6.9(b) has been obtained using 1 Drude component and 4 Lorentz oscillators.

Therefore, from the fit of the reflectivity it is possible to infer the dielectric function of the material, from which all the optical properties can be calculated. The inset of Fig. 6.9(b) shows the penetration depth (λ) of ScV_6Sn_6 obtained using this approach and considering that $\lambda(\omega) = \alpha^{-1}(\omega) = 1/(4\pi n_2(\omega)\omega)$. For a pump photon energy of 1.55 eV we obtain $\lambda \approx 53$ nm. It is worth noting that even if this value has been obtained starting from the reflectivity measured at 300 K, it can safely be used also in the CDW phase. Indeed it has been shown that only the optical properties below ~ 0.5 eV are affected by the CDW transition (*i.e.* the range affected by the opening of the CDW gap) [48, 251].

The saturation fluence obtained with Eq. (6.2) has been calculated by assuming that the pump power is homogeneously distributed inside a disk having the dimensions given by the FWHM of the pump pulse. However, being both the pump and probe pulses characterized by a Gaussian intensity profile, the spatial dependence of their intensity has to be taken into account to properly estimate the absorbed energy density [255]. Therefore we proceed by calculating the scaling factor that allows to obtain, starting from the homogenous case, the effective fluence in the case in which Gaussian beams are considered [190]. We start by defining the total absorbed mean power P in the homogenous case as:

$$P = p \cdot (\pi F_{pu}^2/4),$$

where F_{pu} is the FWHM of the pump pulse and p is the power density. As a second step we consider a gaussian power distribution, characterized by a power density p', normalized in such a way that the total absorbed mean power P is the same of the homogenous case:

$$p' = p \ln 2 e^{-4 \ln 2 r^2 / F_{pu}^2}, \qquad \text{with: } \int_0^{2\pi} d\theta \int_0^{\infty} dr\, p' = P.$$

Following the same approach we define a Gaussian power distribution for the probe beam (s) normalized in such a way that the total power corresponds to the unitary value:

$$s = \frac{4 \ln 2}{\pi F_{pr}^2} e^{-4 \ln 2 r^2 / F_{pr}^2}, \qquad \text{with: } \int_0^{2\pi} d\theta \int_0^{\infty} dr\, s = 1.$$

Starting from these definitions, the effective power density in the case in which the Gaussian intensity profiles are taken into account can be written as [190]:

$$p_{eff} = \frac{4p(\ln 2)^2}{\pi F_{pr}^2} \int_0^{2\pi} d\theta \int_0^{\infty} dr\, r e^{-4 \ln 2 r^2 (1/F_{pr}^2 + 1/F_{pu}^2)} = p \ln 2 \frac{F_{pu}^2}{F_{pu}^2 + F_{pr}^2}.$$

Therefore the power density ratio with respect to the homogeneous case results:

$$p_{eff}/p = \ln 2 \frac{F_{pu}^2}{F_{pu}^2 + F_{pr}^2}, \tag{6.4}$$

which depends on the relative spot sizes of the pump and the probe beams. With our experimental parameters we obtain $p_{\text{eff}}/p = 0.57$, thus leading to a saturation fluence of $140\,\mu\text{J/cm}^2$.

Finally, in general, in order to properly calculate the absorbed energy density, the different penetration depths of the pump and probe pulses have to be taken into account. However, since the mismatch in the present case is smaller than 10 %, this contribution has been ignored.

From the values of electronic specific heat, reflectivity and penetration depth calculated above, we obtain that at the saturation fluence the increase of the electronic temperature is of the order of $\sim 600\,\text{K}$.

To study the effect of an increased electronic temperature on the CDW phase of ScV_6Sn_6, additional calculations have been performed. In particular, the increased electronic temperature of the system has been approximated by applying a Gaussian smearing to the electronic population [256]. The norm of the displacement vector, *i.e.* the equilibrium position of the atoms, has then been calculated by progressively increasing the value of smearing applied to the electronic occupation. The result of this procedure is shown in Fig. 6.8(d). While for small values of smearing the lattice reconstruction is only weakly affected, when the smearing becomes much larger than the size of the electronic gap ($\Delta_{\text{CDW}} \sim 260\,\text{meV}$ [222]), the lattice reconstruction is gradually suppressed. To establish a connection with the experimental results, the top axis in Fig. 6.8(d) shows the electronic temperature that best approximates the Gaussian smearing applied. This estimation was made by convoluting a pristine Fermi-Dirac distribution (at $T = 0\,\text{K}$) with a Gaussian function, and then by fitting the resulting curve using again a pristine Fermi-Dirac distribution with a free electronic temperature.

It is worth emphasizing that the configuration of the system obtained with this procedure is formally different from the one achieved in the time-resolved experiments. Indeed, although the enhanced electronic temperature is obtained by applying a smearing to the electronic population, since the electrons are not decoupled from the lattice (as it happens immediately after the arrival of the pump pulse), the electronic temperature constitutes the temperature of the entire system. Therefore only a qualitative comparison with the experimental results can be made. Despite this, the DFT simulations reported here can provide useful insights on the effect of an increased temperature on the CDW phase. Indeed, by looking at the values of the electronic temperature reported in the top axis of panel (d), it becomes clear that temperatures much higher than the critical one are required to vanish the lattice distortions and hence to drive the phase transition towards the normal phase. We address this behavior to the fact that in the mean-field treatment here presented, the role played by the lattice fluctuations is completely neglected (discussed in Sec. 2.3). As a consequence of that, the complete phase transition is achieved only at a (electronic) temperature of $\sim 2500\,\text{K}$, *i.e.* almost 30 times higher than the real one.

As discussed above, at the saturation fluence we estimate a maximum increase of the transient electronic temperature of $\sim 600\,\text{K}$. At this temperature, as shown by Fig. 6.8(d), the corresponding smearing of the electronic population is of the same order of the CDW gap, and thus the electronic order is strongly suppressed. The key difference with respect to the simulations is that, on this short timescales, the electrons can be thought as decoupled from the lattice. Hence only the electronic order is quenched, while the lattice reconstruction is weakly perturbed [29, 50, 74]. The elevated electronic temperature persist for less than $\sim 1\,\text{ps}$, after which a common temperature with the lattice, determined by the lattice specific heat, is reached. The equilibrium temperature of the system is lower than the critical one. Indeed, we remind that the saturation fluence extracted from these measurements does not correspond to the energy required to completely drive the transition towards the normal phase, as demonstrated by the clear presence of oscillations arising from the excitation of the amplitude mode, well visible even at higher fluences. The phase transition is reached only when the lattice temperature becomes higher than T_{CDW}. As demonstrated by Fig. 6.8(b), for the case of ScV_6Sn_6 this condition is realized only for excitation fluences that are larger than $1\,\text{mJ/cm}^2$, being the AM still visible for lower fluences. Hence, in agreement with what has been observed in other CDW compounds, the saturation of the amplitude of the

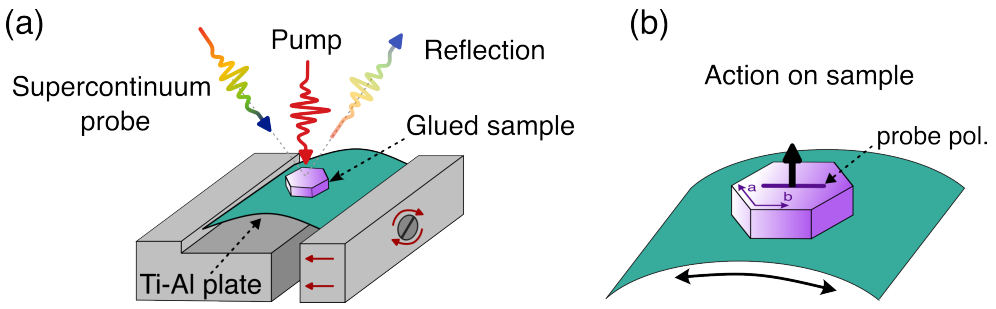

Figure 6.10: (a) Schematics of the strain device. The device consist of two blocks with thin slots to secure the sample plate. One block remains fixed and has a hole with a screw thread, while the other block, which contains the screw, is mechanically activated and is able to deliver strain to the sample plate. Hence the Ti-Al plate mounted in between the two blocks gets squeezed when the two blocks are screwed together. A sketch of the experimental geometry used in the time-resolved reflectivity experiments is also shown. The reflected supercontinuum probe is filtered and detected by an InGaAs photodiode detector. (b) Schematic view of the bending process. Here the hexagon drawn shows the real sample orientation used in the experiments. Hence the measurements have been performed on the plane perpendicular to the *c*-axes, with the probe polarization aligned along one of the in-plane axis. Modified figure based on the preprint version in Tuniz *et al.* [258].

first fast component can be linked to the transient suppression of the electronic order of the system.

At this point it is useful to compare this behavior with the one observed in the sister compound CsV_3Sb_5. Indeed, despite having a similar critical temperature, in CsV_3Sb_5 the charge-ordered phase is melted at a fluence of $\sim 55\,\mu J/cm^2$ [257], demonstrating once again the different origin of the CDW phase in these two kagome compounds. The marked resilience showed by ScV_6Sn_6 upon photoexcitation is in agreement with the scenario of a CDW phase promoted by a strong EPC, in which the transient smearing of the electronic population does not have the dramatic effect observed in the electronically driven CDW phase of CsV_3Sb_5 [9, 257]. The phase transition towards the normal phase proceeds only thanks to the increased lattice fluctuations, therefore a large amount of power has to be delivered to the system to induce the transition.

6.5 STRAIN-INDUCED REDUCTION OF THE AMPLITUDE MODE SOFTENING

The presence of competing lattice instabilities above the critical temperature in ScV_6Sn_6 raises the question of whether a perturbation of the crystal structure could change the balance between the two instabilities or whether it could result in a change of the properties of the dominant charge-ordered state. To investigate this possibility we applied a modest uniaxial strain to the ScV_6Sn_6 crystals while monitoring the effect on the charge-ordered state by means of time-resolved reflectivity experiments.

6.5.1 Characterization of the strain device

Due the sample environment in the cryostat used to perform the reflectivity measurements, a different strain device with respect to the one presented in Ch. 5 has been used. A simple sketch of the device used for the reflectivity experiments is shown in Fig. 6.10(a). This device consists of two parts: a flexible Ti-Al plate (more than 90% Ti and less than 10% Al) and two molybdenum blocks with thin slots to secure the plate. The samples are mounted on top of

the Ti-Al plate by using the same two-component epoxy glue used for the photoemission experiments, which is cured and allowed to cool before the strain is applied. The plate is then mounted in between the two clamps, which can be placed on a standard sample holder or directly on the cold finger of the cryostat. One clamp has a fixed position while the other can be moved mechanically through a screw. Therefore, when the pieces are screwed together a compression is applied to the plate, which bends and delivers the strain to the sample [258]. It is worth noting that, as for the case of VTe_2 the application of the strain was always performed in ambient conditions, with the strain device dismounted from the cryostat.

The main difference with respect to the experiments performed on VTe_2 is that the ScV_6Sn_6 crystals have a strong 3D character, with large forces helding together the different layers. This has resulted in the difficulty to reduce their thickness, being the conventional cleaving techniques (*e.g.* Kapton tape and glued post) mostly ineffective. As a consequence of that, the experiments have been performed on crystals whose thickness was larger than the one of the Ti-Al plate. Therefore in the present case the strain gauges presented in the previous chapter have resulted to be ineffective to quantify the amount of strain transferred to the crystal, since it cannot be assumed that the sample simply bends following the curvature of the plate. Moreover, given the not negligible thickness of the samples, we also expect that the amount of transferred strain can vary at different heights, thus leading to a non-uniform modification of the properties of the crystal. Therefore, to quantify the actual strain transferred to the sample, we rely to x-ray diffraction (XRD) measurements performed by Dr. Federico Mazzola directly on the strained samples. It is worth noting that the XRD measurement have been performed on the same samples and with the same strain device used in the time-resolved reflectivity experiments.

As a final remark, we emphasize that given the large amount of strain transferred to the sample, the Ti-Al plate has been bent beyond the threshold of its elastic deformation. Therefore the strain cannot be discharged by unscrewing the screw that keeps together the two blocks.

6.5.2 Temperature-dependent study of the CDW phase on strained samples

To investigate the effect of the applied strain on the CDW phase we performed time-resolved reflectivity experiments across the phase transition, keeping fixed the excitation fluence and focusing our attention on the evolution of the amplitude mode frequency. The upper panels in Fig. 6.11 show the evolution of the non-equilibrium reflectivity as a function of the temperature (in the temperature range $20 - 120\,K$), for three different strain configurations. These measurements have been performed using an incident fluence of $\sim 170\,\mu J/cm^2$, below the saturation fluence of $\sim 240\,\mu J/cm^2$, thus we reside in the low perturbation regime. To highlight the changes induced by the application of strain on the CDW amplitude mode, in the lower panels of Fig. 6.11 we report the magnitude squared of the Fourier transform (FT) of the coherent part of the $\Delta R/R$ signal, which has been isolated by subtracting a biexponential fit function to the original traces shown in the upper panel. For completeness, to better identify the changes in the non-equilibrium reflectivity induced by the application of strain, in Appendix D we report the traces showing the evolution of the $\Delta R/R$ signal as a function of strain separately.

To quantify the effect of the applied strain on the amplitude mode softening, we fitted the single FT using a Lorentzian function. In particular, to reliably extract the evolution of the peak parameters, and to estimate the corresponding error bars, we evaluated the trend of the χ^2 of the fits while simultaneously changing the width and the position of the Lorentzian peak. To do so, we built a 400×400 grid, corresponding to different pairs of values of width and positions of the Lorentzian peak, and we calculated the resulting χ^2 for every point of the grid (the intensity of the peak has been left free during the fits). The pair of values that minimizes the χ^2 is the one that better describes the FT. The strength of this approach resides however in the possibility to reliably calculate the errors that affect the fitting parameter. Indeed, the

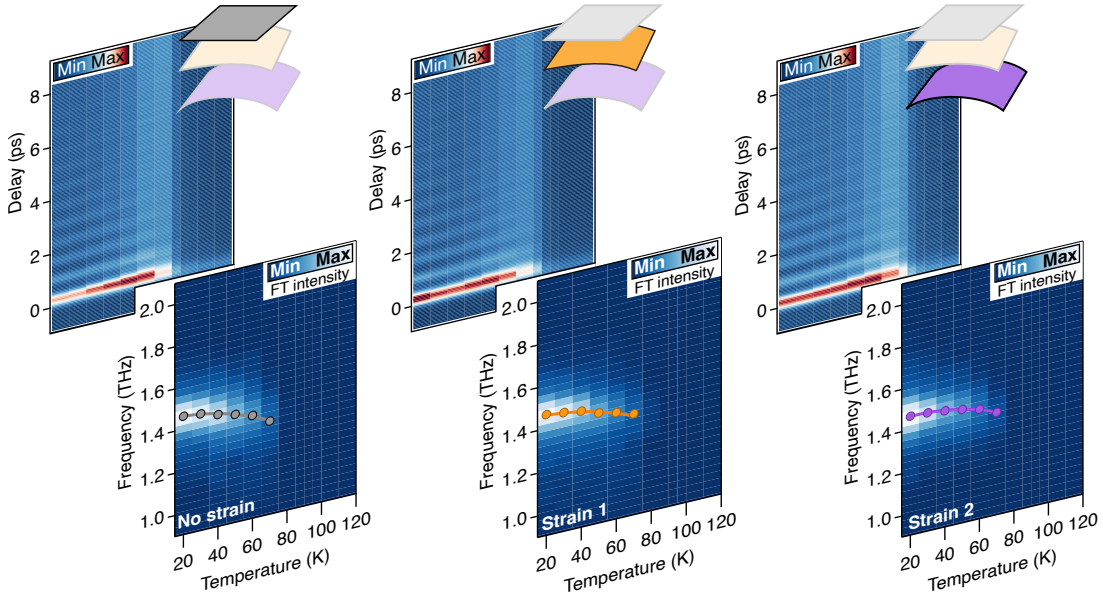

Figure 6.11: The upper panels show the evolution of the $\Delta R/R$ signal as a function of the temperature (x-axis) and of the pump-probe delay, for three different strain configurations. The lower panels show the magnitude squared of the Fourier transform of the coherent part of the $\Delta R/R$ signal extracted from the upper panels. The colored foils depict the bending of the Ti-Al plate, while the colored circles show the central position of the Lorentzian peak used to fit the FT. Modified figure based on the preprint version in Tuniz *et al.* [258].

elliptical region where the χ^2 lays within 10% from its minimum value ($\chi^2/\chi^2_{\text{min}} < 1.10$) allows to calculate the corresponding range of variation in the fitting parameters by simply projecting the ellipse on the x and y-axes (this procedure is shown in Fig. 6.12(c)). Moreover, this procedure allows to take into account the correlation between the different parameters in the calculation of the error bars [202, 203]. Indeed, in general it is possible to infer the correlation between different parameter from the fact that the minimum of the $\chi^2/\chi^2_{\text{min}}$ has a tilted elliptical shape [202, 203]. In the present case, the correlation is weak since the ellipse is only slightly tilted. However, the use of this procedure has been motivated by the fact that the errors provided by the conventional fitting procedure implemented in IGOR Pro were smaller than the size of the circles used in figures and hence unreliable. Finally, we emphasize that this procedure allows to correctly estimate the errors also in the case in which the χ^2 has an asymmetric shape, like the one shown in Fig. 6.12(c). The procedure described here has then been repeated for every temperature and for the three strain configurations. The resulting trends are reported in 6.12(a) and (b).

Figure 6.12(a) shows that the frequency of the amplitude mode is affected by the application of the strain and, unexpectedly, that the magnitude of this effect depends on the temperature of the system. Indeed, while at 20 K no sizable differences are observed for the three strain configurations, upon increasing the temperature towards T_{CDW}, the strain-induced modification of the frequency becomes larger. This results in a reduction of the temperature-dependent softening of the amplitude mode frequency, signaled by the fact that the curvature of the orange and purple traces is reduced with respect to the one of the gray trace (showing the case in which no strain is applied) [258]. Moreover Fig. 6.12(b) shows that the reduction of the amplitude mode softening is accompanied by a temperature-dependent reduction of the width of the Lorentzian peak. This observation is consistent with an increase of the lifetime of the AM. We emphasize that the evolution of the AM frequency and damping have been studied only up to 70 K, because for higher temperatures, due to increased damping of the mode, the frequencies could not be reliably extracted.

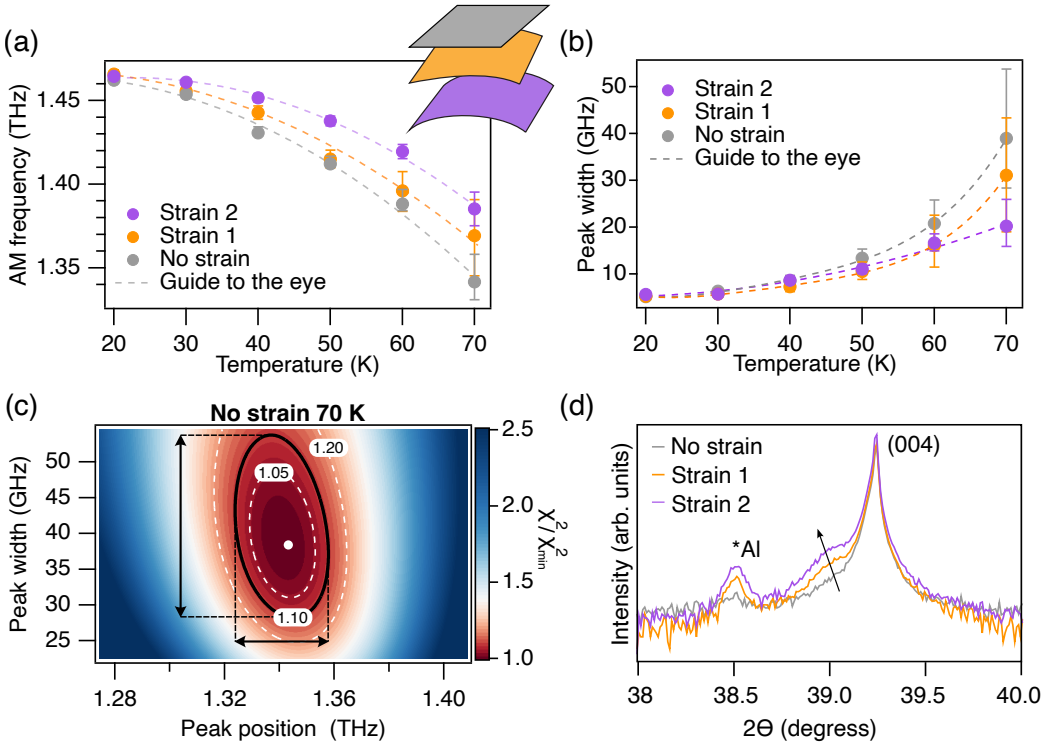

Figure 6.12: (a) Evolution of the AM frequency (*i.e.* position of the Lorentzian peak used in the fit) as a function of the temperature, for three different amounts of strain. The traces correspond to the ones shown in the lower panels of Fig. 6.11. (b) Evolution of the width of the Lorentzian peak used to fit the FT of the coherent part of the $\Delta R/R$ signal. (c) Two-dimensional map showing the evolution of the $\chi^2/\chi^2_{\text{min}}$ as a function of the position and width of the Lorentzian peak. The map shows the results obtained for the measurement performed at 70 K in absence of strain. The frequency and the width values reported in (a) and (b) are the ones that minimize the χ^2, while the error bars have been calculated considering the region where χ^2 lays within 10% from its minimum value ($\chi^2/\chi^2_{\text{min}} = 1.10$). The projection of the black ellipse on the x and y-axis gives the error bars. The contour plots enclosing the regions that lay within 5% and 20% of χ^2_{min} are also shown with dashed white lines. (d) HR-XRD of ScV_6Sn_6 showing that the (004) peak for the unstrained samples is located at $2\theta = 39.2398°$, corresponding to $c \approx 9.1760$ Å. By increasing the amount of strain, an additional peak at smaller 2θ angles appears (indicated by the arrow), indicating a maximum expansion of $0.61 - 0.65\%$ of the c-axis. The * indicates an aluminum spurious peak from the Ti-Al plate. Modified figure based on the preprint version in Tuniz *et al.* [258].

The strain-induced reduction of the AM softening, more pronounced close to T_{CDW} where the CDW order parameter is strongly reduced, could provide the evidence of a strain-induced enhancement of the CDW phase in ScV_6Sn_6. It is worth noting that CDW strain enhancements have also been discussed recently for other systems, such as $TbTe_3$ [259], although these enhancements have a different origin from the one observed in ScV_6Sn_6. This highlights a timely effort in the external control of emerging electronic orders by strain application.

To clarify the effect of our straining procedure on the crystal structure of ScV_6Sn_6, we performed high-resolution x-ray diffraction (HR-XRD) measurements (shown in Fig. 6.12(d)). These experiments were performed using a Malvern Empyrean PANalytical instrument with monochromatized Cu Kα_1 radiation ($\lambda = 1.54056$ Å) and a double-bounce Ge (220) crystal at the diffracted beam. In the experimental configuration used only the (004) Brag peak was visible and hence investigated. On the unstrained sample this peak is found at $2\theta = 39.2398°$, corresponding to $c \approx 9.1760$ Å, in agreement with previous measurements [251]. By applying a tensile strain to the sample, an additional peak appears at lower 2θ angles alongside the

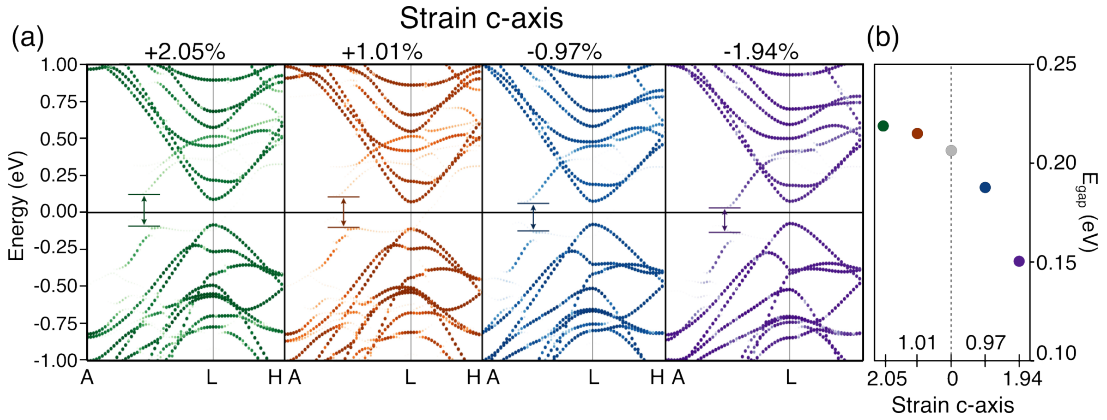

Figure 6.13: (a) Electronic band structure computed along the A-L-H direction in the CDW phase of ScV_6Sn_6, for different amounts of applied strain (expressed in percentage of the *c*-axis). The changes in the gap size are highlighted by the double-sided arrows. (b) Evolution of the size of the gap opened by the CDW, computed at the midway between the A and L high-symmetry points, as a function of the relative change in the length of the *c*-axis. DFT calculations were performed using the VASP package [262, 263] and employing the projector augmented wave (PAW) method [264]. We refer to [258] for further details on the DFT calculations. Modified figure based on the preprint version in Tuniz *et al.* [258].

preexisting (004) peak (Fig. 6.11(c)). The appearance of this second peak at lower angles signals an increase of the *c* lattice parameter to $9.2326 - 9.2359$ Å, indicating a maximum expansion ranging between $0.61 - 0.65\%$. The fact that we do not observe a shift of the whole Bragg peak, but instead we detect the appearance of multiple diffractions peaks, originates from the presence of regions of the crystal with a different length of the *c* lattice parameter [260, 261], hence signaling the presence of a non-uniform strain on the sample. As further corroborated by the DFT calculations shown in the following, since the reflectivity measurements are able to resolve a change in the AM frequency, and the penetration depth of the near infrared probe is much smaller that the one of the X-Ray beam, we speculate that the increase of the *c*-axis is largest at the top surface while it is negligible at the base of the crystal. Therefore the estimation given for the increase of the *c* axis can be thought as an average modification in the near-surface region.

6.5.3 DFT calculations performed on strained ScV_6Sn_6 crystals

To better understand the origin of the strain-induced reduction of the AM softening, extensive DFT calculations have been performed [258]. Ionic relaxations were performed under constant volume conditions, while uniaxial strain was imposed by adjusting the lattice parameters. Specifically, the *a*-axis of the CDW supercell was modified and consequently, given the imposed conservation of the volume, the length of the *c*-axis has been adjusted. However, since the CDW reconstruction mainly involves the movement of the atoms along the out-of-plane direction ($\lambda_z/\lambda \sim 0.75$, with λ being the polarization length), we expect that the change of the length of the *c*-axis is the quantity responsible for the main changes of the CDW properties. Therefore in the following we will consider only the changes in the c-axis, allowing in this way to establish a link with the experimental results. We stress the point that, given the three-dimensional structure of the samples, we rely entirely on the XRD measurements to identify the changes in the unit cell induced by the application of strain.

Figure 6.13(a) shows the calculated band structure in the CDW phase of ScV_6Sn_6 for four strain configurations. This comparison highlights that the energy gap, and thus the CDW phase, are strongly affected by the application of strain. To better quantify these changes, in panel (b) we report the evolution of the CDW gap, computed at the midway between the A

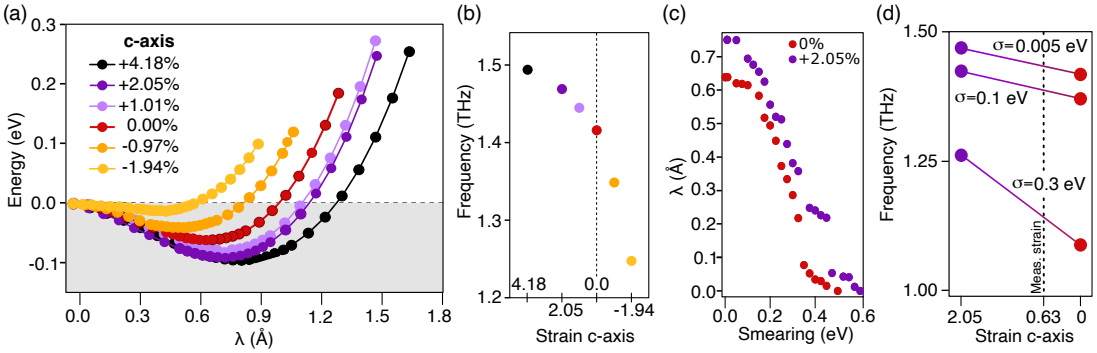

Figure 6.14: (a) Total energy of ScV_6Sn_6 as a function of the polarization length λ. The reported c-axis strain values, for the other panels as well, correspond to the percentage variation of the c-axis of the CDW supercell. All the calculations in this panel have been performed with a smearing $\sigma = 0.005$ meV. (b) Frequency values computed from a quadratic interpolation around the minimum of the total energy contours shown in (a). The same trend found in Fig. 6.13(b) is obtained. (c) Polarization length λ as a function of the electronic smearing σ, for two strain configurations of the c-axis. (d) Amplitude mode frequency as a function of the uniaxial strain, for different smearing values. The destabilized CDW structures (large smearing) show more pronounced frequency variations when strain is applied. The vertical dashed line highlights the maximum strain applied in the experiments. Modified figure based on the preprint version in Tuniz *et al.* [258].

and L high-symmetry points, as a function of the relative change in the length of the c-axis. This graph shows that in the zero-temperature limit, a compression of the c-axis entails a strong reduction of the gap size, while an elongation leads to an increase of the gap size with respect to the pristine material. We can naively interpret this result considering that the CDW phase is characterized by the large out-of-plane movement of the Sc and Sn atoms, thus an increase of the c-axis length would favor their displacements, leading to an enhancement of the CDW order and thus of the CDW gap.

The results reported here suggest the possibility to enhance the CDW phase by applying a positive strain to the c-axis. Therefore to check if this change in the gap size affects the AM frequency, we performed additional calculations. Specifically, we followed the procedures already introduced in Sec. 6.3, and by fitting a quadratic function around the minimum of the Born-Oppenheimer potential corresponding to the CDW phase, we calculated the frequency of the AM for different strain configurations. Fig. 6.14(a) shows the total energy of the system as a function of the polarization length λ (we remind that $\lambda = \left\|\mathbf{r}_{\text{non-pristine}} - \mathbf{r}_{\text{pristine}}\right\|$), for different strain configurations. As observed for the CDW gap, for an elongation of the c-axis the point of minimum energy (for which $\mathbf{r}_{\text{non-pristine}} = \mathbf{r}_{\text{CDW}}$) shift towards larger polarization lengths, indicating a larger lattice reconstruction. We also note that the energy difference between the pristine and the CDW phase depends on the value of the applied strain. In particular, the energy difference is increased for the case in which an elongation of the c-axis is applied (the minimum for the black curve in Fig. 6.14(a) is deeper than the one of the other traces). As a result, the frequency values computed from a quadratic interpolation around the energy minimum reveal a dependence on the applied strain. Figure 6.14(b) shows that the frequency of the AM is enhanced for the case in which the length of the c-axis is increased, revealing a trend similar to the one observed for the CDW gap.

We emphasize that although the DFT simulations discussed up to now go in the correct direction, *i.e.* an increase of the length of the c-axis leads to an enhancement of the CDW phase, these results have been obtained at a single temperature and predict an increase of the AM frequency in the zero temperature limit, that cannot be resolved in our measurements. This difference may arise from the fact that the values of applied strain achieved in the experiments are much smaller than the ones used in the DFT calculations, and thus the

increase of the AM frequency is expected to be strongly reduced. However, our experiments reveal that the effect of the applied strain is larger close to the transition temperature, where the CDW is strongly perturbed. Therefore, to investigate the origin of the reduction of the temperature-dependent softening of the AM frequency, we performed additional calculations. Specifically, following the procedure introduced in Sec. 6.4, we applied a Gaussian smearing to the electronic population with the aim of destabilizing the CDW phase and thus to simulate the effect of an increased temperature.

As discussed in Sec. 6.4, increased values of smearing tend progressively to destabilize the CDW phase, up to the point where the order is melted. Figure 6.14(c) shows the evolution of the polarization length as a function of the electronic smearing for the pristine sample and for the case in which an elongation of the *c*-axis is imposed. This comparison shows that the polarization length for the strained configuration is always larger than the one of the pristine material. As a consequence of that, larger values of smearing are required to completely melt the charge-oder phase in ScV_6Sn_6. This result confirms that also at high temperature the applied strain has the effect of stabilizing the charge-ordered phase. It is worth noting that, here the increased electronic temperature is used only to destabilize the CDW order. As discussed in Sec. 6.4, in the case in which the lattice fluctuations are not considered, much higher temperatures need to be employed to perturb the CDW phase. Hence no direct comparison can be made between the measured temperature and the one used in the calculations.

Additionally, to elucidate the relation between the applied strain and the renormalization of the amplitude mode frequency, in Fig. 6.14(d) we report the evolution of the amplitude mode frequency as a function of the applied strain, for different smearing conditions. Notably, strained CDW phases, when destabilized by large smearing values, exhibit a weaker phonon softening with respect to the unstrained case, in qualitative agreement with the results of our time-resolved reflectivity experiments.

In conclusion, these calculations show that the reduction of the phonon softening results in a marked variation of the AM frequency close to the critical temperature, confirming the possibility to reveal a strain-induced change not detectable at the lowest temperatures. Despite the qualitative agreement between our calculations and experimental data, it is worth noting that the reduction of the AM softening could also arise from alternative scenarios. Indeed in a recent work by Warawa *et al.* [105], it was shown that the reduction of the coupling strength between the phonon modes located at $2k_F$ and the electronic order, could give rise to a change in the frequency of the modes similar to the one observed in our experiments. Alternatively, a change in the temperature dependence of the CDW gap, and not simply on its low-temperature size, could also reproduce our experimental findings. These alternative scenarios require additional calculations to test their applicability to the specific case of ScV_6Sn_6. Hence, further calculations will be performed in the next months.

6.6 CONCLUSIONS

In this chapter we reported a detailed study of the non-equilibrium reflectivity in the kagome compound ScV_6Sn_6. In particular, the low-temperature measurements have revealed the presence of a phonon mode well visible in all the spectral range accessible through our supercontinuum probe. By performing a systematic temperature dependent study across the phase transition, we unveiled the presence of a mean-field like softening of the phonon mode frequency, accompanied by a marked increase of its damping which results in the complete disappearance of the mode at the phase transition. With the aid of DFT calculations, we demonstrated that this mode corresponds to the CDW amplitude mode of the system.

By performing a fluence-dependent study we demonstrated that this system is resilient upon photoexcitation with a near-infrared light pulse. The origin of this behavior is attributable to the fact that the phase transition towards the normal phase proceeds only thanks to the

increased lattice fluctuations, therefore a large amount of power has to be delivered to the system. This observation is corroborated by additional DFT simulations, showing that in the case in which the lattice fluctuations are not taken into account, much higher temperatures are required to drive the phase transition. This result highlights the prominent role played by the lattice fluctuations in the determination of the transition temperature in ScV_6Sn_6. Moreover, studying the evolution of the amplitude of the first fast exponential decay as a function of the excitation fluence, we showed that the fluence for which this behavior deviates from a linear trend corresponds to the one for which the electronic order is quenched. In particular, we demonstrated that, at the saturation fluence the smearing of the electronic population, induced by the transient increase of the electronic temperature, is of the same order of the CDW gap, suggesting that at this fluence the electronic order is transiently quenched. To completely melt the CDW phase, fluences larger than $1\,mJ/cm^2$ need to be used. These results are in strong contrast with the ones obtained in the sister compound CsV_3Sb_5, and support the scenario of a CDW phase driven by a peak in the wavevector-dependent EPC.

Finally, by applying a tensile strain to the ScV_6Sn_6 crystals, we demonstrated that an elongation of the *c*-axis leads to a reduction of the temperature-dependent softening of the CDW amplitude mode. DFT simulations show that this reduction of the amplitude mode softening arises from an enhancement of the CDW phase, that in the strained configuration is characterized by a larger electronic gap and a larger lattice reconstruction. Moreover, additional DFT calculations demonstrate that a compression of the *c*-axis leads to the opposite scenario, suppressing the low-temperature CDW. With these experiments we therefore propose an effective way to tune and control the CDW phase in ScV_6Sn_6 by means of the applied strain. To conclude, we remember that the charge order in this compound arises from the competition between different instabilities, hence the use of external stimuli to destabilize the low-temperature phase could provide additional information on the stabilization mechanism and might even allow to switch to another ground state, as it has been demonstrated on other CDW compounds [259]. This possibility will be investigated in the near future.

7 CONCLUSIONS

Charge-density-wave systems, in which electrons and phonons cooperatively interact to form a new symmetry-broken state, stand as ideal candidates to study the mechanisms governing the melting of a macroscopically ordered phase. Furthermore, given their sensitivity to external stimuli, CDW materials constitute a promising platform to investigate the possibility of controlling their properties. Particularly interesting, although little explored, is the case in which the CDW phase transition is driven by the presence of a strong momentum dependent EPC, since it can lead to significant modifications of the properties of these compounds.

This thesis has been devoted to the study of the out-of-equilibrium dynamics of two strongly-coupled charge-density-wave systems: the transition-metal dichalcogenide compound VTe_2 and the kagome compound ScV_6Sn_6. The non-equilibrium dynamics of these compounds have been investigated by combining time-resolved reflectivity and TR-ARPES experiments, thus allowing to study both the collective excitations of the CDW ground state and the perturbation of the electronic order triggered by a strong optical perturbation.

The first system investigated has been the TMDC compound VTe_2, in which the strong EPC results in a large lattice reconstruction that takes place below 480 K. Given the presence of a charge-ordered phase stable up to high temperatures, as a starting point we studied the low-energy excitations of the CDW phase. Time-resolved reflectivity measurements performed on this compound have revealed that the low-temperature response is dominated by the presence of two coherent phonon modes. Thanks to systematic temperature-dependent measurements, we unveiled the presence of a mean-field like softening of the frequency of both phonon modes, taking place when the temperature of the system is risen towards the CDW critical temperature. This observation, complemented by additional DFT calculations, has allowed to identify the two phonon modes as the amplitude modes of the system. The observation of two AMs, simultaneously linked to the same electronic order parameter, has motivated the study of their possible mutual coupling. This study has required the implementation of a new double-pulse excitation scheme, which has been specifically designed for these measurements. Indeed, by using a double-pump excitation it has been possible to study the indirect effect of the enhancement or suppression of one AM with respect to the other one. Interestingly, these experiments have shown that the two AMs can be independently modulated, thus demonstrating that despite being coupled to the same order parameter, the two modes are independent.

Given the high critical temperature of the CDW phase in VTe_2, the investigation of the non-equilibrium properties of this compound has been carried out only in its low-temperature phase. We showed that the excitation fluences required to drive the phase transition towards the normal phase, starting from a base temperature of 300 K, exceed the damage threshold of the material. Indeed, we demonstrated that high excitation fluences cause the segregation of Te atoms at the surface, with the gradual formation of an at least partially crystalline phase. The presence of this segregated phase has therefore overshadowed the response of the pristine VTe_2 crystals, hindering the investigation of the photoinduced phase transition.

To study the effect of a strong optical perturbation on the electronic order of the CDW ground state of VTe_2, we performed TR-ARPES experiments. Such experiments have required the use of the state-of-the-art HHG source available at the T-ReX laboratory, since it allows to study the electron dynamics up to the edges of the first BZ while keeping an excellent balance between energy and time resolutions. Given the presence of multiple CDW domains in the low temperature phase of VTe_2, these experiments have required the development

of a strain device aimed to promote the formation of larger domains. The measurements performed on a single CDW domain have allowed to unambiguously study the evolution of the CDW gap dynamics triggered by a strong optical perturbation. This study has revealed that the dynamics of the CDW gap is not dominated by the excitation of the CDW amplitude modes, but is rather determined by an incoherent process that evolves on a longer timescale. Starting from this observation, we linked the quench of the electronic order to the partial loss of the CDW long-range order triggered by the pump pulse. To do so, using the evolution of the electronic temperature as a starting point, we implemented a three-temperature model which has allowed to demonstrate that the dynamics over which the CDW evolves follows the population of a subset of strongly-coupled optical phonon modes. The excitation of these strongly coupled modes, with no macroscopic phase coherence, results in a loss of the long-range CDW order of the system, with the consequent quench of the electronic order parameter. These experiments therefore suggest the presence of a light-induced order-disorder transition in VTe_2, similarly to what has been observed in VO_2 [21, 199].

The second system investigated was the kagome compound ScV_6Sn_6, in which the peculiar lattice structure gives naturally rise to electron localization and to electronic instabilities, which coexist together with competing lattice instabilities in the normal phase of this compound. To shed light on these competing instabilities, we investigated the out-of-equilibrium response of ScV_6Sn_6 by performing time-resolved reflectivity experiments across the CDW phase transition. The lower critical temperature with respect to VTe_2 has allowed to study both the low- and high-temperature non-equilibrium dynamics of this compound. These experiments, with the aid of extensive DFT calculations, have allowed to identify the CDW amplitude mode of the system. Moreover, by performing a fluence-dependent study, we showed that at the fluence for which the amplitude of the first fast component of the non-equilibrium reflectivity saturates, the smearing of the electronic occupation induced by the increased electronic temperature is of the same order of the CDW gap, suggesting that at this fluence the electronic order is transiently quenched. The comparison with DFT simulations has also allowed to highlight the prominent role played by the lattice fluctuations in determining the critical temperature of this compound. Indeed, in a mean-field treatment, where fluctuation effects are neglected, much higher temperatures are required to drive the phase transition. Furthermore we showed that, in contrast to what happens in the sister compound CsV_3Sb_5, high excitation fluences ($> 1\,mJ/cm^2$) are required to completely melt the CDW phase. This result demonstrates that ScV_6Sn_6 is resilient upon excitation with a near infrared light pulse, thus supporting the scenario of a CDW phase driven by a strong EPC, where a smearing of the electronic population has a limited effect on the charge-ordered phase. The phase transition towards the normal phase proceeds only thanks to the increased lattice fluctuations, therefore a high amount of power has to be delivered to the system to induce the transition.

Finally, by applying a strain to the ScV_6Sn_6 crystals, we demonstrated that an elongation of the *c*-axis leads to a reduction of the temperature-dependent softening of the CDW amplitude mode. DFT simulations show that this reduction of the mode softening arises from an enhancement of the CDW phase, that in the strained crystals is characterized by larger lattice displacements and by a larger energy gap. Additional DFT calculations also show that a compression of the *c*-axis produces instead the opposite result, hence leading to a suppression of the CDW phase. With these experiments we therefore propose an effective way to tune and control the CDW phase in ScV_6Sn_6 by means of strain application.

The results reported in this thesis show that for both VTe_2 and ScV_6Sn_6, the behavior of the low-energy excitations of the CDW ground state is aligned with the one observed in conventional quasi one-dimensional systems. Indeed, in both cases a mean-field like softening of the CDW amplitude modes has been observed together with an exponential decrease of their lifetime, which results in their disappearance in proximity of the phase transition.

Instead, the presence of a strong EPC affects more strongly the properties of these compounds in proximity of the phase transition. The ARPES experiments performed on VTe_2 show that the quench of the electronic order can be explained by considering the incoherent excitation of a subset of strongly coupled optical phonons, which determine a loss of the long order of the system. It is worth emphasizing that the presence of a CDW phase deriving from strong EPC is key in determining the dynamics observed. Indeed, the presence of a large energy gap (also with respect to the critical temperature) makes the electronic entropy unimportant, thus making visible the role played by the enhanced lattice fluctuations. The fact that the phase transition could be driven by non-CDW phonons that interact with the CDW ground state, requires additional theoretical calculations that will be carried out in the next months. The physical picture here proposed goes beyond the specific case of VTe_2, and stands as a possible scenario to explain the light-induced phase transition in the strongly-coupled CDW systems.

Although for the case of ScV_6Sn_6 the evolution of the electronic order has not been directly studied, the fluence-dependent time-resolved reflectivity experiments performed have revealed a marked resilience of the system upon photoexcitation, attributable to the fact that the phase transition towards the normal phase proceeds only thanks to the increased lattice fluctuations, in agreement with what has been observed in VTe_2. The possibility to perform TR-ARPES experiments on ScV_6Sn_6 crystals will be investigated in the next months. These experiments will be aimed to study the quench of the CDW gap triggered by the absorption of the pump pulse, carefully examining the timescale over which this process evolves.

In conclusion, by studying the non-equilibrium dynamics of two strongly-coupled CDW materials, we showed that the presence of a strong EPC determines the nature of the thermal disordering in these compounds. The photoinduced phase transition arises thanks to the increased lattice fluctuations, hence its understanding requires to carefully take into account the electron-phonon and phonon-phonon interactions. Moreover, the energy flow from the excited electrons to the phonons sets the time required to achieve the photoinduced phase transition. As a consequence of this bottleneck, the transition proceeds on longer timescales with respect to purely electronic phenomena [149].

Generalizing these results to a broader view, CDW systems have been proposed as candidates for the realization of resistive phase change memories [265, 266]. The results reported in this thesis show that devices based on strongly-coupled CDW materials are expected to be less efficient both in terms of switching energy and speed with respect to CDW systems with reduced electron-phonon and phonon-phonon interactions. Specifically, the minimization of the phonon-phonon coupling appears to be an essential ingredient for the realization of switchable CDW devices.

A CDW GAP DYNAMICS ON UNSTRAINED VTe_2 SAMPLES

This appendix is devoted to the presentation of the ARPES and TR-ARPES experiments performed on unstrained VTe_2 samples. In particular, after having discussed the electron dynamics extracted from unstrained VTe_2 crystals, we report a comparison with the dynamics extracted from strained compounds. The appendix ends with a comparison between the dispersion of the vanadium band extracted from strained and from pristine VTe_2 samples.

The measurements reported in the following have been performed with the HHG setup presented in Sec. 3.5. Contrarily to the measurements presented in Ch. 5 however, a grating with an higher density of grooves (gr) has been employed to separate the different harmonics. Specifically, a grating with 400 gr/mm was used, thus resulting in a larger angular separation between the different harmonics but also in a larger pulse-front tilt, with the consequent elongation of the probe pulses. The time resolution of the setup with this configuration turns out to be $\sim$ 170 fs. Except for this difference, the other parameters of the experiment have remained unchanged, thus the measurements have been performed using a probe photon energy of 21.6 eV and a pump photon energy of 1.77 eV.

Analysis of the photoemission intensity in the TR-ARPES experiments

Figure A.1(a) shows a photoemission spectrum acquired along the K-M_2-K direction on a unstrained VTe_2 sample, where the size of the domains is comparable with the size of our HHG probe beam. This image allows to resolve the superposition between V-shaped band coming from the M_1 and the nearly-flat band coming from the M_2 points. To facilitate the distinction between the two, their dispersion is highlighted by the red (M_1) and blue (M_2) dashed lines, obtained by fitting respectively the evolution of the MDCs and the EDCs. This superposition between bands coming from different high-symmetry points of the BZ is clearly resolved also in the TR-ARPES experiments. Figure A.1(b) shows a differential ARPES map, highlighting the changes in the photoemission intensity induced by the arrival of the pump pulse. From this image, both the depletion of the nearly-flat band coming from the M_2 point and of the V-shaped band coming from the M_1 point are resolved. However, being the relaxation dynamics of the V-shaped band faster than the one of the CDW gap, for larger pump-probe delays the differential ARPES maps tend to become more similar to the ones acquired on strained samples, where only the M_2 point is visible. This effect is shown in Fig. A.1(c), which shows a differential map acquired at a pump-probe delay in which the population of the V-shaped band has been partially recovered, while the closure of the CDW has just reached its maximum. Therefore the dynamics extracted by simply studying the evolution of the photoemission intensity in specific regions of the reciprocal space, arise from a superposition of the ones coming from the M_1 and M_2 points. The relative weights of the two depend on the portion of domains illuminated by the probe beam, and thus vary by changing the position of the beam on the sample.

Figure A.1(d) shows the evolution of the dEDCs integrated in the momentum region delimited by the dashed lines shown in (b), as a function of the pump-probe delay. The depletion of the V-shaped band coming from the M_1 point here results in the reduction of the photoemission intensity (blue region) visible just below the Fermi level, immediately after the arrival of the pump pulse. To quantify this effect on the population dynamics, in Fig. A.1(e) we report the traces obtained by integrating the photoemission intensity from

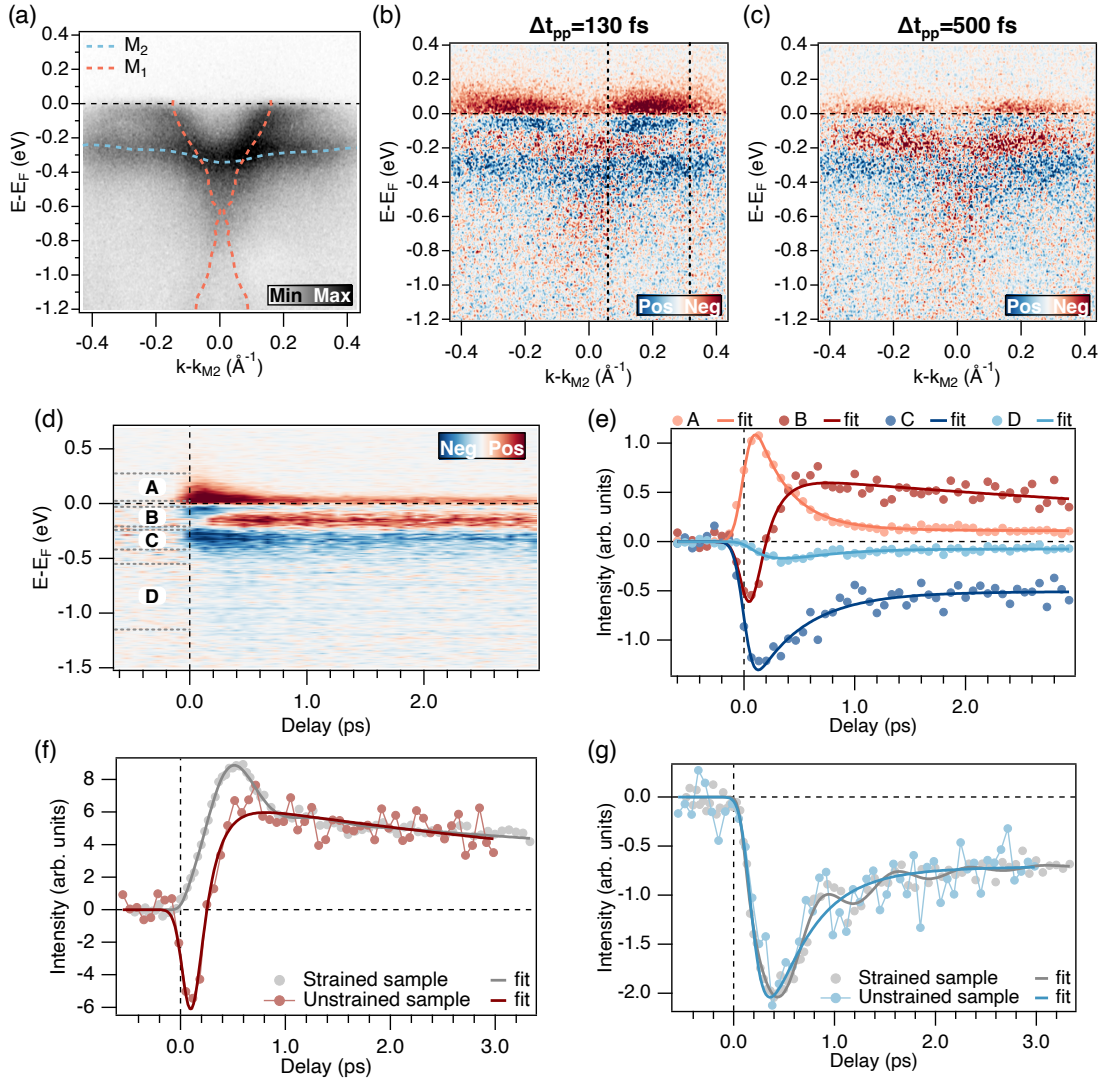

Figure A.1: (a) ARPES map acquired along the K-M_2-K direction on an unstrained sample. The dashed lines show the dispersion of the bands coming from the M_1 (red) and M_2 (blue) points extracted from the fits of the EDCs and the MDCs. The measurement was performed at a base temperature of ~ 120 K. (b) and (c) Differential ARPES maps highlighting the changes in the photoemission intensity induced by the pump pulse. The measurements have been performed at a base temperature of ~ 120 K and using an absorbed fluence of $430\,\mu J/cm^2$. (d) Evolution of the dEDCS extracted by integrating the photoemission intensity from the momentum region delimited by the vertical dashed lines in (b). The measurements have been performed at a base temperature of ~ 120 K and using an absorbed fluence of $600\,\mu J/cm^2$. (e) Evolution of the photoemission intensity extracted from the boxes reported in (d). (f) Comparison between trace B of panel (e) and the equivalent one extracted from a strained sample. (g) Comparison between trace D of panel (e) and the equivalent one extracted from a strained sample. The traces have been normalized to a common intensity in order to facilitate their comparison.

the boxes drawn in (b). In particular, trace B shows the evolution of the photoemission intensity inside the CDW gap. The depletion of the V-shaped band, that overlaps to the CDW gap, causes the negative peak observed immediately after the arrival of the pump pulse. This negative contribution is then overcome by the increase of the intensity arising from the partial closure of the CDW gap. As a consequence of the concomitant presence of these two phenomena, trace B reaches its maximum positive value at a pump-probe delay of ~ 750 fs.

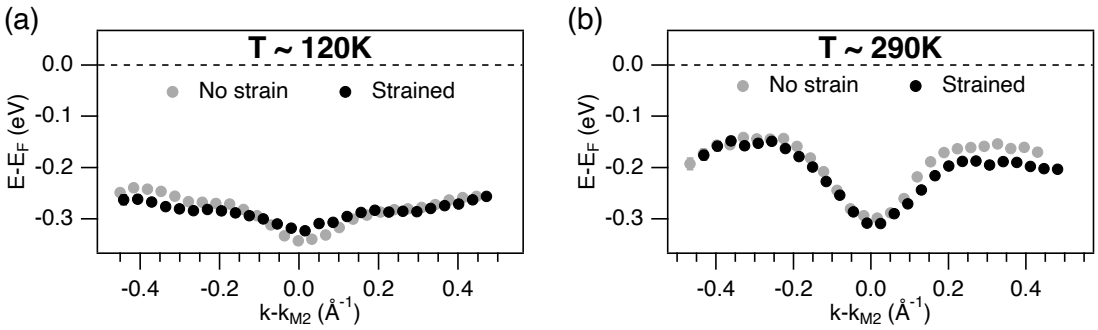

Figure A.2: (a) Comparison between the dispersion of the vanadium band extracted from a strained and a pristine samples at a temperature of 120 K. (b) Comparison between the dispersion of the vanadium band extracted from strained and a pristine samples at a temperature of 290 K. The circles in the two images denote the central position of the Lorentzian peak used to model the photoemission intensity. The error bars estimated by our fitting procedure are smaller than the size of the circles used to mark the dispersion of the band, thus suggesting an underestimation of the errors.

We remind that in the case of strained samples, where only the nearly-flat band coming from the M_2 is resolved, the maximum increase of the photoemission intensity inside the CDW gap is achieved at a pump-probe delay of ~ 500 fs. For clarity we report a comparison between these two traces in panel (f). Despite the differences observed immediately after the arrival of the pump pulse, and attributable to the depletion of V-shaped band, after ~ 1 ps (*i.e.* when the hot carrier recombination process is almost ended) the two become very similar evolve on equivalent timescales. This first comparison therefore suggests that the non-equilibrium dynamics are not affected by the application of strain. To further corroborate this observation, it is useful to consider the photoinduced changes at the states located at higher binding energies. Indeed, as discussed in Ch. 5, the changes observed between 0.5 and 1 eV below the Fermi level, are attributable to the change in the lattice symmetry triggered by the pump pulse. Moreover, the dynamics of these states are less affected by the superposition of multiple domains since the contributions coming from the M_1 are less pronounced. Figure A.1(g) shows a comparison between the evolution of the photoemission intensity extracted from box D and the one extracted from the equivalent energy range in a strained sample. This comparison shows that the dynamics in the two case are completely equivalent thus confirming that the non-equilibrium response of the VTe_2 crystals is not affected by the application of strain. As a final remark, it is worth noting that the fact that the two traces have been fitted with a different function is motivated only by their different statistics. Indeed, the higher statistics of the gray trace has allowed to resolve small damped oscillations linked to the excitation of the AM, therefore a damped cosine has been included to the fit function. In the blue trace these oscillations are completely overshadowed by the noise of the measurement (the amplitude of the oscillation in the gray trace is smaller than the fluctuations of the blue one), and therefore the cosine term has not been included.

Effect of the applied strain on the band dispersion at the M_2 point

Figure A.2(a) shows a comparison between the low-temperature dispersion of the vanadium band, at the M_2 point, extracted from a pristine and a strained VTe_2 samples. To reconstruct the dispersion of the band, the procedure described in Sec. 5.3 has been followed. Therefore the circles reported in figure show the position of the Lorentzian peak used to model the vanadium band. This comparison confirms the band dispersion is not alternated by the application of strain. The differences between the two curves are likely to arise from the fact that the measurements have been performed on different sample that have therefore also a slightly different orientation with respect to the slit of the analyzer. Figure A.2(b) shows the

same comparison but for a temperature of $\sim 290\,K$, at which the strength of the CDW order is reduced. Also in this case only minor differences are resolved, confirming that robustness of the CDW phase is not affected by the application of strain.

Conclusions

In this appendix we reported the results of the TR-ARPES experiments performed on unstrained VTe_2 crystals. These measurements have demonstrated that the superposition of multiple domains can be clearly resolved in both the equilibrium band structure and in the non-equilibrium dynamics. Furthermore, by comparing the non-equilibrium relaxation dynamics extracted from unstrained compounds with the ones extracted from strained samples, it has been demonstrated that these dynamics are not affected by the application of strain. This result, together with the fact that also the band dispersion appears to be unaffected by the application of this amount of strain, confirms that the only effect of the applied strain on the VTe_2 crystals is of promoting the formation of larger domains.

B CDW GAP DYNAMICS IN VTe_2 PROBED WITH A 10.8 eV PHOTON SOURCE

This appendix is devoted to the presentation of the TR-ARPES experiments performed on VTe_2 with the 10.8 eV photon source developed at the T-ReX laboratory [61, 88]. After having introduced the main aspects of this experimental setup, the dynamics of the CDW gap is analyzed and compared to the one obtained using the HHG source and presented in Ch. 5.

The 10.8 eV photon source at the T-ReX laboratory

The 10.8 eV photons are obtained thanks to the generation of the ninth harmonic of the fundamental beam produced by a Yb-fiber based laser source. Specifically, the system is seeded by the Coherent MONACO 1035 which delivers at a repetition rate of 1 MHz a power of 40 W. The pulse duration at the output of the laser is 290 fs. The beam that arrives at the optical table is split in two paths (pump and probe), exploiting a combination of $\lambda/2$ and polarizing beam splitter, which allows therefore also to change the ratio between the two.

The reflected part of the beam is focused into two consequent BBO crystals, generating the second and the third harmonic (fundamental + second harmonic) of the fundamental beam. The third harmonic is then focused by a lens of +100 mm into a gas cell filled with xenon, where, exploiting a third order process, the ninth harmonic of the fundamental at 10.8 eV is generated. The lower order harmonics are filtered out before arriving at the Xe cell by reflection on dichroic mirrors. After the generation, since the 10.8 eV is absorbed by air, the beam is handled in vacuum environment (with the vacuum level at least as good as 10^{-3} mbar). The generation cell is separated from the refocusing chamber by a LiF_2 wedge window (with 5° apex angle) which acts as a dispersive prism, and allows to separate the third from the ninth harmonic. The separation is sufficient to deflect from the beam path almost all the third harmonic which impinges on a beam block. The ninth harmonic is collected by a spherical mirror (250 mm curvature radius), which allows focusing the beam at the sample position. Before entering in the chamber the beam is reflect on a motorized plane mirror which allows to adjust the pointing of the ninth harmonic at the sample position. Finally, a MgF_2 window separates the refocusing chamber from the ultrahigh-vacuum chamber, where the photoemission experiments are performed [61, 88].

The pump beam, after the first beam splitter, is directed to a motorized delay stage to control the relative delay with respect to the probe beam in the time-resolved experiments, and is focused on the sample by a lens of 1 m focal length. The pump power is regulated by a $\lambda/2$ plate placed before a polarizing beam splitter. The angular separation between the pump and the probe beams is minimized thanks to a D-shaped mirror placed into the refocusing chamber, thus reducing the temporal smearing in the time-resolved experiments.

The main drawback of the generation scheme presented here, resides in the use of a wedge prims to separate the third and the ninth harmonics, since it dramatically affects the time resolution of the apparatus. Indeed when traversing the prism, different parts of the Gaussian light beam follow different paths inside the prism, with a consequent retardation of one of the tails with respect to the other, due to the finite refractive index of the prism. Even if in the present configuration this effect has been minimized by reducing the angle of the prism (5°), the tilting of the wavefront results in a degradation of the time resolution of the setup, which in our case turns out to be of $\sim$ 800 fs. It is worth noting that, due to the different refractive index, the time resolution becomes of $\sim$ 1.3 ps in the case in which a MgF_2 wedge is used [61, 88].

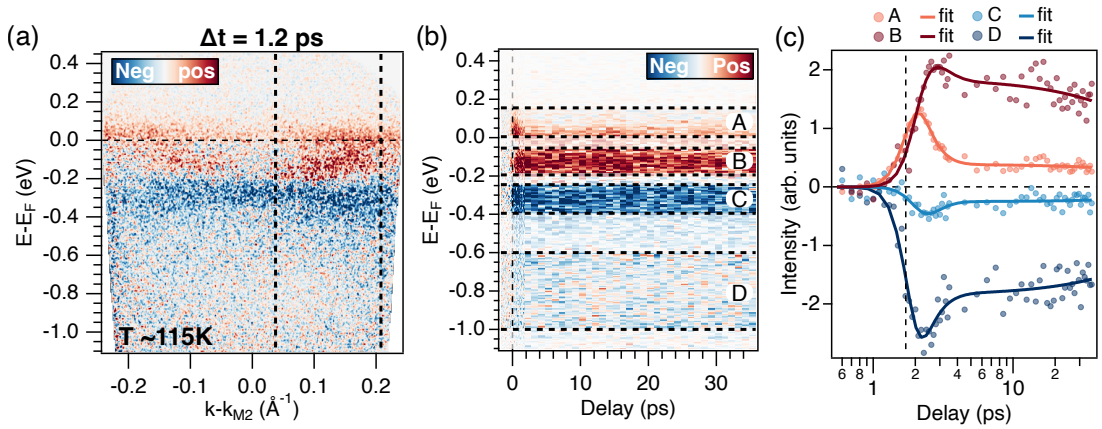

Figure B.1: (a) Differential ARPES map highlighting the changes in the photoemission intensity induced by the pump pulse. The measurement was performed at a base temperature of $\sim$ 115 K, using a pump photon energy of 1.20 eV and an incident fluence of $\sim$ 700 $\mu J/cm^2$. (b) dEDCs extracted by integrating the photoemission intensity from the momentum region delimited by the dashed lines in (a). For better visibility semi-transparent white rectangles have been inserted in between the four boxes delimited by the dashed lines. (c) Evolution of the photoemission intensity extracted from the boxes shown in (b). The traces are plotted on a logarithmic scale (x-axis) for better visibility. The vertical dashed line denotes the arrival time of the pump pulse.

By tuning the splitting between the pump and the probe pulse it is possible to work in a space-charge-free regime, which results in $\sim$ 30 meV of energy resolution [88]. Furthermore, the pulse-picker integrated on the laser source offers the possibility of lowering the effective repetition rate while preserving the same energy per pulse of 40 $\mu J/cm^2$, thus resulting in a reduction of the average power only. This approach has been used to reduce the average heating induced by the pump in the experiments in which high excitations fluences were required, like the ones presented in the next section.

TR-ARPES experiments on VTe_2

This section is devoted to the presentation of the TR-ARPES experiments performed with the 10.8 eV photon source presented in the previous section. The main difference in the experimental scheme with respect to the measurements performed with the HHG setup and presented in Ch. 5, is that, due to the lower photon energy used, the range of tilting angles of our manipulator has not allowed to study the electronic bad structure at the M_2, where the CDW gap opens. Indeed, since the M_2 point is located at $\sim$ 0.9 $Å^{-1}$ from the Γ point, assuming a kinetic energy of 6.5 eV for the photoemitted electrons, the tilting angle required to reach the CDW gap would be of $\sim$ 45°, almost two times higher than the maximum tilting angle allowed. Hence, this limitation has required the use of a copper wedge with a base angle of 30°, on top of which the samples have been glued. As a consequence of that, the measurements presented in this section have not been performed on strained samples, being not possible to mount the strain device on the tilted wedge. Moreover, starting from a photon energy of 10.8 eV and using the estimation for the inner potential of 8.8 eV [124], we obtain $k_z = 2.0\,Å^{-1}$, which places us on the Γ-M plane of the undistorted VTe_2 Brillouin zone, and not on the A-L plane, as it was for the HHG experiments.

Figure B.1(a) shows a differential ARPES map acquired 1.2 ps after the arrival of the pump pulse. This measurement has been performed at a base temperature of $\sim$ 115 K and using an incident fluence of $\sim$ 700 $\mu J/cm^2$. Giving the moderate fluence used, as for the HHG experiments the repetition rate of the laser source has been set to 50 kHz, thus reducing the average heating by the pump pulse. Similarly to what has been observed in the other

TR-ARPES experiments discussed in this thesis, the map reported in panel (a) shows that the pump pulse is able to partially close the CDW gap by triggering the folding of the vanadium band. Figure B.1(b) shows the full temporal evolution of the dEDCs integrated from the momentum region delimited by the dashed lines in panel (a). This map demonstrates that the changes induced by the pump pulse survive for several tens of picoseconds. Figure B.1(c) shows the traces obtained by integrating the photoemission intensity in the boxes drawn in (b). These traces therefore show how the spectral weight dynamics proceed in four different energy regions. Despite the low time resolution of this setup, the comparison reported in panel (b) clearly shows that the maximum change of the photoemission intensity inside the CDW gap (trace B) is achieved with a delay with respect the population of the unoccupied states located immediately above the Fermi level (trace A). Moreover, thanks to the larger time window over which these measurements have been performed (37 ps), by fitting the evolution of trace B using a double exponential fit function, we extracted the relaxation time of the second slow component which turns out to be of 160 ± 60 ps. This result confirms that the recovery of the CDW evolves on a much slower timescale with respect to the typical electron-electron and electron-phonon processes. The timescale here observed is likely related to a heat diffusion process, in agreement with the application of the 3TM model presented in Ch. 5 [24, 207]. Finally, the comparison reported in panel (c) also show that the reduction of the photoemission intensity in boxes C and D evolves on a timescale similar to the one observed in trace B (*i.e* longer than 100 ps), confirming the presence of common origin for these three relaxation dynamics.

Conclusions

In this appendix we reported the results of the TR-ARPES experiments performed with the 10.8 eV photon source developed at the T-ReX laboratory. The results obtained with this setup are in full agreement with the ones presented in Ch. 5, demonstrating that this 10.8 eV photon source, which exploits only the non-linear terms in the susceptibility of crystal and gases, allows to successfully study the electron dynamics that take place at the edges of the first BZ. Although the detailed study of the melting time of the CDW gap has been hindered by the low time resolution of this setup, the traces presented in Fig. B.1(c) clearly show that the increase of the photoemission intensity inside the gap is delayed with respect to the population of states located above the Fermi level. Furthermore these experiments confirm that the recovery of the CDW gap takes place on timescale longer than 100 ps, likely related to a heat diffusion process.

C MODELING OF THE GAP DYNAMICS IN VTe_2 FOR DIFFERENT SET OF PARAMETERS

This appendix is devoted to the presentation of the fits for the band broadening and band position, obtained by starting from different combinations of phonon energy and fraction compared to those presented in Sec. 5.5.2.

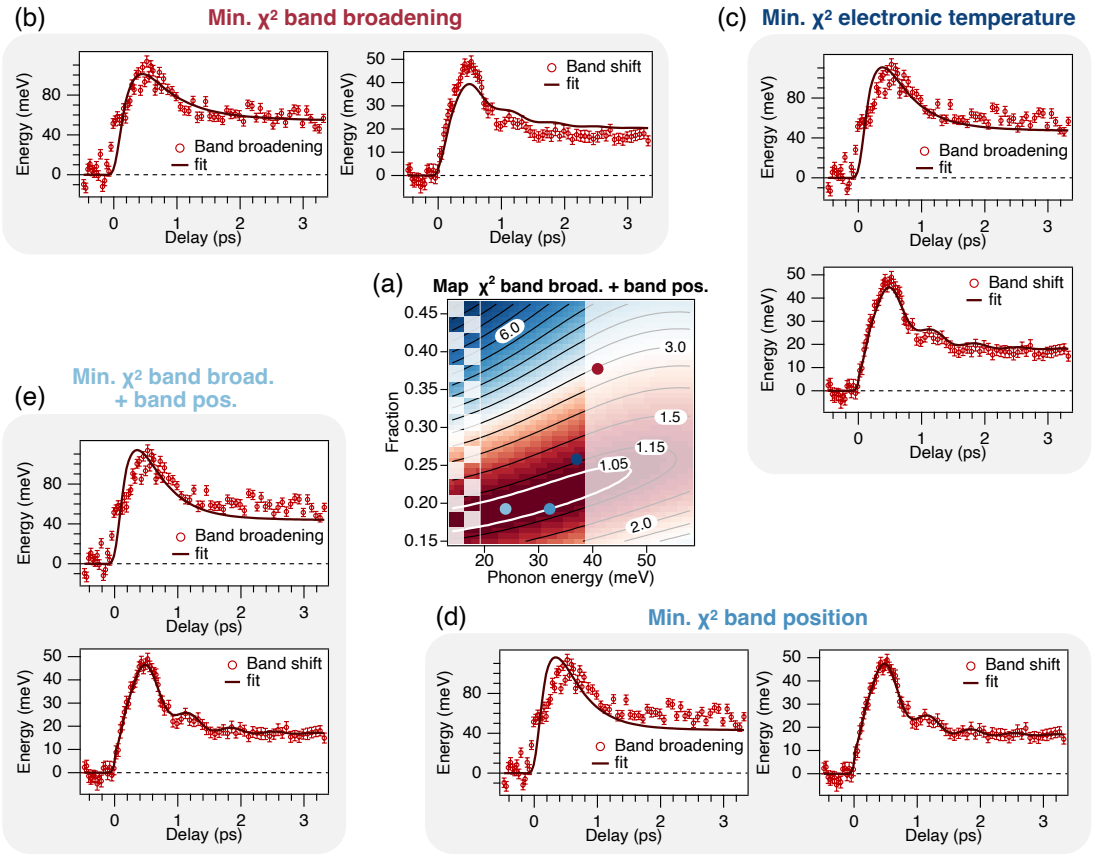

Figure C.1: (a) Two dimensional map showing the evolution of the $\chi^2/\chi^2_{\text{min}}$ obtained by summing the ones deriving from the fit of the band broadening and shift. The semi-transparent white box covers the pairs of parameters for which the phonon energy is higher than ~ 38 meV, which according to our DFT simulations, corresponds to the highest phonon energy present in VTe_2. The same map is shown in Fig. 5.10(d). The colored circles in figure show the position of the minimum of the maps reported in Fig. 5.10. (b) Fit of the band broadening and of the band shift obtained by using the values of phonon energy and frequency that best describe the evolution of the band broadening. (c) Fit of the band broadening and of the band shift obtained by using the values of phonon energy and frequency that best describe the evolution of the electronic temperature. (d) Fit of the band broadening and of the band shift obtained by using the values of phonon energy and frequency that best describe the evolution of the band position. (e) Fit of the band broadening and of the band shift obtained by using the values of phonon energy and frequency that best describe the simultaneous evolution of band broadening and band position. The different colors used for the titles of panels (b-e) correspond to the ones used for the colored circles in panel (a).

The values of energy (24 meV) and fraction (19 %) used in Sec. 5.5.2 have been chosen since they minimize the χ^2 resulting from the simultaneous fit of band broadening and shift. For completeness in Fig. C.1 we report the results obtained starting from the pairs of parameter (energy and fraction) than minimize separately the χ^2 resulting from the fit of: band broadening (panel (b)), electronic temperature (panel (c)) and band position (panel (d)). By comparing the results shown in the different panels, it is possible to notice that despite the different values of phonon energy and fraction used as a starting conditions, a reasonable agreement is maintained between our model and the experimental data. In particular, a good agreement is observed for the couple of parameters that minimize the χ^2 resulting from the fit of the electronic temperature. Despite this good agreement, the choice of using the pair of parameters that better describe simultaneously the evolution of band broadening and shift (which lead to the fits reported in the main text of the thesis and in panel (e)) originate from the fact that they correspond to a phonon branch really observed in VTe_2 [209]. Furthermore, from the fit of the electronic temperature alone it is difficult to reliably extract the values of phonon energy and fraction. This observation is confirmed by Fig. 5.10(a), where a very large minimum in the evolution of the χ^2 is observed (thus a sizable change in the phonon energy and fraction will give a similar agreement of the final fit).

As a final remark it is worth noting that the best fit for the evolution of the band broadening is obtained starting from a phonon energy higher than the ones really existing in VTe_2 (panel (b)). This however does not affect the applicability of our model since the study of the χ^2 allows to obtain only the pair of parameters for which the fits give the best results. The constraints regarding the allowed phonon energies and the strength of the EPC are imposed as a second step, and allow to reduce the rage over which the parameters can vary.

D NON-EQUILIBRIUM REFLECTIVITY MEASUREMENTS ON ScV_6Sn_6 FOR DIFFERENT STRAIN CONFIGURATIONS

This appendix is devoted to the presentation of the raw non-equilibrium reflectivity data acquired on strained ScV_6Sn_6 crystals. In particular, the traces shown Fig. D.1(a)-(c) have been

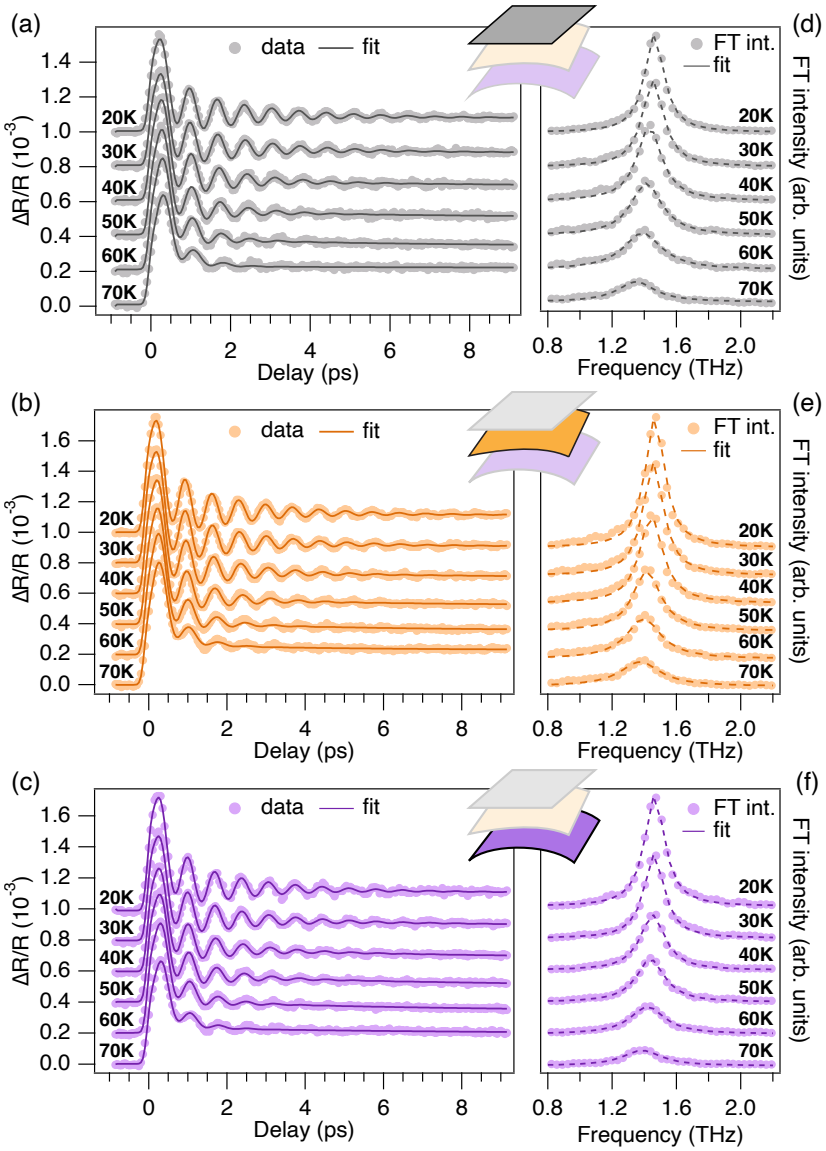

Figure D.1: (a)-(c) Traces extracted form the upper panels of Fig. 6.11 showing the evolution of the non-equilibrium reflectivity as a function of the temperature for different strain configurations. The fits obtained by using Eq. (6.1) are superimposed to the data. (d)-(f) Traces extracted form the lower panels of Fig. 6.11 showing the evolution of the FT of the coherent part of the $\Delta R/R$ signal as a function of temperature for different strain configurations. The Lorentzian fits are superimposed to the data.

extracted from the upper panels of Fig. 6.11 and thus allow to directly observe the differences induced by the application of strain on the response of the system. For completeness, also the traces showing the evolution of the FT of the coherent part of the $\Delta R/R$ signal (extracted from the lower panels of Fig. 6.11) as a function of temperature and for different strain configurations are reported in panels (d)-(f).

E EFFECT OF Ti DOPING ON THE CDW PHASE OF VTe_2

As discussed in Ch. 4, VTe_2 is characterized by a CDW critical temperature of $\sim 480\,K$ [46]. This high critical temperature hinders the study of the normal phase of this compound since high temperatures and high excitations fluences result in a fast sample degradation. One possible solution to overcome this limitation is to exploit the sensitivity of the CDW phase with respect to chemical doping. Indeed it has been demonstrated that in $V_{1-x}Ti_xTe_2$ crystals, by increasing the percentage of titanium atoms, it is possible to progressively suppress the CDW phase, thus lowering the transition temperature [124]. In Fig. E.1(a) we report a schematic electronic phase diagram of $V_{1-x}Ti_xTe_2$, based on temperature-dependent ARPES measurements, which shows the evolution of the critical temperature as a function of the Ti content [124]. The phase transition is progressively moved towards lower temperatures, completely disappearing for Ti contents higher than $x = 0.3$ [124]. It is worth noting that the CDW suppression, induced by Ti doping, has been confirmed also by complementary resistivity measurements performed on polycrystalline samples [124].

In this appendix we report the temperature- and fluence-dependent time-resolved reflectivity measurements performed on a $V_{1-0.05}Ti_{0.05}Te_2$ crystal. As shown by Fig. E.1(a), a Ti content of $x = 5\%$ is expected to lower the transition temperature of $\sim 100\,K$, making it to stay anyhow well above room temperature. Hence also here only the response of the low-temperature CDW phase has been investigated. The aim of these experiments is therefore to study the effect of the Ti doping on the CDW amplitude modes of the system, and to compare these results with the ones obtained for the pristine VTe_2 crystals. The measurements reported in this appendix have been performed using the time-resoled reflectivity setup presented in Sec. 3.7.

Temperature dependent study of the CDW amplitude mode in $V_{1-0.05}Ti_{0.05}Te_2$

The two-dimensional map reported in Fig. E.1(b) shows the evolution of the non-equilibrium reflectivity of $V_{1-0.05}Ti_{0.05}Te_2$ as a function of the temperature of the system. These measurements have been performed using a probe wavelength of 1.03 eV (1200 nm) and using an absorbed fluence of $\sim 300\,\mu J/cm^2$. To better visualize the temperature evolution of the $\Delta R/R$ signal, in Fig. E.1(c) are reported 5 traces extracted from (b) at selected temperatures. A close inspection to these traces reveals that the low-energy excitations of the CDW ground state are profoundly affected by the titanium doping. Specifically, only the AM with a low temperature frequency of $\sim 2.5\,THz$ can be unambiguously resolved, while the other (with a low temperature frequency of $\sim 1.6\,THz$) appears to be strongly suppressed. This first observation is supported by the good agreement between the low-temperature data and the fits obtained using Eq. (4.2), in which only one oscillating component has been considered. The strong suppression of one of the two amplitude modes is further supported by the magnitude of the Fourier Transform (FT) of the coherent part of the $\Delta R/R$ signal reported in panel (d), in which only a single peak located at ~ 2.5 THz can be identified. This map also shows that the worst agreement between data and fit function observed in panel (c) for the highest temperatures, is not due to the appearance of additional peaks in the FT, but is likely to arise from the appearance of anharmonic contributions, which entail an asymmetric broadening of the main peak.

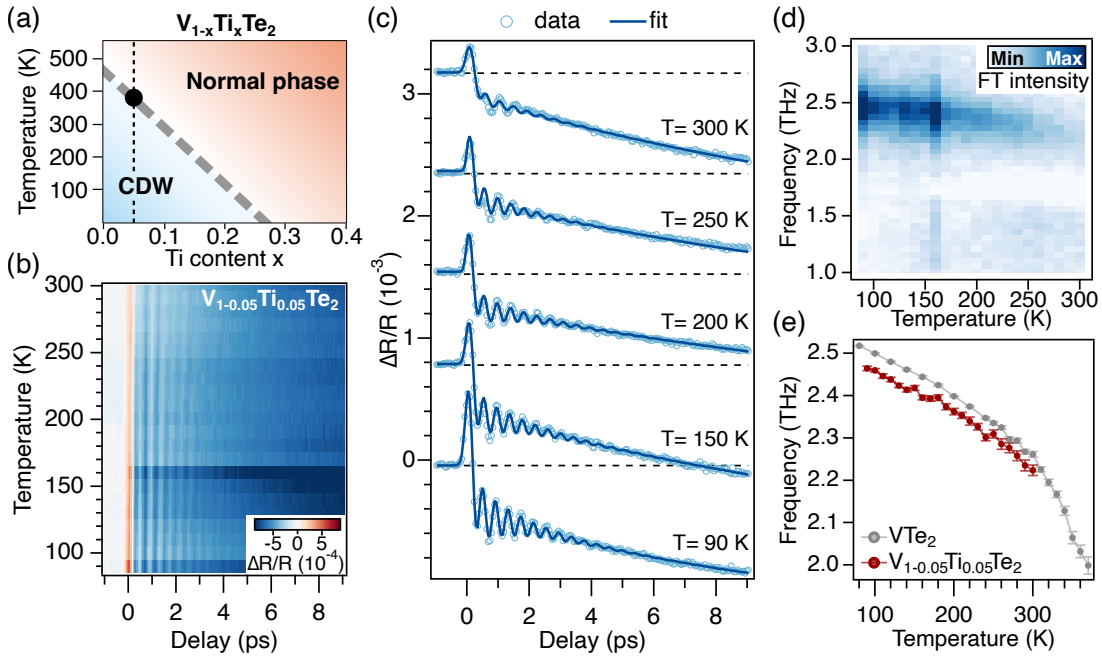

Figure E.1: (a) Schematic phase diagram of $V_{1-x}Ti_xTe_2$ based on temperature-dependent ARPES measurements. Adapted from [124]. (b) Two-dimensional map showing the evolution of the $\Delta R/R$ signal of $V_{1-0.05}Ti_{0.05}Te_2$ as a function of the temperature and of the pump-probe delay. The measurements have been performed at a probe photon energy of 1.03 eV (1200 nm) and using an absorbed fluence of $\sim 300\,\mu J/cm^2$. The marked changes in the intensity observed at specific temperatures (*e.g.* 160 K) can be addressed to a change in the sample position due to the elongation/compression of the cryostat arising from the change in the temperature. (c) Traces extracted from (b) showing the evolution of the $\Delta R/R$ signal as a function of the pump-probe delay for five selected temperatures. (d) Two-dimensional map showing the evolution of the magnitude of the Fourier transform of the coherent part of the $\Delta R/R$ signal as a function of the temperature. (e) Comparison between the temperature evolution of the AM frequency extracted from panel (d) and the one extracted from a pristine VTe_2 crystal and shown in Ch. 4.

At this point it is therefore useful to compare the temperature evolution of the CDW amplitude mode extracted from the Ti doped compound with the one observed in the pristine VTe_2 crystals. This comparison is reported in Fig. E.1(e). Despite the presence of a vertical offset (the frequency of the Ti doped compound is always lower), the two compounds show a very similar AM softening, with a strong renormalization of the phonon frequency that takes place when the temperature is risen towards the CDW critical temperature. Hence, despite of the moderate reduction of the critical temperature, the softening of the AM appears to be only weakly affected in the temperature range investigated.

Fluence dependent study of the CDW amplitude mode in $V_{1-0.05}Ti_{0.05}Te_2$

The two-dimensional map reported in Fig. E.2(a) shows the evolution of the $\Delta R/R$ signal as a function of the absorbed fluence. The traces that compose this map have been renormalized to the absorbed fluence to facilitate the comparison between curves whose intensity would otherwise differ by more than one order of magnitude. The observation of clear oscillations linked to the excitation of the CDW amplitude mode up to the highest fluence used in these measurements, shows that the photoinduced phase transition has not been achieved in the Ti doped crystals. These results therefore confirm the marked resilience of these compounds upon a photoexcitation with a near infrared light pulse.

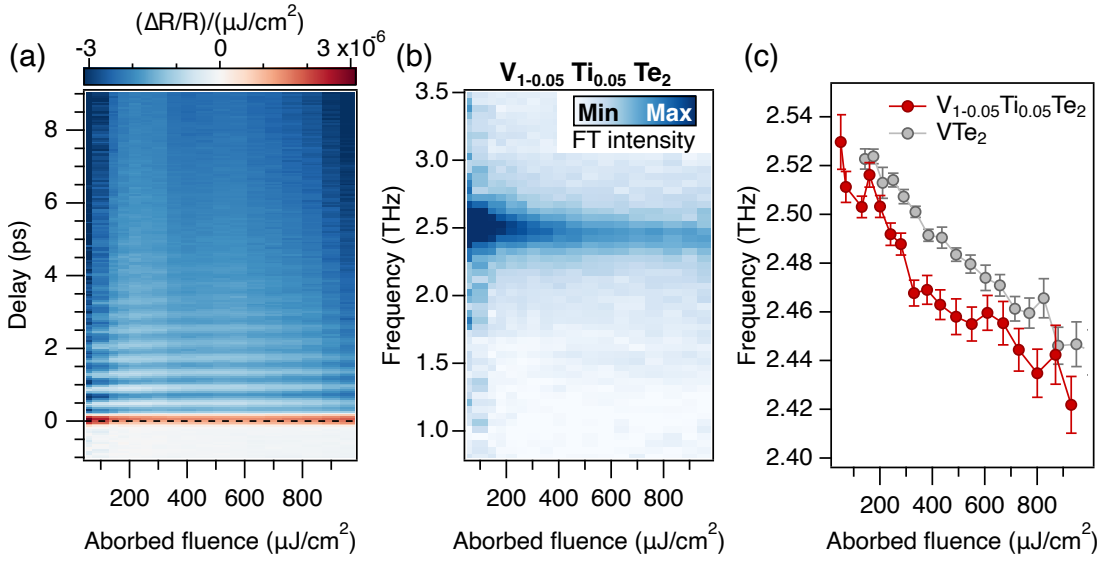

Figure E.2: (a) Two-dimensional map showing the evolution of the $\Delta R/R$ signal, normalized to the absorbed fluence, as a function of the absorbed fluence and of the pump-probe delay. The measurements have been performed at a base temperature of 80 K. (b) Two-dimensional map showing the evolution of the magnitude of the Fourier transform of the coherent part of the $\Delta R/R$ signal as a function of the absorbed fluence. (c) Comparison between the evolution of the AM frequency extracted from (b) and the one obtained from a pristine VTe_2 crystal and shown in Ch. 4.

To study the effect of an increased excitation fluence on the CDW amplitude mode, in panel (b) we show the evolution of the magnitude of the FT of the coherent part of the $\Delta R/R$ signal, isolated by subtracting a double exponential fit function to the data reported in (a). As for the pristine VTe_2 crystals, this map shows that the frequency of the AM is only weakly affected by increase excitation fluence. The fluence-induced AM softening is better quantified in panel (c), which shows the evolution of the AM frequency extracted by fitting FT traces reported in (b) using a Lorentzian function. As for the temperature dependent measurements, this graph shows that except for a vertical offset (the frequency is always lower for the Ti doped compound) the fluence-induced AM softening is similar to the one observed in the pristine sample and attributable to the increase lattice temperature.

Conclusions

In this appendix we reported the time-resolved reflectivity measurements performed on a $V_{1-0.05}Ti_{0.05}Te_2$ crystal. These experiments revealed that the low-temperature response of Ti doped VTe_2 samples is characterized by the presence of a single CDW amplitude mode, with a temperature and fluence evolution very similar to the ones observed in the pristine VTe_2 crystals. The strong suppression of one of the two AM amplitude modes is however unexpected, being the lattice symmetry of the doped compounds equal to the pristine case [124]. The results presented in this appendix require therefore further corroboration, carefully checking the good crystallinity of the compounds investigated, and testing also other values of Ti doping. In particular, higher values of Ti doping, further lowering the CDW critical temperature, would allow to investigate the high-temperature response of these compounds.

BIBLIOGRAPHY

[1] B. Keimer and J. E. Moore. "The physics of quantum materials". In: *Nature Physics* 13.11 (2017), pp. 1045–1055. ISSN: 1745-2481. DOI: 10.1038/nphys4302. URL: https://doi.org/10.1038/nphys4302 (cit. on p. 1).

[2] D. N. Basov, R. D. Averitt, and D. Hsieh. "Towards properties on demand in quantum materials". In: *Nature Materials* 16.11 (2017), pp. 1077–1088. ISSN: 1476-4660. DOI: 10.1038/nmat5017. URL: https://doi.org/10.1038/nmat5017 (cit. on p. 1).

[3] J. G. Bednorz and K. A. Müller. "Possible highTc superconductivity in the Ba-La-Cu-O system". In: *Zeitschrift für Physik B Condensed Matter* 64.2 (1986), pp. 189–193. ISSN: 1431-584X. DOI: 10.1007/BF01303701. URL: https://doi.org/10.1007/BF01303701 (cit. on p. 1).

[4] G. Grüner. "The dynamics of charge-density waves". In: *Rev. Mod. Phys.* 60 (4 1988), pp. 1129–1181. DOI: 10.1103/RevModPhys.60.1129. URL: https://link.aps.org/doi/10.1103/RevModPhys.60.1129 (cit. on pp. 1, 12).

[5] K. S. Burch, D. Mandrus, and J.-G. Park. "Magnetism in two-dimensional van der Waals materials". In: *Nature* 563.7729 (2018), pp. 47–52. ISSN: 1476-4687. DOI: 10.1038/s41586-018-0631-z. URL: https://doi.org/10.1038/s41586-018-0631-z (cit. on p. 1).

[6] J. Bardeen, L. N. Cooper, and J. R. Schrieffer. "Theory of Superconductivity". In: *Phys. Rev.* 108 (5 1957), pp. 1175–1204. DOI: 10.1103/PhysRev.108.1175. URL: https://link.aps.org/doi/10.1103/PhysRev.108.1175 (cit. on p. 1).

[7] M. X. Na et al. "Direct determination of mode-projected electron-phonon coupling in the time domain". In: *Science* 366.6470 (2019), pp. 1231–1236. DOI: 10.1126/science.aaw1662. URL: https://www.science.org/doi/abs/10.1126/science.aaw1662 (cit. on pp. 1, 20–21).

[8] K Rossnagel. "On the origin of charge-density waves in select layered transition-metal dichalcogenides". In: *Journal of Physics: Condensed Matter* 23.21 (2011), p. 213001. DOI: 10.1088/0953-8984/23/21/213001. URL: https://dx.doi.org/10.1088/0953-8984/23/21/213001 (cit. on pp. 1, 5–11).

[9] M. Kang et al. "Twofold van Hove singularity and origin of charge order in topological kagome superconductor CsV3Sb5". In: *Nature Physics* 18.3 (2022), pp. 301–308. ISSN: 1745-2481. DOI: 10.1038/s41567-021-01451-5. URL: https://doi.org/10.1038/s41567-021-01451-5 (cit. on pp. 1, 75–79, 89).

[10] G. Coslovich et al. "Evidence for a photoinduced nonthermal superconducting-to-normal-state phase transition in overdoped $Bi_2Sr_2Ca_{0.92}Y_{0.08}Cu_2O_{8+\delta}$". In: *Phys. Rev. B* 83 (6 2011), p. 064519. DOI: 10.1103/PhysRevB.83.064519. URL: https://link.aps.org/doi/10.1103/PhysRevB.83.064519 (cit. on pp. 1, 83).

[11] G. Grüner. *Density Waves In Solids*. MA: Addison-Wesley, 1994 (cit. on pp. 1, 5–9, 11–13, 37, 72).

[12] W. L. McMillan. "Microscopic model of charge-density waves in $2H - TaSe_2$". In: *Phys. Rev. B* 16 (2 1977), pp. 643–650. DOI: 10.1103/PhysRevB.16.643. URL: https://link.aps.org/doi/10.1103/PhysRevB.16.643 (cit. on pp. 1–2, 6, 9–11, 32, 60, 64, 72, 80).

[13] C. M. Varma and A. L. Simons. "Strong-Coupling Theory of Charge-Density-Wave Transitions". In: *Phys. Rev. Lett.* 51 (2 1983), pp. 138–141. DOI: 10.1103/PhysRevLett.51.138. URL: https://link.aps.org/doi/10.1103/PhysRevLett.51.138 (cit. on p. 1).

[14] J. Inglesfield. "Bonding and charge density wave phase transitions". In: *Physica B+C* 99.1 (1980), pp. 238–242. ISSN: 0378-4363. DOI: https://doi.org/10.1016/0378-4363(80)90238-7. URL: https://www.sciencedirect.com/science/article/pii/0378436380902387 (cit. on p. 1).

[15] X. Zhu et al. "Classification of charge density waves based on their nature". In: *Proceedings of the National Academy of Sciences* 112.8 (2015), pp. 2367–2371. DOI: 10.1073/pnas.1424791112. URL: https://www.pnas.org/doi/abs/10.1073/pnas.1424791112 (cit. on p. 1).

[16] R. Tediosi et al. "Evidence for strongly coupled charge-density-wave ordering in three-dimensional $R_5Ir_4Si_{10}$ compounds from optical measurements". In: *Phys. Rev. B* 80 (3 2009), p. 035107. DOI: 10.1103/PhysRevB.80.035107. URL: https://link.aps.org/doi/10.1103/PhysRevB.80.035107 (cit. on p. 1).

[17] P. Hofmann et al. "Strong-coupling charge density wave in a one-dimensional topological metal". In: *Phys. Rev. B* 99 (3 2019), p. 035438. DOI: 10.1103/PhysRevB.99.035438. URL: https://link.aps.org/doi/10.1103/PhysRevB.99.035438 (cit. on p. 1).

[18] S. Cao et al. "Competing charge-density wave instabilities in the kagome metal ScV6Sn6". In: *Nature Communications* 14.1 (2023), p. 7671. ISSN: 2041-1723. DOI: 10.1038/s41467-023-43454-1. URL: https://doi.org/10.1038/s41467-023-43454-1 (cit. on pp. 1, 9, 77, 80–81).

[19] E. Tosatti. *Surface States, Surface Metal-Insulator, and Surface Insulator-Metal Transitions*. 1995. URL: https://arxiv.org/abs/cond-mat/9505057 (cit. on pp. 2, 9, 72).

[20] M. Fechner et al. "Quenched lattice fluctuations in optically driven $SrTiO_3$". In: *Nature Materials* 23.3 (2024), pp. 363–368. ISSN: 1476-4660. DOI: 10.1038/s41563-023-01791-y. URL: https://doi.org/10.1038/s41563-023-01791-y (cit. on p. 2).

[21] S. Wall et al. "Ultrafast disordering of vanadium dimers in photoexcited VO_2". In: *Science* 362.6414 (2018), pp. 572–576. DOI: 10.1126/science.aau3873. URL: https://www.science.org/doi/abs/10.1126/science.aau3873 (cit. on pp. 2, 10–11, 60, 64–65, 73, 98).

[22] A. Damascelli, Z. Hussain, and Z.-X. Shen. "Angle-resolved photoemission studies of the cuprate superconductors". In: *Rev. Mod. Phys.* 75 (2 2003), pp. 473–541. DOI: 10.1103/RevModPhys.75.473. URL: https://link.aps.org/doi/10.1103/RevModPhys.75.473 (cit. on pp. 2, 15–18).

[23] F. Boschini et al. "Collapse of superconductivity in cuprates via ultrafast quenching of phase coherence". In: *Nature Materials* 17.5 (2018), pp. 416–420. ISSN: 1476-4660. DOI: 10.1038/s41563-018-0045-1. URL: https://doi.org/10.1038/s41563-018-0045-1 (cit. on pp. 2, 20–21).

[24] J. Maklar et al. "Nonequilibrium charge-density-wave order beyond the thermal limit". In: *Nature Communications* 12.1 (2021), p. 2499. ISSN: 2041-1723. DOI: 10.1038/s41467-021-22778-w. URL: https://doi.org/10.1038/s41467-021-22778-w (cit. on pp. 2, 20, 39, 54, 61, 69, 107).

[25] A. van Houselt and H. J. W. Zandvliet. "Colloquium: Time-resolved scanning tunneling microscopy". In: *Rev. Mod. Phys.* 82 (2 2010), pp. 1593–1605. DOI: 10.1103/RevModPhys.82.1593. URL: https://link.aps.org/doi/10.1103/RevModPhys.82.1593 (cit. on p. 2).

[26] S. Duan et al. "Optical manipulation of electronic dimensionality in a quantum material". In: *Nature* 595.7866 (2021), pp. 239–244. ISSN: 1476-4687. DOI: 10.1038/s41586-021-03643-8. URL: https://doi.org/10.1038/s41586-021-03643-8 (cit. on p. 2).

[27] C. Giannetti et al. "Ultrafast optical spectroscopy of strongly correlated materials and high-temperature superconductors: a non-equilibrium approach". In: *Advances in Physics* 65.2 (2016), pp. 58–238. ISSN: 0001-8732. DOI: 10.1080/00018732.2016.1194044. URL: https://doi.org/10.1080/00018732.2016.1194044 (cit. on pp. 2, 18, 26).

[28] J. Demsar, K. Biljaković, and D. Mihailovic. "Single Particle and Collective Excitations in the One-Dimensional Charge Density Wave Solid $K_{0.3}MoO_3$ Probed in Real Time by Femtosecond Spectroscopy". In: *Phys. Rev. Lett.* 83 (4 1999), pp. 800–803. DOI: 10.1103/PhysRevLett.83.800. URL: https://link.aps.org/doi/10.1103/PhysRevLett.83.800 (cit. on pp. 2, 13, 26, 34–35, 37, 44, 82–83).

[29] H. Schaefer et al. "Dynamics of charge density wave order in the quasi one dimensional conductor (TaSe4)2I probed by femtosecond optical spectroscopy". In: *The European Physical Journal Special Topics* 222.5 (2013), pp. 1005–1016. ISSN: 1951-6401. DOI: 10.1140/epjst/e2013-01902-4. URL: https://doi.org/10.1140/epjst/e2013-01902-4 (cit. on pp. 2, 34, 37, 39, 44, 83–86, 88).

[30] H. Schaefer, V. V. Kabanov, and J. Demsar. "Collective modes in quasi-one-dimensional charge-density wave systems probed by femtosecond time-resolved optical studies". In: *Phys. Rev. B* 89 (4 2014), p. 045106. DOI: 10.1103/PhysRevB.89.045106. URL: https://link.aps.org/doi/10.1103/PhysRevB.89.045106 (cit. on pp. 2, 34, 37, 44, 83).

[31] H. Schäfer et al. "Disentanglement of the Electronic and Lattice Parts of the Order Parameter in a 1D Charge Density Wave System Probed by Femtosecond Spectroscopy". In: *Phys. Rev. Lett.* 105 (6 2010), p. 066402. DOI: 10.1103/PhysRevLett.105.066402. URL: https://link.aps.org/doi/10.1103/PhysRevLett.105.066402 (cit. on pp. 2, 34, 37, 83).

[32] R. Peierls. *Quantum Theory of Solids*. ISBN: 9780198507819 (cit. on p. 5).

[33] H. Fröhlich. "On the theory of superconductivity: the one-dimensional case". In: *Proceedings of the Royal Society of London. Series A. Mathematical and Physical Sciences* 223.1154 (1954), pp. 296–305. DOI: 10.1098/rspa.1954.0116 (cit. on p. 5).

[34] H. Li et al. "Observation of Unconventional Charge Density Wave without Acoustic Phonon Anomaly in Kagome Superconductors AV_3Sb_5 (A=Rb, Cs)". In: *Phys. Rev. X* 11 (3 2021), p. 031050. DOI: 10.1103/PhysRevX.11.031050. URL: https://link.aps.org/doi/10.1103/PhysRevX.11.031050 (cit. on p. 6).

[35] M. Rice and S. Strässler. "Theory of the soft phonon mode and dielectric constant below the Peierls transition temperature". In: *Solid State Communications* 13.12 (1973), pp. 1931–1933. ISSN: 0038-1098. DOI: https://doi.org/10.1016/0038-1098(73)90003-3. URL: https://www.sciencedirect.com/science/article/pii/0038109873900033 (cit. on p. 6).

[36] L. Degiorgi et al. "Fluctuation effects in quasi-one-dimensional conductors: Optical probing of thermal lattice fluctuations". In: *Phys. Rev. B* 52 (8 1995), pp. 5603–5610. DOI: 10.1103/PhysRevB.52.5603. URL: https://link.aps.org/doi/10.1103/PhysRevB.52.5603 (cit. on pp. 8–9).

[37] T. Yokoya et al. "Role of charge-density-wave fluctuations on the spectral function in a metallic charge-density-wave system". In: *Phys. Rev. B* 71 (14 2005), p. 140504. DOI: 10.1103/PhysRevB.71.140504. URL: https://link.aps.org/doi/10.1103/PhysRevB.71.140504 (cit. on p. 8).

[38] R. H. McKenzie and J. W. Wilkins. "Effect of Lattice Zero-Point Motion on Electronic Properties of the Peierls-Fröhlich State". In: *Phys. Rev. Lett.* 69 (7 1992), pp. 1085–1088. DOI: 10.1103/PhysRevLett.69.1085. URL: https://link.aps.org/doi/10.1103/PhysRevLett.69.1085 (cit. on p. 9).

[39] R. H. McKenzie. "Microscopic theory of the pseudogap and Peierls transition in quasi-one-dimensional materials". In: *Phys. Rev. B* 52 (23 1995), pp. 16428–16442. DOI: 10.1103/PhysRevB.52.16428. URL: https://link.aps.org/doi/10.1103/PhysRevB.52.16428 (cit. on pp. 9, 55).

[40] A. Korshunov et al. "Softening of a flat phonon mode in the kagome ScV6Sn6". In: *Nature Communications* 14.1 (2023), p. 6646. ISSN: 2041-1723. DOI: 10.1038/s41467-023-42186-6. URL: https://doi.org/10.1038/s41467-023-42186-6 (cit. on pp. 9–10, 80).

[41] R. S. Kwok, G. Gruner, and S. E. Brown. "Fluctuations and thermodynamics of the charge-density-wave phase transition". In: *Phys. Rev. Lett.* 65 (3 1990), pp. 365–368. DOI: 10.1103/PhysRevLett.65.365. URL: https://link.aps.org/doi/10.1103/PhysRevLett.65.365 (cit. on pp. 9, 62).

[42] S. V. Borisenko et al. "Pseudogap and Charge Density Waves in Two Dimensions". In: *Phys. Rev. Lett.* 100 (19 2008), p. 196402. DOI: 10.1103/PhysRevLett.100.196402. URL: https://link.aps.org/doi/10.1103/PhysRevLett.100.196402 (cit. on p. 10).

[43] T. Aruga. "Surface Peierls transition on Cu(001) covered with heavier p-block metals". In: *Surface Science Reports* 61.6 (2006), pp. 283–302. ISSN: 0167-5729. DOI: https://doi.org/10.1016/j.surfrep.2006.04.002. URL: https://www.sciencedirect.com/science/article/pii/S0167572906000434 (cit. on p. 10).

[44] D. Subires et al. "Order-disorder charge density wave instability in the kagome metal (Cs,Rb)V3Sb5". In: *Nature Communications* 14.1 (2023), p. 1015. ISSN: 2041-1723. DOI: 10.1038/s41467-023-36668-w. URL: https://doi.org/10.1038/s41467-023-36668-w (cit. on p. 10).

[45] V. Ilakovac et al. "Order-disorder type of Peierls instability in $BaVS_3$". In: *Phys. Rev. B* 103 (1 2021), p. 014306. DOI: 10.1103/PhysRevB.103.014306. URL: https://link.aps.org/doi/10.1103/PhysRevB.103.014306 (cit. on p. 10).

[46] A. A. Vinokurov et al. "Thermodynamic properties of VTe2". In: *Inorganic Materials* 45.5 (2009), pp. 480–485. ISSN: 1608-3172. DOI: 10.1134/S0020168509050045. URL: https://doi.org/10.1134/S0020168509050045 (cit. on pp. 10, 31, 61, 113).

[47] A. S. Johnson et al. "Ultrafast X-ray imaging of the light-induced phase transition in VO2". In: *Nature Physics* 19.2 (2023), pp. 215–220. ISSN: 1745-2481. DOI: 10.1038/s41567-022-01848-w. URL: https://doi.org/10.1038/s41567-022-01848-w (cit. on p. 11).

[48] S. Kim et al. "Observation of a massive phason in a charge-density-wave insulator". In: *Nature Materials* 22.4 (2023), pp. 429–433. ISSN: 1476-4660. DOI: 10.1038/s41563-023-01504-5. URL: https://doi.org/10.1038/s41563-023-01504-5 (cit. on pp. 12, 87).

[49] R. Yusupov et al. "Coherent dynamics of macroscopic electronic order through a symmetry breaking transition". In: *Nature Physics* 6.9 (2010), pp. 681–684. ISSN: 1745-2481. DOI: 10.1038/nphys1738. URL: https://doi.org/10.1038/nphys1738 (cit. on pp. 12–13).

[50] A. Tomeljak et al. "Dynamics of Photoinduced Charge-Density-Wave to Metal Phase Transition in $\mathbf{K}_{0.3}MoO_3$". In: *Phys. Rev. Lett.* 102 (6 2009), p. 066404. DOI: 10.1103/PhysRevLett.102.066404. URL: https://link.aps.org/doi/10.1103/PhysRevLett.102.066404 (cit. on pp. 12–13, 37, 39, 85, 88).

[51] A. R. Pokharel et al. "Dynamics of collective modes in an unconventional charge density wave system BaNi2As2". In: *Communications Physics* 5.1 (2022), p. 141. ISSN: 2399-3650. DOI: 10.1038/s42005-022-00919-x. URL: https://doi.org/10.1038/s42005-022-00919-x (cit. on pp. 12–13).

[52] T. Huber et al. "Coherent Structural Dynamics of a Prototypical Charge-Density-Wave-to-Metal Transition". In: *Phys. Rev. Lett.* 113 (2 2014), p. 026401. DOI: 10.1103/PhysRevLett.113.026401. URL: https://link.aps.org/doi/10.1103/PhysRevLett.113.026401 (cit. on pp. 12–13, 60).

[53] F. Schmitt et al. "Transient Electronic Structure and Melting of a Charge Density Wave in $TbTe_3$". In: *Science* 321.5896 (2008), pp. 1649–1652. DOI: 10.1126/science.1160778. URL: https://www.science.org/doi/abs/10.1126/science.1160778 (cit. on pp. 12, 54).

[54] T. E. Glier et al. "Superconducting Higgs particle observed by non-equilibrium Raman scattering". In: (2024). URL: https://arxiv.org/abs/2310.08162 (cit. on p. 13).

[55] D. Pekker and C. Varma. "Amplitude/Higgs Modes in Condensed Matter Physics". In: *Annual Review of Condensed Matter Physics* 6.Volume 6, 2015 (2015), pp. 269–297. ISSN: 1947-5462. DOI: https://doi.org/10.1146/annurev-conmatphys-031214-014350. URL: https://www.annualreviews.org/content/journals/10.1146/annurev-conmatphys-031214-014350 (cit. on p. 13).

[56] P. W. Anderson. "Coherent Excited States in the Theory of Superconductivity: Gauge Invariance and the Meissner Effect". In: *Phys. Rev.* 110 (4 1958), pp. 827–835. DOI: 10.1103/PhysRev.110.827. URL: https://link.aps.org/doi/10.1103/PhysRev.110.827 (cit. on p. 13).

[57] S. Hüfner. *Photoelectron Spectroscopy*. Springer Berlin, Heidelberg, 2023. DOI: https://doi.org/10.1007/978-3-662-09280-4 (cit. on p. 15).

[58] J. A. Sobota, Y. He, and Z.-X. Shen. "Angle-resolved photoemission studies of quantum materials". In: *Rev. Mod. Phys.* 93 (2 2021), p. 025006. DOI: 10.1103/RevModPhys.93.025006. URL: https://link.aps.org/doi/10.1103/RevModPhys.93.025006 (cit. on pp. 15–16, 18).

[59] H. Zhang et al. "Angle-resolved photoemission spectroscopy". In: *Nature Reviews Methods Primers* 2.1 (2022), p. 54. ISSN: 2662-8449. DOI: 10.1038/s43586-022-00133-7. URL: https://doi.org/10.1038/s43586-022-00133-7 (cit. on p. 16).

[60] M. P. Seah and W. A. Dench. "Quantitative electron spectroscopy of surfaces: A standard data base for electron inelastic mean free paths in solids". In: *Surface and Interface Analysis* 1.1 (1979), pp. 2–11. DOI: https://doi.org/10.1002/sia.740010103. URL: https://analyticalsciencejournals.onlinelibrary.wiley.com/doi/abs/10.1002/sia.740010103 (cit. on p. 16).

[61] D. Puntel. "Ultrafast photoelectron spectroscopy of quantum materials with a novel 10.8 eV photon source". PhD Thesis. Università degli studi di Trieste, 2023. URL: https://hdl.handle.net/11368/3059201 (cit. on pp. 16, 105).

[62] J. Minár et al. "Calculation of angle-resolved photo emission spectra within the one-step model of photo emission—Recent developments". In: *Journal of Electron Spectroscopy and Related Phenomena* 184.3 (2011). Advances in Vacuum Ultraviolet and X-ray Physics, pp. 91–99. ISSN: 0368-2048. DOI: https://doi.org/10.1016/j.elspec.2011.01.009. URL: https://www.sciencedirect.com/science/article/pii/S0368204811000156 (cit. on p. 16).

[63] C. N. Berglund and W. E. Spicer. "Photoemission Studies of Copper and Silver: Theory". In: *Phys. Rev.* 136 (4A 1964), A1030–A1044. DOI: 10.1103/PhysRev.136.A1030. URL: https://link.aps.org/doi/10.1103/PhysRev.136.A1030 (cit. on p. 16).

[64] S. Moser. "An experimentalist's guide to the matrix element in angle resolved photoemission". In: *Journal of Electron Spectroscopy and Related Phenomena* 214 (2017), pp. 29–52. ISSN: 0368-2048. DOI: https://doi.org/10.1016/j.elspec.2016.11.007. URL: https://www.sciencedirect.com/science/article/pii/S0368204816301724 (cit. on p. 17).

[65] Y. Cao et al. "Mapping the orbital wavefunction of the surface states in three-dimensional topological insulators". In: *Nature Physics* 9.8 (2013), pp. 499–504. ISSN: 1745-2481. DOI: 10.1038/nphys2685. URL: https://doi.org/10.1038/nphys2685 (cit. on p. 17).

[66] R. Comin and A. Damascelli. "ARPES: A Probe of Electronic Correlations". In: *Strongly Correlated Systems: Experimental Techniques*. Ed. by A. Avella and F. Mancini. Berlin, Heidelberg: Springer Berlin Heidelberg, 2015, pp. 31–71. ISBN: 978-3-662-44133-6. DOI: 10.1007/978-3-662-44133-6_2. URL: https://doi.org/10.1007/978-3-662-44133-6_2 (cit. on p. 17).

[67] G. D. Mahan. *Many-Particle Physics*. Boston, MA: Springer US, 2000, p. 785. ISBN: 978-1-4757-5714-9. DOI: https://doi.org/10.1007/978-1-4757-5714-9. URL: https://doi.org/10.1007/978-1-4757-5714-9 (cit. on p. 17).

[68] F. Boschini, M. Zonno, and A. Damascelli. "Time-resolved ARPES studies of quantum materials". In: *Rev. Mod. Phys.* 96 (1 2024), p. 015003. DOI: 10.1103/RevModPhys.96.015003. URL: https://link.aps.org/doi/10.1103/RevModPhys.96.015003 (cit. on pp. 17–20).

[69] S Doniach and E. H. Sondheimer. *Green's Functions for Solid State Physicists*. Published by Imperial College Press and distributed by World Scientific Publishing CO., 1998. DOI: 10.1142/p067. URL: https://www.worldscientific.com/doi/abs/10.1142/p067 (cit. on p. 17).

[70] A. Altland and B. D. Simons. *Condensed Matter Field Theory*. 2nd ed. Cambridge University Press, 2010 (cit. on p. 17).

[71] J. C. Johannsen et al. "Direct View of Hot Carrier Dynamics in Graphene". In: *Phys. Rev. Lett.* 111 (2 2013), p. 027403. DOI: 10.1103/PhysRevLett.111.027403. URL: https://link.aps.org/doi/10.1103/PhysRevLett.111.027403 (cit. on pp. 19–20).

[72] P. E. Majchrzak et al. "Van der Waals Engineering of Ultrafast Carrier Dynamics in Magnetic Heterostructures". In: *Nano Letters* 23.2 (2023), pp. 414–421. ISSN: 1530-6984. DOI: 10.1021/acs.nanolett.2c03075. URL: https://doi.org/10.1021/acs.nanolett.2c03075 (cit. on p. 19).

[73] M. Puppin et al. "Excited-state band structure mapping". In: *Phys. Rev. B* 105 (7 2022), p. 075417. DOI: 10.1103/PhysRevB.105.075417. URL: https://link.aps.org/doi/10.1103/PhysRevB.105.075417 (cit. on pp. 19–20).

[74] L. Perfetti et al. "Ultrafast Electron Relaxation in Superconducting $Bi_2Sr_2CaCu_2O_{8+\delta}$ by Time-Resolved Photoelectron Spectroscopy". In: *Phys. Rev. Lett.* 99 (19 2007), p. 197001. DOI: 10.1103/PhysRevLett.99.197001. URL: https://link.aps.org/doi/10.1103/PhysRevLett.99.197001 (cit. on pp. 19–20, 39, 57–59, 69, 88).

[75] S. Ulstrup et al. "Extracting the temperature of hot carriers in time- and angle-resolved photoemission". In: *Review of Scientific Instruments* 85.1 (Jan. 2014), p. 013907. ISSN: 0034-6748. DOI: 10.1063/1.4863322. URL: https://doi.org/10.1063/1.4863322 (cit. on p. 19).

[76] L. Rettig et al. "Persistent order due to transiently enhanced nesting in an electronically excited charge density wave". In: *Nature Communications* 7.1 (2016), p. 10459. ISSN: 2041-1723. DOI: 10.1038/ncomms10459. URL: https://doi.org/10.1038/ncomms10459 (cit. on pp. 20, 54, 57).

[77] P. Hein et al. "Mode-resolved reciprocal space mapping of electron-phonon interaction in the Weyl semimetal candidate Td-WTe2". In: *Nature Communications* 11.1 (2020), p. 2613. ISSN: 2041-1723. DOI: 10.1038/s41467-020-16076-0. URL: https://doi.org/10.1038/s41467-020-16076-0 (cit. on p. 20).

[78] L. Perfetti et al. "Time Evolution of the Electronic Structure of $1T-TaS_2$ through the Insulator-Metal Transition". In: *Phys. Rev. Lett.* 97 (6 2006), p. 067402. DOI: 10.1103/PhysRevLett.97.067402. URL: https://link.aps.org/doi/10.1103/PhysRevLett.97.067402 (cit. on p. 20).

[79] F Boschini et al. "Role of matrix elements in the time-resolved photoemission signal". In: *New Journal of Physics* 22.2 (2020), p. 023031. DOI: 10.1088/1367-2630/ab6eb1. URL: https://dx.doi.org/10.1088/1367-2630/ab6eb1 (cit. on p. 20).

[80] M. Na, A. K. Mills, and D. J. Jones. "Advancing time- and angle-resolved photoemission spectroscopy: The role of ultrafast laser development". In: *Physics Reports* 1036 (2023), pp. 1–47. ISSN: 0370-1573. DOI: https://doi.org/10.1016/j.physrep.2023.09.005. URL: https://www.sciencedirect.com/science/article/pii/S0370157323003010 (cit. on pp. 20–22).

[81] D. J. Rahn et al. "Gaps and kinks in the electronic structure of the superconductor 2*H*-$NbSe_2$ from angle-resolved photoemission at 1 K". In: *Phys. Rev. B* 85 (22 2012), p. 224532. DOI: 10.1103/PhysRevB.85.224532. URL: https://link.aps.org/doi/10.1103/PhysRevB.85.224532 (cit. on p. 20).

[82] F. Randi, D. Fausti, and M. Eckstein. "Bypassing the energy-time uncertainty in time-resolved photoemission". In: *Phys. Rev. B* 95 (11 2017), p. 115132. DOI: 10.1103/PhysRevB.95.115132. URL: https://link.aps.org/doi/10.1103/PhysRevB.95.115132 (cit. on p. 20).

[83] E. J. Sie et al. "Time-resolved XUV ARPES with tunable 24–33 eV laser pulses at 30 meV resolution". In: *Nature Communications* 10.1 (2019), p. 3535. ISSN: 2041-1723. DOI: 10.1038/s41467-019-11492-3. URL: https://doi.org/10.1038/s41467-019-11492-3 (cit. on p. 21).

[84] C. Sohrt et al. "How fast can a Peierls–Mott insulator be melted?" In: *Faraday Discuss.* 171 (0 2014), pp. 243–257. DOI: 10.1039/C4FD00042K. URL: http://dx.doi.org/10.1039/C4FD00042K (cit. on pp. 21, 54).

[85] X. Zhou et al. "Space charge effect and mirror charge effect in photoemission spectroscopy". In: *Journal of Electron Spectroscopy and Related Phenomena* 142.1 (2005), pp. 27–38. ISSN: 0368-2048. DOI: https://doi.org/10.1016/j.elspec.2004.08.004. URL: https://www.sciencedirect.com/science/article/pii/S0368204804003421 (cit. on p. 21).

[86] S Hellmann et al. "Time-resolved x-ray photoelectron spectroscopy at FLASH". In: *New Journal of Physics* 14.1 (2012), p. 013062. DOI: 10.1088/1367-2630/14/1/013062. URL: https://dx.doi.org/10.1088/1367-2630/14/1/013062 (cit. on p. 21).

[87] J. Faure et al. "Full characterization and optimization of a femtosecond ultraviolet laser source for time and angle-resolved photoemission on solid surfaces". In: *Review of Scientific Instruments* 83.4 (Apr. 2012), p. 043109. ISSN: 0034-6748. DOI: 10.1063/1.3700190. URL: https://doi.org/10.1063/1.3700190 (cit. on p. 22).

[88] S. Peli et al. "Time-resolved VUV ARPES at 10.8 eV photon energy and MHz repetition rate". In: *Journal of Electron Spectroscopy and Related Phenomena* 243 (2020), p. 146978. ISSN: 0368-2048. DOI: https://doi.org/10.1016/j.elspec.2020.146978. URL: https://www.sciencedirect.com/science/article/pii/S0368204820300463 (cit. on pp. 22, 105–106).

[89] M. Lewenstein et al. "Theory of high-harmonic generation by low-frequency laser fields". In: *Phys. Rev. A* 49 (3 1994), pp. 2117–2132. DOI: 10.1103/PhysRevA.49.2117. URL: https://link.aps.org/doi/10.1103/PhysRevA.49.2117 (cit. on pp. 22–23).

[90] P. B. Corkum. "Plasma perspective on strong field multiphoton ionization". In: *Phys. Rev. Lett.* 71 (13 1993), pp. 1994–1997. DOI: 10.1103/PhysRevLett.71.1994. URL: https://link.aps.org/doi/10.1103/PhysRevLett.71.1994 (cit. on p. 22).

[91] S. Eich et al. "Time- and angle-resolved photoemission spectroscopy with optimized high-harmonic pulses using frequency-doubled Ti:Sapphire lasers". In: *Journal of Electron Spectroscopy and Related Phenomena* 195 (2014), pp. 231–236. ISSN: 0368-2048. DOI: https://doi.org/10.1016/j.elspec.2014.04.013. URL: https://www.sciencedirect.com/science/article/pii/S036820481400108X (cit. on p. 23).

[92] F. Calegari et al. "Advances in attosecond science". In: *Journal of Physics B: Atomic, Molecular and Optical Physics* 49.6 (2016), p. 062001. DOI: 10.1088/0953-4075/49/6/062001. URL: https://dx.doi.org/10.1088/0953-4075/49/6/062001 (cit. on p. 23).

[93] P. M. Paul et al. "Observation of a Train of Attosecond Pulses from High Harmonic Generation". In: *Science* 292.5522 (2001), pp. 1689–1692. DOI: 10.1126/science.1059413. URL: https://www.science.org/doi/abs/10.1126/science.1059413 (cit. on p. 23).

[94] G. Sansone et al. "Isolated Single-Cycle Attosecond Pulses". In: *Science* 314.5798 (2006), pp. 443–446. DOI: 10.1126/science.1132838. URL: https://www.science.org/doi/abs/10.1126/science.1132838 (cit. on p. 23).

[95] J. Rothhardt et al. "Absorption-limited and phase-matched high harmonic generation in the tight focusing regime". In: *New Journal of Physics* 16.3 (2014), p. 033022. DOI: 10.1088/1367-2630/16/3/033022. URL: https://dx.doi.org/10.1088/1367-2630/16/3/033022 (cit. on p. 23).

[96] M. Puppin et al. "Time- and angle-resolved photoemission spectroscopy of solids in the extreme ultraviolet at 500 kHz repetition rate". In: *Review of Scientific Instruments* 90.2 (Feb. 2019), p. 023104. ISSN: 0034-6748. DOI: 10.1063/1.5081938. URL: https://doi.org/10.1063/1.5081938 (cit. on p. 23).

[97] C.-J. Lai et al. "Wavelength Scaling of High Harmonic Generation Close to the Multiphoton Ionization Regime". In: *Phys. Rev. Lett.* 111 (7 2013), p. 073901. DOI: 10.1103/PhysRevLett.111.073901. URL: https://link.aps.org/doi/10.1103/PhysRevLett.111.073901 (cit. on p. 23).

[98] H. Wang et al. "Bright high-repetition-rate source of narrowband extreme-ultraviolet harmonics beyond 22 eV". In: *Nature Communications* 6.1 (2015), p. 7459. ISSN: 2041-1723. DOI: 10.1038/ncomms8459. URL: https://doi.org/10.1038/ncomms8459 (cit. on p. 23).

[99] R. Cucini et al. "Coherent narrowband light source for ultrafast photoelectron spectroscopy in the 17–31 eV photon energy range". In: *Structural Dynamics* 7.1 (Jan. 2020), p. 014303. ISSN: 2329-7778. DOI: 10.1063/1.5131216. URL: https://doi.org/10.1063/1.5131216 (cit. on pp. 23–25, 45).

[100] L. Poletto and F. Frassetto. "Time-preserving grating monochromators for ultrafast extreme-ultraviolet pulses". In: *Appl. Opt.* 49.28 (2010), pp. 5465–5473. DOI: 10.1364/AO.49.005465. URL: https://opg.optica.org/ao/abstract.cfm?URI=ao-49-28-5465 (cit. on pp. 24–25).

[101] R. W. Boyd. *Chapter 2 - Wave-Equation Description of Nonlinear Optical Interactions*. Ed. by R. W. Boyd. Third Edition. Burlington: Academic Press, 2008, pp. 69–133. ISBN: 978-0-12-369470-6. DOI: https://doi.org/10.1016/B978-0-12-369470-6.00002-2. URL: https://www.sciencedirect.com/science/article/pii/B9780123694706000022 (cit. on p. 24).

[102] F. Frassetto et al. "Single-grating monochromator for extreme-ultraviolet ultrashort pulses". In: *Opt. Express* 19.20 (2011), pp. 19169–19181. DOI: 10.1364/OE.19.019169. URL: https://opg.optica.org/oe/abstract.cfm?URI=oe-19-20-19169 (cit. on pp. 24–25).

[103] C. J. Sayers et al. "Spectrally Resolving the Phase and Amplitude of Coherent Phonons in the Charge Density Wave State of 1T-TaSe2". In: *Advanced Optical Materials* 10.14 (2022), p. 2200362. DOI: https://doi.org/10.1002/adom.202200362. URL: https://onlinelibrary.wiley.com/doi/abs/10.1002/adom.202200362 (cit. on pp. 26, 43).

[104] S. D. Conte et al. "Disentangling the Electronic and Phononic Glue in a High-T_c Superconductor". In: *Science* 335.6076 (2012), pp. 1600–1603. DOI: 10.1126/science.1216765. URL: https://www.science.org/doi/abs/10.1126/science.1216765 (cit. on pp. 26, 60, 66).

[105] K. Warawa et al. "Combined investigation of collective amplitude and phase modes in a quasi-one-dimensional charge density wave system over a wide spectral range". In: *Phys. Rev. B* 108 (4 2023), p. 045147. DOI: 10.1103/PhysRevB.108.045147. URL: https://link.aps.org/doi/10.1103/PhysRevB.108.045147 (cit. on pp. 26, 95).

[106] D. Polli, L. Lüer, and G. Cerullo. "High-time-resolution pump-probe system with broadband detection for the study of time-domain vibrational dynamics". In: *Review of Scientific Instruments* 78.10 (Oct. 2007), p. 103108. ISSN: 0034-6748. DOI: 10.1063/1.2800778. URL: https://doi.org/10.1063/1.2800778 (cit. on p. 26).

[107] P. Franceschini et al. "Coherent control of the orbital occupation driving the insulator-to-metal Mott transition in V_2O_3". In: *Phys. Rev. B* 107 (16 2023), p. L161110. DOI: 10.1103/PhysRevB.107.L161110. URL: https://link.aps.org/doi/10.1103/PhysRevB.107.L161110 (cit. on p. 26).

[108] D. Bossini et al. "Femtosecond phononic coupling to both spins and charges in a room-temperature antiferromagnetic semiconductor". In: *Phys. Rev. B* 104 (22 2021), p. 224424. DOI: 10.1103/PhysRevB.104.224424. URL: https://link.aps.org/doi/10.1103/PhysRevB.104.224424 (cit. on p. 26).

[109] D. Soranzio et al. "Ultrafast broadband optical spectroscopy for quantifying subpicometric coherent atomic displacements in WTe_2". In: *Phys. Rev. Res.* 1 (3 2019), p. 032033. DOI: 10.1103/PhysRevResearch.1.032033. URL: https://link.aps.org/doi/10.1103/PhysRevResearch.1.032033 (cit. on pp. 26–27, 43).

[110] M. Tuniz et al. "Ultrafast all-optical manipulation of the charge-density wave in VTe_2". In: *Phys. Rev. Res.* 5 (4 2023), p. 043276. DOI: 10.1103/PhysRevResearch.5.043276. URL: https://link.aps.org/doi/10.1103/PhysRevResearch.5.043276 (cit. on pp. 26–27, 32, 34, 36–37, 41, 43, 51).

[111] F. Giusti et al. "Anisotropic time-domain electronic response in cuprates driven by midinfrared pulses". In: *Phys. Rev. B* 104 (12 2021), p. 125121. DOI: 10.1103/PhysRevB.104.125121. URL: https://link.aps.org/doi/10.1103/PhysRevB.104.125121 (cit. on p. 26).

[112] M. Perlangeli et al. "Polarization-resolved broadband time-resolved optical spectroscopy for complex materials: application to the case of MoTe2 polytypes". In: *Opt. Express* 28.6 (2020), pp. 8819–8829. DOI: 10.1364/OE.385419. URL: https://opg.optica.org/oe/abstract.cfm?URI=oe-28-6-8819 (cit. on p. 27).

[113] C.-H. Lu et al. "Generation of intense supercontinuum in condensed media". In: *Optica* 1.6 (2014), pp. 400–406. DOI: 10.1364/OPTICA.1.000400. URL: https://opg.optica.org/optica/abstract.cfm?URI=optica-1-6-400 (cit. on p. 27).

[114] M. Bradler, P. Baum, and E. Riedle. "Femtosecond continuum generation in bulk laser host materials with sub-μJ pump pulses". In: *Applied Physics B* 97.3 (2009), pp. 561–574. ISSN: 1432-0649. DOI: 10.1007/s00340-009-3699-1. URL: https://doi.org/10.1007/s00340-009-3699-1 (cit. on p. 27).

[115] F. Bencivenga et al. "Nanoscale transient gratings excited and probed by extreme ultraviolet femtosecond pulses". In: *Science Advances* 5.7 (2019), eaaw5805. DOI: 10.1126/sciadv.aaw5805. URL: https://www.science.org/doi/abs/10.1126/sciadv.aaw5805 (cit. on p. 28).

[116] F. Wooten. *Optical properties of solids*. ACADEMIC PRESS, INC., 1972 (cit. on pp. 29, 87).

[117] S. Manzeli et al. "2D transition metal dichalcogenides". In: *Nature Reviews Materials* 2.8 (2017), p. 17033. ISSN: 2058-8437. DOI: 10.1038/natrevmats.2017.33. URL: https://doi.org/10.1038/natrevmats.2017.33 (cit. on p. 31).

[118] R. G. Dickinson and L. Pauling. "THE CRYSTAL STRUCTURE OF MOLYBDENITE". In: *Journal of the American Chemical Society* 45.6 (1923), pp. 1466–1471. ISSN: 0002-7863. DOI: 10.1021/ja01659a020. URL: https://doi.org/10.1021/ja01659a020 (cit. on p. 31).

[119] Y. Yang et al. "Advance in twisted transition metal dichalcogenides: synthesis, characterization, and properties". In: *Journal of Physics: Materials* 7.2 (2024), p. 022002. DOI: 10.1088/2515-7639/ad2b7b. URL: https://dx.doi.org/10.1088/2515-7639/ad2b7b (cit. on p. 31).

[120] D. Soranzio et al. "Impact of MoS2 Monolayers on the Thermoelastic Response of Silicon Heterostructures". In: *ACS Applied Nano Materials* 7.13 (2024), pp. 15317–15324. DOI: 10.1021/acsanm.4c02096. URL: https://doi.org/10.1021/acsanm.4c02096 (cit. on p. 31).

[121] I. Vaskivskyi et al. "A high-efficiency programmable modulator for extreme ultraviolet light with nanometre feature size based on an electronic phase transition". In: *Nature Photonics* 18.5 (2024), pp. 458–463. ISSN: 1749-4893. DOI: 10.1038/s41566-024-01389-z. URL: https://doi.org/10.1038/s41566-024-01389-z (cit. on p. 31).

[122] K. Cho et al. "Using controlled disorder to probe the interplay between charge order and superconductivity in NbSe2". In: *Nature Communications* 9.1 (2018), p. 2796. ISSN: 2041-1723. DOI: 10.1038/s41467-018-05153-0. URL: https://doi.org/10.1038/s41467-018-05153-0 (cit. on p. 31).

[123] J. Ravnik et al. "A time-domain phase diagram of metastable states in a charge ordered quantum material". In: *Nature Communications* 12.1 (2021), p. 2323. ISSN: 2041-1723. DOI: 10.1038/s41467-021-22646-7. URL: https://doi.org/10.1038/s41467-021-22646-7 (cit. on p. 31).

[124] N. Mitsuishi et al. "Switching of band inversion and topological surface states by charge density wave". In: *Nature Communications* 11.1 (2020), p. 2466. ISSN: 2041-1723. DOI: 10.1038/s41467-020-16290-w. URL: https://doi.org/10.1038/s41467-020-16290-w (cit. on pp. 31, 33, 49–51, 106, 113–115).

[125] J. Hwang et al. "Charge density waves in two-dimensional transition metal dichalcogenides". In: *Reports on Progress in Physics* 87.4 (2024), p. 044502. DOI: 10.1088/1361-6633/ad36d3. URL: https://dx.doi.org/10.1088/1361-6633/ad36d3 (cit. on p. 31).

[126] D. Lin et al. "Patterns and driving forces of dimensionality-dependent charge density waves in 2H-type transition metal dichalcogenides". In: *Nature Communications* 11.1 (2020), p. 2406. ISSN: 2041-1723. DOI: 10.1038/s41467-020-15715-w. URL: https://doi.org/10.1038/s41467-020-15715-w (cit. on p. 31).

[127] K. Bronsema, G. Bus, and G. Wiegers. "The crystal structure of vanadium ditelluride, $V_{1+x}Te_2$". In: *Journal of Solid State Chemistry* 53.3 (1984), pp. 415–421. ISSN: 0022-4596. DOI: https://doi.org/10.1016/0022-4596(84)90120-8. URL: https://www.sciencedirect.com/science/article/pii/0022459684901208 (cit. on pp. 31–32, 45–46).

[128] T. Ohtani et al. "Phase transition in $V_{1+x}Te_2$ $(0.04 < x < 0.11)$". In: *Solid State Communications* 40.5 (1981), pp. 629–631. ISSN: 0038-1098. DOI: https://doi.org/10.1016/0038-1098(81)90590-1. URL: https://www.sciencedirect.com/science/article/pii/0038109881905901 (cit. on pp. 31–32).

[129] B. E. Brown. "The crystal structures of NbT_2 and $TaTe_2$". In: *Acta Crystallographica* 20.2 (1966), pp. 264–267. DOI: 10.1107/S0365110X66000501. URL: https://doi.org/10.1107/S0365110X66000501 (cit. on p. 32).

[130] D. E. Moncton, J. D. Axe, and F. J. DiSalvo. "Neutron scattering study of the charge-density wave transitions in $2H-TaSe_2$ and $2H-NbSe_2$". In: *Phys. Rev. B* 16 (2 1977), pp. 801–819. DOI: 10.1103/PhysRevB.16.801. URL: https://link.aps.org/doi/10.1103/PhysRevB.16.801 (cit. on p. 32).

[131] R. Bianco et al. "Weak Dimensionality Dependence and Dominant Role of Ionic Fluctuations in the Charge-Density-Wave Transition of $NbSe_2$". In: *Phys. Rev. Lett.* 125 (10 2020), p. 106101. DOI: 10.1103/PhysRevLett.125.106101. URL: https://link.aps.org/doi/10.1103/PhysRevLett.125.106101 (cit. on pp. 33, 81).

[132] M. Calandra, I. I. Mazin, and F. Mauri. "Effect of dimensionality on the charge-density wave in few-layer $2H$-$NbSe_2$". In: *Phys. Rev. B* 80 (24 2009), p. 241108. DOI: 10.1103/PhysRevB.80.241108. URL: https://link.aps.org/doi/10.1103/PhysRevB.80.241108 (cit. on p. 33).

[133] T. Suzuki et al. "Ultrafast control of the crystal structure in a topological charge-density-wave material". In: *Phys. Rev. B* 108 (18 2023), p. 184305. DOI: 10.1103/PhysRevB.108.184305. URL: https://link.aps.org/doi/10.1103/PhysRevB.108.184305 (cit. on p. 33).

[134] A. Nakamura et al. "Nanoscale Imaging of Unusual Photoacoustic Waves in Thin Flake VTe2". In: *Nano Letters* 20.7 (2020). PMID: 32463678, pp. 4932–4938. DOI: 10.1021/acs.nanolett.0c01006. URL: https://doi.org/10.1021/acs.nanolett.0c01006 (cit. on p. 33).

[135] A. Nakamura et al. "Evaluation of photo-induced shear strain in monoclinic VTe2 by ultrafast electron diffraction". In: *Applied Physics Express* 11.9 (2018), p. 092601. DOI: 10.7567/APEX.11.092601. URL: https://dx.doi.org/10.7567/APEX.11.092601 (cit. on p. 33).

[136] N. Yoshikawa et al. "Ultrafast switching to an insulating-like metastable state by amplitudon excitation of a charge density wave". In: *Nature Physics* 17.8 (2021), pp. 909–914. ISSN: 1745-2481. DOI: 10.1038/s41567-021-01267-3. URL: https://doi.org/10.1038/s41567-021-01267-3 (cit. on pp. 34, 37, 83).

[137] M Porer et al. "Non-thermal separation of electronic and structural orders in a persisting charge density wave". In: *Nature Materials* 13.9 (Sept. 2014), pp. 857–861 (cit. on p. 34).

[138] M. Eichberger et al. "Snapshots of cooperative atomic motions in the optical suppression of charge density waves". In: *Nature* 468.7325 (2010), pp. 799–802. ISSN: 1476-4687. DOI: 10.1038/nature09539. URL: https://doi.org/10.1038/nature09539 (cit. on pp. 34, 37, 39, 82).

[139] H. Tanimura et al. "Nonthermal melting of charge density wave order via nucleation in VTe_2". In: *Phys. Rev. B* 105 (24 2022), p. 245402. DOI: 10.1103/PhysRevB.105.245402. URL: https://link.aps.org/doi/10.1103/PhysRevB.105.245402 (cit. on p. 35).

[140] H. J. Zeiger et al. "Theory for displacive excitation of coherent phonons". In: *Phys. Rev. B* 45 (2 1992), pp. 768–778. DOI: 10.1103/PhysRevB.45.768. URL: https://link.aps.org/doi/10.1103/PhysRevB.45.768 (cit. on p. 35).

[141] D. M. Riffe and A. J. Sabbah. "Coherent excitation of the optic phonon in Si: Transiently stimulated Raman scattering with a finite-lifetime electronic excitation". In: *Phys. Rev. B* 76 (8 2007), p. 085207. DOI: 10.1103/PhysRevB.76.085207. URL: https://link.aps.org/doi/10.1103/PhysRevB.76.085207 (cit. on p. 35).

[142] E. M. Bothschafter et al. "Ultrafast Evolution of the Excited-State Potential Energy Surface of TiO_2 Single Crystals Induced by Carrier Cooling". In: *Phys. Rev. Lett.* 110 (6 2013), p. 067402. DOI: 10.1103/PhysRevLett.110.067402. URL: https://link.aps.org/doi/10.1103/PhysRevLett.110.067402 (cit. on p. 35).

[143] P. Giannozzi et al. "QUANTUM ESPRESSO: a modular and open-source software project for quantum simulations of materials". In: *Journal of Physics: Condensed Matter* 21.39 (2009), p. 395502. DOI: 10.1088/0953-8984/21/39/395502. URL: https://dx.doi.org/10.1088/0953-8984/21/39/395502 (cit. on p. 36).

[144] P Giannozzi et al. "Advanced capabilities for materials modelling with Quantum ESPRESSO". In: *Journal of Physics: Condensed Matter* 29.46 (2017), p. 465901. DOI: 10.1088/1361-648X/aa8f79. URL: https://dx.doi.org/10.1088/1361-648X/aa8f79 (cit. on p. 36).

[145] P. Giannozzi et al. "Quantum ESPRESSO toward the exascale". In: *The Journal of Chemical Physics* 152.15 (Apr. 2020), p. 154105. ISSN: 0021-9606. DOI: 10.1063/5.0005082. URL: https://doi.org/10.1063/5.0005082 (cit. on p. 36).

[146] S. Baroni et al. "Phonons and related crystal properties from density-functional perturbation theory". In: *Rev. Mod. Phys.* 73 (2 2001), pp. 515–562. DOI: 10.1103/RevModPhys.73.515. URL: https://link.aps.org/doi/10.1103/RevModPhys.73.515 (cit. on p. 36).

[147] T. Takeda. "The scalar relativistic approximation". In: *Zeitschrift für Physik B Condensed Matter* 32.1 (1978), pp. 43–48. ISSN: 1431-584X. DOI: 10.1007/BF01322185. URL: https://doi.org/10.1007/BF01322185 (cit. on p. 36).

[148] R. Y. Chen et al. "Revealing Extremely Low Energy Amplitude Modes in the Charge-Density-Wave Compound $LaAgSb_2$". In: *Phys. Rev. Lett.* 118 (10 2017), p. 107402. DOI: 10.1103/PhysRevLett.118.107402. URL: https://link.aps.org/doi/10.1103/PhysRevLett.118.107402 (cit. on pp. 37, 83).

[149] S. Hellmann et al. "Time-domain classification of charge-density-wave insulators". In: *Nature Communications* 3.1 (2012), p. 1069. ISSN: 2041-1723. DOI: 10.1038/ncomms2078. URL: https://doi.org/10.1038/ncomms2078 (cit. on pp. 37, 99).

[150] C. Monney et al. "Robustness of the charge-ordered phases in $IrTe_2$ against photoexcitation". In: *Phys. Rev. B* 97 (7 2018), p. 075110. DOI: 10.1103/PhysRevB.97.075110. URL: https://link.aps.org/doi/10.1103/PhysRevB.97.075110 (cit. on pp. 37, 39, 57).

[151] P. J. M. Johnson, V. I. Prokhorenko, and R. J. D. Miller. "Stable UV to IR supercontinuum generation in calcium fluoride with conserved circular polarization states". In: *Opt. Express* 17.24 (2009), pp. 21488–21496. DOI: 10.1364/OE.17.021488. URL: https://opg.optica.org/oe/abstract.cfm?URI=oe-17-24-21488 (cit. on p. 40).

[152] L. Stojchevska et al. "Ultrafast Switching to a Stable Hidden Quantum State in an Electronic Crystal". In: *Science* 344.6180 (2014), pp. 177–180. DOI: 10.1126/science.1241591. URL: https://www.science.org/doi/abs/10.1126/science.1241591 (cit. on p. 40).

[153] T. Fukuda et al. "Photo-Induced Tellurium Segregation in MoTe2". In: *physica status solidi (RRL) – Rapid Research Letters* 16.9 (2022), p. 2100633. DOI: https://doi.org/10.1002/pssr.202100633. URL: https://onlinelibrary.wiley.com/doi/abs/10.1002/pssr.202100633 (cit. on p. 40).

[154] T. Shimada et al. "Indication of Te segregation in laser-irradiated ZnTe observed by in situ coherent-phonon spectroscopy". In: *Applied Physics Letters* 105.11 (Sept. 2014), p. 111908. ISSN: 0003-6951. DOI: 10.1063/1.4896039. URL: https://doi.org/10.1063/1.4896039 (cit. on p. 40).

[155] K. Norimatsu et al. "Dynamics of all the Raman-active coherent phonons in Sb2Te3 revealed via transient reflectivity". In: *Journal of Applied Physics* 117.14 (Apr. 2015), p. 143102. ISSN: 0021-8979. DOI: 10.1063/1.4917384. URL: https://doi.org/10.1063/1.4917384 (cit. on p. 40).

[156] N. Kamaraju et al. "Large-amplitude chirped coherent phonons in tellurium mediated by ultrafast photoexcited carrier diffusion". In: *Phys. Rev. B* 82 (19 2010), p. 195202. DOI: 10.1103/PhysRevB.82.195202. URL: https://link.aps.org/doi/10.1103/PhysRevB.82.195202 (cit. on p. 40).

[157] P. Kusar et al. "Anharmonic order-parameter oscillations and lattice coupling in strongly driven 1T-TaS_2 and $TbTe_3$ charge-density-wave compounds: A multiple-pulse femtosecond laser spectroscopy study". In: *Physical Review B* 83.3 (2011), p. 035104. DOI: 10.1103/PhysRevB.83.035104. URL: https://link.aps.org/doi/10.1103/PhysRevB.83.035104 (cit. on p. 41).

[158] D. Mihailovic et al. "Femtosecond data storage, processing, and search using collective excitations of a macroscopic quantum state". In: *Applied Physics Letters* 80.5 (Feb. 2002), pp. 871–873. ISSN: 0003-6951. DOI: 10.1063/1.1447594. URL: https://doi.org/10.1063/1.1447594 (cit. on p. 41).

[159] O. Y. Gorobtsov et al. "Femtosecond control of phonon dynamics near a magnetic order critical point". In: *Nature Communications* 12.1 (2021), p. 2865. ISSN: 2041-1723. DOI: 10.1038/s41467-021-23059-2. URL: https://doi.org/10.1038/s41467-021-23059-2 (cit. on p. 41).

[160] M. J. Neugebauer et al. "Optical control of vibrational coherence triggered by an ultrafast phase transition". In: *Phys. Rev. B* 99 (22 2019), p. 220302. DOI: 10.1103/PhysRevB.99.220302. URL: https://link.aps.org/doi/10.1103/PhysRevB.99.220302 (cit. on p. 41).

[161] S. Michael and H. C. Schneider. "Optical amplification in a charge density wave phase of a quasi-two-dimensional material". In: *Phys. Rev. B* 105 (23 2022), p. 235108. DOI: 10.1103/PhysRevB.105.235108. URL: https://link.aps.org/doi/10.1103/PhysRevB.105.235108 (cit. on p. 41).

[162] K. G. Nakamura et al. "Ultrafast quantum-path interferometry revealing the generation process of coherent phonons". In: *Phys. Rev. B* 99 (18 2019), p. 180301. DOI: 10.1103/PhysRevB.99.180301. URL: https://link.aps.org/doi/10.1103/PhysRevB.99.180301 (cit. on p. 41).

[163] A. Bartels et al. "Coherent control of acoustic phonons in semiconductor superlattices". In: *Applied Physics Letters* 72.22 (June 1998), pp. 2844–2846. ISSN: 0003-6951. DOI: 10.1063/1.121476. URL: https://doi.org/10.1063/1.121476 (cit. on p. 41).

[164] L. Rettig et al. "Coherent dynamics of the charge density wave gap in tritellurides". In: *Faraday Discuss.* 171 (0 2014), pp. 299–310. DOI: 10.1039/C4FD00045E. URL: http://dx.doi.org/10.1039/C4FD00045E (cit. on pp. 41–42).

[165] T. Onozaki et al. "Coherent Double-Pulse Excitation of Charge-Density-Wave Oscillation". In: *Japanese Journal of Applied Physics* 46.2R (2007), p. 870. DOI: 10.1143/JJAP.46.870. URL: https://dx.doi.org/10.1143/JJAP.46.870 (cit. on p. 42).

[166] H. Sasaki et al. "Coherent control theory and experiment of optical phonons in diamond". In: *Scientific Reports* 8.1 (2018), p. 9609. ISSN: 2045-2322. DOI: 10.1038/s41598-018-27734-1. URL: https://doi.org/10.1038/s41598-018-27734-1 (cit. on p. 42).

[167] Y.-H. Cheng et al. "Coherent control of optical phonons in bismuth". In: *Phys. Rev. B* 96 (13 2017), p. 134302. DOI: 10.1103/PhysRevB.96.134302. URL: https://link.aps.org/doi/10.1103/PhysRevB.96.134302 (cit. on p. 42).

[168] J.-H. Chu et al. "Divergent Nematic Susceptibility in an Iron Arsenide Superconductor". In: *Science* 337.6095 (2012), pp. 710–712. DOI: 10.1126/science.1221713. URL: https://www.science.org/doi/abs/10.1126/science.1221713 (cit. on p. 46).

[169] C. W. Hicks et al. "Strong Increase of T_c of Sr_2RuO_4 Under Both Tensile and Compressive Strain". In: *Science* 344.6181 (2014), pp. 283–285. DOI: 10.1126/science.1248292. URL: https://www.science.org/doi/abs/10.1126/science.1248292 (cit. on p. 46).

[170] D. O. Brodsky et al. "Strain and vector magnetic field tuning of the anomalous phase in $Sr_3Ru_2O_7$". In: *Science Advances* 3.2 (2017), e1501804. DOI: 10.1126/sciadv.1501804. URL: https://www.science.org/doi/abs/10.1126/sciadv.1501804 (cit. on p. 46).

[171] H.-H. Kim et al. "Uniaxial pressure control of competing orders in a high-temperature superconductor". In: *Science* 362.6418 (2018), pp. 1040–1044. DOI: 10.1126/science.aat4708. URL: https://www.science.org/doi/abs/10.1126/science.aat4708 (cit. on p. 46).

[172] R. Roldán et al. "Strain engineering in semiconducting two-dimensional crystals". In: *Journal of Physics: Condensed Matter* 27.31 (2015), p. 313201. DOI: 10.1088/0953-8984/27/31/313201. URL: https://dx.doi.org/10.1088/0953-8984/27/31/313201 (cit. on p. 46).

[173] V. Sunko et al. "Direct observation of a uniaxial stress-driven Lifshitz transition in Sr2RuO4". In: *npj Quantum Materials* 4.1 (2019), p. 46. ISSN: 2397-4648. DOI: 10.1038/s41535-019-0185-9. URL: https://doi.org/10.1038/s41535-019-0185-9 (cit. on p. 46).

[174] S. Riccò et al. "In situ strain tuning of the metal-insulator-transition of Ca2RuO4 in angle-resolved photoemission experiments". In: *Nature Communications* 9.1 (2018), p. 4535. ISSN: 2041-1723. DOI: 10.1038/s41467-018-06945-0. URL: https://doi.org/10.1038/s41467-018-06945-0 (cit. on pp. 46, 48).

[175] C. W. Nicholson et al. "Gap collapse and flat band induced by uniaxial strain in $1T-TaS_2$". In: *Phys. Rev. B* 109 (3 2024), p. 035167. DOI: 10.1103/PhysRevB.109.035167. URL: https://link.aps.org/doi/10.1103/PhysRevB.109.035167 (cit. on p. 46).

[176] C. W. Nicholson et al. "Uniaxial strain-induced phase transition in the 2D topological semimetal IrTe2". In: *Communications Materials* 2.1 (2021), p. 25. ISSN: 2662-4443. DOI: 10.1038/s43246-021-00130-5. URL: https://doi.org/10.1038/s43246-021-00130-5 (cit. on pp. 46, 48).

[177] K. Hoffmann. *Applying the Wheatstone Bridge Circuit*. Technical note: HBM S1569-1.1. 2001 (cit. on p. 48).

[178] L. X. Yang et al. "Bypassing the Structural Bottleneck in the Ultrafast Melting of Electronic Order". In: *Phys. Rev. Lett.* 125 (26 2020), p. 266402. DOI: 10.1103/PhysRevLett.125.266402. URL: https://link.aps.org/doi/10.1103/PhysRevLett.125.266402 (cit. on pp. 54–55, 70, 73).

[179] A. Crepaldi et al. "Ultrafast photodoping and effective Fermi-Dirac distribution of the Dirac particles in Bi_2Se_3". In: *Phys. Rev. B* 86 (20 2012), p. 205133. DOI: 10.1103/PhysRevB.86.205133. URL: https://link.aps.org/doi/10.1103/PhysRevB.86.205133 (cit. on p. 54).

[180] F Schmitt et al. "Ultrafast electron dynamics in the charge density wave material TbTe3". In: *New Journal of Physics* 13.6 (2011), p. 063022. DOI: 10.1088/1367-2630/13/6/063022. URL: https://dx.doi.org/10.1088/1367-2630/13/6/063022 (cit. on p. 54).

[181] J. Maklar et al. "Coherent light control of a metastable hidden state". In: *Science Advances* 9.47 (2023), eadi4661. DOI: 10.1126/sciadv.adi4661. URL: https://www.science.org/doi/abs/10.1126/sciadv.adi4661 (cit. on p. 54).

[182] L. Perfetti et al. "Mobile small polarons and the Peierls transition in the quasi-one-dimensional conductor $K_{0.3}MoO_3$". In: *Phys. Rev. B* 66 (7 2002), p. 075107. DOI: 10.1103/PhysRevB.66.075107. URL: https://link.aps.org/doi/10.1103/PhysRevB.66.075107 (cit. on p. 55).

[183] J. Maklar et al. "Coherent Modulation of Quasiparticle Scattering Rates in a Photoexcited Charge-Density-Wave System". In: *Phys. Rev. Lett.* 128 (2 2022), p. 026406. DOI: 10.1103/PhysRevLett.128.026406. URL: https://link.aps.org/doi/10.1103/PhysRevLett.128.026406 (cit. on p. 56).

[184] J. M. Harris et al. "Anomalous superconducting state gap size versus T_c behavior in underdoped $Bi_2Sr_2Ca_{1-x}Dy_xCu_2O_{8+\delta}$". In: *Phys. Rev. B* 54 (22 1996), R15665–R15668. DOI: 10.1103/PhysRevB.54.R15665. URL: https://link.aps.org/doi/10.1103/PhysRevB.54.R15665 (cit. on p. 56).

[185] H. Ding et al. "Spectroscopic evidence for a pseudogap in the normal state of underdoped high-Tc superconductors". In: *Nature* 382.6586 (1996), pp. 51–54. ISSN: 1476-4687. DOI: 10.1038/382051a0. URL: https://doi.org/10.1038/382051a0 (cit. on p. 56).

[186] A. G. Loeser et al. "Excitation Gap in the Normal State of Underdoped $Bi_2Sr_2CaCu_2O_{8+\delta}$". In: *Science* 273.5273 (1996), pp. 325–329. DOI: 10.1126/science.273.5273.325. URL: https://www.science.org/doi/abs/10.1126/science.273.5273.325 (cit. on p. 56).

[187] S. I. Anisimov, B. L. Kapeliovich, and T. L. Perel'Man. "Electron emission from metal surfaces exposed to ultrashort laser pulses". In: *Soviet Journal of Experimental and Theoretical Physics* 39 (Aug. 1974), pp. 375–377 (cit. on p. 57).

[188] P. B. Allen. "Theory of thermal relaxation of electrons in metals". In: *Phys. Rev. Lett.* 59 (13 1987), pp. 1460–1463. DOI: 10.1103/PhysRevLett.59.1460. URL: https://link.aps.org/doi/10.1103/PhysRevLett.59.1460 (cit. on pp. 57–59).

[189] P. E. Dolgirev et al. "Amplitude dynamics of the charge density wave in $LaTe_3$: Theoretical description of pump-probe experiments". In: *Phys. Rev. B* 101 (5 2020), p. 054203. DOI: 10.1103/PhysRevB.101.054203. URL: https://link.aps.org/doi/10.1103/PhysRevB.101.054203 (cit. on pp. 57–58, 61).

[190] F. Cilento. "Non-equilibrium phase diagram of $Bi_2Sr_2Y_{0.08}Ca_{0.92}Cu_2O_{8+\delta}$ cuprate superconductors revealed by ultrafast optical spectroscopy". PhD Thesis. Università degli studi di Trieste, 2012. URL: http://hdl.handle.net/10077/6689 (cit. on pp. 58–60, 87).

[191] S. Brorson et al. "Femtosecond thermomodulation study of high-Tc superconductors". In: *Solid State Communications* 74.12 (1990), pp. 1305–1308. ISSN: 0038-1098. DOI: https://doi.org/10.1016/0038-1098(90)90997-P. URL: https://www.sciencedirect.com/science/article/pii/003810989090997P (cit. on p. 58).

[192] L. Waldecker et al. "Electron-Phonon Coupling and Energy Flow in a Simple Metal beyond the Two-Temperature Approximation". In: *Phys. Rev. X* 6 (2 2016), p. 021003. DOI: 10.1103/PhysRevX.6.021003. URL: https://link.aps.org/doi/10.1103/PhysRevX.6.021003 (cit. on p. 58).

[193] J. D. Rameau et al. "Energy dissipation from a correlated system driven out of equilibrium". In: *Nature Communications* 7.1 (2016), p. 13761. ISSN: 2041-1723. DOI: 10.1038/ncomms13761. URL: https://doi.org/10.1038/ncomms13761 (cit. on p. 60).

[194] L. P. René de Cotret et al. "Time- and momentum-resolved phonon population dynamics with ultrafast electron diffuse scattering". In: *Phys. Rev. B* 100 (21 2019), p. 214115. DOI: 10.1103/PhysRevB.100.214115. URL: https://link.aps.org/doi/10.1103/PhysRevB.100.214115 (cit. on pp. 60, 62, 73).

[195] S. Girault, A. H. Moudden, and J. P. Pouget. "Critical x-ray scattering at the Peierls transition of the blue bronze". In: *Phys. Rev. B* 39 (7 1989), pp. 4430–4434. DOI: 10.1103/PhysRevB.39.4430. URL: https://link.aps.org/doi/10.1103/PhysRevB.39.4430 (cit. on p. 60).

[196] J. D. Budai et al. "Metallization of vanadium dioxide driven by large phonon entropy". In: *Nature* 515.7528 (2014), pp. 535–539. ISSN: 1476-4687. DOI: 10.1038/nature13865. URL: https://doi.org/10.1038/nature13865 (cit. on pp. 60, 64–65, 73).

[197] A. D. Bruce. "Structural phase transitions. II. Static critical behaviour". In: *Advances in Physics* 29.1 (1980), pp. 111–217. DOI: 10.1080/00018738000101356. URL: https://doi.org/10.1080/00018738000101356 (cit. on p. 60).

[198] A. M. Lindenberg et al. "Atomic-Scale Visualization of Inertial Dynamics". In: *Science* 308.5720 (2005), pp. 392–395. DOI: 10.1126/science.1107996. URL: https://www.science.org/doi/abs/10.1126/science.1107996 (cit. on p. 60).

[199] G. A. de la Peña Muñoz et al. "Ultrafast lattice disordering can be accelerated by electronic collisional forces". In: *Nature Physics* 19.10 (2023), pp. 1489–1494. ISSN: 1745-2481. DOI: 10.1038/s41567-023-02118-z. URL: https://doi.org/10.1038/s41567-023-02118-z (cit. on pp. 60, 73, 98).

[200] D. A. Keen and A. L. Goodwin. "The crystallography of correlated disorder". In: *Nature* 521.7552 (2015), pp. 303–309. ISSN: 1476-4687. DOI: 10.1038/nature14453. URL: https://doi.org/10.1038/nature14453 (cit. on p. 60).

[201] A. S. Johnson et al. "All-optical seeding of a light-induced phase transition with correlated disorder". In: *Nature Physics* 20.6 (2024), pp. 970–975. ISSN: 1745-2481. DOI: 10.1038/s41567-024-02474-4. URL: https://doi.org/10.1038/s41567-024-02474-4 (cit. on p. 60).

[202] S. Baronio et al. "Vibrational Fine Structure in C 1s High-Resolution Core-Level Spectra of CO Chemisorbed on Ir(111)". In: *The Journal of Physical Chemistry C* 126.3 (2022), pp. 1411–1419. DOI: 10.1021/acs.jpcc.1c09646. URL: https://doi.org/10.1021/acs.jpcc.1c09646 (cit. on pp. 61, 91).

[203] M Bianchi et al. "Surface core level shifts of clean and oxygen covered Ir(111)". In: *New Journal of Physics* 11.6 (2009), p. 063002. DOI: 10.1088/1367-2630/11/6/063002. URL: https://dx.doi.org/10.1088/1367-2630/11/6/063002 (cit. on pp. 61, 91).

[204] S. Cha et al. "Order-disorder phase transition driven by interlayer sliding in lead iodides". In: *Nature Communications* 14.1 (2023), p. 1981. ISSN: 2041-1723. DOI: 10.1038/s41467-023-37740-1. URL: https://doi.org/10.1038/s41467-023-37740-1 (cit. on p. 64).

[205] A. Picano, F. Grandi, and M. Eckstein. "Inhomogeneous disordering at a photoinduced charge density wave transition". In: *Phys. Rev. B* 107 (24 2023), p. 245112. DOI: 10.1103/PhysRevB.107.245112. URL: https://link.aps.org/doi/10.1103/PhysRevB.107.245112 (cit. on p. 64).

[206] N. Erasmus et al. "Ultrafast Dynamics of Charge Density Waves in $4H_b-TaSe_2$ Probed by Femtosecond Electron Diffraction". In: *Phys. Rev. Lett.* 109 (16 2012), p. 167402. DOI: 10.1103/PhysRevLett.109.167402. URL: https://link.aps.org/doi/10.1103/PhysRevLett.109.167402 (cit. on p. 64).

[207] A. Block et al. "Tracking ultrafast hot-electron diffusion in space and time by ultrafast thermomodulation microscopy". In: *Science Advances* 5.5 (2019), eaav8965. DOI: 10.1126/sciadv.aav8965. URL: https://www.science.org/doi/abs/10.1126/sciadv.aav8965 (cit. on pp. 64, 107).

[208] D. Perez-Salinas et al. "Multi-mode excitation drives disorder during the ultrafast melting of a C4-symmetry-broken phase". In: *Nature Communications* 13.1 (2022), p. 238. ISSN: 2041-1723. DOI: 10.1038/s41467-021-27819-y. URL: https://doi.org/10.1038/s41467-021-27819-y (cit. on p. 64).

[209] D. Won et al. "Polymorphic Spin, Charge, and Lattice Waves in Vanadium Ditelluride". In: *Advanced Materials* 32.11 (2020), p. 1906578. DOI: https://doi.org/10.1002/adma.201906578. URL: https://onlinelibrary.wiley.com/doi/abs/10.1002/adma.201906578 (cit. on pp. 66, 110).

[210] G Grimvall. "The Electron-Phonon Interaction in Normal Metals". In: *Physica Scripta* 14.1-2 (1976), p. 63. DOI: 10.1088/0031-8949/14/1-2/013. URL: https://dx.doi.org/10.1088/0031-8949/14/1-2/013 (cit. on p. 66).

[211] R. Mankowsky et al. "Dynamical Stability Limit for the Charge Density Wave in $K_{0.3}MoO_3$". In: *Phys. Rev. Lett.* 118 (11 2017), p. 116402. DOI: 10.1103/PhysRevLett.118.116402. URL: https://link.aps.org/doi/10.1103/PhysRevLett.118.116402 (cit. on p. 67).

[212] C. Monney et al. "Revealing the role of electrons and phonons in the ultrafast recovery of charge density wave correlations in 1T−$TiSe_2$". In: *Phys. Rev. B* 94 (16 2016), p. 165165. DOI: 10.1103/PhysRevB.94.165165. URL: https://link.aps.org/doi/10.1103/PhysRevB.94.165165 (cit. on pp. 67, 69).

[213] K. M. Siddiqui et al. "Ultrafast optical melting of trimer superstructure in layered 1T-$TaTe_2$". In: *Communications Physics* 4.1 (2021), p. 152. ISSN: 2399-3650. DOI: 10.1038/s42005-021-00650-z. URL: https://doi.org/10.1038/s42005-021-00650-z (cit. on p. 67).

[214] T. E. Glover et al. "Observation of Laser Assisted Photoelectric Effect and Femtosecond High Order Harmonic Radiation". In: *Phys. Rev. Lett.* 76 (14 1996), pp. 2468–2471. DOI: 10.1103/PhysRevLett.76.2468. URL: https://link.aps.org/doi/10.1103/PhysRevLett.76.2468 (cit. on p. 69).

[215] Z. Tao et al. "Direct time-domain observation of attosecond final-state lifetimes in photoemission from solids". In: *Science* 353.6294 (2016), pp. 62–67. DOI: 10.1126/science.aaf6793. URL: https://www.science.org/doi/abs/10.1126/science.aaf6793 (cit. on p. 69).

[216] G. Saathoff et al. "Laser-assisted photoemission from surfaces". In: *Phys. Rev. A* 77 (2 2008), p. 022903. DOI: 10.1103/PhysRevA.77.022903. URL: https://link.aps.org/doi/10.1103/PhysRevA.77.022903 (cit. on p. 69).

[217] T. Valla et al. "Many-Body Effects in Angle-Resolved Photoemission: Quasiparticle Energy and Lifetime of a Mo(110) Surface State". In: *Phys. Rev. Lett.* 83 (10 1999), pp. 2085–2088. DOI: 10.1103/PhysRevLett.83.2085. URL: https://link.aps.org/doi/10.1103/PhysRevLett.83.2085 (cit. on p. 71).

[218] M. Kang et al. "Dirac fermions and flat bands in the ideal kagome metal FeSn". In: *Nature Materials* 19.2 (2020), pp. 163–169. ISSN: 1476-4660. DOI: 10.1038/s41563-019-0531-0. URL: https://doi.org/10.1038/s41563-019-0531-0 (cit. on p. 75).

[219] M. Kang et al. "Topological flat bands in frustrated kagome lattice CoSn". In: *Nature Communications* 11.1 (2020), p. 4004. ISSN: 2041-1723. DOI: 10.1038/s41467-020-17465-1. URL: https://doi.org/10.1038/s41467-020-17465-1 (cit. on pp. 75–76).

[220] V. I. Iglovikov et al. "Superconducting transitions in flat-band systems". In: *Phys. Rev. B* 90 (9 2014), p. 094506. DOI: 10.1103/PhysRevB.90.094506. URL: https://link.aps.org/doi/10.1103/PhysRevB.90.094506 (cit. on p. 75).

[221] K. Jiang et al. "Kagome superconductors AV3Sb5 (A = K, Rb, Cs)". In: *National Science Review* 10.2 (Sept. 2022), nwac199. ISSN: 2095-5138. DOI: 10.1093/nsr/nwac199. URL: https://doi.org/10.1093/nsr/nwac199 (cit. on p. 75).

[222] S. Lee et al. "Nature of charge density wave in kagome metal ScV6Sn6". In: *npj Quantum Materials* 9.1 (2024), p. 15. ISSN: 2397-4648. DOI: 10.1038/s41535-024-00620-y. URL: https://doi.org/10.1038/s41535-024-00620-y (cit. on pp. 75, 77–81, 88).

[223] S. D. Huber and E. Altman. "Bose condensation in flat bands". In: *Phys. Rev. B* 82 (18 2010), p. 184502. DOI: 10.1103/PhysRevB.82.184502. URL: https://link.aps.org/doi/10.1103/PhysRevB.82.184502 (cit. on p. 75).

[224] T. Neupert et al. "Fractional Quantum Hall States at Zero Magnetic Field". In: *Phys. Rev. Lett.* 106 (23 2011), p. 236804. DOI: 10.1103/PhysRevLett.106.236804. URL: https://link.aps.org/doi/10.1103/PhysRevLett.106.236804 (cit. on p. 75).

[225] A Mielke. "Exact ground states for the Hubbard model on the Kagome lattice". In: *Journal of Physics A: Mathematical and General* 25.16 (1992), p. 4335. DOI: 10.1088/0305-4470/25/16/011. URL: https://dx.doi.org/10.1088/0305-4470/25/16/011 (cit. on p. 75).

[226] Y. Xie et al. "Spin excitations in metallic kagome lattice FeSn and CoSn". In: *Communications Physics* 4.1 (2021), p. 240. ISSN: 2399-3650. DOI: 10.1038/s42005-021-00736-8. URL: https://doi.org/10.1038/s42005-021-00736-8 (cit. on p. 75).

[227] B. Sutherland. "Localization of electronic wave functions due to local topology". In: *Phys. Rev. B* 34 (8 1986), pp. 5208–5211. DOI: 10.1103/PhysRevB.34.5208. URL: https://link.aps.org/doi/10.1103/PhysRevB.34.5208 (cit. on p. 75).

[228] H.-M. Guo and M. Franz. "Topological insulator on the kagome lattice". In: *Phys. Rev. B* 80 (11 2009), p. 113102. DOI: 10.1103/PhysRevB.80.113102. URL: https://link.aps.org/doi/10.1103/PhysRevB.80.113102 (cit. on p. 75).

[229] K. Sun et al. "Nearly Flatbands with Nontrivial Topology". In: *Phys. Rev. Lett.* 106 (23 2011), p. 236803. DOI: 10.1103/PhysRevLett.106.236803. URL: https://link.aps.org/doi/10.1103/PhysRevLett.106.236803 (cit. on p. 75).

[230] Y. Hu et al. "Rich nature of Van Hove singularities in Kagome superconductor CsV3Sb5". In: *Nature Communications* 13.1 (2022), p. 2220. ISSN: 2041-1723. DOI: 10.1038/s41467-022-29828-x. URL: https://doi.org/10.1038/s41467-022-29828-x (cit. on p. 76).

[231] S.-L. Yu and J.-X. Li. "Chiral superconducting phase and chiral spin-density-wave phase in a Hubbard model on the kagome lattice". In: *Phys. Rev. B* 85 (14 2012), p. 144402. DOI: 10.1103/PhysRevB.85.144402. URL: https://link.aps.org/doi/10.1103/PhysRevB.85.144402 (cit. on p. 76).

[232] S. Cho et al. "Emergence of New van Hove Singularities in the Charge Density Wave State of a Topological Kagome Metal RbV_3Sb_5". In: *Phys. Rev. Lett.* 127 (23 2021), p. 236401. DOI: 10.1103/PhysRevLett.127.236401. URL: https://link.aps.org/doi/10.1103/PhysRevLett.127.236401 (cit. on pp. 76, 79).

[233] X. Zhou et al. "Origin of charge density wave in the kagome metal CsV_3Sb_5 as revealed by optical spectroscopy". In: *Phys. Rev. B* 104 (4 2021), p. L041101. DOI: 10.1103/PhysRevB.104.L041101. URL: https://link.aps.org/doi/10.1103/PhysRevB.104.L041101 (cit. on p. 76).

[234] Z. Liu et al. "Charge-Density-Wave-Induced Bands Renormalization and Energy Gaps in a Kagome Superconductor RbV_3Sb_5". In: *Phys. Rev. X* 11 (4 2021), p. 041010. DOI: 10.1103/PhysRevX.11.041010. URL: https://link.aps.org/doi/10.1103/PhysRevX.11.041010 (cit. on p. 76).

[235] M. L. Kiesel and R. Thomale. "Sublattice interference in the kagome Hubbard model". In: *Phys. Rev. B* 86 (12 2012), p. 121105. DOI: 10.1103/PhysRevB.86.121105. URL: https://link.aps.org/doi/10.1103/PhysRevB.86.121105 (cit. on p. 76).

[236] M. L. Kiesel, C. Platt, and R. Thomale. "Unconventional Fermi Surface Instabilities in the Kagome Hubbard Model". In: *Phys. Rev. Lett.* 110 (12 2013), p. 126405. DOI: 10.1103/PhysRevLett.110.126405. URL: https://link.aps.org/doi/10.1103/PhysRevLett.110.126405 (cit. on p. 76).

[237] K. Kuroda et al. "Evidence for magnetic Weyl fermions in a correlated metal". In: *Nature Materials* 16.11 (2017), pp. 1090–1095. ISSN: 1476-4660. DOI: 10.1038/nmat4987. URL: https://doi.org/10.1038/nmat4987 (cit. on p. 76).

[238] Z. Lin et al. "Flatbands and Emergent Ferromagnetic Ordering in Fe_3Sn_2 Kagome Lattices". In: *Phys. Rev. Lett.* 121 (9 2018), p. 096401. DOI: 10.1103/PhysRevLett.121.096401. URL: https://link.aps.org/doi/10.1103/PhysRevLett.121.096401 (cit. on p. 76).

[239] M. Tuniz et al. "Dynamics and resilience of the unconventional charge density wave in ScV6Sn6 bilayer kagome metal". In: *Communications Materials* 4.1 (2023), p. 103. ISSN: 2662-4443. DOI: 10.1038/s43246-023-00430-y. URL: https://doi.org/10.1038/s43246-023-00430-y (cit. on pp. 77–81, 83–85).

[240] G. Pokharel et al. "Electronic properties of the topological kagome metals YV_6Sn_6 and GdV_6Sn_6". In: *Phys. Rev. B* 104 (23 2021), p. 235139. DOI: 10.1103/PhysRevB.104.235139. URL: https://link.aps.org/doi/10.1103/PhysRevB.104.235139 (cit. on p. 77).

[241] E. Rosenberg et al. "Uniaxial ferromagnetism in the kagome metal TbV_6Sn_6". In: *Phys. Rev. B* 106 (11 2022), p. 115139. DOI: 10.1103/PhysRevB.106.115139. URL: https://link.aps.org/doi/10.1103/PhysRevB.106.115139 (cit. on p. 77).

[242] A. K. Kundu et al. "Low-energy electronic structure in the unconventional charge-ordered state of ScV6Sn6". In: *Nature Communications* 15.1 (2024), p. 5008. ISSN: 2041-1723. DOI: 10.1038/s41467-024-48883-0. URL: https://doi.org/10.1038/s41467-024-48883-0 (cit. on p. 77).

[243] H. W. S. Arachchige et al. "Charge Density Wave in Kagome Lattice Intermetallic ScV_6Sn_6". In: *Phys. Rev. Lett.* 129 (21 2022), p. 216402. DOI: 10.1103/PhysRevLett.129.216402. URL: https://link.aps.org/doi/10.1103/PhysRevLett.129.216402 (cit. on pp. 77–78, 81, 86).

[244] G. Venturini. "Filling the CoSn host-cell: the HfFe6Ge6-type and the related structures". In: *Zeitschrift für Kristallographie - Crystalline Materials* 221.5-7 (2006), pp. 511–520. DOI: doi:10.1524/zkri.2006.221.5-7.511. URL: https://doi.org/10.1524/zkri.2006.221.5-7.511 (cit. on p. 77).

[245] B. R. Ortiz et al. "New kagome prototype materials: discovery of KV_3Sb_5, RbV_3Sb_5, and CsV_3Sb_5". In: *Phys. Rev. Mater.* 3 (9 2019), p. 094407. DOI: 10.1103/PhysRevMaterials.3.094407. URL: https://link.aps.org/doi/10.1103/PhysRevMaterials.3.094407 (cit. on p. 77).

[246] K. Nakayama et al. "Multiple energy scales and anisotropic energy gap in the charge-density-wave phase of the kagome superconductor CsV_3Sb_5". In: *Phys. Rev. B* 104 (16 2021), p. L161112. DOI: 10.1103/PhysRevB.104.L161112. URL: https://link.aps.org/doi/10.1103/PhysRevB.104.L161112 (cit. on p. 79).

[247] T. Kato et al. "Three-dimensional energy gap and origin of charge-density wave in kagome superconductor KV3Sb5". In: *Communications Materials* 3.1 (2022), p. 30. ISSN: 2662-4443. DOI: 10.1038/s43246-022-00255-1. URL: https://doi.org/10.1038/s43246-022-00255-1 (cit. on p. 79).

[248] R. V. Yusupov et al. "Single-Particle and Collective Mode Couplings Associated with 1- and 2-Directional Electronic Ordering in Metallic RTe_3 (R = Ho, Dy, Tb)". In: *Phys. Rev. Lett.* 101 (24 2008), p. 246402. DOI: 10.1103/PhysRevLett.101.246402. URL: https://link.aps.org/doi/10.1103/PhysRevLett.101.246402 (cit. on p. 83).

[249] V. V. Kabanov et al. "Quasiparticle relaxation dynamics in superconductors with different gap structures: Theory and experiments on $YBa_2Cu_3O_{7-\text{ffi}}$". In: *Phys. Rev. B* 59 (2 1999), pp. 1497–1506. DOI: 10.1103/PhysRevB.59.1497. URL: https://link.aps.org/doi/10.1103/PhysRevB.59.1497 (cit. on p. 83).

[250] J. Demsar et al. "Femtosecond snapshots of gap-forming charge-density-wave correlations in quasi-two-dimensional dichalcogenides 1T-TaS_2 and 2H-$TaSe_2$". In: *Phys. Rev. B* 66 (4 2002), p. 041101. DOI: 10.1103/PhysRevB.66.041101. URL: https://link.aps.org/doi/10.1103/PhysRevB.66.041101 (cit. on p. 83).

[251] T. Hu et al. "Optical spectroscopy and band structure calculations of the structural phase transition in the vanadium-based kagome metal ScV_6Sn_6". In: *Phys. Rev. B* 107 (16 2023), p. 165119. DOI: 10.1103/PhysRevB.107.165119. URL: https://link.aps.org/doi/10.1103/PhysRevB.107.165119 (cit. on pp. 86–87, 92).

[252] N. Ashcroft and N. Mermin. *Solid State Physics*. HRW international editions. Holt, Rinehart and Winston, 1976. ISBN: 9780030839931. URL: https://books.google.it/books?id=1C9HAQAAIAAJ (cit. on p. 86).

[253] E. Uykur et al. "Low-energy optical properties of the nonmagnetic kagome metal CsV_3Sb_5". In: *Phys. Rev. B* 104 (4 2021), p. 045130. DOI: 10.1103/PhysRevB.104.045130. URL: https://link.aps.org/doi/10.1103/PhysRevB.104.045130 (cit. on p. 87).

[254] X. Zhou et al. "Origin of charge density wave in the kagome metal CsV_3Sb_5 as revealed by optical spectroscopy". In: *Phys. Rev. B* 104 (4 2021), p. L041101. DOI: 10.1103/PhysRevB.104.L041101. URL: https://link.aps.org/doi/10.1103/PhysRevB.104.L041101 (cit. on p. 87).

[255] P. Kusar et al. "Controlled Vaporization of the Superconducting Condensate in Cuprate Superconductors by Femtosecond Photoexcitation". In: *Phys. Rev. Lett.* 101 (22 2008), p. 227001. DOI: 10.1103/PhysRevLett.101.227001. URL: https://link.aps.org/doi/10.1103/PhysRevLett.101.227001 (cit. on p. 87).

[256] F. J. dos Santos and N. Marzari. "Fermi energy determination for advanced smearing techniques". In: *Phys. Rev. B* 107 (19 2023), p. 195122. DOI: 10.1103/PhysRevB.107.195122. URL: https://link.aps.org/doi/10.1103/PhysRevB.107.195122 (cit. on p. 88).

[257] Z. X. Wang et al. "Unconventional charge density wave and photoinduced lattice symmetry change in the kagome metal CsV_3Sb_5 probed by time-resolved spectroscopy". In: *Phys. Rev. B* 104 (16 2021), p. 165110. DOI: 10.1103/PhysRevB.104.165110. URL: https://link.aps.org/doi/10.1103/PhysRevB.104.165110 (cit. on p. 89).

[258] M. Tuniz et al. *Strain-induced enhancement of the charge-density-wave in the kagome metal ScV_6Sn_6*. 2024. URL: https://arxiv.org/abs/2403.18046 (cit. on pp. 89–94).

[259] S. Kim et al. "Emergent symmetry in TbTe3 revealed by ultrafast reflectivity under anisotropic strain". In: *Reports on Progress in Physics* 87.10 (2024), p. 100501. DOI: 10.1088/1361-6633/ad71ee. URL: https://dx.doi.org/10.1088/1361-6633/ad71ee (cit. on pp. 92, 96).

[260] S. Dolabella et al. "Lattice Strain and Defects Analysis in Nanostructured Semiconductor Materials and Devices by High-Resolution X-Ray Diffraction: Theoretical and Practical Aspects". In: *Small Methods* 6.2 (2022), p. 2100932. DOI: https://doi.org/10.1002/smtd.202100932. URL: https://onlinelibrary.wiley.com/doi/abs/10.1002/smtd.202100932 (cit. on p. 93).

[261] J. López-Villegas et al. "Structure and non-uniform strain analysis on p-type porous silicon by X-ray reflectometry and X-ray diffraction". In: *Thin Solid Films* 276.1 (1996). Papers presented at the European Materials Research Society 1995 Spring Conference, Symposium I: Porous Silicon: Material, Technology and Devices, pp. 238–240. ISSN: 0040-6090. DOI: https://doi.org/10.1016/0040-6090(95)08130-5. URL: https://www.sciencedirect.com/science/article/pii/0040609095081305 (cit. on p. 93).

[262] G. Kresse and J. Furthmüller. "Efficient iterative schemes for ab initio total-energy calculations using a plane-wave basis set". In: *Phys. Rev. B* 54 (16 1996), pp. 11169–11186. DOI: 10.1103/PhysRevB.54.11169. URL: https://link.aps.org/doi/10.1103/PhysRevB.54.11169 (cit. on p. 93).

[263] G. Kresse and D. Joubert. "From ultrasoft pseudopotentials to the projector augmented-wave method". In: *Phys. Rev. B* 59 (3 1999), pp. 1758–1775. DOI: 10.1103/PhysRevB.59.1758. URL: https://link.aps.org/doi/10.1103/PhysRevB.59.1758 (cit. on p. 93).

[264] P. E. Blöchl. "Projector augmented-wave method". In: *Phys. Rev. B* 50 (24 1994), pp. 17953–17979. DOI: 10.1103/PhysRevB.50.17953. URL: https://link.aps.org/doi/10.1103/PhysRevB.50.17953 (cit. on p. 93).

[265] I. Vaskivskyi et al. "Controlling the metal-to-insulator relaxation of the metastable hidden quantum state in 1T-TaS_2". In: *Science Advances* 1.6 (2015), e1500168. DOI: 10.1126/sciadv.1500168 (cit. on p. 99).

[266] D. Loke et al. "Breaking the Speed Limits of Phase-Change Memory". In: *Science* 336.6088 (2012), pp. 1566–1569. DOI: 10.1126/science.1221561. URL: https://www.science.org/doi/abs/10.1126/science.1221561 (cit. on p. 99).

LIST OF PUBLICATIONS

1. **Manuel Tuniz**, Armando Consiglio, Ganesh Pokharel, Fulvio Parmigiani, Titus Neupert, Ronny Thomale, Giorgio Sangiovanni, Stephen D. Wilson, Ivana Vobornik, Federico Salvador, Federico Cilento, Domenico Di Sante and Federico Mazzola, "Strain-induced enhancement of the charge-density-wave in the kagome metal ScV_6Sn_6". Preprint at arXiv:2403.18046, submitted to PRL.

2. **Manuel Tuniz**, Davide Soranzio, Davide Bidoggia, Denny Puntel, Wibke Bronsch, Steven L. Johnson, Maria Peressi, Fulvio Parmigiani and Federico Cilento, "Ultrafast all-optical manipulation of the charge-density-wave in VTe_2". Phys. Rev. Research 5, 043276 (2023).

3. **Manuel Tuniz**, Armando Consiglio, Denny Puntel, Chiara Bigi, Stefan Enzner, Ganesh Pokharel, Pasquale Orgiani, Wibke Bronsch, Fulvio Parmigiani, Vincent Polewczyk, Phil D. C. King, Justin W. Wells, Ilija Zeljkovic, Pietro Carrara, Giorgio Rossi, Jun Fujii, Ivana Vobornik, Stephen D. Wilson, Ronny Thomale, Tim Wehling, Giorgio Sangiovanni, Giancarlo Panaccione, Federico Cilento, Domenico Di Sante and Federico Mazzola, "Dynamics and Resilience of the Charge Density Wave in a bilayer kagome metal". Commun. Mater. 4, 103 (2023).

4. Davide Soranzio, Denny Puntel, **Manuel Tuniz**, Paulina E. Majchrzak, Alessandra Milloch, Nicholas M. Olsen, Wibke Bronsch, Bjarke S. Jessen, Danny Fainozzi, Jacopo S. Pelli Cresi, Dario De Angelis, Laura Foglia, Riccardo Mincigrucci, Xiaoyang Zhu, Cory R. Dean, Søren Ulstrup, Francesco Banfi, Claudio Giannetti, Fulvio Parmigiani, Filippo Bencivenga, and Federico Cilento, "Impact of a MoS_2 monolayer on the nanoscale thermoelastic response of silicon heterostructures". ACS Appl. Nano Mater. (2024).

5. Wibke Bronsch, **Manuel Tuniz**, Denny Puntel, Alessandro Giammarino, Fulvio Parmigiani, Yanghao Chan, and Federico Cilento, "Ultrafast Band Structure Dynamics in Bulk 1T-VSe_2". Preprint at arXiv:2403.18046 (2024).

6. Denny Puntel, Wibke Bronsch, **Manuel Tuniz**, Mingu Kang, Paul M. Neves, Shiang Fang, Efthimios Kaxiras, Joseph G. Checkelsky, Riccardo Comin, Fulvio Parmigiani, and Federico Cilento, "Photoinduced dynamics of flat bands in the kagome metal CoSn". Phys. Rev. B 109, L081104 (2023).

7. Paulina Ewa Majchrzak, Yuntian Liu, Klara Volckaert, Deepnarayan Biswas, Chakradhar Sahoo, Denny Puntel, Wibke Bronsch, **Manuel Tuniz**, Federico Cilento, Xing-Chen Pan, Qihang Liu, Yong P. Chen, and Søren Ulstrup, "Van der Waals Engineering of Ultrafast Carrier Dynamics in Magnetic Heterostructures". Nano Lett. 23, 2, 414-421 (2023).

8. Stefania Baronio, Valeria De Leo, Ginevra Lautizi, Paola Mantegazza, Eleonora Natale, **Manuel Tuniz**, Stefano Vigneri, Luca Bignardi, Paolo Lacovig, Silvano Lizzit, and Alessandro Baraldi, "Vibrational Fine Structure in C 1s High-Resolution Core-Level Spectra of CO Chemisorbed on Ir(111)". The Journal of Physical Chemistry C, 126, 3 (2022).

9. Wibke Bronsch, **Manuel Tuniz**, Giuseppe Crupi, Michela de Col, Denny Puntel, Davide Soranzio, Alessandro Giammarino, Michele Perlangeli, Dario de Angelis, Danny Fainozzi, Ettore Paltanin, Stefano Peli Cresi, Riccardo Mincigrucci, Laura Foglia, Fulvio Parmigiani, Filippo Bencivenga, and Federico Cilento, "Ultrafast dynamics in $(TaSe_4)_2I$ triggered by valence and core-level excitations". Faraday Discuss. 237 (2022).

In preparation:

- **Manuel Tuniz**, Denny Puntel, Wibke Bronsch, Francesco Sammartino, Fulvio Parmigiani, Massimo Capone and Federico Cilento, "Ultrafast quench of the electronic order in VTe_2 by enhanced lattice fluctuations".
- Federico Mazzola, Wojciech Brzezicki, Chiara Bigi, Armando Consiglio, Luciano Jacopo D'Onofrio, Maria Teresa Mercaldo, Adam Klosinski, Francois Bertran, Patrick Le Fevre, Oliver J. Clark, **Manuel Tuniz**, Alessandro De Vita, Jeppe B. Jacobsen, Kim Lefmann, Henrik Jacobsen, Jill A. Miwa, Justin W. Wells, Anupam Jana, Ivana Vobornik, Jun Fujii, Fabio Miletto Granozio, Giorgio Sangiovanni, Brenden R. Ortiz, Ganesh Pokharel, Stephen D. Wilson, Domenico Di Sante, Carmine Ortix, and Mario Cuoco, "Anomalous spin-optical chiral effect in Ti-based kagome metal".
- Valentina Gosetti, Jorge Cervantes-Villanueva, Selene Mor, Davide Sangalli, Alejandro Molina-Sánchez, V. F. Agekyan, **Manuel Tuniz**, Denny Puntel, Wibke Bronsch, Federico Cilento and Stefania Pagliara, "Following the early-stage exciton dynamics in a multidimensional space".